Nonconforming Immersed Finite Element Methods for Interface Problems

Xu Zhang

Dissertation submitted to the Faculty of the
Virginia Polytechnic Institute and State University
in partial fulfillment of the requirements for the degree of

Doctor of Philosophy
in
Mathematics

Tao Lin, Chair
Slimane Adjerid
Eric de Sturler
Yuriko Renardy

April 4, 2013
Blacksburg, Virginia

Keywords: Immersed Finite Element, Elliptic Interface Problems, Cartesian Mesh, Nonconforming Rotated Q_1 Finite Element, Error Analysis, Elasticity Interface Problems, Moving Interface Problems, Discontinuous Galerkin Methods

Nonconforming Immersed Finite Element Methods for Interface Problems

Xu Zhang

(ABSTRACT)

In science and engineering, many simulations are carried out over domains consisting of multiple materials separated by curves/surfaces. If partial differential equations (PDEs) are used to model these simulations, it usually leads to the so-called interface problems of PDEs whose coefficients are discontinuous. In this dissertation, we consider nonconforming immersed finite element (IFE) methods and error analysis for interface problems.

We first consider the second order elliptic interface problem with a discontinuous diffusion coefficient. We propose new IFE spaces based on the nonconforming rotated Q_1 finite elements on Cartesian meshes. The degrees of freedom of these IFE spaces are determined by midpoint values or average integral values on edges. We investigate fundamental properties of these IFE spaces, such as unisolvency and partition of unity, and extend well-known trace inequalities and inverse inequalities to these IFE functions. Through interpolation error analysis, we prove that these IFE spaces have optimal approximation capabilities.

We use these IFE spaces to develop partially penalized Galerkin (PPG) IFE schemes whose bilinear forms contain penalty terms over interface edges. Error estimation is carried out for these IFE schemes. We prove that the PPG schemes with IFE spaces based on integral-value degrees of freedom have the optimal convergence in an energy norm. Following a similar approach, we prove that the interior penalty discontinuous Galerkin schemes based on these IFE functions also have the optimal convergence. However, for the PPG schemes based on midpoint-value degrees of freedom, we prove that they have at least a sub-optimal convergence. Numerical experiments are provided to demonstrate features of these IFE methods and compare them with other related numerical schemes.

We extend nonconforming IFE schemes to the planar elasticity interface problem with discontinuous Lamé parameters. Vector-valued nonconforming rotated Q_1 IFE functions with integral-value degrees of freedom are unisolvent with appropriate interface jump conditions. More importantly, the Galerkin IFE scheme using these vector-valued nonconforming rotated Q_1 IFE functions are "locking-free" for nearly incompressible elastic materials.

In the last part of this dissertation, we consider potential applications of IFE methods to time dependent PDEs with moving interfaces. Using IFE functions in the discretization in space enables the applicability of the method of lines. Crank-Nicolson type fully discrete schemes are also developed as alternative approaches for solving moving interface problems.

This work received support from NSF grants DMS-0713763 and DMS-1016313.

Dedication

To Yi and Olivia.

Acknowledgments

I would like to take this opportunity to look over the past five years and remember all the friends and family who helped and supported me along this fulfilling journey.

First of all, I want to express my heartfelt gratitude to my advisor, Dr. Tao Lin, who led me into this exciting finite element world. His constant guidance and support have greatly helped me work through numerous challenging problems. His integrity and enthusiasm inspire me to become better as a scholar, an educator, and a person. I hope that one day I would become as good an advisor to my students as Dr. Lin has been to me.

Members of Ph.D. committee Dr. Slimane Adjerid, Dr. Eric de Sturler, and Dr. Yuriko Renardy deserve my sincerest thanks. I have learned a lot from each of them and I am grateful for their valuable advises and insightful comments on my research and dissertation.

I am thankful to Dr. Oleg Roderick for offering me a wonderful summer research experience at Argonne National Laboratory and leading me to the uncertainty quantification research. I would also like to thank Dr. Yanping Lin, Dr. Dongwoo Sheen, Dr. Xiaoming He, and Dr. Zhu Wang for their help and collaboration in various research projects.

Special thanks to Ms. Eileen Shugart, Ms. Margaret McQuain and Dr. Donald McKeon for being my teaching mentors for the past years and sharing a lot of their valuable experiences with me.

I wish to express my sincerest gratitude to my parents. Their constant support provides inspiration and driving force for me to pursue in the academic road.

I am thankful to my wife Yi, without whom, the dissertation could not be completed. I will always appreciate her love and support, sometimes even sacrifices to help me focus on my work.

Contents

List of Figures **vii**

List of Tables **x**

1 Introduction **1**

1.1 Interface Problems and Their Applications 1

1.2 Survey of Numerical Methods for Interface Problems 3

1.3 Survey of Previous Work for Immersed Finite Element Methods 4

1.4 Motivations to Study Nonconforming IFE Methods 12

1.5 Outline of the Dissertation 14

2 Nonconforming IFE Spaces **16**

2.1 Preliminaries and Notations 16

2.2 Nonconforming Rotated Q_1 Functions 18

2.3 Nonconforming IFE Space $S_h^P(\Omega)$ 20

2.4 Nonconforming IFE Space $S_h^I(\Omega)$ 24

3 Properties of IFE Spaces **29**

3.1 Fundamental Properties 29

3.2 Approximation Capabilities 39

3.2.1 Error Analysis of Interpolation on $S_h^P(\Omega)$ 40

3.2.2 Error Analysis of Interpolation on $S_h^I(\Omega)$ 53

3.3 Numerical Experiments 55

4 IFE Methods and Error Estimation **58**

4.1 IFE Methods 58

4.1.1 Galerkin IFE Methods 59

4.1.2 Partially Penalized Galerkin IFE Methods 60

4.1.3 IPDG IFE Methods 63

4.2 Error Estimation 64

4.2.1 Error Estimation for PPG IFE Solutions in $S_h^I(\Omega)$ 64

4.2.2 Error Estimation for IFE Solutions in $S_h^P(\Omega)$ 79

4.2.3 Error Estimation for IPDG IFE Solutions 87

4.3 Discussions on Related Schemes 92

5 Nonconforming IFE Methods for Elasticity Interface Problems **103**

5.1 Introduction 104

5.2 Vector-Valued Nonconforming IFE Spaces 107

5.2.1 Nonconforming IFE functions 108

5.2.2 Properties of Nonconforming Rotated Q_1 IFE Spaces 113

5.2.3 Interpolation and Galerkin Method 116

5.3 Numerical Experiments 118

6 Applications of IFEs to Moving Interface Problems **127**

6.1 Introduction 128

6.2 IFE Method of Lines Semi-Discrete Schemes 130

6.3 Crank-Nicolson IFE Fully Discrete Algorithms 135

6.4 Implementation for Moving Interfaces 139

6.5 Numerical Experiments 143

7 Future Work **154**

Bibliography **156**

List of Figures

1.1 A sketch of solution domain for interface problems. 2

1.2 Comparison of a body-fitting triangular mesh (left) and non-body-fitting rectangular (middle) and triangular (right) meshes. 3

1.3 One dimensional linear IFE local basis functions 5

1.4 One dimensional quadratic IFE local basis functions 6

1.5 One dimensional cubic IFE local basis functions. 6

1.6 One dimensional linear, quadratic, and cubic IFE global basis functions. . . . 6

1.7 Interface edges (marked by red color) on a Cartesian mesh. 8

1.8 Two dimensional linear FE (left) and IFE (right) local basis functions. . . . 8

1.9 Two dimensional linear FE (left) and IFE (right) global basis functions. . . . 9

1.10 Two dimensional bilinear FE/IFE local basis functions. From left to right: FE basis, Type I IFE basis, Type II IFE basis. 10

1.11 Two dimensional bilinear FE (left) and IFE (right) global basis functions. . . 10

1.12 The left plot is a rectangular domain with a circular interface. The right plot is the point-wise error of a bilinear IFE solution to an elliptic interface problem define on the geometry on the left. 14

2.1 A non-interface rectangular element. 18

2.2 Type I interface rectangles: Case 1,2,3 (midpoint-value degrees of freedom). . 21

2.3 Type II interface rectangles: Case 1,2 (midpoint-value degrees of freedom). . 21

2.4 Nonconforming rotated Q_1 FE (left), Type I (middle) and Type II (right) IFE local basis functions with midpoint-value degrees of freedom. 23

2.5 Nonconforming rotated Q_1 FE (left) and IFE (right) global basis functions with midpoint-value degrees of freedom. 24

2.6 Type I and Type II interface rectangles (integral-value degrees of freedom). . 25

2.7 Nonconforming rotated Q_1 FE (left), Type I (middle) and Type II (right) IFE local basis functions with integral-value degrees of freedom. 27

2.8 Nonconforming rotated Q_1 FE (left) and IFE (right) global basis functions with integral-value degrees of freedom. 28

3.1 A sketch of interface rectangle: Type I, Case 2. 42

3.2 Points selected to calculate the L^∞ norm on a rectangular element T. 56

4.1 Comparison of errors in different nonconforming rotated Q_1 IFE methods with $\beta^- = 1$, $\beta^+ = 10$. 94

4.2 Point-wise error comparison of Galerkin solution and NPPG solution u_h^P. . . 95

4.3 Point-wise error comparison of Galerkin solution and NPPG solution u_h^I. . . 97

4.4 Point-wise error comparison of bilinear Galerkin IFE solution and NPPG IFE solution u_h. 99

4.5 Comparison of errors in different Galerkin IFE methods. 100

4.6 Comparison of errors in different NPPG IFE methods. 100

4.7 Comparison of discontinuity for different IFE global basis functions with fixed value $\beta^- = 1$ and different values of $\beta^+ = 1, 5, 1000$. 101

5.1 The domain of planar elasticity interface problems. 104

5.2 A vector-valued nonconforming rotated Q_1 finite element local basis function. 112

5.3 A vector-valued nonconforming rotated Q_1 IFE local basis function on a Type I interface element. 112

5.4 A vector-valued nonconforming rotated Q_1 IFE local basis function on a Type II interface element. 113

5.5 Errors of bilinear IFE solutions and nonconforming rotated Q_1 IFE solutions u_{1h}. From left to right: L^∞, L^2, H^1 norms. 121

5.6 A comparison of body-fitting triangular mesh with a non-body-fitting Cartesian mesh for a boundary layer problem. 125

5.7 Errors of nonconforming rotated Q_1 IFE solutions $\mathbf{u}_h$ for the boundary layer example in different norms. 126

6.1 Solution domain of moving interface problems. 128

6.2 A body-fitting triangular mesh (left) and a non-body-fitting triangular Cartesian mesh (right). 131

6.3 A sketch of the interface configuration in a triangle at time t. 141

6.4 Cases of interface triangle cut by two interface line segments that intersect inside the triangle. 143

6.5 Cases of interface triangle cut by two interface line segments that intersect outside the triangle. 143

6.6 Cases of Type I interface rectangle cut by two interface line segments that intersect inside the rectangle. 143

6.7 Cases of Type I interface rectangle cut by two interface line segments that intersect outside the rectangle. 143

6.8 Cases of Type II interface rectangle cut by two interface line segments that intersect inside the rectangle. 144

6.9 Cases of Type II reference rectangle cut by two interface line segments that intersect outside the rectangle. 144

6.10 The left plot shows how the radius $r(t)$ of the interface circle $\Gamma(t)$ changes; the right plot is for the time step sizes used by the IFE-MoL combined with the adaptive DIRK45 ODE solver. 148

6.11 The left plot contains curves of L^∞ norm error for three IFE solutions generated on the same mesh with $h = 1/64$. The right plot is the enlarged part for time between 0.8 to 1. 149

List of Tables

3.1 Errors of IFE interpolations $I_h^I u$ with $\beta^- = 1$, $\beta^+ = 10$. 56

3.2 Errors of IFE interpolations $I_h^P u$ with $\beta^- = 1$, $\beta^+ = 10$. 57

3.3 Errors of IFE interpolations $I_h^I u$ with $\beta^- = 1$, $\beta^+ = 10000$. 57

3.4 Errors of IFE interpolations $I_h^P u$ with $\beta^- = 1$, $\beta^+ = 10000$. 57

4.1 Errors of NPPG IFE solutions $u - u_h^I$ with $\beta^- = 1$, $\beta^+ = 10$. 78

4.2 Errors of SPPG IFE solutions $u - u_h^I$ with $\beta^- = 1$, $\beta^+ = 10$. 78

4.3 Errors of IPPG IFE solutions $u - u_h^I$ with $\beta^- = 1$, $\beta^+ = 10$. 78

4.4 Errors of NPPG IFE solutions $u - u_h^I$ with $\beta^- = 1$, $\beta^+ = 10000$. 79

4.5 Errors of SPPG IFE solutions $u - u_h^I$ with $\beta^- = 1$, $\beta^+ = 10000$. 79

4.6 Errors of IPPG IFE solutions $u - u_h^I$ with $\beta^- = 1$, $\beta^+ = 10000$. 80

4.7 Errors of NPPG IFE solutions $u - u_h^P$ with $\beta^- = 1$, $\beta^+ = 10$. 88

4.8 Errors of SPPG IFE solutions $u - u_h^P$ with $\beta^- = 1$, $\beta^+ = 10$. 88

4.9 Errors of IPPG IFE solutions $u - u_h^P$ with $\beta^- = 1$, $\beta^+ = 10$. 88

4.10 Errors of NIPDG IFE solutions $u - u_h^{DG}$ with $\beta^- = 1$, $\beta^+ = 10$. 92

4.11 Errors of SIPDG IFE solutions $u - u_h^{DG}$ with $\beta^- = 1$, $\beta^+ = 10$. 93

4.12 Errors of IIPDG IFE solutions $u - u_h^{DG}$ with $\beta^- = 1$, $\beta^+ = 10$. 93

4.13 Errors of Galerkin IFE solutions $u - u_h^P$ with $\beta^- = 1$, $\beta^+ = 10$. 94

4.14 Errors of Galerkin IFE solutions $u - u_h^I$ with $\beta^- = 1$, $\beta^+ = 10$. 95

4.15 Errors of Galerkin IFE solutions $u - u_h^I$ with $\beta^- = 1$, $\beta^+ = 10000$. 96

4.16 Errors of bilinear Galerkin IFE solutions $u - u_h$ with $\beta^- = 1$, $\beta^+ = 10$. . . . 97

4.17 Errors of bilinear NPPG IFE solutions $u - u_h$ with $\beta^- = 1$, $\beta^+ = 10$. 98

4.18 Errors of bilinear SPPG IFE solutions $u - u_h$ with $\beta^- = 1$, $\beta^+ = 10$. 98

4.19 Errors of bilinear IPPG IFE solutions $u - u_h$ with $\beta^- = 1$, $\beta^+ = 10$. 98

5.1 Errors of nonconforming rotated Q_1 IFE interpolations and Galerkin IFE solutions with $\lambda^+ = 5$, $\lambda^- = 1$, $\mu^+ = 10$, $\mu^- = 2$, $\nu^\pm = 0.1667$. 120

5.2 Errors of nonconforming rotated Q_1 IFE interpolations and Galerkin IFE solutions with $\lambda^+ = 100$, $\lambda^- = 1$, $\mu^+ = 200$, $\mu^- = 2$, $\nu^\pm = 0.1667$. 120

5.3 Errors of nonconforming rotated Q_1 IFE interpolations and Galerkin IFE solutions with $\lambda^+ = 1$, $\lambda^- = 100$, $\mu^+ = 2$, $\mu^- = 200$, $\nu^\pm = 0.1667$. 121

5.4 Errors of bilinear and nonconforming rotated Q_1 Galerkin IFE solutions in "locking" test with $\lambda^+ = 20$, $\lambda^- = 1$, $\mu^+ = 0.02$, $\mu^- = 0.001$, $\nu^\pm \approx 0.4995$. . . 122

5.5 Errors of bilinear and nonconforming rotated Q_1 Galerkin IFE solutions in "locking" test with $\lambda^+ = 200$, $\lambda^- = 1$, $\mu^+ = 0.2$, $\mu^- = 0.001$, $\nu^\pm \approx 0.4995$. . . 122

5.6 Errors of nonconforming rotated Q_1 Galerkin IFE solutions for problems whose interfaces are at different locations. 124

5.7 Comparison of errors of the linear FE and nonconforming rotated Q_1 IFE solutions for the boundary layer example with $\lambda^+ = 2$, $\lambda^- = 1$, $\mu^+ = 3$, $\mu^- = 2$, $\nu^+ = 0.2, \nu^- \approx 0.1667$. 125

5.8 Errors of nonconforming rotated Q_1 IFE solutions for the boundary layer example with $\lambda^+ = 2$, $\lambda^- = 1$, $\mu^+ = 3$, $\mu^- = 2$, $\nu^+ = 0.2, \nu^- \approx 0.1667$. 126

5.9 Errors of nonconforming rotated Q_1 IFE solutions for the boundary layer example with $\lambda^+ = 2000$, $\lambda^- = 1000$, $\mu^+ = 3$, $\mu^- = 1$, $\nu^+ \approx 0.4993$, and $\nu^- \approx 0.4995$. 126

6.1 Errors of linear IFE solutions with $\beta^- = 1$ using DIRK2 at time $t = 1$. . . . 145

6.2 Errors of linear IFE solutions with $\beta^- = 1$, $\beta^+ = 2$ using 4th order schemes at time $t = 1$. 146

6.3 Errors of linear IFE adaptive DIRK45 solutions with $\beta^- = 0.5$, $\beta^+ = 2$ at time $t = 1$. 148

6.4 Errors of linear CN-IFE solutions with $\beta^- = 1$, $\beta^+ = 2$ and $\tau = h$ at time $t = 1$. 150

6.5 Errors of linear CN-IFE solutions with $\beta^- = 1$, $\beta^+ = 2$ and $\tau = \frac{1}{8}h$ at time $t = 1$. 151

6.6 Errors of linear CN-IFE solution with $\beta^- = 1$, $\beta^+ = 100$ and $\tau = \frac{1}{8}h$ at time $t = 1$. 152

6.7 Errors of linear IFE solutions in CN-IFE Algorithm 3 with $\beta^- = 1$ and $\beta^+ = 100$ at time $t = 1$. 152

6.8 Errors of linear IFE solution using CN-IFE-A1* with $\beta^- = 1$ and $\tau = h$ at time $t = 1$. 153

Chapter 1

Introduction

In this chapter, we start with the introduction to the typical second order elliptic interface problems and their applications. Next we provide a brief survey of numerical methods for interface problems and a short review of the recently developed immersed finite element (IFE) methods. Our motivations to work on nonconforming IFE methods are presented at the end of this chapter.

1.1 Interface Problems and Their Applications

We consider the classic second order elliptic interface problem that appears in many applications:

$$-\nabla \cdot (\beta \nabla u) = f, \quad \text{in } \Omega, \tag{1.1}$$

$$u = g, \quad \text{on } \partial\Omega, \tag{1.2}$$

where the physical domain $\Omega \subset \mathbb{R}^d$, $d = 1, 2, 3$, is assumed to be formed by multiple materials. Without loss of generality, we assume that the domain Ω is separated by an interface Γ into two sub-domains Ω^+, Ω^-, such that $\overline{\Omega} = \overline{\Omega^+ \cup \Omega^- \cup \Gamma}$, see Figure 1.1 for an illustration. Each sub-domain contains only one material. The coefficient function $\beta(X)$ is discontinuous across the interface Γ due to the change in material properties. For simplicity, we assume $\beta(X)$ is a piece-wise constant function defined by

$$\beta(X) = \begin{cases} \beta^-, & \text{if } X \in \Omega^-, \\ \beta^+, & \text{if } X \in \Omega^+, \end{cases} \tag{1.3}$$

where $\beta^-, \beta^+ > 0$. Across the interface Γ, the solution $u(x, y)$ is assumed to satisfy the jump conditions:

$$[u]_\Gamma = 0, \tag{1.4}$$

$$\left[\beta \nabla u \cdot \mathbf{n}\right]_\Gamma = 0, \tag{1.5}$$

where $\mathbf{n}$ is the unit normal vector of the interface Γ. Here, for every piece-wise function v defined as

$$v(X) = \begin{cases} v^-(X), & \text{if } X \in \Omega^-, \\ v^+(X), & \text{if } X \in \Omega^+, \end{cases}$$

we let $[v]_\Gamma = v^+|_\Gamma - v^-|_\Gamma$.

Figure 1.1: A sketch of solution domain for interface problems.

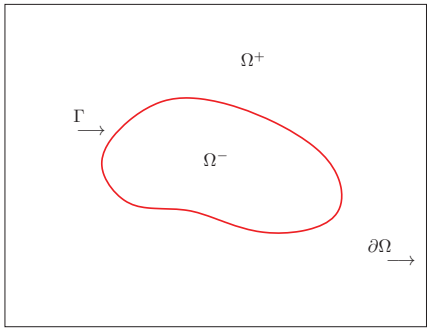

The elliptic interface problem arises in many applications, one of which is the plasma particle simulations in ion thruster optics [24, 83, 84]. An ion thruster is a type of electric propulsion device which emits a high-energy ion beam to propel a spacecraft. The standard algorithm to model a plasma is particle-in-cell (PIC) in which the the propellant beam ions are represented by macro particles. The trajectory of each ion plasma particle is determined by Newton's second law:

$$m\mathbf{p}_i'' = m\mathbf{a}_i = \mathbf{F}_i(\Phi), \qquad i = 1, 2, \cdots, M, \tag{1.6}$$

where $\mathbf{p}_i$ is the position of each particle, M is the total number of particles, and Φ is the electric potential. The electric field is governed by the elliptic equation:

$$-\nabla \cdot (\beta \nabla \Phi) = f(\Phi). \tag{1.7}$$

These two sets of equations are coupled through $\mathbf{F}(\Phi)$ and $f(\Phi)$ due to Lorentz force and other pertinent physical laws [83]. Note that the simulation domain of the electric fields is usually chosen as a three dimensional domain containing the ion thruster with parts formed by different materials under investigation; hence, this simulation domain consists of multiple materials and leads to the interface model problems (1.1) - (1.5).

Other applications for the elliptic interface problems include plasma simulations in spacecraft charging in space [69, 141], the projection methods to solve the Navier-Stokes problems involving multi-phase flows [40, 77], and topology optimization of heat conduction problems [56], to name just a few.

1.2 Survey of Numerical Methods for Interface Problems

A large number of numerical methods have been developed for interface problems such as finite difference (FD) methods and finite element (FE) methods. These conventional methods, especially finite element methods [26, 39, 149], can be applied to solve interface problems, provided that solution meshes are tailored to fit the interface; otherwise, the convergence of the numerical solutions might be impaired [9]. Such meshes are often called body-fitting, as illustrated in the left plot of Figure 1.2. Geometrically, the body-fitting restriction requires each element to be placed essentially on one side of a material interface. Physically, it means each element in a mesh to be occupied mainly by one of the materials.

Figure 1.2: Comparison of a body-fitting triangular mesh (left) and non-body-fitting rectangular (middle) and triangular (right) meshes.

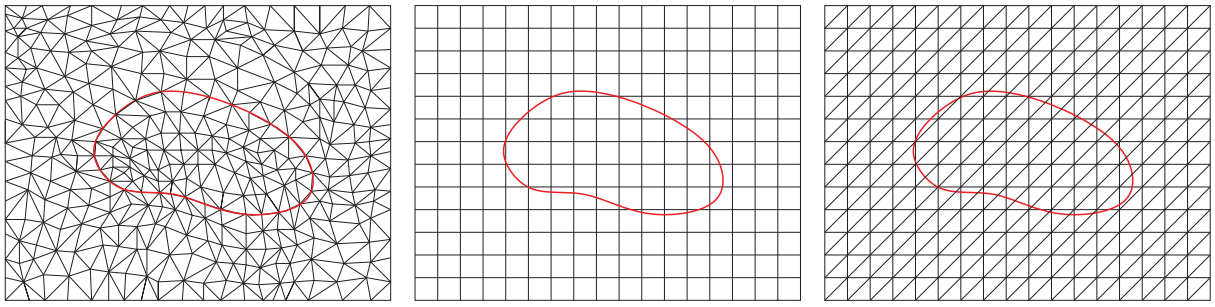

On the other hand, it is usually time consuming to generate a satisfactory body-fitting mesh for an interface problem in which the interface separating the materials is geometrically complicated. Such a difficulty becomes even more severe if the interface evolves in a simulation because a new mesh has to be generated for each of the material configurations to be considered. For many applications, it is therefore desirable to develop numerical methods that can be used with non-body-fitting meshes, such as the Cartesian meshes in the plot in the middle and on right in Figure 1.2, to solve interface problems. A Cartesian mesh can also be obviously advantageous in many simulations. Particle-In-Cell method for plasma particle simulations [83, 84, 106, 107] is a typical example that prefers the electric potential interface problem (1.7) to be solved on a Cartesian mesh for efficient particle tracking.

Many numerical methods based on Cartesian meshes have been developed for interface problems. In the finite difference formulation, Peskin developed *the immersed boundary method* [120, 121, 128] in 1977 to study flow patterns around heart valves. Since then, various finite difference schemes using Cartesian meshes were proposed, such as *the immersed interface method* [51, 90, 92, 94], *the ghost fluid method* [54, 111, 112], *the matched interface and boundary method* [154, 155, 156], and *the Cartesian grid method* [2, 32, 119], to name just a

few.

In the finite element formulation, special treatments need to be taken for elements around the interface. One way is to modify the weak formulation of finite element equations near the interface. *The penalty finite element method* [9, 18] penalizes the solution jump around interface. *The unfitted finite element method* [65, 66, 148] using Nitsche's scheme, modifies the bilinear form near interface by using the weighted average flux. *Discontinuous Galerkin formulation methods* [20, 63] penalize the interface jump conditions to solve interface problems.

Another approach is to modify the finite element functions around the interface. *The general finite element method* [10, 11, 14, 15] utilizes special shape functions to capture critical features of the unknown solution and they can be non-polynomials for some cases. *The multi-scale finite element method* [43, 52, 78] modifies the basis functions around the interface by solving an auxiliary "subgrid" problem. Other methods in this category include *the extended finite element method* [49, 80, 115, 135], *the partition of unity method* [12, 13, 17]. The recently proposed *immersed finite element methods* also fall into this framework. Since they are closely related with the research presented in this dissertation, we will give a more detailed introduction in the next section.

1.3 Survey of Previous Work for Immersed Finite Element Methods

Immersed finite element (IFE) methods have been developed for over a decade since the first article [93] was published. The main idea for IFE methods is to adapt finite element functions instead of solution meshes for interface problems. IFE methods can use non-body-fitting meshes for interface problems, such as Cartesian meshes, which are independent of the interface. Consequently the interface are allowed to cut the interior of elements, in other words, the interface can be immersed in some of the elements, and this is where the name "immersed" originated. In an IFE method, elements are divided into two categories: **interface elements**, whose interior intersects with the interface, and **non-interface elements**, consisting of the rest of elements. Standard finite element functions are utilized on non-interface elements, while special IFE functions are constructed on interface elements. According to the interface location, IFE functions are constructed in the form of piece-wise polynomials on interface elements to incorporate interface jump conditions.

In this section, we give a short review of previous work on IFE methods for different types of interface problems.

IFE Methods for One Dimensional Elliptic Interface Problems

In 1998, Li introduced a linear IFE method for one dimensional two-point boundary value problem with one interface point [93]:

$$-(\beta(x)u'(x))' + q(x)u(x) = f(x), \quad 0 < x < 1, \tag{1.8}$$

$$u(0) = 0, \quad u(1) = 0. \tag{1.9}$$

The jump condition at the interface $\alpha \in (0, 1)$ is given by:

$$[u(\alpha)] = 0, \quad [\beta u'(\alpha)] = 0. \tag{1.10}$$

To capture essential features of the solution across the interface, IFE basis functions on an interface element were defined by piece-wise linear polynomials satisfying interface jump conditions (1.10). To be more specific, on an interface element $T = (x_1, x_2)$, with $T^- = (x_1, \alpha)$ and $T^+ = (\alpha, x_2)$, the local linear IFE space was defined as follows:

$$S_h(T) = \{\phi : \phi|_{T^s} \in \mathcal{P}_1(T^s), s = +, -, \text{ and } [\phi(\alpha)] = 0, [\beta\phi'(\alpha)] = 0\}. \tag{1.11}$$

Local linear IFE basis functions ϕ_i, $i = 1, 2$ were chosen from $S_h(T)$ such that

$$\phi_i(x_j) = \delta_{ij}, \quad i, j = 1, 2. \tag{1.12}$$

IFE spaces formed by higher degree polynomials have been constructed. In particular, several types of quadratic IFE basis functions were introduced in [33, 99]. The approximation capability of corresponding IFE spaces was analyzed. IFE spaces with an arbitrary polynomial degree p were developed in [1].

Figure 1.3: One dimensional linear IFE local basis functions

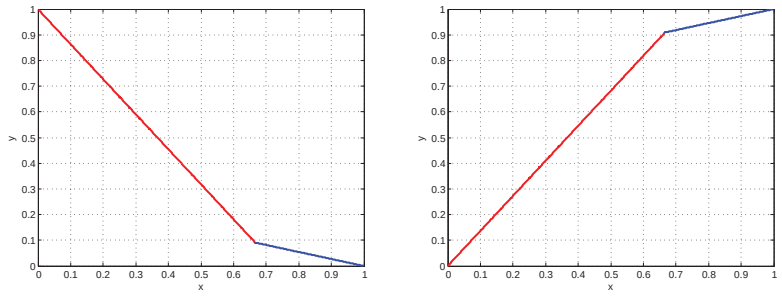

We illustrate the linear, quadratic and cubic IFE local basis functions in Figure 1.3, Figure 1.4, and Figure 1.5, respectively. Global IFE basis functions are illustrated in Figure 1.6.

These one dimensional IFE functions are continuous; hence, they are in $H^1(\Omega)$. A Galerkin scheme using any of these IFE spaces is a conforming finite element method. Approximation

Figure 1.4: One dimensional quadratic IFE local basis functions

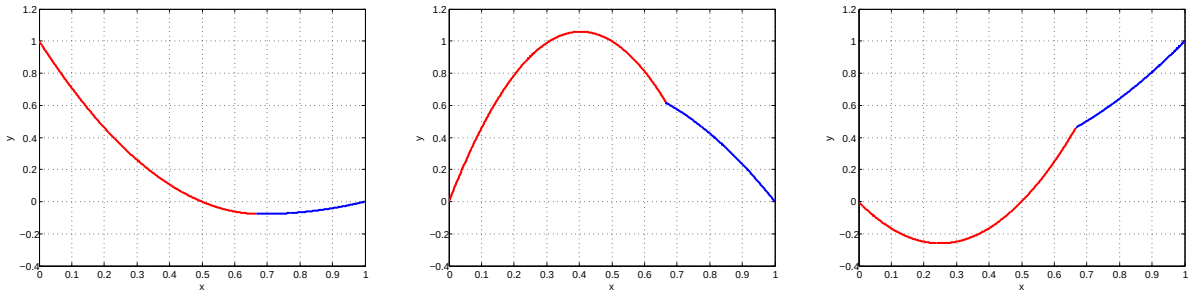

Figure 1.5: One dimensional cubic IFE local basis functions.

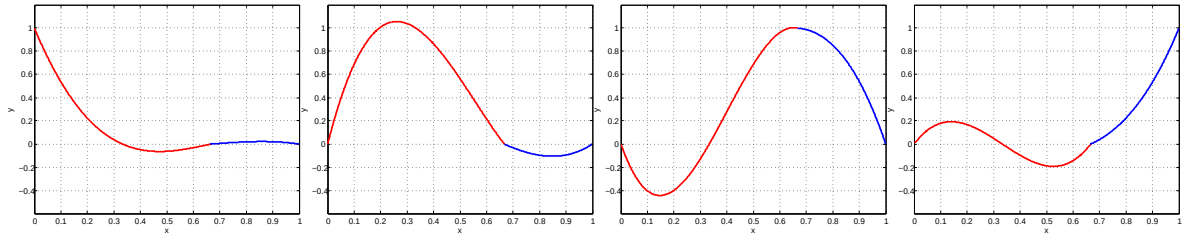

Figure 1.6: One dimensional linear, quadratic, and cubic IFE global basis functions.

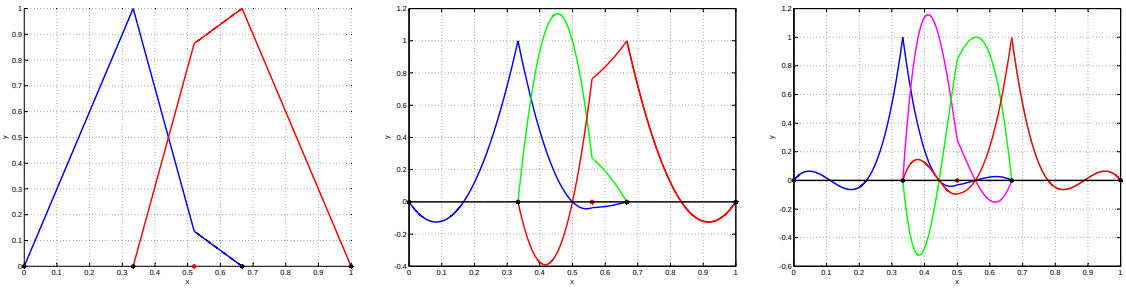

capabilities of these IFE spaces and error estimates of related IFE solutions have been proved to be optimal in both L^2 and H^1 norms [1]. We recall their results in the following two theorems. Let

$$\tilde{H}^p(\Omega) = \left\{ u \in C(\Omega) : u|_{\Omega^s} \in H^{p+1}(\Omega^s), s = +, -, \text{ and } \left[\beta u^{(j)}(\alpha)\right] = 0,\ j = 1, 2, \cdots, p \right\}.$$

Theorem 1.1. *There exists a constant C independent of interface α, such that for all $u \in$*

$\tilde{H}^p(\Omega)$

$$\|I_p u - u\|_0 + h\|I_p u - u\|_1 \leq C\frac{4^p}{(p-1)!}h^{p+1}|u|_{p+1}. \tag{1.13}$$

Here $I_p u$ is the p-th degree IFE interpolation of u.

Theorem 1.2. *There exists a constant C independent of interface α, such that*

$$\|u_h - u\|_0 + h\|u_h - u\|_1 \leq C\frac{4^p}{(p-1)!}h^{p+1}|u|_{p+1}. \tag{1.14}$$

Here u_h is the p-th degree IFE solution for 1D elliptic interface problems, and $u \in \tilde{H}^p(\Omega)$ is the solution to the interface problem defined by (1.8)-(1.10).

IFE Methods for Two Dimensional Elliptic Interface Problems

IFE methods for two dimensional elliptic interface problems have been extensively studied in the past decade, see for instance, [41, 42, 60, 61, 69, 70, 73, 87, 95, 96, 98, 130, 147], and the references therein.

Note that the above mentioned one dimensional IFE spaces [1, 93] are conforming, *i.e.*, each of these IFE function spaces is a subset of the trial function space $H^1(\Omega)$ of weak formulation of the elliptic interface problem. However, for higher dimensional cases, the global continuity of IFE functions cannot be guaranteed in general. In fact, locally imposing the interface jump condition on each interface element only guarantees the continuity of IFE functions within an element, but IFE functions are usually discontinuous across edges which are cut by interfaces as those edges marked by red color in Figure 1.7.

In [96], both conforming and nonconforming linear IFE methods have been developed on triangular meshes for the two dimensional elliptic interface problem. The nonconforming linear IFE space is a natural extension of the one dimensional IFE spaces to two dimensional case. The nonconforming IFE spaces have many advantages. First, the construction of IFE functions is rather straightforward because one only need to consider a single element and neglect the continuity between elements. Second, the resulting IFE linear system has the same structure as standard FE linear system on the same mesh, which makes efficient solvers for FEs applicable for solving interface problems. The disadvantages are due to its nonconformity which makes the error estimation more challenging.

On the other hand, in the conforming IFE method proposed in [96], to maintain the continuity along edges, each conforming IFE basis has an enlarged support and takes an average or a weighted average value of nonconforming IFE basis with the same values at nodal points. One benefit of the conforming IFEs is that convergence analysis can be established straightforward via *Céa's lemma* [44]. However, one obvious drawback is that the construction of its basis is more complicated than nonconforming linear IFE functions. Also, due to a larger

Figure 1.7: Interface edges (marked by red color) on a Cartesian mesh.

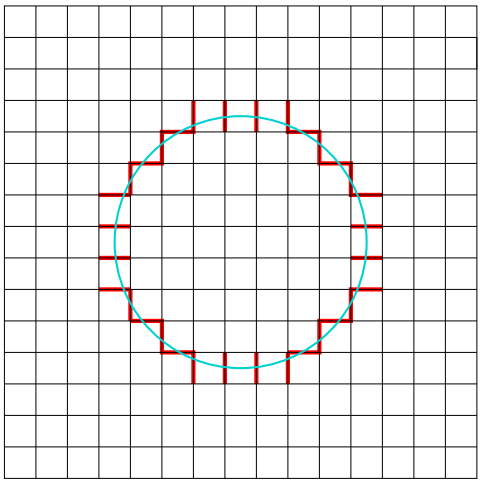

support of every global basis function, the global stiffness matrix is usually denser than the matrix from a nonconforming IFE method. Moreover, it is much more complicated to extend this conforming IFE method to deal with more complicated PDEs or using higher degree polynomials.

A comparison of the nonconforming linear FE and IFE local basis functions is illustrated in Figure 1.8. Global FE and IFE functions are illustrated in Figure 1.9. These plots demonstrate that linear IFE basis functions are continuous within an interface element, but discontinuous across interface edges.

Figure 1.8: Two dimensional linear FE (left) and IFE (right) local basis functions.

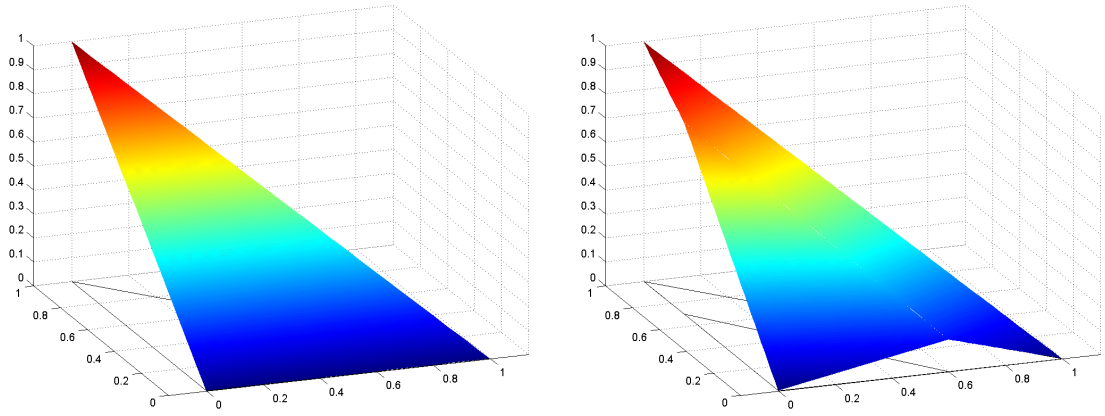

Figure 1.9: Two dimensional linear FE (left) and IFE (right) global basis functions.

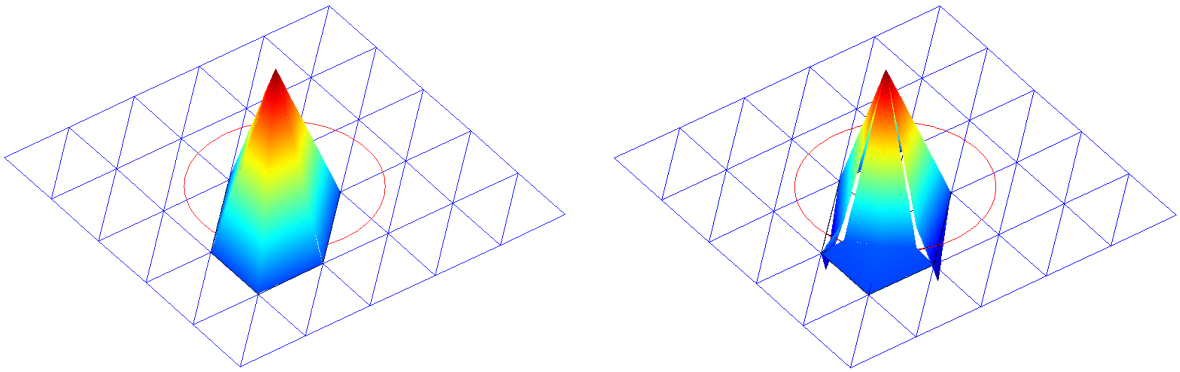

Approximation capabilities of the nonconforming linear IFE spaces was studied in [95]. Instead of using the standard scaling argument, the authors extended the multi-point Taylor expansion idea [28, 35] to prove that the Lagrange type IFE interpolation can achieve the optimal convergence orders $O(h^2)$ in L^2 norm and $O(h)$ in H^1 norm.

Higher degree IFEs for two dimensional elliptic interface problems based on triangular meshes were studied in [129]. Their numerical experiments suggested that interior penalty terms are required in the computational schemes in order to obtain the optimal convergence. For three dimensional elliptic interface problem, nonconforming linear IFE spaces based on tetrahedra meshes were constructed and applied to plasma simulation based on the particle-in-cell formulation [82, 84].

When the solution domain is rectangular or polygonal that can be divided into several rectangles, it is often preferable and more natural to use a Cartesian mesh formed by rectangles, see right plot in Figure 1.2 as an illustration. A bilinear IFE space on the Cartesian rectangular meshes was introduced in [98]. Note that an interface curve may intersect a rectangle at two adjacent edges of a rectangle or at two opposite edges of the rectangle. Procedures of constructing bilinear IFE functions on these two types of interface rectangles were discussed [70, 98].

Comparisons of local and global bilinear FE and IFE basis are illustrated in Figure 1.10 and Figure 1.11, respectively. Again, these bilinear IFE spaces are nonconforming because functions in these spaces are not continuous across interface edges as illustrated by the plot in the right in Figure 1.11. Approximation capabilities of the bilinear IFE spaces were studied in [69, 70]. Their analysis indicated that bilinear IFE spaces retain optimal approximation capabilities in L^2 and H^1 norms as the standard bilinear FE spaces. These bilinear IFE functions have been used in Galerkin method [69], interior penalty discontinuous Galerkin method [72], and finite volume method [71] for solving elliptic interface problems. For three dimensional elliptic interface problem, a trilinear IFE method has been developed for solving

the electroencephalography forward problem on parallelepiped meshes [139].

For elliptic interface problems with nonhomogeneous flux jump, local IFE spaces were enriched by adding another piece-wise polynomial function which vanishes at all nodes but with discontinuous flux [73]. An alternative approach to handle nonhomogeneous flux jump was introduced in [61].

Figure 1.10: Two dimensional bilinear FE/IFE local basis functions. From left to right: FE basis, Type I IFE basis, Type II IFE basis.

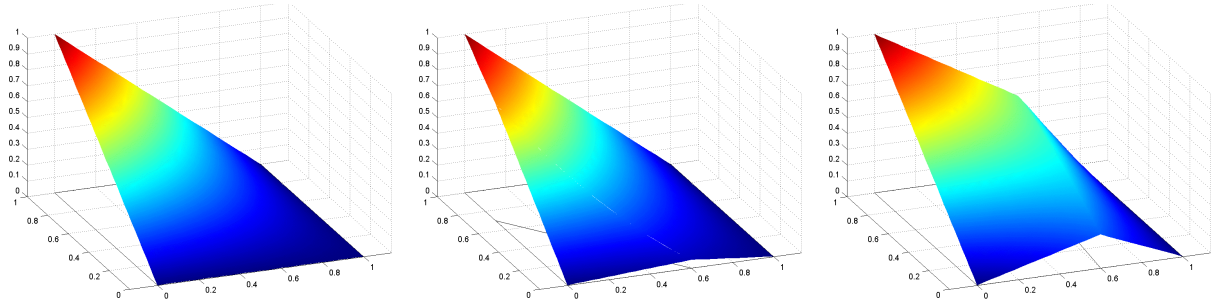

Figure 1.11: Two dimensional bilinear FE (left) and IFE (right) global basis functions.

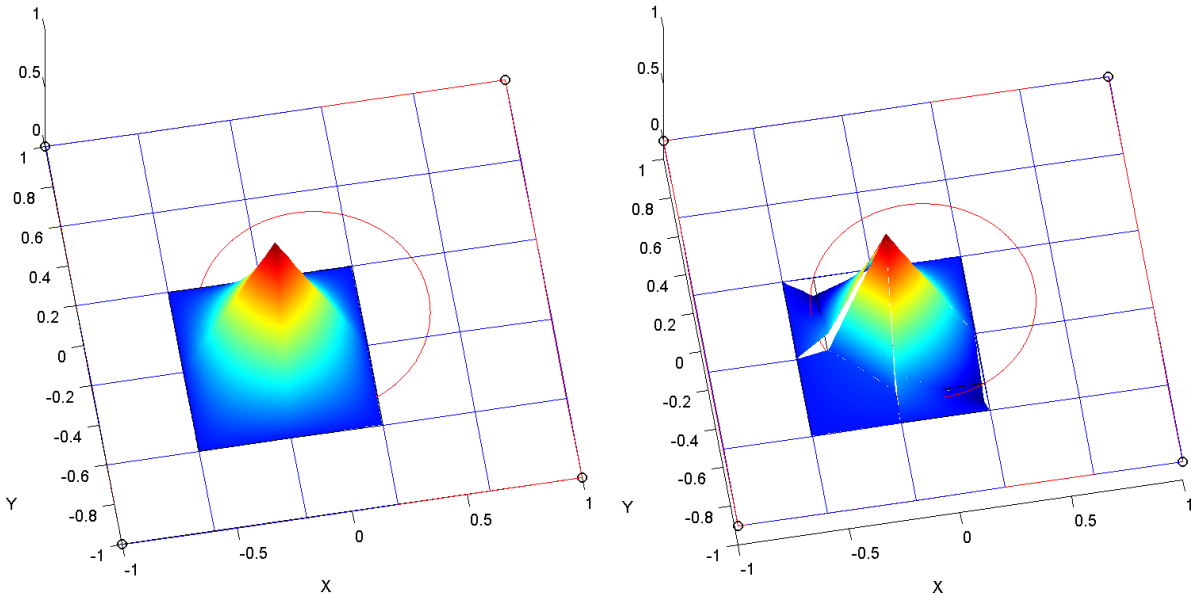

IFE Methods for Other Interface Problems

IFE methods have been extended to other types of interface problems involving a system of PDEs, time dependent PDEs, and higher order PDEs.

For planar elasticity interface problems, a nonconforming linear IFE method based on the triangular Cartesian mesh was presented in [60, 97, 150] and the authors concluded that this method has at least $O(h)$ convergence in L^∞ norm. In [60, 62], the authors developed a conforming linear IFE method where the optimal convergence rate in L^∞ norm was observed. However, in this conforming IFE configuration, global IFE basis functions have a rather complicated and larger support around the interface. In [108], a nonconforming bilinear IFE method was developed for the elasticity interface problems. The authors studied error behaviors for both linear and bilinear IFE methods in L^2 and H^1 norms. More importantly, they discovered that linear and bilinear IFE functions for elasticity interface problems do not always have the unisolvent property. As a result, in some configurations of interface location elasticity materials, linear and bilinear IFE functions cannot be constructed. Also in [108], the authors analyzed the unisolvent property and proposed an approach to identify a class of elastic materials for which the linear and bilinear IFE functions are guaranteed to be uniquely constructed. Their analysis indicated that the bilinear IFE functions are guaranteed to be applicable for elasticity interface problems for a larger class of elasticity material configurations than linear IFE functions.

For time dependent problems, IFE methods have been used to solve the parabolic interface problems with static interfaces. In [8] the authors proposed a backward Euler scheme using IFEs to solve a semi-linear parabolic interface problem and studied corresponding error estimation. In [104], a novel approach was proposed using IFEs together with the Laplace transform to solve a parabolic interface problem. Unlike classic time-marching algorithms, for which solution on new time step necessitates information from previous time step, the Laplace transformation in time led to a set of Helmholtz-like interface problems independent of each other, which can be solved with IFE functions in parallel. In [142], an immersed Eulerian-Lagrangian localized adjoint method was developed for transient advection-diffusion interface problems.

IFE methods have been used also for time dependent problems with moving interfaces. In [75], the authors developed several fully discrete Crank-Nicolson (CN) type IFE algorithms for solving parabolic equation with moving interfaces. All of these algorithms have been observed to have optimal convergence rates. These CN-IFE algorithms are consistent with the standard CN-FE scheme for the parabolic equation in the sense that they become the standard CN scheme if the coefficient function is continuous or if the interface Γ does not change with time and a body-fitting mesh is used. In [102], the authors demonstrated that IFEs methods can be used together with the method of lines (MoL) to solve parabolic interface problems. They observed that using IFEs and a suitably chosen ODE solver can efficiently and reliably solve parabolic moving interface problems on a fixed Cartesian mesh. In particular, an adaptive IFE-MoL scheme can be a very effective and efficient approach for

a moving interface problem where the interface changes with respect to time in a complicated way. The IFE-MoL schemes were extended to handle the non-homogeneous flux jump in a moving interface problem [101].

For interface problems involving fourth order PDEs, IFE methods were used to solve the one dimensional beam interface problem and the two dimensional bi-harmonic interface problem [100]. To avoid using higher degree polynomials ($p \geq 2$), these methods used a mixed formulation with linear IFE functions.

1.4 Motivations to Study Nonconforming IFE Methods

This dissertation focuses on nonconforming IFE methods for interface problems. First we would like to clarify the terminology *nonconforming*. The nonconforming here is different from the one used traditionally in the finite element literatures. Note that most of the two and three dimensional IFE spaces in the literatures, except for the only one in [96], are nonconforming in the traditional sense because their IFE functions are discontinuous across interface edges. However, these nonconforming IFE spaces are constructed using linear or bilinear polynomials with their degrees of freedom determined by the nodal values on vertices, which is a key ingredient for "conforming" finite elements. In this dissertation, we propose new IFE spaces with their DOF determined by the midpoint values or average integral values over edges, which are nonconforming finite element ideas.

One can see this difference from another point of view. IFE spaces can be viewed as locally modified finite element spaces for interface problems in the sense that finite element functions are adjusted to satisfy interface jump conditions. Most of the IFE spaces in the literatures modify conforming finite element spaces such as the usual linear or bilinear finite element spaces. Functions in IFE spaces proposed in this dissertation are revised nonconforming finite element functions according to specific interface problems; hence, they are called nonconforming IFE spaces. To be specific, we adapt the simplest nonconforming finite elements on rectangular meshes, *i.e.* the nonconforming rotated Q_1 finite elements [36, 38, 85, 86, 123].

Nonconforming finite element methods have been widely used especially in the solid mechanics and fluid mechanics due to their better stability than conforming finite element methods. The simplest nonconforming finite element on a triangular mesh, known as *nonconforming P_1 element* or *Crouzeix-Raviart element*, was first introduced in 1973 by Crouzeix and Raviart [47]. The simplest nonconforming finite elements on a rectangular mesh are called *nonconforming rotated Q_1 elements* which were first introduced by Rannacher and Turek [123] for solving the Stokes problem. Degrees of freedom for these nonconforming finite elements are determined by

- the midpoint values on edges, or

- the average integral values over edges.

In the following discussion, we will use $S_h^P(\Omega)$ to denote the nonconforming FE/IFE space of the first type, with P in $S_h^P(\Omega)$ to emphasize that the degrees of freedom of this finite element is determined by **point** values. We will use $S_h^I(\Omega)$ to denote the nonconforming FE/IFE space of the second type, with I in $S_h^I(\Omega)$ to emphasize that the degrees of freedom of this finite element is determined by **integral** values over element edges. Note that the nonconforming P_1 element [47] coincides for both cases, i.e., $S_h^P(\Omega) = S_h^I(\Omega)$. For nonconforming rotated Q_1 finite elements, these two types are different.

Nonconforming finite element methods are used for solving elliptic problems [50, 85, 118] and elasticity problems [29, 53, 88]. We refer readers to [25, 28, 37, 44] and the reference therein for more details about nonconforming finite elements methods. In [87], Kwak, Wee and Chang developed IFE methods based on nonconforming P_1 finite element for the second order elliptic interface problem. According to the authors, the difficulty of dealing with nonconformity in the error analysis seems to be significantly reduced.

Our motivations to study nonconforming IFE methods are from three aspects. First, the convergence and error estimation for conforming type IFE methods are usually challenging. There have been a few attempts [42, 69, 74, 143] in the study of error estimates of linear [95] and bilinear IFE [70] solutions to the two dimensional elliptic interface problem. The difficulties in the analysis stem from the error estimation of the integrations over interface edges. The estimation is challenging because conforming type IFE functions, such as linear and bilinear IFE functions, are discontinuous across interface edges. Nonconforming finite elements, such as Crouzeix-Raviart element and rotated Q_1 element, impose the degrees of freedom, in other words the continuity of IFE functions, through edges instead of vertices; hence, we hope the continuity conditions of the IFE functions can be improved on interface edges. These nonconforming IFE functions with improved continuity condition may further help us in the error analysis of IFE methods.

The second motivation to study nonconforming IFE methods is with regard to improving the numerical performance. It has been observed that conforming type IFE solutions are not as accurate around the interface as places away from the interface. For instance, we plot the error of a bilinear IFE solution to an elliptic problem with a circular interface in Figure 1.12. The numerical solution error is observed to have the "crown" effect, *i.e.*, the bilinear IFE solution has much larger error near the interface than the rest of the domain. We guess this is caused by the poor continuity condition of conforming type IFE functions on interface edges. This might be the reason that the convergence of conforming type IFE solutions cannot achieve optimal rate in L^∞ norm. Since nonconforming finite elements strengthen continuity condition on edges, therefore we hope that using nonconforming IFE methods can eliminate this "crown" effect and improve the overall numerical performance.

The third motivation to study nonconforming IFE methods is that nonconforming finite elements are usually preferable to deal with more complicated PDEs arising from solid and

Figure 1.12: The left plot is a rectangular domain with a circular interface. The right plot is the point-wise error of a bilinear IFE solution to an elliptic interface problem define on the geometry on the left.

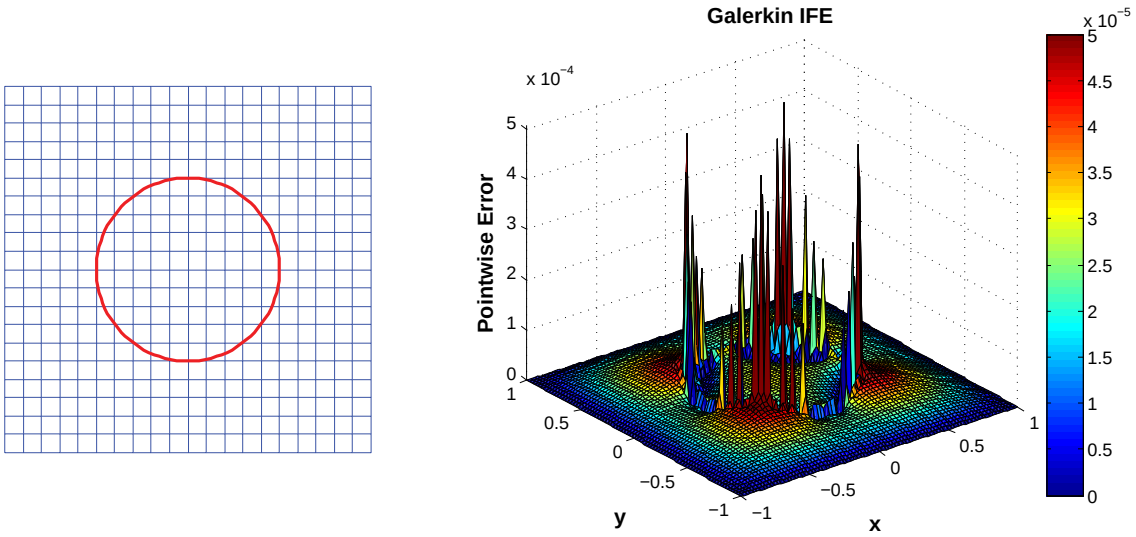

fluid mechanics due to their reliability and simplicity. In linear elasticity system, low order conforming FE methods usually encounter the so-called *"locking"* phenomenon as the elastic material becomes nearly incompressible [16, 45]. Nonconforming finite elements, on the other hand, are usually "locking" free and are tested to be more robust for these applications. In Stokes system, the fluid velocity field is assumed to be divergence free which characterizes an incompressible fluid flow. There are no conforming finite element spaces with piecewise polynomials of degree less than five that can satisfy the divergence free condition [37]; hence it is usually very expensive to use conforming finite element methods to solve Stokes equations. On the other hand, divergence free nonconforming finite element spaces can be constructed with lowest order polynomials, such as nonconforming P_1 element [27] on triangular meshes and nonconforming rotated Q_1 element [25, 37] on rectangular meshes. When we deal with interface problems involving more complicated PDE models such as the linear elasticity system and Stokes equations, it is desirable to develop IFE methods based on nonconforming rather than conforming finite elements.

1.5 Outline of the Dissertation

In this dissertation, we focus on the nonconforming rotated Q_1 IFE methods and their error analysis for elliptic and elasticity interface problems. The rest of the dissertation is organized

as follows.

In Chapter 2, we construct IFE spaces based on nonconforming rotated Q_1 finite elements on Cartesian meshes for second order elliptic interface problems. The discussion covers both midpoint value and integral value degrees of freedom of these IFE spaces.

In Chapter 3, we investigate properties of these nonconforming IFE spaces. Fundamental properties such as partition of unity, trace inequalities, and inverse inequalities are proved. The approximation capabilities of these IFE spaces will be analyzed via the error estimation of interpolations. Some numerical examples will be provided at the end of this chapter.

In Chapter 4, we develop numerical schemes based on nonconforming IFE spaces for solving the elliptic interface problems. Error estimation for these schemes will be carried out. Numerical experiments are provided to demonstrate features of these new IFE methods. Related numerical methods are compared at the end of this chapter.

In Chapter 5, we extend these nonconforming IFE methods to planar elasticity interface problems. We discuss how to construct vector-valued IFE spaces for the elasticity system and investigate fundamental features of these IFE spaces. Numerical examples are provided to demonstrate the "locking" free property of the new IFE methods.

In Chapter 6, we extend IFE methods to parabolic type moving interface problems. Both semi-discrete and fully discrete schemes are developed. Numerical results are provided to demonstrate performance of these schemes.

In Chapter 7, we briefly discuss our future research plan.

Chapter 2

Nonconforming IFE Spaces

In this chapter, we develop nonconforming IFE spaces $S_h^P(\Omega)$ and $S_h^I(\Omega)$ with midpoint-value and integral-value degrees of freedom, respectively. These new IFE functions are derived from the well-known nonconforming rotated Q_1 finite elements [123]. In Section 2.1, we introduce some preliminary results and notations that will be frequently used throughout this dissertation. In Section 2.2, we recall the basic framework of nonconforming rotated Q_1 finite elements which are used on non-interface elements of a Cartesian mesh. In Section 2.3, we construct local IFE spaces $S_h^P(T)$ on interface elements using the midpoint-value degrees of freedom, and then form the corresponding global IFE space $S_h^P(\Omega)$. In Section 2.4, we construct local IFE spaces $S_h^I(T)$ on interface elements using the integral-value degrees of freedom, and then form the corresponding global IFE space $S_h^I(\Omega)$.

2.1 Preliminaries and Notations

Throughout the dissertation, $\Omega \subset \mathbb{R}^2$ denotes a bounded domain formed by a union of rectangles. Let $\mathcal{D}(\Omega)$ denote the space of C^∞ functions with compact support in Ω. The dual space $\mathcal{D}'(\Omega)$ is the space of distributions. For any multi-index $\alpha = (\alpha_1, \alpha_2)$ and $|\alpha| = \alpha_1 + \alpha_2$, the weak derivative D^α is defined by [28]:

$$D^\alpha v(\phi) = (-1)^{|\alpha|} \int_\Omega v \frac{\partial^{|\alpha|}\phi}{\partial x^{\alpha_1} \partial y^{\alpha_2}} \mathrm{d}x\mathrm{d}y, \quad \forall\ \phi \in \mathcal{D}(\Omega).$$

We use the Sobolev space

$$W^{k,p}(\Omega) = \{v : \|v\|_{k,p,\Omega} < \infty\},$$

with non-negative integer index k and $1 \le p \le \infty$. The associated norm $\|\cdot\|_{k,p,\Omega}$ is defined

by

$$\|v\|_{k,p,\Omega} = \left(\sum_{|\alpha| \leq k} \|D^\alpha v\|_{0,p,\Omega}^p \right)^{1/p},$$

where

$$\|v\|_{0,p,\Omega} = \left(\int_\Omega |v|^p \mathrm{d}X \right)^{1/p},$$

in the case $1 \leq p < \infty$. If $p = \infty$, we define

$$\|v\|_{k,\infty,\Omega} = \max_{|\alpha| \leq k} \|D^\alpha v\|_{0,\infty,\Omega},$$

where

$$\|v\|_{0,\infty,\Omega} = \operatorname{ess\,sup}\{|v(X)| : X \in \Omega\}.$$

The Sobolev semi-norm $|\cdot|_{k,p,\Omega}$ associated with $W^{k,p}(\Omega)$ is defined by $|v|_{k,p,\Omega} = \|D^\alpha v\|_{0,p,\Omega}$, where $|\alpha| = k$. In the case $p = 2$, the Sobolev space $W^{k,p}(\Omega)$ becomes a Hilbert space and we denote it by $H^k(\Omega) = W^{k,2}(\Omega)$. We omit the index 2 in associated norms for simplicity, *i.e.* $\|v\|_{k,2,\Omega} = \|v\|_{k,\Omega}$, and $|v|_{k,2,\Omega} = |v|_{k,\Omega}$.

For interface problem, we assume that the physical domain $\Omega \subset \mathbb{R}^2$ is formed by multiple materials. Without loss of generality, Ω is assumed to be separated by an interface curve Γ into two sub-domains Ω^+, Ω^-, such that $\overline{\Omega} = \overline{\Omega^+ \cup \Omega^- \cup \Gamma}$, see Figure 1.1. Each sub-domain contains only one material. The solution spaces of interface problems usually have low global regularity due to changes of solution properties across interfaces. If $v|_{\Omega^s} \in W^{k,p}(\Omega^s)$, $s = +, -$, and $v \notin W^{k,p}(\Omega)$, then the notations of norm $\|v\|_{k,p,\Omega}$ and semi-norm $|v|_{k,p,\Omega}$ should be understood as follows

$$\|v\|_{k,p,\Omega} = \left(\|v\|_{k,p,\Omega^+}^2 + \|v\|_{k,p,\Omega^-}^2 \right)^{1/2}, \quad |v|_{k,p,\Omega} = \left(|v|_{k,p,\Omega^+}^2 + |v|_{k,p,\Omega^-}^2 \right)^{1/2}, \tag{2.1}$$

for $1 \leq p < \infty$, and

$$\|v\|_{k,\infty,\Omega} = \max\left(\|v\|_{k,\infty,\Omega^+}, \|v\|_{k,\infty,\Omega^-} \right), \quad |v|_{k,\infty,\Omega} = \max\left(|v|_{k,\infty,\Omega^+}, |v|_{k,\infty,\Omega^-} \right), \tag{2.2}$$

for $p = \infty$.

Let $\mathcal{T}_h$ be a Cartesian mesh of the solution domain Ω with the maximum length of edge h. For each element $T \in \mathcal{T}_h$, we call it an interface element if the interior of T intersects with the interface Γ; otherwise, we name it a non-interface element. Without loss of generality, we assume that interface elements in $\mathcal{T}_h$ satisfy the following hypotheses when the mesh size h is small enough [70]:

(H1) The interface Γ cannot intersect an edge of any rectangular element at more than two points unless the edge is part of Γ;

(H2) If Γ intersects the boundary of a rectangular element at two points, these intersection points must be on different edges of this element.

We let $\mathcal{T}_h^i$ be the collection of interface elements, and $\mathcal{T}_h^n = \mathcal{T}_h / \mathcal{T}_h^i$ be the collection of non-interface elements. Moreover, we denote the collection of all edges in the mesh $\mathcal{T}_h$ by $\mathcal{E}_h$ and denote the collections of interface edges and non-interface edges by $\mathcal{E}_h^i$ and $\mathcal{E}_h^n$, respectively.

2.2 Nonconforming Rotated Q_1 Functions

In this section, we recall the nonconforming rotated Q_1 finite elements [123]. In our IFE methods, standard nonconforming rotated Q_1 finite element functions are used on all non-interface elements. On interface elements, these functions are locally modified to satisfy interface jump conditions.

We first consider a typical non-interface element $T \in \mathcal{T}_h^n$ with the following vertices:

$$A_1 = (0,0)^t, \quad A_2 = (h,0)^t, \quad A_3 = (0,h)^t, \quad A_4 = (h,h)^t. \tag{2.3}$$

We label four edges of T as follows:

$$b_1 = \overline{A_1A_2}, \quad b_2 = \overline{A_2A_4}, \quad b_3 = \overline{A_4A_3}, \quad b_4 = \overline{A_3A_1}, \tag{2.4}$$

and let M_i be the midpoint of b_i, $i = 1, 2, 3, 4$, respectively. See Figure 2.1 for an illustration of a non-interface element.

Figure 2.1: A non-interface rectangular element.

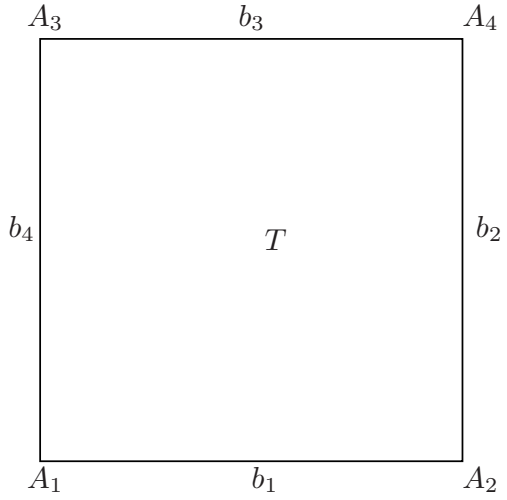

As proposed in [123], there are two types of degrees of freedom for nonconforming rotated Q_1 finite elements. Here we follow Ciarlet's triplet definition [44] of a finite element to differentiate these two finite elements. The first type of nonconforming rotated Q_1 finite elements is defined by (T, Π_T, Σ_T^P), where

$$\Pi_T = \text{Span}\{1, x, y, x^2 - y^2\}, \tag{2.5}$$

and

$$\Sigma_T^P = \{\psi_T^P(M_i) : i = 1, 2, 3, 4, \forall \psi_T^P \in \Pi_T\}. \tag{2.6}$$

We use the superscript P to emphasize that the degrees of freedom are determined by the *point values* at the midpoints. It is easy to check that this Lagrange type finite element (T, Π_T, Σ_T^P) is unisolvent, *i.e.*, for given values $v_i \in \mathbb{R}$, $i = 1, 2, 3, 4$, there exists a unique function $\psi_T^P \in \Pi_T$ such that

$$\psi_T^P(M_i) = v_i, \quad \forall\ i = 1, 2, 3, 4. \tag{2.7}$$

The local finite element basis functions $\psi_{j,T}^P$, $j = 1, 2, 3, 4$ are chosen such that

$$\psi_{j,T}^P(M_i) = \delta_{ij}, \quad \forall\ i, j = 1, 2, 3, 4. \tag{2.8}$$

In particular, if the vertices of T are given by (2.3), then

$$\psi_{1,T}^P = \frac{1}{4h^2}(3h^2 + 4hx - 8hy - 4(x^2 - y^2)), \tag{2.9a}$$

$$\psi_{2,T}^P = \frac{1}{4h^2}(-h^2 + 4hy + 4(x^2 - y^2)), \tag{2.9b}$$

$$\psi_{3,T}^P = \frac{1}{4h^2}(-h^2 + 4hx - 4(x^2 - y^2)), \tag{2.9c}$$

$$\psi_{4,T}^P = \frac{1}{4h^2}(3h^2 - 8hx + 4hy + 4(x^2 - y^2)). \tag{2.9d}$$

The second type of nonconforming rotated Q_1 finite elements is defined by the triplet (T, Π_T, Σ_T^I), where

$$\Sigma_T^I = \left\{ \frac{1}{|b_i|} \int_{b_i} \psi_T^I(X) \mathrm{d}s : i = 1, 2, 3, 4, \forall \psi_T^I \in \Pi_T \right\}, \tag{2.10}$$

and $|b_i|$ denotes the length of the edge b_i. Here we use superscript I to emphasize that the degrees of freedom are given by average *integral values* over edges. Again, it is not hard to verify that (T, Π_T, Σ_T^I) is unisolvent. We choose the local basis functions $\psi_{j,T}^I$, $j = 1, 2, 3, 4$, such that

$$\frac{1}{|b_i|} \int_{b_i} \psi_{j,T}^I(X) \mathrm{d}s = \delta_{ij}. \tag{2.11}$$

In particular, if the vertices of T are given by (2.3), then

$$\psi_{1,T}^I = \frac{1}{4h^2}(3h^2 + 6hx - 10hy - 6(x^2 - y^2)), \tag{2.12a}$$

$$\psi_{2,T}^I = \frac{1}{4h^2}(-h^2 - 2hx + 6hy + 6(x^2 - y^2)), \tag{2.12b}$$

$$\psi_{3,T}^I = \frac{1}{4h^2}(-h^2 + 6hx - 2hy - 6(x^2 - y^2)), \tag{2.12c}$$

$$\psi_{4,T}^I = \frac{1}{4h^2}(3h^2 - 10hx + 6hy + 6(x^2 - y^2)). \tag{2.12d}$$

We define nonconforming rotated Q_1 local finite element spaces with midpoint-value and integral-value degrees of freedom by

$$S_h^{P,n}(T) = \text{Span}\{\psi_{i,T}^P : i = 1, 2, 3, 4\}, \tag{2.13}$$

$$S_h^{I,n}(T) = \text{Span}\{\psi_{i,T}^I : i = 1, 2, 3, 4\}. \tag{2.14}$$

Direct comparison shows that these local basis function $\psi_{j,T}^P$, and $\psi_{j,T}^I$, $j = 1, 2, 3, 4$ are different. Nevertheless, on each non-interface element $T \in \mathcal{T}_h^n$, it can be easily verified that $S_h^{P,n}(T) = S_h^{I,n}(T) = \Pi_T$. From now on, we use the uniform notation $S_h^n(T)$ to represent the local nonconforming rotated Q_1 finite element space on an element T.

2.3 Nonconforming IFE Space $S_h^P(\Omega)$

In an IFE method, we modify the local basis functions and local IFE spaces on interface elements to accomodate the interface jump conditions. In this section, we construct IFE basis functions whose degrees of freedom are determined by midpoint values on each interface element $T \in \mathcal{T}_h^i$, and then use them to form local and global IFE spaces.

We exemplify the procedure of constructing an IFE function with a typical interface element $T \in \mathcal{T}_h^i$ whose geometrical configuration is specified in (2.3) - (2.4). Based on the Hypotheses **(H1)** and **(H2)**, we assume that an interface curve Γ intersects T at two different points D, E, and the segment $\overline{DE}$ separates T into two sub-elements T^+ and T^-. We call an element T a Type I interface element if Γ intersects with T at two adjacent edges, or a Type II interface element if Γ intersects with T at two opposite edges. For the degrees of freedom determined by midpoint values, there are three geometric configurations of the midpoints of a Type I interface element:

Case 1: all the midpoints M_i, $i = 1, 2, 3, 4$ are on one side of $\overline{DE}$.

Case 2: three midpoints are on one side of $\overline{DE}$, and one midpoint is on the other side.

Case 3: two midpoints are on one side of $\overline{DE}$, and two midpoints are on the other side.

Similarly, there are two geometric configurations of the midpoints of a Type II interface element:

Case 1: three midpoints are on one side of $\overline{DE}$, and one midpoint is on the other side.

Case 2: two midpoints are on one side of $\overline{DE}$, and two midpoints are on the other side.

See Figures 2.2 and Figure 2.3 for illustrations of interface elements of different types and cases.

Figure 2.2: Type I interface rectangles: Case 1,2,3 (midpoint-value degrees of freedom).

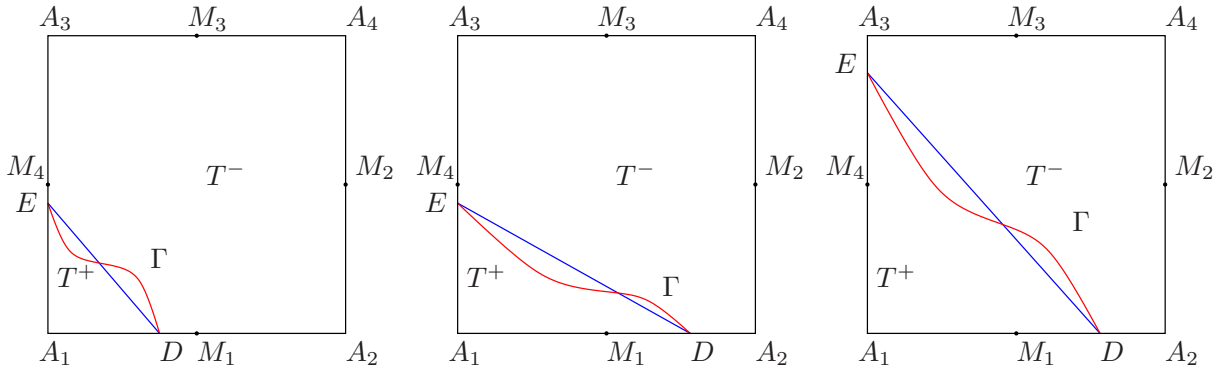

Figure 2.3: Type II interface rectangles: Case 1,2 (midpoint-value degrees of freedom).

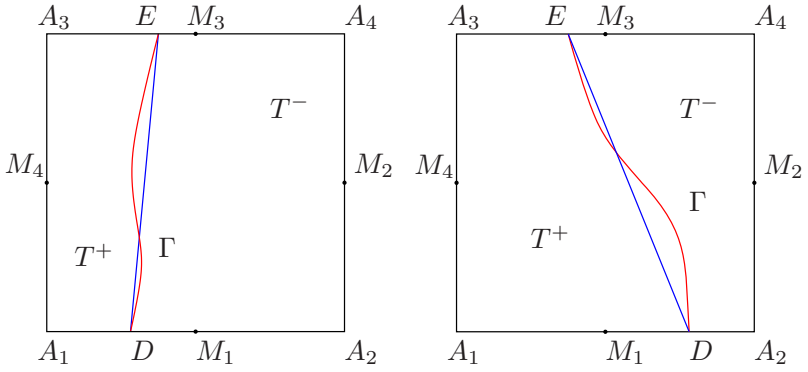

IFE basis functions are constructed via a similar approach for interface elements with different types and cases. In the following discussion we exemplify the approach for a Type I Case 2 interface element. We assume that the interface points D and E in this case are specified as follows

$$D = (dh, 0)^t, \quad E = (0, eh)^t,$$

where $1/2 \leq d \leq 1$, and $0 < e \leq 1/2$. We define an IFE function ϕ_T^P to be a piece-wise rotated Q_1 polynomial:

$$\phi_T^P(x,y) = \begin{cases} \phi_T^{P,+}(x,y) = v_1\psi_{1,T}^P + c_2\psi_{2,T}^P + c_3\psi_{3,T}^P + c_4\psi_{4,T}^P, & \text{if } (x,y)^t \in T^+, \\ \phi_T^{P,-}(x,y) = c_1\psi_{1,T}^P + v_2\psi_{2,T}^P + v_3\psi_{3,T}^P + v_4\psi_{4,T}^P, & \text{if } (x,y)^t \in T^-. \end{cases} \tag{2.15}$$

Here v_i, $i = 1,2,3,4$ are point values at midpoints M_i, $i = 1,2,3,4$. The function $\psi_{i,T}^P$, $i = 1,2,3,4$ are nonconforming rotated Q_1 finite element local basis functions defined in (2.8). The coefficients c_i, $i = 1,2,3,4$ are determined by imposing the following interface jump conditions to interpret (1.4) and (1.5). We enforce the continuity of ϕ_T^P through

- two intersection points D and E:

$$[\phi_T^P(x_D, y_D)] = 0, \quad [\phi_T^P(x_E, y_E)] = 0, \tag{2.16}$$

- the second order terms in ϕ_T^P:

$$\left[\frac{\partial^2 \phi_T^P}{\partial x^2}\right] = 0, \tag{2.17}$$

- the flux in the following sense:

$$\int_{\overline{DE}} [\beta \nabla \phi_T^P(x,y) \cdot \mathbf{n}_{\overline{DE}}] \mathrm{d}s = 0. \tag{2.18}$$

We will show that these conditions are linearly independent so that they can uniquely determine a nonconforming rotated Q_1 local IFE function ϕ_T^P on an interface element T. Note that, to maintain the continuity across $\overline{DE}$, instead of (2.17), it seems to be more natural to impose the following condition:

$$\left[\phi_T^P\left(\frac{x_D + x_E}{2}, \frac{y_D + y_E}{2}\right)\right] = 0, \tag{2.19}$$

because $\left[\phi_T^P\right]|_{\overline{DE}}$ is a quadratic polynomial which can usually be determined by its values at three points. However, when the slope of $\overline{DE}$ is -1 in a Type I Case 2 interface element, conditions (2.16) and (2.19) lose their linear independence. On the other hand, conditions (2.16) and (2.17) are always linearly independent. In addition, when the slope of $\overline{DE}$ is not -1, conditions (2.16) and (2.17) are equivalent to (2.16) and (2.19). These observations suggest us to use (2.17) instead of (2.19).

Equations (2.16), (2.17), and (2.18) lead to the following algebraic system $M_c\mathbf{C} = M_v\mathbf{V}$ to solve coefficients c_i, $i = 1,2,3,4$, *i.e.*,

$$\begin{pmatrix} (3/4) + d - d^2 & 1/4 - d^2 & 1/4 - d + d^2 & -(3/4) + 2d - d^2 \\ (3/4) - 2e + e^2 & 1/4 - e + e^2 & 1/4 - e^2 & -(3/4) - e + e^2 \\ 2/h^2 & 2/h^2 & -(2/h^2) & 2/h^2 \\ \beta^- d(2d-e)h & \beta^+ d^2 h & \beta^+ deh & \beta^+ d(d-2e)h \end{pmatrix} \begin{pmatrix} c_1 \\ c_2 \\ c_3 \\ c_4 \end{pmatrix} =$$

$$\begin{pmatrix} (3/4)+d-d^2 & 1/4-d^2 & 1/4-d+d^2 & -(3/4)+2d-d^2 \\ (3/4)-2e+e^2 & 1/4-e+e^2 & 1/4-e^2 & -(3/4)-e+e^2 \\ 2/h^2 & 2/h^2 & -(2/h^2) & 2/h^2 \\ \beta^+ d(2d-e)h & \beta^- d^2 h & \beta^- deh & \beta^- d(d-2e)h \end{pmatrix} \begin{pmatrix} v_1 \\ v_2 \\ v_3 \\ v_4 \end{pmatrix}. \tag{2.20}$$

Note that for all numbers d, e, satisfying $0 < e \leq 1/2 \leq d < 1$, the determinant of M_c is strictly negative, *i.e.*,

$$\det(M_c) = \frac{-2d}{h}\left(\beta^-(2d-1)(2d-e)e + \beta^+(d^2(2-4e)+e^2+2de(1+e))\right) < 0. \tag{2.21}$$

Thus, the IFE functions ϕ_T^P is uniquely determined by its midpoint values v_i, $i = 1, 2, 3, 4$.

To form IFE basis functions, we let $\mathbf{V} = \mathbf{V}_i = (v_1, \cdots, v_4)^t \in \mathbb{R}^4$ be the i-th canonical unit vector such that $v_i = 1$ and $v_j = 0$ if $j \neq i$. Then we solve for $\mathbf{C}_i = (c_1, \cdots, c_4)^t$ from (2.20) and apply its values in (2.15) to form the i-th nonconforming rotated Q_1 local IFE basis function $\phi_{i,T}^P$.

A nonconforming rotated Q_1 local FE basis function and the corresponding IFE basis functions on Type I and Type II interface elements are illustrated in Figure 2.4. Note that the IFE basis functions are made by piece-wise polynomials and satisfying interface jump conditions (2.16) - (2.18).

Figure 2.4: Nonconforming rotated Q_1 FE (left), Type I (middle) and Type II (right) IFE local basis functions with midpoint-value degrees of freedom.

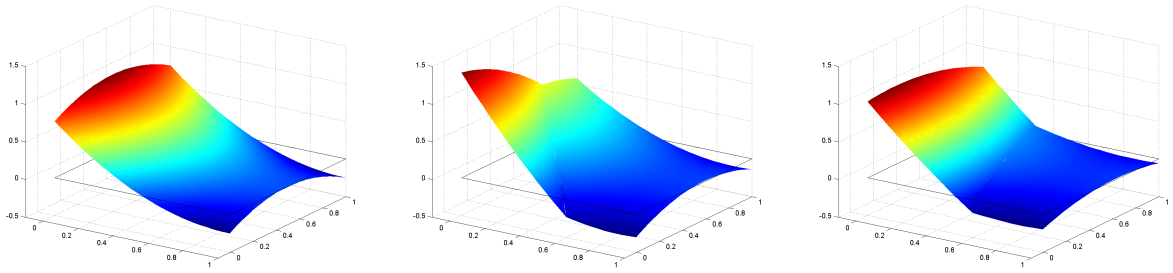

We define the nonconforming rotated Q_1 local IFE space on an interface element $T \in \mathcal{T}_h^i$ to be

$$S_h^{P,i}(T) = \text{Span}\{\phi_{i,T}^P : i = 1, 2, 3, 4\}. \tag{2.22}$$

The corresponding global IFE space is defined by enforcing the continuity through interior midpoints

$$\begin{aligned} S_h^P(\Omega) \quad = \quad & \Big\{ v \in L^2(\Omega) : \ v|_T \in S_h^n(T) \text{ if } T \in \mathcal{T}_h^n, v|_T \in S_h^{P,i}(T) \text{ if } T \in \mathcal{T}_h^i; \\ & \text{if } T_1 \cap T_2 = b \text{ whose midpoint is } M_b, \text{ then } v|_{T_1}(M_b) = v|_{T_2}(M_b) \Big\}. \end{aligned} \tag{2.23}$$

Each global IFE function ϕ_i^P is associated with an edge $b_i \in \mathcal{E}_h$. The support of a global IFE basis function is one or two elements depending on whether the associated edge is a boundary edge or an interior edge. Note that a global nonconforming rotated Q_1 IFE basis function is usually supported on a smaller region compared with the global bilinear IFE basis function whose support is four elements that sharing a common vertex [70]. A comparison of a nonconforming rotated Q_1 global FE and IFE basis functions associated with an interior edge is provided in Figure 2.5. We note that a global IFE basis function is continuous at the midpoint on the associated edge but not continuous throughout the entire edge as the standard FE basis function.

Figure 2.5: Nonconforming rotated Q_1 FE (left) and IFE (right) global basis functions with midpoint-value degrees of freedom.

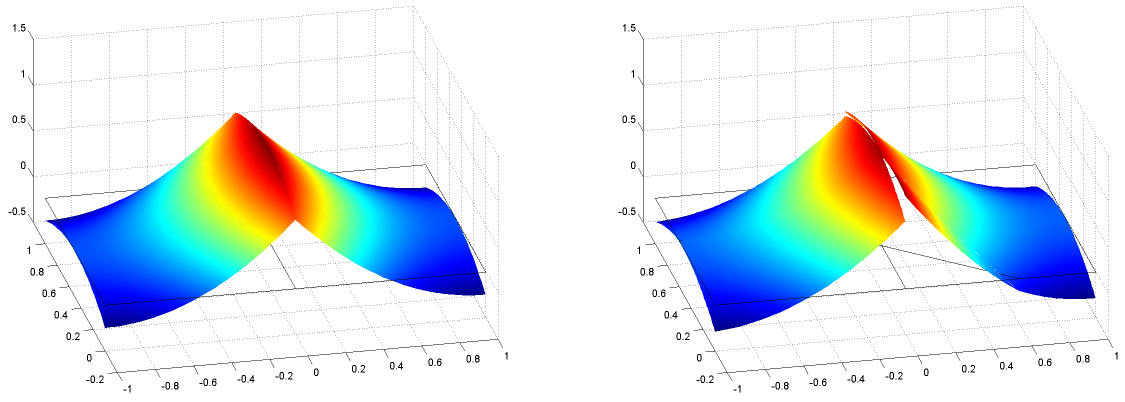

2.4 Nonconforming IFE Space $S_h^I(\Omega)$

In this section, we construct the nonconforming rotated Q_1 IFE function ϕ_T^I on each interface element $T \in \mathcal{T}_h^i$ using degrees of freedom determined by integral values over edges, and then form the corresponding IFE space $S_h^I(\Omega)$.

Likewise, there are two types of interface elements depending on the location of interface points D and E. However, it is unnecessary to subdivide each type of interface elements into different cases as we did for IFE functions with midpoint-value degrees of freedom in Section 2.3, because it does not matter how many midpoints are in each piece of an interface element if the degrees of freedom are determined by edge integral values. As before, we denote an element as Type I interface element if Γ intersects with it at two adjacent edges, and Type II interface element if Γ intersects with it at two opposite edges. See Figure 2.6 for an illustration of the different types of interface elements.

Figure 2.6: Type I and Type II interface rectangles (integral-value degrees of freedom).

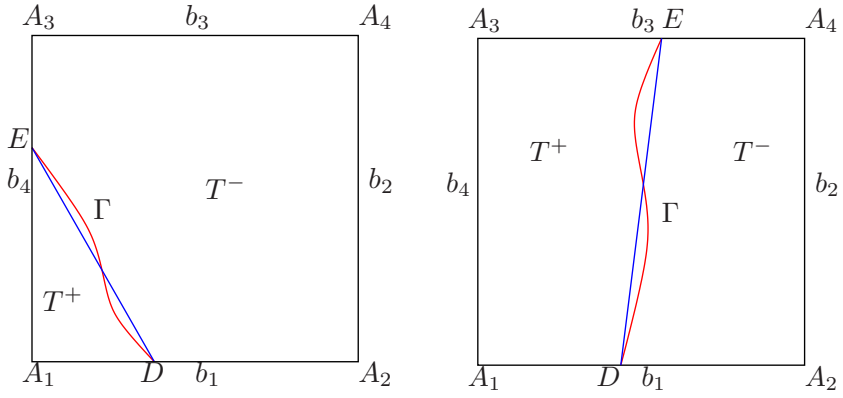

We use Type II interface element as an example to demonstrate the construction of its local IFE space. Assume that the interface points D and E are

$$D = (dh, 0)^t, \quad E = (eh, h)^t,$$

with $0 < d < 1$ and $0 < e < 1$. The IFE function ϕ_T^I is defined as follows:

$$\phi_T^I(x,y) = \begin{cases} \phi_T^{I,+}(x,y) = c_1\psi_{1,T}^I + c_2\psi_{2,T}^I + c_3\psi_{3,T}^I + v_4\psi_{4,T}^I, & \text{if } (x,y)^t \in T^+, \\ \phi_T^{I,-}(x,y) = c_4\psi_{1,T}^I + v_2\psi_{2,T}^I + c_5\psi_{3,T}^I + c_6\psi_{4,T}^I, & \text{if } (x,y)^t \in T^-. \end{cases} \tag{2.24}$$

Here v_i, $i = 2, 4$ are average values over edges b_i, $i = 2, 4$. Coefficients c_i, $i = 1, \cdots, 6$ are determined by the following conditions:

- average values v_i, $i = 1, 3$:

$$\frac{1}{|b_i|}\int_{b_i} \phi_T^I(x,y)\mathrm{d}s = v_i, \quad i = 1, 3, \tag{2.25}$$

- the continuity at two intersection points:

$$[\phi_T^I(x_D, y_D)] = 0, \quad [\phi_T^I(x_E, y_E)] = 0, \tag{2.26}$$

- the second derivative continuity:

$$\left[\frac{\partial^2 \phi_T^I}{\partial x^2}\right] = 0, \tag{2.27}$$

- the weak flux jump continuity:

$$\int_{\overline{DE}} [\beta \nabla \phi_T^I(x,y) \cdot \mathbf{n}_{\overline{DE}}]\mathrm{d}s = 0. \tag{2.28}$$

Combining (2.25) - (2.28) leads to the following algebraic system

$$M_c\mathbf{C} = M_v\mathbf{V}, \tag{2.29}$$

where $\mathbf{C} = (c_1, c_2, \cdots, c_6)^t$, $\mathbf{V} = (v_1, \cdots, v_4)^t$, $M_c = (M_c^1, M_c^2)$, and

$$M_c^1 = \begin{pmatrix} d(3+3d-2d^2) & d(-1-d+2d^2) & -d(1-3d+2d^2) \\ -e(1-3e+2e^2) & e(-1-e+2e^2) & e(3+3e-2e^2) \\ 3(-1-2d+2d^2) & 1+2d-6d^2 & 1-6d+6d^2 \\ 1-6e+6e^2 & 1+2e-6e^2 & 3(-1-2e+2e^2) \\ 12/h^2 & -(12/h^2) & 12/h^2 \\ 2\beta^+(3-5d-e)h & 2\beta^+(-1+3d+3e)h & 2\beta^+(3-d-5e)h \end{pmatrix},$$

$$M_c^2 = \begin{pmatrix} 4-3d-3d^2+2d^3 & d(1-3d+2d^2) & -d(3-5d+2d^2) \\ e(1-3e+2e^2) & 4-3e-3e^2+2e^3 & -e(3-5e+2e^2) \\ 3+6d-6d^2 & -1+6d-6d^2 & 3-10d+6d^2 \\ -1+6e-6e^2 & 3+6e-6e^2 & 3-10e+6e^2 \\ -(12/h^2) & -(12/h^2) & 12/h^2 \\ 2\beta^-(-3+5d+e)h & 2\beta^-(-3+d+5e)h & 2\beta^-(5-3d-3e)h \end{pmatrix},$$

and

$$M_v = \begin{pmatrix} 4 & d(-1-d+2d^2) & 0 & -d(3-5d+2d^2) \\ 0 & e(-1-e+2e^2) & 4 & -e(3-5e+2e^2) \\ 0 & 1+2d-6d^2 & 0 & 3-10d+6d^2 \\ 0 & 1+2e-6e^2 & 0 & 3-10e+6e^2 \\ 0 & -(12/h^2) & 0 & 12/h^2 \\ 0 & 2\beta^-(-1+3d+3e)h & 0 & -2\beta^+(-5+3d+3e)h \end{pmatrix}.$$

Note that for $0 < d < 1$ and $0 < e < 1$, the determinant of M_c satisfies

$$\begin{aligned} \det(M_c) &= \frac{3}{2h}\Big(\beta^+(4-5d+10d^2-5d^3-5e-2de-d^2e+10e^2-de^2-5e^3) \\ &\quad +\beta^-(5d-6d^2+5d^3+5e-6de+d^2e-6e^2+de^2+5e^3)\Big) > 0. \end{aligned} \tag{2.30}$$

Thus, the IFE function ϕ_T^I is uniquely determined by its average values v_i over edges b_i, $i = 1, 2, 3, 4$. To form the local IFE basis function $\phi_{i,T}^I$, we let $\mathbf{V} = \mathbf{V}_i = (v_1, \cdots, v_4)^t \in \mathbb{R}^4$ be the i-th canonical unit vector such that $v_i = 1$ and $v_j = 0$ for $j \neq i$. Then we solve for $\mathbf{C}_i = (c_1, \cdots, c_6)^t$ in (2.29) and use these values in (2.24) to form $\phi_{i,T}^I$. See Figure 2.7 for an illustration of nonconforming rotated Q_1 local FE and IFE basis functions.

Denote the nonconforming rotated Q_1 local IFE space to be

$$S_h^{I,i}(T) = \text{Span}\{\phi_{j,T}^I : j = 1, 2, 3, 4\}. \tag{2.31}$$

Figure 2.7: Nonconforming rotated Q_1 FE (left), Type I (middle) and Type II (right) IFE local basis functions with integral-value degrees of freedom.

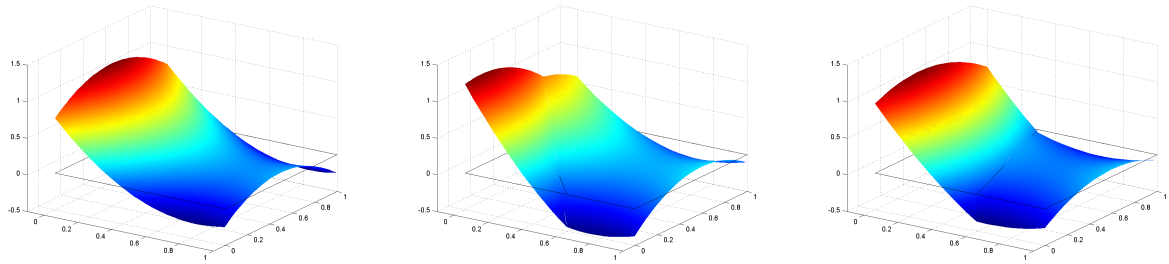

The global IFE space with integral-value degrees of freedom is defined as follows

$$\begin{aligned} S_h^I(\Omega) \quad = \quad & \Big\{ v \in L^2(\Omega) : \ v|_T \in S_h^n(T) \text{ if } T \in \mathcal{T}_h^n, v|_T \in S_h^{I,i}(T) \text{ if } T \in \mathcal{T}_h^i; \\ & \text{if } T_1 \cap T_2 = b, \text{ then } \int_b v|_{T_1} \mathrm{d}s = \int_b v|_{T_2} \mathrm{d}s \Big\}. \end{aligned} \tag{2.32}$$

Each global IFE function ϕ_i^I is associated with an interior or boundary edge $b_i \in \mathcal{E}_h$. A comparison of the nonconforming rotated Q_1 global FE and IFE basis functions associated with an interior edge is illustrated in Figure 2.8. We can observe that a global IFE basis function is discontinuous across the common edge of the two elements in its support. However, the average values of a global IFE basis on the common edge calculated from either of these two elements in its support are the same.

Remark 2.1. *It can be easily shown that for every interface element, the nonconforming rotated Q_1 local IFE spaces with midpoint-value and integral-value degrees of freedom coincide, i.e.,*

$$S_h^{P,i}(T) = S_h^{I,i}(T), \quad \forall\, T \in \mathcal{T}_h^i. \tag{2.33}$$

From now on, we use the uniform notation $S_h^i(T)$ to denote the local IFE space on an interface element T.

Remark 2.2. *The nonconforming rotated Q_1 global IFE spaces with midpoint-value and integral-value degrees of freedom differ, i.e.,*

$$S_h^P(\Omega) \neq S_h^I(\Omega). \tag{2.34}$$

To see (2.34), Assume $\phi^I \in S_h^I(\Omega)$ is a global IFE basis function associated with an interior edge, as illustrated on the right plot in Figure 2.8. It can be easily observed that ϕ^I is not zero at the midpoint on right side edge of the element on the right. On the other hand, this IFE function is zero outside these two elements. This means ϕ^I is not continuous at the midpoint mentioned above; hence, it is not in $S_h^P(\Omega)$. Therefore, (2.34) is true.

Figure 2.8: Nonconforming rotated Q_1 FE (left) and IFE (right) global basis functions with integral-value degrees of freedom.

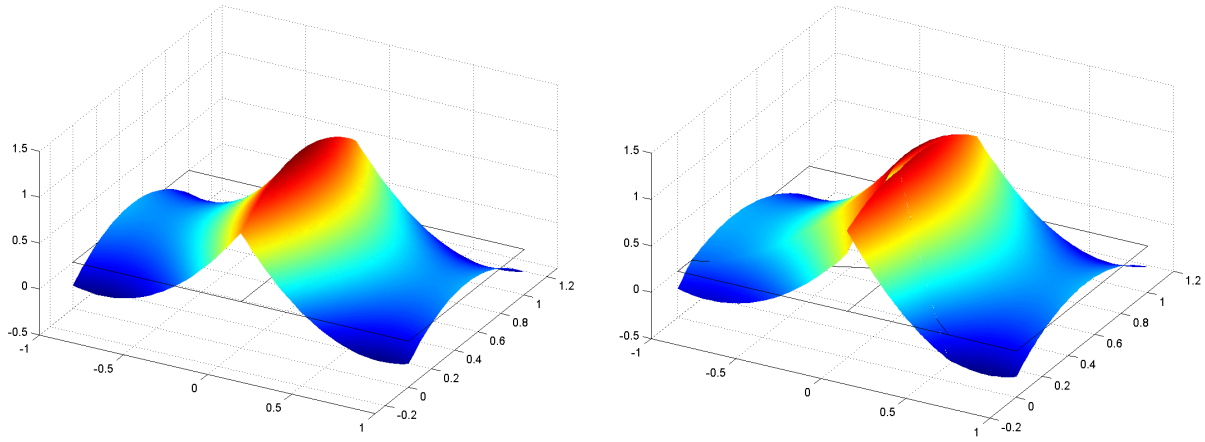

Chapter 3

Properties of IFE Spaces

In this chapter, we investigate properties of nonconforming rotated Q_1 IFE spaces $S_h^P(\Omega)$ and $S_h^I(\Omega)$. In Section 3.1, we show that these IFE functions inherit a few desirable features from the standard nonconforming rotated Q_1 finite element spaces such as unisolvency, continuity within an element, partition of unity and so forth. We derive trace inequalities and inverse inequalities for IFE functions which play important roles in error estimation in Chapter 4. In Section 3.2, we discuss the approximation capabilities of these IFE spaces by analyzing the corresponding IFE interpolation errors. In Section 3.3, we use numerical examples to confirm our error analysis of IFE interpolations.

3.1 Fundamental Properties

In this section, we present several fundamental and useful properties for local IFE spaces $S_h^i(T)$ and global IFE spaces $S_h^P(\Omega)$ and $S_h^I(\Omega)$.

First, as we mentioned in Section 2.3 and 2.4, a nonconforming rotated Q_1 IFE function possesses the unisolvent property.

Lemma 3.1. (Unisolvency) *On each interface element $T \in \mathcal{T}_h^i$, an IFE function $\phi_T^P \in S_h^i(T)$ (resp. $\phi_T^I \in S_h^i(T)$) can be uniquely determined by its midpoint values on edges (resp. average values over edges) and interface jump conditions.*

Proof. It can be verified straightforwardly that the coefficient matrix M_c in (2.21) for the midpoint-value degrees of freedom or (2.30) for the integral-value degrees of freedom is non-singular for arbitrary configuration of the diffusion coefficient β and interface location, reflected by d and e. Thus, an IFE function $\phi_T^P \in S_h^i(T)$ (resp. $\phi_T^I \in S_h^i(T)$) can be uniquely determined by its midpoint values (resp. average values) and interface jump conditions. □

The following lemma shows that an IFE function is continuous within each interface element.

Lemma 3.2. (Continuity) *On each interface element $T \in \mathcal{T}_h^i$, the local IFE space $S_h^i(T)$ is a subspace of $C(T)$.*

Proof. Since each function $\phi_T \in S_h^i(T)$ is a piece-wise polynomial on T^+ and T^-, then it suffices to show that ϕ_T is continuous across the straight line $\overline{DE}$. For each function $\phi_T \in S_h^i(T)$, using continuity of the second order derivative condition (2.17) or (2.27) we can write it as follows:

$$\phi_T(x,y) = \begin{cases} \phi_T^+(x,y) = a^+ + b^+x + c^+y + d(x^2-y^2), & \text{if } (x,y)^t \in T^+, \\ \phi_T^-(x,y) = a^- + b^-x + c^-y + d(x^2-y^2), & \text{if } (x,y)^t \in T^-, \end{cases}$$

where $a^+, a^-, b^+, b^-, c^+, c^-$ and d are coefficients. Therefore, the jump of the function ϕ_T is a linear function as follows

$$[\phi_T(x,y)] = \phi_T^+(x,y) - \phi_T^-(x,y) = (a^+ - a^-) + (b^+ - b^-)x + (c^+ - c^-)y.$$

By definition, the function $[\phi_T]$ vanishes at two different points D and E; hence, it vanishes on the whole line segment $\overline{DE}$. Thus ϕ_T is continuous across $\overline{DE}$. □

The next lemma shows that the nonconforming IFE functions inherit the partition of unity property from standard finite element functions.

Lemma 3.3. (Partition of Unity) *On each interface element $T \in \mathcal{T}_h^i$, IFE basis functions $\phi_{i,T}^P$ and $\phi_{i,T}^I$ satisfy the partition of unity property, i.e.,*

$$\sum_{i=1}^4 \phi_{i,T}^P(x,y) = 1, \quad \forall\ (x,y)^t \in T, \tag{3.1a}$$

and

$$\sum_{i=1}^4 \phi_{i,T}^I(x,y) = 1, \quad \forall\ (x,y)^t \in T. \tag{3.1b}$$

Proof. We prove (3.1a) for the Type I Case 2 interface elements, and the other types and cases can be verified similarly. We define an IFE function ϕ_T^P to be the sum of four local IFE basis functions, *i.e.*,

$$\phi_T^P(x,y) = \sum_{i=1}^4 \phi_{i,T}^P(x,y).$$

Then function ϕ_T^P can be determined by letting $\mathbf{V} = (1,1,1,1)^t$ in (2.20), solving for $\mathbf{C}$ and plugging these values to (2.15). Direct calculation leads to $\mathbf{C} = (1,1,1,1)^t$. Hence, we obtain the two pieces $\phi_T^{P,+}$ and $\phi_T^{P,-}$ of ϕ_T^P satisfying

$$\phi_T^{P,+}(x,y) = \phi_T^{P,-}(x,y) = \sum_{i=1}^4 \psi_{i,T}^P(x,y).$$

Note that the standard nonconforming finite element basis functions $\psi_{i,T}^P$ possess the partition of unity which can be verified by summing up the four basis functions given in (2.9a) - (2.9d); hence,

$$\phi_T^P(x,y) = 1.$$

The result (3.1b) can be verified similarly. □

One of the important features of nonconforming rotated Q_1 IFE functions is that they can weakly preserve the flux continuity across the actual interface curve Γ although the flux continuity is enforced on the line segment $\overline{DE}$.

Lemma 3.4. (Flux continuity on Γ) *Let T be an interface element. For every IFE function $\phi_T \in S_h^i(T)$, we have*

$$\int_{\Gamma\cap T} [\beta\nabla\phi_T \cdot \mathbf{n}]\, ds = 0, \tag{3.2}$$

where $\mathbf{n}$ is the normal vector of Γ.

Proof. Let T^* be the region enclosed by $\Gamma \cap T$ with $\overline{DE}$. Then we have

$$\begin{aligned}
& \int_{T^*} \left[-div\left(\beta\nabla\phi_T\right)\right] \mathrm{d}x\mathrm{d}y \\
= & \int_{T^*} \left(-div\left(\beta^+\nabla\phi_T^+\right)\right) - \left(-div\left(\beta^-\nabla\phi_T^-\right)\right) \mathrm{d}x\mathrm{d}y \\
= & \int_{T^*} \left(-\beta^+\left(\frac{\partial^2\phi_T^+}{\partial x^2} + \frac{\partial^2\phi_T^+}{\partial y^2}\right)\right) - \left(-\beta^-\left(\frac{\partial^2\phi_T^-}{\partial x^2} + \frac{\partial^2\phi_T^-}{\partial y^2}\right)\right) \mathrm{d}x\mathrm{d}y \\
= & \ 0.
\end{aligned}$$

The last equality is due to

$$\frac{\partial^2\phi_T^s}{\partial x^2} + \frac{\partial^2\phi_T^s}{\partial y^2} = 0, \quad s = +, -,$$

for every function $\phi_T \in S_h^i(T)$. By divergence theorem, we obtain

$$\int_{\Gamma\cap T} [\beta\nabla\phi_T \cdot \mathbf{n}]\mathrm{d}s = \int_{\partial T^*} [\beta\nabla\phi_T \cdot \mathbf{n}]\mathrm{d}s - \int_{\overline{DE}} [\beta\nabla\phi_T \cdot \mathbf{n}]\mathrm{d}s = \int_{T^*} \left[-div\left(\beta\nabla\phi_T\right)\right] \mathrm{d}x\mathrm{d}y = 0.$$

□

The following theorem states that the nonconforming rotated Q_1 IFE functions are consistent with standard FE functions.

Theorem 3.1. (Consistency) *IFE basis functions on each interface element $T \in \mathcal{T}_h^i$ are consistent with the finite element basis functions in the sense that*

1. *if the coefficient has no discontinuity, i.e., $\beta^+ = \beta^-$, the IFE basis functions $\phi_{i,T}^P$ and $\phi_{i,T}^I$ become the standard FE basis functions $\psi_{i,T}^P$ and $\psi_{i,T}^I$, respectively.*
2. *if $\min\{|T^+|, |T^-|\}$ shrinks to zero, then IFE basis functions $\phi_{i,T}^P$ and $\phi_{i,T}^I$ become the standard FE basis functions $\psi_{i,T}^P$ and $\psi_{i,T}^I$, respectively. Here $|T^s|$ denotes the area of T^s, $s = +, -$.*

Proof. We prove the consistency of the IFE basis functions $\phi_{i,T}^P$ only, and the consistency of IFE basis functions $\phi_{i,T}^I$ can be shown similarly.

For the first property, if we let $\beta^+ = \beta^-$ in (2.20) for the Type I Case 2 interface elements, then by straightforward calculation we obtain $M_c = M_v$. Solve the linear system (2.20) we obtain $\mathbf{C} = \mathbf{V}$ in these equations, and this leads to $\phi_{i,T}^{P,+} = \phi_{i,T}^{P,-} = \psi_{i,T}^P$, $i = 1, 2, 3, 4$. The first property follows from this result and the definition of $\phi_{i,T}^P$. The consistency of interface elements of other types and cases can be verified similarly.

For the second property, without loss of generality, we assume that the sub-element T^+ shrinks to zero. We prove the consistency for Type I Case 2 interface elements, and the other types and cases can be shown in a similar argument. Note that $|T^+| \to 0$ implies $e \to 0$. Letting $e = 0$ in (2.20), we obtain $c_1 = v_1$; hence,

$$\phi_T^P = \phi_T^{P,-} = \sum_{i=1}^{4} v_i \psi_{i,T}^P.$$

By choosing suitable values for v_i, we have $\phi_{i,T}^P = \psi_{i,T}^P$. □

Remark 3.1. *The first consistency property in Theorem 3.1 indicates that if $\beta^+ = \beta^-$, then IFE spaces $S_h^P(\Omega)$ and $S_h^I(\Omega)$ become standard FE spaces. Corresponding IFE methods, which will be introduced in Section 4.1, become standard finite element methods.*

Remark 3.2. *The second consistency property in Theorem 3.1 is critical when applying IFE functions to solve moving interface problems, which will be discussed in Chapter 6, because the consistency implies that once an interface curve moves out of an element, the IFE functions on that element will continuously become the standard finite element functions.*

The following theorem is about bounds on the rotated Q_1 IFE basis functions.

Theorem 3.2. (Bound of IFE basis functions) *There exists a constant C, independent of interface location but depending on the diffusion coefficient, such that for $i = 1, 2, 3, 4$, and $k = 0, 1, 2$, the IFE basis functions on every interface element T have the following bounds:*

$$|\phi_{i,T}^P|_{k,\infty,T} \leq Ch^{-k}, \tag{3.3a}$$

and

$$|\phi_{i,T}^I|_{k,\infty,T} \le Ch^{-k}. \tag{3.3b}$$

Proof. We prove (3.3a) only, and (3.3b) can be verified using similar arguments. For the Type I Case 2 interface elements, note that the coefficients c_i of the IFE function ϕ_T^P can be calculated explicitly from (2.20) as follows

$$\begin{aligned}
c_1 &= \frac{1}{W_{I,2}}\Big(2(\beta^- - \beta^+)(v_2+v_4)d^2e + 2(\beta^- - \beta^+)(v_3-2v_4)de^2 \\
&\quad +2\beta^+v_1d^2 + (\beta^+ - \beta^-)(v_2+v_4)de + ((\beta^+ - \beta^-)(v_3-2v_4) + 2\beta^+v_1)e^2\Big), \\
c_2 &= \frac{1}{W_{I,2}}\Big(2(\beta^- - \beta^+)(2v_1+v_2-v_4)d^2e + 2(\beta^- - \beta^+)(v_3-2v_4)de^2 \\
&\quad +2\beta^+v_1d^2 + (\beta^+ - \beta^-)(v_2+v_4)de + ((\beta^+ - \beta^-)(v_3-2v_4) + 2\beta^+v_1)e^2\Big), \\
c_3 &= \frac{1}{W_{I,2}}\Big(2(\beta^- - \beta^+)(2v_1-v_2+2v_3-v_4)d^2e + 2(\beta^- - \beta^+)(v_3-2v_4)de^2 \\
&\quad +2\beta^+v_1d^2 + (\beta^+ - \beta^-)(v_2+v_4)de + ((\beta^+ - \beta^-)(v_3-2v_4) + 2\beta^+v_1)e^2\Big), \\
c_4 &= \frac{1}{W_{I,2}}\Big(2(\beta^- - \beta^+)(2v_1-v_2+v_4)d^2e + 2(\beta^- - \beta^+)(v_3-2v_4)de^2 \\
&\quad +2\beta^+v_1d^2 + (\beta^+ - \beta^-)(v_2+v_4)de + ((\beta^+ - \beta^-)(v_3-2v_4) + 2\beta^+v_1)e^2\Big),
\end{aligned}$$

where

$$W_{I,2} = (\beta^-(-1+2d)(2d-e)e + \beta^+(d^2(2-4e) + e^2 + 2de(1+e))) > 0.$$

Note that

$$W_{I,2} \ge \beta^+(d^2(2-4e) + e^2 + 2de(1+e)) \ge \begin{cases} \beta^+(d^2(2-4e)) \ge \beta^+d^2 \ge \frac{1}{4}\beta^+, & \text{if } 0 < e \le \frac{1}{4}, \\ \beta^+(e^2 + 2de(1+e)) \ge \frac{3}{8}\beta^+, & \text{if } \frac{1}{4} \le e \le \frac{1}{2}. \end{cases}$$

Thus there exists a constant C depends only on β^s, $s = +, -$, and midpoint values v_i, $i = 1, 2, 3, 4$, such that

$$c_i \le C.$$

Note that for standard nonconforming FE basis $\psi_{i,T}^P$, it can be verified directly from (2.9a) - (2.9d) that

$$|\psi_{i,T}^P|_{k,\infty,T} \le Ch^{-k}, \quad k = 0, 1, 2.$$

The bound of IFE basis functions (3.3a) follows from that the IFE basis function $\phi_{i,T}^P$ are linear combination of $\psi_{i,T}^P$ with coefficient v_i, and c_i. Interface elements of other types and cases can be verified by similar arguments. □

Trace Inequalities

Trace inequalities are important for the finite element analysis, especially for the estimation on the boundary terms. It is well-known [125] that the following trace inequalities hold on each non-interface element $T \in \mathcal{T}_h^n$: There exists a constant C such that

$$\|v\|_{0,b} \leq C|b|^{1/2}|T|^{-1/2}\left(\|v\|_{0,T} + h_T\|\nabla v\|_{0,T}\right), \quad \forall v \in H^1(T), \tag{3.4}$$

$$\|\nabla v \cdot \mathbf{n}\|_{0,b} \leq C|b|^{1/2}|T|^{-1/2}\left(\|\nabla v\|_{0,T} + h_T\|\nabla^2 v\|_{0,T}\right), \quad \forall v \in H^2(T). \tag{3.5}$$

Here $b \subset \partial T$ is an edge of T and h_T is the diameter of T. $|b|$ and $|T|$ denotes the length of b and area of T, respectively.

We note from Lemma 3.2 that on each $T \in \mathcal{T}_h^i$, the IFE space $S_h^i(T) \subset H^1(T)$; hence the trace inequality (3.4) is true for IFE functions in $S_h^i(T)$. However, $S_h^i(T) \nsubseteq H^2(T)$ since an IFE function $\phi_T \in S_h^i(T)$ is not C^1; hence, the result (3.5) cannot be applied to IFE function $v \in S_h^i(T)$ in general.

In the following discussion, we derive a trace inequality similar to (3.5) for IFE functions. Let $\phi_T \in S_h^i(T)$ be a rotated Q_1 IFE function defined on $T = \square A_1A_2A_3A_4$ whose vertices are given by

$$A_1 = (x_0, y_0)^t, \quad A_2 = (x_0 + h, y_0)^t, \quad A_3 = (x_0, y_0 + h)^t, \quad A_4 = (x_0 + h, y_0 + h)^t.$$

Then, we can write ϕ_T in the following form:

$$\phi_T(x,y) = \begin{cases} c_1^- + c_2^-(x - x_0) + c_3^-(y - y_0) + c_4^-((x - x_0)^2 - (y - y_0)^2), & \text{in } T^-, \\ c_1^+ + c_2^+(x - x_0) + c_3^+(y - y_0) + c_4^+((x - x_0)^2 - (y - y_0)^2), & \text{in } T^+. \end{cases} \tag{3.6}$$

To simplify the notations, we only consider the case $x_0 = y_0 = 0$ and a general interface element can be mapped to this element via translation. Thus (3.6) becomes

$$\phi_T(x,y) = \begin{cases} \phi_T^-(x,y) = c_1^- + c_2^- x + c_3^- y + c_4^-(x^2 - y^2), & \text{if } (x,y) \in T^-, \\ \phi_T^+(x,y) = c_1^+ + c_2^+ x + c_3^+ y + c_4^+(x^2 - y^2), & \text{if } (x,y) \in T^+. \end{cases} \tag{3.7}$$

Without loss of generality, we assume that the interface points D, E satisfy

$$D = (dh, 0)^t \in \overline{A_1A_2}, \quad E = (0, eh)^t \in \overline{A_1A_3},$$

for Type I interface element with $0 < d \leq 1$, $0 < e \leq 1$, and

$$D = (dh, 0)^t \in \overline{A_1A_2}, \quad E = (eh, h)^t \in \overline{A_3A_4},$$

for Type II interface element with $0 < d < 1$, $0 < e < 1$. First we derive a bound for the coefficients c_j^s, $j = 1, 2, 3, 4$, $s = +, -$ of an IFE function ϕ_T defined in (3.7).

Lemma 3.5. *There exists a constant $C > 1$, depending on the diffusion coefficient β but independent of interface location D, E and the element size h, such that for every IFE function ϕ_T defined by* (3.7) *on any interface element T, we have*

$$\frac{1}{C}\left(|c_2^+| + |c_3^+| + h|c_4^+|\right) \le |c_2^-| + |c_3^-| + h|c_4^-| \le C\left(|c_2^+| + |c_3^+| + h|c_4^+|\right), \tag{3.8}$$

and

$$|c_1^+| \le C\left(|c_1^-| + h|c_2^-| + h|c_3^-| + h^2|c_4^-|\right), \quad |c_1^-| \le C\left(|c_1^+| + h|c_2^+| + h|c_3^+| + h^2|c_4^+|\right). \tag{3.9}$$

Proof. Since $\phi_T \in S_h^i(T)$, then the two pieces ϕ_T^- and ϕ_T^+ satisfy the interface jump conditions (2.16) - (2.18), or (2.26) - (2.28). By direct calculation, we have

$$\begin{pmatrix} c_1^- \\ c_2^- \\ c_3^- \\ c_4^- \end{pmatrix} = \begin{pmatrix} 1 & \frac{(\beta^- - \beta^+)de^2}{\beta^-(d^2+e^2)}h & \frac{(\beta^- - \beta^+)d^2e}{\beta^-(d^2+e^2)}h & 0 \\ 0 & \frac{\beta^- d^2 + \beta^+ e^2}{\beta^-(d^2+e^2)} & \frac{(\beta^+ - \beta^-)de}{\beta^-(d^2+e^2)} & 0 \\ 0 & \frac{(\beta^+ - \beta^-)de}{\beta^-(d^2+e^2)} & \frac{\beta^+ d^2 + \beta^- e^2}{\beta^-(d^2+e^2)} & 0 \\ 0 & 0 & 0 & 1 \end{pmatrix} \begin{pmatrix} c_1^+ \\ c_2^+ \\ c_3^+ \\ c_4^+ \end{pmatrix}, \tag{3.10}$$

for Type I interface element, and

$$\begin{pmatrix} c_1^- \\ c_2^- \\ c_3^- \\ c_4^- \end{pmatrix} = \begin{pmatrix} 1 & \frac{(\beta^- - \beta^+)d}{\beta^-(1+(d-e)^2)}h & \frac{(\beta^- - \beta^+)d(d-e)}{\beta^-(1+(d-e)^2)}h & \frac{2(\beta^- - \beta^+)de}{\beta^-(1+(d-e)^2)}h^2 \\ 0 & \frac{\beta^-(d-e)^2 + \beta^+}{\beta^-(1+(d-e)^2)} & \frac{(\beta^+ - \beta^-)(d-e)}{\beta^-(1+(d-e)^2)} & \frac{2(\beta^+ - \beta^-)e}{\beta^-(1+(d-e)^2)}h \\ 0 & \frac{(\beta^+ - \beta^-)(d-e)}{\beta^-(1+(d-e)^2)} & \frac{\beta^- + \beta^+(d-e)^2}{\beta^-(1+(d-e)^2)} & \frac{2(\beta^+ - \beta^-)(d-e)e}{\beta^-(1+(d-e)^2)}h \\ 0 & 0 & 0 & 1 \end{pmatrix} \begin{pmatrix} c_1^+ \\ c_2^+ \\ c_3^+ \\ c_4^+ \end{pmatrix}, \tag{3.11}$$

for Type II interface element. It is easy to check that every entry in the coefficient matrices in (3.10) and (3.11), regardless of h, can be bounded above by a constant C independent of d, e, with the assumption $d, e \in [0, 1]$. Then using (3.10) or (3.11) we can obtain the second parts of the estimates in (3.8) and (3.9). The first parts of the estimates (3.8) and (3.9) can be proved similarly. □

To extend the trace inequality (3.5) to an interface element T, we first work on a sub-element $\tilde{T} \subset T$. We partition T into four congruent squares T_i, $i = 1, 2, 3, 4$, by connecting two pairs of midpoints on opposite edges of T. It is easy to verify that, for either Type I or Type II interface element, there exists a sub-element T_i which is completely inside of either T^- or T^+, and we denote this sub-element by $\tilde{T}$. The following lemma provides an estimate of ϕ_T on $\tilde{T}$.

Lemma 3.6. *There exists a constant C independent of interface location and the element size h_T such that for every IFE function ϕ_T defined by* (3.7) *on any interface element T, we have*

$$\frac{h_T}{|\tilde{T}|}\|\nabla \phi_T\|_{0,\tilde{T}}^2 \ge C h_T\left((c_2^s)^2 + (c_3^s)^2 + h_T^2 (c_4^s)^2\right), \quad s = +, -, \tag{3.12}$$

where $\tilde{T}$ is a sub-element defined above.

Proof. Without loss of generality, we assume $\tilde{T} = T_4$ which is the upper right sub-element and $\tilde{T} \subset T^-$. By Young's inequality, there exists a positive σ_1 such that

$$\begin{aligned} \|\partial_x \phi_T\|^2_{0,\tilde{T}} &= \frac{h_T^2}{12}\left(3(c_2^-)^2 + 9c_2^- c_4^- h_T + 7(c_4^-)^2 h_T^2\right) \\ &\geq \frac{h_T^2}{12}\left(\left(3 - \frac{9}{2\sigma_1}\right)(c_2^-)^2 + \left(7 - \frac{9\sigma_1}{2}\right)(c_4^-)^2 h_T^2\right). \end{aligned}$$

Similarly, there exists a positive σ_2 such that

$$\begin{aligned} \|\partial_y \phi_T\|^2_{0,\tilde{T}} &= \frac{h_T^2}{12}\left(3(c_3^-)^2 - 9c_3^- c_4^- h_T + 7(c_4^-)^2 h_T^2\right) \\ &\geq \frac{h_T^2}{12}\left(\left(3 - \frac{9}{2\sigma_2}\right)(c_3^-)^2 + \left(7 - \frac{9\sigma_2}{2}\right)(c_4^-)^2 h_T^2\right). \end{aligned}$$

Let $\sigma_i \in (\frac{3}{2}, \frac{14}{9})$, $i = 1, 2$, then by direct calculation we obtain

$$\|\nabla \phi_T\|^2_{0,\tilde{T}} \geq C h_T^2 \left((c_2^-)^2 + (c_3^-)^2 + h_T^2 (c_4^-)^2\right). \tag{3.13}$$

Applying the coefficients equivalence result (3.8) in Lemma 3.5 to the above inequality, we obtain

$$\|\nabla \phi_T\|^2_{0,\tilde{T}} \geq C h_T^2 \left((c_2^+)^2 + (c_3^+)^2 + h_T^2 (c_4^+)^2\right). \tag{3.14}$$

Note that $|\tilde{T}| = \frac{h_T^2}{4}$, then (3.12) follows from (3.13) and (3.14). □

Now we are ready to establish the trace inequality for IFE functions on an interface element T.

Theorem 3.3. (Trace Inequality) *There exists a constant C depending only on the diffusion coefficient β such that for every nonconforming rotated Q_1 IFE function ϕ_T on any interface element T, we have*

$$\|\beta \nabla \phi_T \cdot \mathbf{n}\|_{0,b} \leq C h_T^{1/2} |T|^{-1/2} \|\sqrt{\beta} \nabla \phi_T\|_{0,T}, \tag{3.15}$$

where $b \subset \partial T$ is an interface edge of T, and $\mathbf{n}$ is the unit outer normal of T.

Proof. Without loss of generality, we consider an interface element T whose vertices are given by (2.3); hence, ϕ_T can be written as (3.7). Let $b = \overline{A_1 A_3}$, with $b^+ = \overline{A_1 E}$, and $b^- = \overline{E A_3}$.

By direct calculations, we obtain

$$\begin{aligned}
\|\phi^+_{T,x}\|^2_{0,b^+} &= (c^+_2)^2 e h_T \le (c^+_2)^2 h_T,\\
\|\phi^+_{T,y}\|^2_{0,b^+} &= (c^+_3)^2 e h_T - 2c^+_3 c^+_4 e^2 h^2_T + \frac{4}{3}(c^+_4)^2 e^3 h^3_T \le \frac{7}{3}\left((c^+_3)^2 + (c^+_4 h_T)^2\right) h_T,\\
\|\phi^-_{T,x}\|^2_{0,b^-} &= (c^-_2)^2 (1-e) h_T \le (c^-_2)^2 h_T,\\
\|\phi^-_{T,y}\|^2_{0,b^-} &= (c^-_3)^2 (1-e) h_T - 2c^-_3 c^-_4 (1-e^2) h^2_T + \frac{4}{3}(c^-_4)^2 (1-e^3) h^3_T\\
&\le \frac{7}{3}\left((c^-_3)^2 + (c^-_4 h_T)^2\right) h_T.
\end{aligned}$$

Applying the estimate (3.12) to the above inequalities, we obtain

$$\|\phi_{T,p}\|^2_{0,b^s} \le C\frac{h_T}{|\tilde{T}|}\|\nabla\phi_T\|^2_{0,\tilde{T}}, \qquad p = x, y, \quad s = +, -.$$

Hence,

$$\begin{aligned}
\|\beta\nabla\phi_T \cdot \mathbf{n}\|^2_{0,b} &\le \beta_{max}(\|\phi_{T,x}\|^2_{0,b} + \|\phi_{T,y}\|^2_{0,b})\\
&\le C\frac{\beta_{max}}{\beta_{min}}\frac{4h_T}{|T|}\|\sqrt{\beta}\nabla\phi_T\|^2_{0,\tilde{T}}\\
&\le C\frac{h_T}{|T|}\|\sqrt{\beta}\nabla\phi_T\|^2_{0,T}, \qquad (3.16)
\end{aligned}$$

where $\beta_{max} = \max\{\beta^-, \beta^+\}$ and $\beta_{min} = \min\{\beta^-, \beta^+\}$. The estimate in (3.15) follows from taking square root of both sides in (3.16). □

Inverse Inequalities

Another important property of finite element functions is the inverse inequalities [28]: There exists a constant C such that for all $v \in S_h(T)$

$$\|v\|_{l,p,T} \le Ch^{m-l+\frac{n}{p}-\frac{n}{q}}\|v\|_{m,q,T}, \qquad (3.17)$$

where $S_h(T)$ is a finite element subspace of $W^{l,p}(T) \cap W^{m,q}(T)$ with $1 \le p \le \infty$, $1 \le q \le \infty$, and $0 \le m \le l$. In (3.17), n is the dimension of T, *i.e.*, $T \subset \mathbb{R}^n$ and h is the diameter of T.

The above inverse estimates are true for finite element functions which are uniform polynomials in each element. However, the IFE functions are piece-wise polynomials in interface elements; hence, the inverse inequality (3.17) cannot be applied for IFE functions directly. The following theorem establishes inverse inequalities for IFE functions.

Theorem 3.4. (Inverse Inequalities) *There exists a constant C depending only on the diffusion coefficient β such that every nonconforming rotated Q_1 IFE function ϕ_T on any interface element T satisfies*

$$|\phi_T|_{k,\infty,T} \leq Ch_T^{-1}|\phi_T|_{k,T}, \tag{3.18}$$

and

$$|\phi_T|_{k,T} \leq Ch_T^{l-k}|\phi_T|_{l,T} \tag{3.19}$$

for all $0 \leq l \leq k \leq 2$.

Proof. For (3.18), we prove the case $k = 1$, the other cases can be verified similarly. Consider the typical interface element $T = \square A_1A_2A_3A_4$ whose vertices are given in (2.3). By the coefficient equivalent property (3.8) in Lemma 3.5 and (3.12) in Lemma 3.6, we obtain,

$$\begin{aligned}
|\phi_T|_{1,\infty,T} &= \max\{|\phi_T|_{1,\infty,T^-}, |\phi_T|_{1,\infty,T^+}\} \\
&\leq \max\{|c_2^-| + |c_3^-| + 4h|c_4^-|, |c_2^+| + |c_3^+| + 4h|c_4^+|\} \\
&\leq C(|c_2^-| + |c_3^-| + h|c_4^-|) \\
&\leq Ch_T^{-1}\|\nabla\phi_T\|_{0,\tilde{T}} \\
&\leq Ch_T^{-1}|\phi_T|_{1,T}.
\end{aligned}$$

For (3.19), we prove the case $k = 1$, $l = 0$, and the other cases can be verified similarly. Using the coefficient equivalent property (3.8) again, we obtain

$$\begin{aligned}
|\phi_T|_{1,T}^2 &= |\phi_T|_{1,T^+}^2 + |\phi_T|_{1,T^-}^2 \\
&= \int_{T^+} (c_2^+ + 2c_4^+x)^2 + (c_3^+ - 2c_4^+y)^2 \mathrm{d}x\mathrm{d}y + \int_{T^-} (c_2^- + 2c_4^-x)^2 + (c_3^- - 2c_4^-y)^2 \mathrm{d}x\mathrm{d}y \\
&= \int_T (c_2^+ + 2c_4^+x)^2 + (c_3^+ - 2c_4^+y)^2 + (c_2^- + 2c_4^-x)^2 + (c_3^- - 2c_4^-y)^2 \mathrm{d}x\mathrm{d}y \\
&= h^2\left((c_2^+)^2 + (c_3^+)^2 + 2hc_2^+c_4^+ - 2hc_3^+c_4^+ + \frac{8}{3}h^2(c_4^+)^2\right) \\
&\quad + h^2\left((c_2^-)^2 + (c_3^-)^2 + 2hc_2^-c_4^- - 2hc_3^-c_4^- + \frac{8}{3}h^2(c_4^-)^2\right) \\
&\leq Ch^2\left((c_2^-)^2 + (c_3^-)^2 + h^2(c_4^-)^2\right). \\
&\leq C|\phi_T|_{1,\tilde{T}}^2.
\end{aligned} \tag{3.20}$$

On the other hand, we note that ϕ_T on $\tilde{T}$ is a uniform polynomial; hence the standard inverse inequality (3.17) can be applied on $\tilde{T}$ to have

$$|\phi_T|_{1,\tilde{T}}^2 \leq Ch^{-2}|\phi_T|_{0,\tilde{T}}^2 \leq Ch^{-2}|\phi_T|_{0,T}^2. \tag{3.21}$$

Combining the estimates (3.20) and (3.21), we obtain

$$|\phi_T|_{1,T} \leq Ch^{-1}|\phi_T|_{0,T}.$$

□

The trace inequality (3.15) and inverse inequalities (3.18), (3.19) for IFE functions play important roles in the error estimation of related IFE methods, which we will discuss in Chapter 4.

Remark 3.3. *Similar trace inequalities and inverse inequalities for linear and bilinear IFE functions can be proved in a similar approach. We refer a recent article [103] for more details.*

3.2 Approximation Capabilities

In this section, we discuss the approximation capabilities of nonconforming rotated Q_1 IFE spaces $S_h^P(\Omega)$ and $S_h^I(\Omega)$.

Recall that on each non-interface element $T \in \mathcal{T}_h^n$, the local interpolation can be defined in two ways based on two different types of finite element basis $\{\psi_{i,T}^P\}_{i=1}^4$ and $\{\psi_{i,T}^I\}_{i=1}^4$. The first type is associated with midpoint-value degrees of freedom and the local interpolation operator $I_{h,T}^P : H^2(T) \to S_h^n(T)$ is defined as follows:

$$I_{h,T}^P u = \sum_{i=1}^4 u(M_i)\psi_{i,T}^P, \tag{3.22}$$

where M_i, $i = 1, 2, 3, 4$ are midpoints of edges of T. Using the local basis of integral-value degrees of freedom, the local interpolation operator $I_{h,T}^I : H^2(T) \to S_h^n(T)$ is defined as follows:

$$I_{h,T}^I u = \sum_{i=1}^4 \left(\frac{1}{|b_i|} \int_{b_i} u \mathrm{d}s \right) \psi_{i,T}^I. \tag{3.23}$$

Error estimation for both of these interpolations are analyzed in [123] using the standard scaling argument:

$$\|I_{h,T}^P u - u\|_{0,T} + h\|I_{h,T}^P u - u\|_{1,T} \le Ch^2|u|_{2,T}, \quad \forall\, T \in \mathcal{T}_h^n, \tag{3.24a}$$

and

$$\|I_{h,T}^I u - u\|_{0,T} + h\|I_{h,T}^I u - u\|_{1,T} \le Ch^2|u|_{2,T}, \quad \forall\, T \in \mathcal{T}_h^n. \tag{3.24b}$$

The interpolations operators $I_{h,T}^P$ and $I_{h,T}^I$ can be defined similarly on an interface element $T \in \mathcal{T}_h^i$ by replacing the FE local basis functions with the IFE local basis functions. In the following subsections, we focus on the error analysis for $\|I_{h,T}^P u - u\|_{k,T}$ and $\|I_{h,T}^I u - u\|_{k,T}$ on an interface element $T \in \mathcal{T}_h^i$. The main ideas of our analysis are

- Using multi-point Taylor expansion techniques to derive a uniform bound for $I_{h,T}^P u - u$ on each interface element T

$$\|I_{h,T}^P u - u\|_{k,T} \le Ch^{2-k}\|u\|_{2,T}, \quad k = 0, 1,$$

where C is independent of the interface location.

- Deriving a uniform error bound for the difference of the two interpolations

$$\|I_{h,T}^P u - I_{h,T}^I u\|_{k,T} \leq Ch^{2-k}\|u\|_{2,T}, \quad k = 0, 1,$$

then we apply the triangular inequality and the two estimates above to obtain a uniform error bound for $I_{h,T}^I u - u$:

$$\|I_{h,T}^I u - u\|_{k,T} \leq Ch^{2-k}\|u\|_{2,T}, \quad k = 0, 1.$$

3.2.1 Error Analysis of Interpolation on $S_h^P(\Omega)$

We use the multi-point Taylor expansion idea [28, 35] to analyze the interpolation error $I_{h,T}^P u - u$. We note that this idea has been used for error analysis of the linear [95] and bilinear IFE interpolations [70].

On each interface element $T \in \mathcal{T}_h^i$, we assume that the interface Γ intersects T at two points, denoted by D and E. We use the line segment $\overline{DE}$ to approximate the actual interface $\Gamma \cap T$. The segment $\overline{DE}$ separates T into two sub-elements, denoted by T^+ and T^- where $T = T^+ \cup T^- \cup \overline{DE}$. Note that there is a small region enclosed by $\Gamma \cap T$ and $\overline{DE}$, denoted by T^* where $T^* = (\Omega^+ \cap T^-) \cup (\Omega^- \cap T^+)$. Then, an interface element T is subdivided into up to four pieces, *i.e.*,

$$T = \left(\Omega^+ \cap T^+\right) \cup \left(\Omega^- \cap T^-\right) \cup \left(\Omega^+ \cap T^-\right) \cup \left(\Omega^- \cap T^+\right). \tag{3.25}$$

For every interface element $T \in \mathcal{T}_h^i$, we define the following space

$$PH^m(T) = \left\{u : u|_{\Omega^s \cap T} \in H^m(\Omega^s \cap T), s = +, -\right\}.$$

The equipped norm for every function $u \in PH^m(T)$ is defined as follows

$$\|u\|_{m,T}^2 = \|u\|_{m,\Omega^- \cap T}^2 + \|u\|_{m,\Omega^+ \cap T}^2,$$

and the semi-norm is defined by

$$|u|_{m,T}^2 = |u|_{m,\Omega^- \cap T}^2 + |u|_{m,\Omega^+ \cap T}^2.$$

Then we define the following spaces on an interface element $T \in \mathcal{T}_h^i$ whose functions satisfy the interface jump conditions (1.4) and (1.5).

$$\begin{aligned} PH_{int}^m(T) &= \left\{u \in C(T), u|_{\Omega^s \cap T} \in H^m(\Omega^s \cap T), s = +, -, [\beta \nabla u \cdot \mathbf{n}_\Gamma] = 0 \text{ on } \Gamma \cap T\right\}, \\ PC_{int}^m(T) &= \left\{u \in C(T), u|_{\Omega^s \cap T} \in C^m(\Omega^s \cap T), s = +, -, [\beta \nabla u \cdot \mathbf{n}_\Gamma] = 0 \text{ on } \Gamma \cap T\right\}. \end{aligned}$$

Similarly, we define the following spaces on the whole domain Ω:

$$\begin{aligned} PH^m_{int}(\Omega) &= \{u \in C(\Omega), u|_{\Omega^s} \in H^m(\Omega^s), s = +, -, [\beta \nabla u \cdot \mathbf{n}_\Gamma] = 0 \text{ on } \Gamma\}, \\ PC^m_{int}(\Omega) &= \{u \in C(\Omega), u|_{\Omega^s} \in C^m(\Omega^s), s = +, -, [\beta \nabla u \cdot \mathbf{n}_\Gamma] = 0 \text{ on } \Gamma\}. \end{aligned}$$

Here $m \geq 2$. Clearly, we have the inclusion $PC^2_{int}(T) \subset PH^2_{int}(T)$, for every $T \in \mathcal{T}_h^i$.

On an interface element T, we consider the interpolation $I^P_{h,T} : PH^2_{int}(T) \to S^i_h(T)$ defined by

$$I^P_{h,T} u(X) = \sum_{i=1}^{4} u(M_i) \phi^P_{i,T}(X), \tag{3.26}$$

where $\phi^P_{i,T}$, $i = 1, 2, 3, 4$, are nonconforming rotated Q_1 local IFE basis functions with midpoint-value degrees of freedom. We define the global IFE interpolation $I^P_h : PH^2_{int}(\Omega) \to S^P_h(\Omega)$ as follows

$$(I^P_h u)|_T = I^P_{h,T} u, \quad \forall\, T \in \mathcal{T}_h, \tag{3.27}$$

where the local interpolation $I^P_{h,T}$ is defined in (3.22) or (3.26) depending on whether T is a non-interface or an interface element.

We assume that the interface Γ and the partition $\mathcal{T}_h$ satisfy the following assumptions [70, 95]:

(H3) The interface Γ is defined by a piecewise C^2 function, and the partition $\mathcal{T}_h$ is formed such that the subset of Γ in every interface element $T \in \mathcal{T}_h^i$ is C^2.

(H4) The interface Γ is smooth enough so that $PC^3_{int}(T)$ is dense in $PH^2_{int}(T)$ for every interface element $T \in \mathcal{T}_h^i$.

Note that the hypothesis **(H4)** holds if the interface is smooth enough [114, 146].

Let $\tilde{\rho} = \frac{\beta^-}{\beta^+}$, and $\rho = \frac{\beta^+}{\beta^-}$. For any point $\widetilde{M} \in \Gamma \cap T$, let $\widetilde{M}^\perp$ be the orthogonal projection of $\widetilde{M}$ onto $\overline{DE}$. We first recall several results in [70].

Lemma 3.7. *Let $\widetilde{M}$ be an arbitrary point on $\Gamma \cap T$ and $X_{\overline{DE}}$ be an arbitrary point on $\overline{DE}$. Assume $\mathbf{n}(\widetilde{M}) = (n_x(\widetilde{M}), n_y(\widetilde{M}))^t$ is the unit normal vector of Γ at $\widetilde{M}$, and $\mathbf{n}(\overline{DE}) = (\bar{n}_x, \bar{n}_y)^t$ is the unit normal vector of $\overline{DE}$. Then, for any $u \in PC^2_{int}(T)$, we have*

$$\nabla u^+(\widetilde{M}) = N^-(\widetilde{M}) \nabla u^-(\widetilde{M}), \quad \nabla u^-(\widetilde{M}) = N^+(\widetilde{M}) \nabla u^+(\widetilde{M}), \tag{3.28}$$

where

$$N^-(\widetilde{M}) = \begin{pmatrix} n_y(\widetilde{M})^2 + \rho n_x(\widetilde{M})^2 & (\rho - 1) n_x(\widetilde{M}) n_y(\widetilde{M}) \\ (\rho - 1) n_x(\widetilde{M}) n_y(\widetilde{M}) & n_x(\widetilde{M})^2 + \rho n_y(\widetilde{M})^2 \end{pmatrix},$$

$$N^+(\widetilde{M}) = \begin{pmatrix} n_y(\widetilde{M})^2 + \tilde{\rho} n_x(\widetilde{M})^2 & (\tilde{\rho} - 1) n_x(\widetilde{M}) n_y(\widetilde{M}) \\ (\tilde{\rho} - 1) n_x(\widetilde{M}) n_y(\widetilde{M}) & n_x(\widetilde{M})^2 + \tilde{\rho} n_y(\widetilde{M})^2 \end{pmatrix}.$$

Moreover, for any $v \in S_h^i(T)$, we have

$$\nabla v^+(X_{\overline{DE}}) = N^-_{\overline{DE}} \nabla v^-(X_{\overline{DE}}), \quad \nabla v^-(X_{\overline{DE}}) = N^+_{\overline{DE}} \nabla v^+(X_{\overline{DE}}), \tag{3.29}$$

where

$$N^-_{\overline{DE}} = \begin{pmatrix} \bar{n}_y^2 + \rho \bar{n}_x^2 & (\rho - 1)\bar{n}_x \bar{n}_y \\ (\rho - 1)\bar{n}_x \bar{n}_y & \bar{n}_x^2 + \rho \bar{n}_y^2 \end{pmatrix},$$

$$N^+_{\overline{DE}} = \begin{pmatrix} \bar{n}_y^2 + \tilde{\rho} \bar{n}_x^2 & (\tilde{\rho} - 1)\bar{n}_x \bar{n}_y \\ (\tilde{\rho} - 1)\bar{n}_x \bar{n}_y & \bar{n}_x^2 + \tilde{\rho} \bar{n}_y^2 \end{pmatrix}.$$

Lemma 3.8. *For any point $\widetilde{M} \in \Gamma \cap T$, there exists a constant $C > 0$ such that*

$$\|\widetilde{M} - \widetilde{M}^\perp\| \leq Ch^2, \tag{3.30}$$

and

$$\|N^s_{\overline{DE}} - N^s(\widetilde{M})\| \leq Ch, \quad s = +, -. \tag{3.31}$$

Figure 3.1: A sketch of interface rectangle: Type I, Case 2.

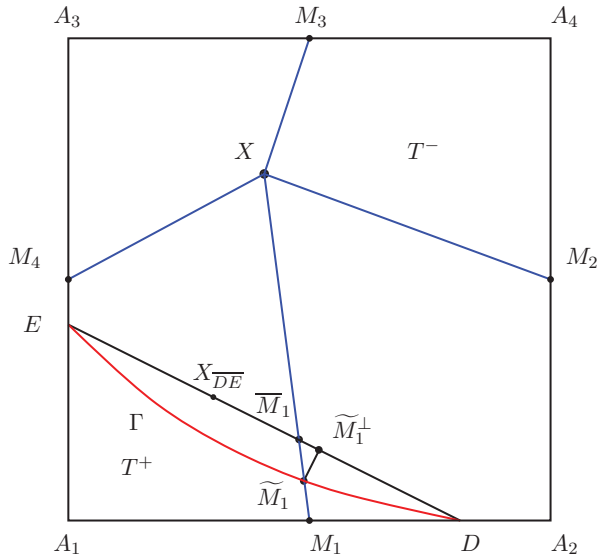

We use the Type I Case 2 interface element, illustrated in Figure 3.1, to present our analysis and interface elements of other types and cases can be discussed similarly. First we consider the interpolation error estimation on $\Omega^- \cap T^-$. Let $X = (x, y)^t \in \Omega^- \cap T^-$. Assume the line segments $\overline{XM_i}$, $i = 2, 3, 4$ do not intersect with the interface Γ and $\overline{DE}$, whereas $\overline{XM_1}$

meets Γ and $\overline{DE}$ at $\widetilde{M}_1$, and $\overline{M}_1$, respectively. One can find an illustration of the related geometry in Figure 3.1 . We also assume that

$$\widetilde{M}_1 = \tilde{t}M_1 + (1-\tilde{t})X = (\tilde{x}_1, \tilde{y}_1)^t, \quad \overline{M}_1 = \bar{t}M_1 + (1-\bar{t})X = (\bar{x}_1, \bar{y}_1)^t,$$

for some positives $0 \le \tilde{t}, \bar{t} \le 1$. Therefore,

$$\tilde{t}(M_1 - \widetilde{M}_1) = (1-\tilde{t})(\widetilde{M}_1 - X), \quad \bar{t}(M_1 - \overline{M}_1) = (1-\bar{t})(\overline{M}_1 - X).$$

We define the operator $\ominus$ by

$$X_1 \ominus X_2 \triangleq (x_1 - x_2, y_2 - y_1)^t, \tag{3.32}$$

for any two points $X_1 = (x_1, y_1)^t$, $X_2 = (x_2, y_2)^t$.

Lemma 3.9. *For any number $p, r \in \mathbb{R}$, any vector $\mathbf{q} \in \mathbb{R}^2$, and any point $X \in \Omega^- \cap T^-$, $X_{\overline{DE}} \in \overline{DE}$, there exists an IFE function $v \in S_h^i(T)$ such that*

$$v(X) = p, \quad \nabla v(X) = \mathbf{q}, \quad \frac{\partial^2 v(X)}{\partial x^2} = 2r, \tag{3.33}$$

and

$$\begin{aligned} & \mathbf{q} \cdot \sum_{i=1}^{4} (M_i - X)\phi_{i,T}^P(X) \qquad (3.34) \\ = \; & -(N_{\overline{DE}}^- - I)\mathbf{q} \cdot (M_1 - \widetilde{M}_1)\phi_{1,T}^P(X) - (N_{\overline{DE}}^- - I)\mathbf{q} \cdot (\widetilde{M}_1 - X_{\overline{DE}})\phi_{1,T}^P(X) - rF_0(X), \end{aligned}$$

where

$$\begin{aligned} F_0(X) \; = \; & \sum_{i=2}^{4} ((x_i - x)^2 - (y_i - y)^2)\phi_{i,T}^P(X) \\ & + 2N_{\overline{DE}}^-(X_{\overline{DE}} \ominus X) \cdot (M_1 - X_{\overline{DE}})\phi_{1,T}^P(X) \qquad (3.35) \\ & + ((x_{\overline{DE}} - x)^2 - (y_{\overline{DE}} - y)^2)\phi_{1,T}^P(X) + ((x_1 - x_{\overline{DE}})^2 - (y_1 - y_{\overline{DE}})^2)\phi_{1,T}^P(X). \end{aligned}$$

Proof. Note that a local IFE function $v \in S_h^i(T)$ can be written as

$$v(Y) = \begin{cases} v^-(Y) = a^- + b^- x + c^- y + d^-(x^2 - y^2), & \text{if } Y \in T^-, \\ v^+(Y) = a^+ + b^+ x + c^+ y + d^+(x^2 - y^2), & \text{if } Y \in T^+, \end{cases}$$

for every point $Y = (x, y)^t \in T$. Since the point X is in T^-, then we can uniquely determine coefficients a^-, b^-, c^-, d^- by solving a small linear system defined by (3.33). The coefficients a^+, b^+, c^+, d^+ in the plus piece v^+ of the IFE function v, can be determined by the following interface jump conditions

$$v^+(D) = v^-(D), \quad v^+(E) = v^-(E), \quad d^+ = d^-,$$

and

$$\int_{\overline{DE}} \beta^+ \nabla v^+(Y) \cdot \mathbf{n}_{\overline{DE}} \mathrm{d}s = \int_{\overline{DE}} \beta^- \nabla v^-(Y) \cdot \mathbf{n}_{\overline{DE}} \mathrm{d}s.$$

We then apply the Taylor expansion to express $v(M_i)$, $i = 2, 3, 4$ at X as follows

$$v(M_i) = v^-(M_i) = v^-(X) + \nabla v^-(X) \cdot (M_i - X) + d^-((x_i - x)^2 - (y_i - y)^2), \quad i = 2, 3, 4. \tag{3.36}$$

Next we expand $v(M_1)$ at X using the interface jump conditions (1.4) - (1.5) and the derivative relation (3.29) given in Lemma 3.7 as follows

$$\begin{aligned}
v(M_1) &= v^+(M_1) \\
&= v^+(X_{\overline{DE}}) + \nabla v^+(X_{\overline{DE}}) \cdot (M_1 - X_{\overline{DE}}) + d^+((x_1 - x_{\overline{DE}})^2 - (y_1 - y_{\overline{DE}})^2) \\
&= v^-(X_{\overline{DE}}) + N^-_{\overline{DE}} \nabla v^-(X_{\overline{DE}}) \cdot (M_1 - X_{\overline{DE}}) + d^-((x_1 - x_{\overline{DE}})^2 - (y_1 - y_{\overline{DE}})^2) \\
&= v^-(X) + \nabla v^-(X) \cdot (X_{\overline{DE}} - X) + d^-((x_{\overline{DE}} - x)^2 - (y_{\overline{DE}} - y)^2) \\
&\quad + N^-_{\overline{DE}} \nabla v^-(X_{\overline{DE}}) \cdot (M_1 - X_{\overline{DE}}) + d^-((x_1 - x_{\overline{DE}})^2 - (y_1 - y_{\overline{DE}})^2) \\
&= v^-(X) + \nabla v^-(X) \cdot (M_1 - X) - \nabla v^-(X) \cdot (M_1 - X_{\overline{DE}}) \\
&\quad + d^-((x_{\overline{DE}} - x)^2 - (y_{\overline{DE}} - y)^2) + N^-_{\overline{DE}} \nabla v^-(X_{\overline{DE}}) \cdot (M_1 - X_{\overline{DE}}) \\
&\quad + d^-((x_1 - x_{\overline{DE}})^2 - (y_1 - y_{\overline{DE}})^2) \\
&= v^-(X) + \nabla v^-(X) \cdot (M_1 - X) + (N^-_{\overline{DE}} - I) \nabla v^-(X) \cdot (M_1 - X_{\overline{DE}}) \\
&\quad + N^-_{\overline{DE}} (\nabla v^-(X_{\overline{DE}}) - \nabla v^-(X)) \cdot (M_1 - X_{\overline{DE}}) \\
&\quad + d^-((x_{\overline{DE}} - x)^2 - (y_{\overline{DE}} - y)^2) + d^-((x_1 - x_{\overline{DE}})^2 - (y_1 - y_{\overline{DE}})^2) \\
&= v^-(X) + \nabla v^-(X) \cdot (M_1 - X) + (N^-_{\overline{DE}} - I) \nabla v^-(X) \cdot (M_1 - \widetilde{M}_1) \\
&\quad + (N^-_{\overline{DE}} - I) \nabla v^-(X) \cdot (\widetilde{M}_1 - X_{\overline{DE}}) + 2d^- N^-_{\overline{DE}} (X_{\overline{DE}} \ominus X) \cdot (M_1 - X_{\overline{DE}}) \\
&\quad + d^-((x_{\overline{DE}} - x)^2 - (y_{\overline{DE}} - y)^2) + d^-((x_1 - x_{\overline{DE}})^2 - (y_1 - y_{\overline{DE}})^2).
\end{aligned} \tag{3.37}$$

Here the last equality is due to

$$\nabla v^-(X_{\overline{DE}}) - \nabla v^-(X) = \begin{pmatrix} b^- + 2d^- x_{\overline{DE}} \\ c^- - 2d^- y_{\overline{DE}} \end{pmatrix} - \begin{pmatrix} b^- + 2d^- x \\ c^- - 2d^- y \end{pmatrix} = 2d^-(X_{\overline{DE}} \ominus X).$$

Applying (3.36) and (3.37) to the IFE local interpolation (3.26) yields

$$\begin{aligned} I_{h,T}^P v(X) &= \sum_{i=1}^4 v(M_i)\phi_{i,T}^P(X) \\ &= \sum_{i=1}^4 v(X)\phi_{i,T}^P(X) + \sum_{i=1}^4 \nabla v(X)\cdot(M_i - X)\phi_{i,T}^P(X) \\ &\quad + d^- \sum_{i=2}^4 ((x_i - x)^2 - (y_i - y)^2)\phi_{i,T}^P(X) \\ &\quad + (N_{\overline{DE}}^- - I)\nabla v^-(X)\cdot(M_1 - \widetilde{M}_1)\phi_{1,T}^P(X) \\ &\quad + (N_{\overline{DE}}^- - I)\nabla v^-(X)\cdot(\widetilde{M}_1 - X_{\overline{DE}})\phi_{1,T}^P(X) \\ &\quad + 2d^- N_{\overline{DE}}^-(X_{\overline{DE}} \ominus X)\cdot(M_1 - X_{\overline{DE}})\phi_{1,T}^P(X) \\ &\quad + d^-((x_{\overline{DE}} - x)^2 - (y_{\overline{DE}} - y)^2)\phi_{1,T}^P(X) \\ &\quad + d^-((x_1 - x_{\overline{DE}})^2 - (y_1 - y_{\overline{DE}})^2)\phi_{1,T}^P(X). \end{aligned} \tag{3.38}$$

Using the partition of unity property (3.1a) in Lemma 3.3, we obtain

$$\sum_{i=1}^4 v(X)\phi_{i,T}^P(X) = v(X) = I_{h,T}^P v(X). \tag{3.39}$$

Applying (3.39) to the first term on the right hand side of (3.38) yields

$$\begin{aligned} &\sum_{i=1}^4 \nabla v(X)\cdot(M_i - X)\phi_{i,T}^P(X) \\ = \; &-(N_{\overline{DE}}^- - I)\nabla v^-(X)\cdot(M_1 - \widetilde{M}_1)\phi_{1,T}^P(X) \\ &-(N_{\overline{DE}}^- - I)\nabla v^-(X)\cdot(\widetilde{M}_1 - X_{\overline{DE}})\phi_{1,T}^P(X) - rF_0(X). \end{aligned} \tag{3.40}$$

The identity (3.34) follows from substituting $\mathbf{q}$ for $\nabla v(X)$ in (3.40). □

The next lemma provides upper bounds of $F_0(X)$ and $\nabla F_0(X)$.

Lemma 3.10. *There exists a constant $C > 0$ such that $F_0(X)$ given in* (3.35) *satisfies*

$$|F_0(X)| \le Ch^2, \tag{3.41}$$

and

$$\|\nabla F_0(X)\| \le Ch, \tag{3.42}$$

for every point $X \in \Omega^- \cap T^-$, and $X_{\overline{DE}} \in \overline{DE}$.

Proof. We recall the upper bounds of the IFE basis functions (3.3a) in Theorem 3.2. Then by direct calculations we obtain

$$\begin{aligned}
|F_0(X)| &\le \sum_{i=2}^{4} |((x_i-x)^2-(y_i-y)^2)||\phi_{i,T}^P(X)| \\
&\quad +2\|N_{\overline{DE}}^-\|\|X_{\overline{DE}}\ominus X\|\|M_1-X_{\overline{DE}}\||\phi_{1,T}^P(X)| \\
&\quad +|(x_{\overline{DE}}-x)^2-(y_{\overline{DE}}-y)^2||\phi_{1,T}^P(X)|+|(x_1-x_{\overline{DE}})^2-(y_1-y_{\overline{DE}})^2||\phi_{1,T}^P(X)| \\
&\le C\sum_{i=2}^{4} |((x_i-x)^2-(y_i-y)^2)|+C\|N_{\overline{DE}}^-\|\|X_{\overline{DE}}\ominus X\|\|M_1-X_{\overline{DE}}\| \\
&\quad +C|(x_{\overline{DE}}-x)^2-(y_{\overline{DE}}-y)^2|+C|(x_1-x_{\overline{DE}})^2-(y_1-y_{\overline{DE}})^2| \\
&\le Ch^2, \qquad (3.43)
\end{aligned}$$

which proves (3.41). For estimate (3.42), first we note that

$$\begin{aligned}
&\partial_x F_0(X) \\
=\ &\sum_{i=2}^{4} -2(x_i-x)\phi_{i,T}^P(X)+\sum_{i=2}^{4}((x_i-x)^2-(y_i-y)^2)\phi_{i,T,x}^P(X) \\
&+2N_{\overline{DE}}^-(-1,0)^t\cdot(M_1-X_{\overline{DE}})\phi_{1,T}^P(X)+2N_{\overline{DE}}^-(X_{\overline{DE}}\ominus X)\cdot(M_1-X_{\overline{DE}})\phi_{1,T,x}^P(X) \\
&+-2(x_{\overline{DE}}-x)\phi_{1,T}^P(X)+((x_{\overline{DE}}-x)^2-(y_{\overline{DE}}-y)^2)\phi_{1,T,x}^P(X) \\
&+((x_1-x_{\overline{DE}})^2-(y_1-y_{\overline{DE}})^2)\phi_{1,T,x}^P(X).
\end{aligned}$$

Then we use Theorem 3.2 again and follow similar arguments in (3.43) to obtain

$$|\partial_x F_0(X)|\le Ch. \qquad (3.44)$$

Similarly, we can obtain the bound $|\partial_y F_0(X)|\le Ch$. The estimate (3.42) follows immediately. □

Now we are ready to derive an expansion of the IFE interpolation error.

Theorem 3.5. *Let $T\in\mathcal{T}_h^i$ be an interface element, and $u\in PC_{int}^2(T)$. For every point $X\in\Omega^-\cap T^-$, and $X_{\overline{DE}}\in\overline{DE}$, we have*

$$I_{h,T}^P u(X)-u(X)=(F_1+F_2)\phi_{1,T}^P(X)-\frac{1}{2}F_0u_{xx}(X)+\sum_{i=1}^{4} I_i\phi_{i,T}^P(X), \qquad (3.45)$$

where

$$
\begin{aligned}
F_1(X) &= (N^-(\widetilde{M}_1) - N^-_{\overline{DE}})\nabla u^-(X)\cdot(M_1-\widetilde{M}_1), && (3.46a)\\
F_2(X) &= -(N^-_{\overline{DE}} - I)\nabla u^-(X)\cdot(\widetilde{M}_1 - X_{\overline{DE}}), && (3.46b)\\
I_{1,1}(X) &= (N^-(\widetilde{M}_1) - I)\int_0^1 \frac{d}{dt}(\nabla u^-(t\widetilde{M}_1+(1-t)X))(M_1-\widetilde{M}_1)\,dt, && (3.46c)\\
I_{1,2}(X) &= \int_0^{\tilde{t}} (1-t)\frac{d^2}{dt^2}u(tM_1+(1-t)X)dt, && (3.46d)\\
I_{1,3}(X) &= \int_{\tilde{t}}^1 (1-t)\frac{d^2}{dt^2}u(tM_1+(1-t)X)dt, && (3.46e)\\
I_1(X) &= I_{1,1}(X)+I_{1,2}(X)+I_{1,3}(X), && (3.46f)\\
I_i(X) &= \int_0^1 (1-t)\frac{d^2}{dt^2}u(tM_i+(1-t)X)dt, \quad i=2,3,4. && (3.46g)
\end{aligned}
$$

Proof. First we note that $u(M_i)$, $i=2,3,4$ can be expanded at X as follows

$$
u(M_i) = u(X)+\nabla u(X)\cdot(M_i-X)+\int_0^1 (1-t)\frac{d^2}{dt^2}u(tM_i+(1-t)X)dt, \quad i=2,3,4. \tag{3.47}
$$

For $u(M_1)$, the expansion is derived as follows

$$
\begin{aligned}
& u(M_1)\\
= \;& u(X)+\int_0^{\tilde{t}}\frac{d}{dt}u(tM_1+(1-t)X)dt+\int_{\tilde{t}}^1\frac{d}{dt}u(tM_1+(1-t)X)dt\\
= \;& u(X)+\nabla u^-(X)\cdot(M_1-X)-(1-\tilde{t})\nabla u^-(\widetilde{M}_1)\cdot(M_1-X)\\
& +\int_0^{\tilde{t}}(1-t)\frac{d^2}{dt^2}u^-(tM_1+(1-t)X)dt+(1-\tilde{t})\nabla u^+(\widetilde{M}_1)\cdot(M_1-X)\\
& +\int_{\tilde{t}}^1(1-t)\frac{d^2}{dt^2}u^+(tM_1+(1-t)X)dt\\
= \;& u(X)+\nabla u^-(X)\cdot(M_1-X)+(N^-(\widetilde{M}_1)-I)\nabla u^-(\widetilde{M}_1)\cdot(M_1-X)(1-\tilde{t})\\
& +\int_0^{\tilde{t}}(1-t)\frac{d^2}{dt^2}u^-(tM_1+(1-t)X)dt+\int_{\tilde{t}}^1(1-t)\frac{d^2}{dt^2}u^+(tM_1+(1-t)X)dt\\
= \;& u(X)+\nabla u^-(X)\cdot(M_1-X)+(N^-(\widetilde{M}_1)-I)\nabla u^-(X)\cdot(M_1-X)(1-\tilde{t})\\
& (N^-(\widetilde{M}_1)-I)\int_0^1\frac{d}{dt}(\nabla u^-(t\widetilde{M}_1+(1-t)X))\cdot(M_1-X)(1-\tilde{t})dt \qquad (3.48)\\
& +\int_0^{\tilde{t}}(1-t)\frac{d^2}{dt^2}u^-(tM_1+(1-t)X)dt+\int_{\tilde{t}}^1(1-t)\frac{d^2}{dt^2}u^+(tM_1+(1-t)X)dt.
\end{aligned}
$$

Using the expansions (3.47) and (3.48) to substitute $u(M_i)$ in (3.26), and letting $p = u(X)$, $\mathbf{q} = \nabla u^-(X)$, $2r = u^-_{xx}(X)$ in (3.34), then we can see (3.45) follows from applying (3.34) to (3.26). □

Now we are ready to derive the interpolation error in L^2 norm.

Theorem 3.6. *There exists a constant $C > 0$ independent of interface location such that*

$$\|I^P_{h,T}u - u\|_{0,\Omega^-\cap T^-} \le Ch^2\|u\|_{2,T}, \tag{3.49}$$

for every $u \in PH^2_{int}(T)$ on any interface element $T \in \mathcal{T}^i_h$.

Proof. First we assume $u \in PC^2_{int}(T)$. Then by Theorem 3.5 we can expand $I^P_{h,T}u(X) - u(X)$ as (3.45). Taking the absolute value of both sides on (3.45) and applying triangle inequality we have

$$\begin{aligned}\left|I^P_{h,T}u(X) - u(X)\right| \;\le\; & (|F_1| + |F_2|)\left|\phi^P_{1,T}(X)\right| + |F_0||u_{xx}(X)| \\ & +(|I_{1,1}| + |I_{1,2}| + |I_{1,3}|)\left|\phi^P_{1,T}(X)\right| + \sum_{i=2}^{4}|I_i|\left|\phi^P_{i,T}(X)\right|\end{aligned}$$

Note that in Theorem 3.2 we have shown that IFE basis functions are bounded (3.3a); hence

$$\begin{aligned}\left\|I^P_{h,T}u - u\right\|_{0,\Omega^-\cap T^-} \;\le\; & C\Big(\|F_1\|_{0,\Omega^-\cap T^-} + \|F_2\|_{0,\Omega^-\cap T^-} + |F_0|_{0,\infty,\Omega^-\cap T^-}\|u_{xx}\|_{0,\Omega^-\cap T^-} \\ & \|I_{1,1}\|_{0,\Omega^-\cap T^-} + \|I_{1,2}\|_{0,\Omega^-\cap T^-} + \|I_{1,3}\|_{0,\Omega^-\cap T^-} + \sum_{i=2}^{4}\|I_i\|_{0,\Omega^-\cap T^-}\Big).\end{aligned} \tag{3.50}$$

To estimate the term involving F_1 in (3.50), we apply (3.31) from Lemma 3.8 to obtain

$$\|F_1\|_{0,\Omega^-\cap T^-} \le \|N^-(\widetilde{M}_1) - N^-_{\overline{DE}}\|\;\|M_1 - \widetilde{M}_1\|\;\|\nabla u^-\|_{0,\Omega^-\cap T^-} \le Ch^2\|u\|_{2,\Omega^-\cap T^-}. \tag{3.51}$$

To bound the term involving F_2 in (3.50), we let $X_{\overline{DE}} = \widetilde{M}_1^{\perp}$ in (3.46b), and use the estimate (3.30) from Lemma 3.8 to obtain

$$\|F_2\|_{0,\Omega^-\cap T^-} \le \|N^-_{\overline{DE}} - I\|\;\|\widetilde{M}_1 - \widetilde{M}_1^{\perp}\|\;\|\nabla u^-\|_{0,\Omega^-\cap T^-} \;\le Ch^2\|u\|_{2,\Omega^-\cap T^-}. \tag{3.52}$$

Applying the estimate of F_0 in (3.41) from Lemma 3.10, we have

$$|F_0|_{0,\infty,\Omega^-\cap T^-}\|u_{xx}\|_{0,\Omega^-\cap T^-} \le Ch^2|u|_{2,\Omega^-\cap T^-}. \tag{3.53}$$

To bound the term involving $I_{1,1}$, we let $\xi = t\tilde{x}_1 + (1-t)x$, $\eta = t\tilde{y}_1 + (1-t)y$, and note that

$$\begin{aligned}
& \frac{d}{dt}(\nabla u^-(t\widetilde{M}_1 + (1-t)X)) \cdot (M_1 - \widetilde{M}_1) \\
= \; & \frac{d}{dt}\left(u_\xi(t\widetilde{M}_1 + (1-t)X), u_\eta(t\widetilde{M}_1 + (1-t)X)\right) \cdot (M_1 - \widetilde{M}_1) \\
= \; & u_{\xi\xi}(\xi,\eta)(\tilde{x}_1 - x)(x_1 - \tilde{x}_1) + u_{\xi\eta}(\xi,\eta)(\tilde{y}_1 - y)(x_1 - \tilde{x}_1) \\
& + u_{\eta\xi}(\xi,\eta)(\tilde{x}_1 - x)(y_1 - \tilde{y}_1) + u_{\eta\eta}(\xi,\eta)(\tilde{y}_1 - y)(y_1 - \tilde{y}_1) \\
\leq \; & h^2|u_{\xi\xi}(\xi,\eta)| + 2h^2|u_{\xi\eta}(\xi,\eta)| + h^2|u_{\eta\eta}(\xi,\eta)|.
\end{aligned}$$

Therefore, by Cauchy-Schwarz inequality, we have

$$\begin{aligned}
|I_{1,1}|^2 &\leq C\|N^-(\widetilde{M}_1) - I\|^2 \left(\int_0^1 h^2|u_{\xi\xi}(\xi,\eta)| + 2h^2|u_{\xi\eta}(\xi,\eta)| + h^2|u_{\eta\eta}(\xi,\eta)|\mathrm{d}t\right)^2 \\
&\leq Ch^4 \int_0^1 |u_{\xi\xi}(\xi,\eta)|^2 + |u_{\xi\eta}(\xi,\eta)|^2 + |u_{\eta\eta}(\xi,\eta)|^2 \mathrm{d}t. \qquad (3.54)
\end{aligned}$$

Note that the point (ξ,η) is in $\Omega^- \cap T^-$ since the entire line segment $\overline{X\widetilde{M}_1}$ is inside $\Omega^- \cap T^-$. Thus, we integrate (3.54) over $\Omega^- \cap T^-$ to have the following bound

$$\begin{aligned}
\|I_{1,1}\|^2_{0,\Omega^-\cap T^-} &= \int_{\Omega^-\cap T^-} |I_{1,1}|^2 \mathrm{d}\xi\mathrm{d}\eta \\
&\leq Ch^4 \int_0^1 \left(\int_{\Omega^-\cap T^-} |u_{\xi\xi}(\xi,\eta)|^2 + |u_{\xi\eta}(\xi,\eta)|^2 + |u_{\eta\eta}(\xi,\eta)|^2 \mathrm{d}\xi\mathrm{d}\eta\right) \mathrm{d}t \\
&\leq Ch^4 \|u\|^2_{2,\Omega^-\cap T^-}, \qquad (3.55)
\end{aligned}$$

Similarly, we bound $I_{1,2}$ as follows

$$\begin{aligned}
& |I_{1,2}|^2 \\
\leq \; & C\left(\int_0^{\tilde{t}} (1-t)\frac{d^2}{dt^2} u^-(tM_1 + (1-t)X)dt\right)^2 \\
\leq \; & \left(\int_0^{\tilde{t}} (1-t)\left(u^-_{\xi\xi}(\xi,\eta)(x_1 - x)^2 + 2u^-_{\xi\eta}(\xi,\eta)(x_1 - x)(y_1 - y) + u^-_{\eta\eta}(\xi,\eta)(y_1 - y)^2\right) dt\right)^2 \\
\leq \; & Ch^4 \int_0^{\tilde{t}} (1-t)^2 \left(|u^-_{\xi\xi}(\xi,\eta)|^2 + |u^-_{\xi\eta}(\xi,\eta)|^2 + |u^-_{\eta\eta}(\xi,\eta)|^2\right) dt. \qquad (3.56)
\end{aligned}$$

Hence, by integrating (3.56) over $\Omega^- \cap T^-$

$$\begin{aligned}
\|I_{1,2}\|^2_{0,\Omega^-\cap T^-} &\leq Ch^4 \int_0^{\tilde{t}} (1-t)^2 \int_{\Omega^-\cap T^-} \left(|u^-_{\xi\xi}(\xi,\eta)|^2 + |u^-_{\xi\eta}(\xi,\eta)|^2 + |u^-_{\eta\eta}(\xi,\eta)|^2\right) \mathrm{d}\xi\mathrm{d}\eta dt \\
&\leq Ch^4 |u|^2_{2,\Omega^-\cap T^-}. \qquad (3.57)
\end{aligned}$$

We bound $|I_{1,3|}$ as follows

$$\begin{aligned}
&|I_{1,3}|^2 \\
\leq\ & \left(\int_{\tilde{t}}^1 (1-t)\frac{d^2}{dt^2}u^+(tM_1+(1-t)X)dt\right)^2 \\
\leq\ & \left(\int_{\tilde{t}}^1 (1-t)\left(u^+_{\xi\xi}(\xi,\eta)(x_1-x)^2+2u^+_{\xi\eta}(\xi,\eta)(x_1-x)(y_1-y)+u^+_{\eta\eta}(\xi,\eta)(y_1-y)^2\right)dt\right)^2 \\
\leq\ & Ch^4\int_{\tilde{t}}^1 (1-t)^2\left(|u^+_{\xi\xi}(\xi,\eta)|^2+|u^+_{\xi\eta}(\xi,\eta)|^2+|u^+_{\eta\eta}(\xi,\eta)|^2\right)dt. \qquad (3.58)
\end{aligned}$$

Hence, integrating (3.58) over $\Omega^-\cap T^-$ yields

$$\begin{aligned}
\|I_{1,3}\|^2_{0,\Omega^-\cap T^-} \leq\ & \int_T Ch^4\int_{\tilde{t}}^1 (1-t)^2\left(|u^+_{\xi\xi}(\xi,\eta)|^2+|u^+_{\xi\eta}(\xi,\eta)|^2+|u^+_{\eta\eta}(\xi,\eta)|^2\right)dt\mathrm{d}\xi\mathrm{d}\eta \\
\leq\ & Ch^4\int_{\tilde{t}}^1 (1-t)^2\left(\int_{T/\Omega^-}|u^+_{\xi\xi}(\xi,\eta)|^2+|u^+_{\xi\eta}(\xi,\eta)|^2+|u^+_{\eta\eta}(\xi,\eta)|^2\mathrm{d}\xi\mathrm{d}\eta\right)dt \\
\leq\ & Ch^4|u|^2_{2,T/\Omega^-},
\end{aligned}$$

i.e.,

$$\|I_{1,3}\|^2_{0,\Omega^-\cap T^-}\leq Ch^2|u|_{2,T/\Omega^-}\leq Ch^2|u|_{2,T}. \qquad (3.59)$$

Similarly, we can show

$$\|I_i\|^2_{0,\Omega^-\cap T^-}\leq Ch^2|u|_{2,\Omega^-\cap T^-},\quad i=2,3,4. \qquad (3.60)$$

Applying the above estimates (3.51), (3.52), (3.53), (3.55), (3.57), (3.59), and (3.60) to (3.50), we obtain (3.49) for u in $PC^2_{int}(T)$. Finally, we apply the density hypothesis **(H4)** to obtain the estimate (3.49) for u in $PH^2_{int}(T)$. □

Now we estimate the interpolation error using semi-H^1 norm. The following theorem gives the Taylor expansion of the first order derivatives of the interpolation error.

Theorem 3.7. *Let $T\in\mathcal{T}_h^i$ be an interface element, and $u\in PC^3_{int}(T)$. For every point $X\in\Omega^-\cap T^-$, and $X_{\overline{DE}}\in\overline{DE}$, we have*

$$\partial_x\left(I^P_{h,T}u(X)-u(X)\right)=(F_1+F_2)\phi^P_{1,T,x}(X)-\frac{1}{2}F_{0,x}u_{xx}(X)+\sum_{i=1}^4 I_i\phi^P_{i,T,x}(X), \qquad (3.61)$$

and

$$\partial_y\left(I^P_{h,T}u(X)-u(X)\right)=(F_1+F_2)\phi^P_{1,T,y}(X)-\frac{1}{2}F_{0,y}u_{xx}(X)+\sum_{i=1}^4 I_i\phi^P_{i,T,y}(X), \qquad (3.62)$$

where F_0, F_1, F_2, and I_i, $i=1,\cdots,4$ are defined in (3.35), (3.46a) - (3.46g), *and $F_{0,x}=\partial_xF_0$, and $F_{0,y}=\partial_yF_0$.*

Proof. We only prove (3.61), and similar arguments can be used to establish (3.62). Taking the x-derivative on both sides of the equation (3.45), we obtain

$$\begin{aligned}
&\partial_x \left(I_{h,T}^P u(X) - u(X)\right) \\
= \;& (F_{1,x} + F_{2,x})\phi_{1,T}^P(X) + (F_1 + F_2)\phi_{1,T,x}^P(X) - \frac{1}{2}F_{0,x}u_{xx}(X) - \frac{1}{2}F_0 u_{xxx}(X) \\
&+ \sum_{i=1}^4 \left(I_{i,x}\phi_{i,T}^P(X) + I_i\phi_{i,T,x}^P(X)\right). \qquad (3.63)
\end{aligned}$$

Taking the x-derivative of (3.47) and (3.48) yields

$$\begin{aligned}
I_{1,x} &= -\nabla u_x(X)\cdot(M_1 - X) - \frac{\partial}{\partial x}\left((N^-(\widetilde{M}_1) - I)(\nabla u^-(X))\cdot(M_1 - \widetilde{M}_1)\right), \\
I_{i,x} &= -\nabla u_x(X)\cdot(M_i - X), \quad i = 2,3,4.
\end{aligned}$$

Therefore,

$$\begin{aligned}
\sum_{i=1}^4 I_{i,x}\phi_{i,T}^P(X) &= -\sum_{i=1}^4 \nabla u_x(X)\cdot(M_i - X)\phi_{i,T}^P(X) \\
&\quad -\frac{\partial}{\partial x}\left((N^-(\widetilde{M}_1) - I)(\nabla u^-(X))\cdot(M_1 - \widetilde{M}_1)\right)\phi_{1,T}^P(X). \qquad (3.64)
\end{aligned}$$

We let $\mathbf{q} = \nabla u_x(X) = (u_{xx}(X), u_{xy}(X))^t$, $2d = u_{xxx}(X)$ and use them in (3.34) from Lemma 3.9, then we obtain

$$\begin{aligned}
&\sum_{i=1}^4 \nabla u_x(X)\cdot(M_i - X)\phi_{i,T}^P(X) \\
= \;& -(N_{\overline{DE}}^- - I)\nabla u_x(X)\cdot(M_1 - \widetilde{M}_1)\phi_{1,T}^P(X) \\
&-(N_{\overline{DE}}^- - I)\nabla u_x(X)\cdot(\widetilde{M}_1 - X_{\overline{DE}})\phi_{1,T}^P(X) - \frac{1}{2}u_{xxx}(X)F_0(X). \qquad (3.65)
\end{aligned}$$

Replacing the first term on the right hand side of (3.64) by (3.65) yields

$$\begin{aligned}
&\sum_{i=1}^4 I_{i,x}\phi_{i,T}^P(X) \\
= \;& (N_{\overline{DE}}^- - I)\nabla u_x(X)\cdot(M_1 - \widetilde{M}_1)\phi_{1,T}^P(X) \\
&+(N_{\overline{DE}}^- - I)\nabla u_x(X)\cdot(\widetilde{M}_1 - X_{\overline{DE}})\phi_{1,T}^P(X) \\
&+\frac{1}{2}u_{xxx}(X)F_0(X) - \partial_x\left((N^-(\widetilde{M}_1) - I)(\nabla u^-(X))\cdot(M_1 - \widetilde{M}_1)\right)\phi_{1,T}^P(X). \qquad (3.66)
\end{aligned}$$

Plugging (3.66) in (3.63) we have

$$\begin{aligned}
\partial_x \left(I_{h,T}^P u(X) - u(X)\right) &= (F_{1,x} + F_{2,x} + F_4 + F_5 + F_{6,x})\phi_{1,T}^P(X) + (F_1 + F_2)\phi_{1,T,x}^P(X) \\
&\quad -\frac{1}{2}F_{0,x}u_{xx}(X) + \sum_{i=1}^4 I_i\phi_{i,T,x}^P(X), \qquad (3.67)
\end{aligned}$$

where

$$\begin{aligned} F_4 &= (N^-_{\overline{DE}} - I)\nabla u_x(X) \cdot (M_1 - \widetilde{M}_1), \\ F_5 &= (N^-_{\overline{DE}} - I)\nabla u_x(X) \cdot (\widetilde{M}_1 - X_{\overline{DE}}), \\ F_{6,x} &= -\partial_x \left((N^-(\widetilde{M}_1) - I)(\nabla u^-(X)) \cdot (M_1 - \widetilde{M}_1) \right). \end{aligned}$$

Note that

$$\begin{aligned} & F_{1,x} + F_{2,x} + F_{6,x} \\ = \; & \partial_x \bigg((I - N^-_{\overline{DE}})\nabla u^-(X) \cdot (M_1 - \widetilde{M}_1) - (N^-_{\overline{DE}} - I)\nabla u^-(X) \cdot (\widetilde{M}_1 - X_{\overline{DE}}) \bigg) \\ = \; & (N^-_{\overline{DE}} - I)\nabla u^-_x(X) \cdot (X_{\overline{DE}} - M_1). \end{aligned}$$

Then, it can be verified by direct calculations that

$$F_{1,x} + F_{2,x} + F_4 + F_5 + F_{6,x} = 0. \tag{3.68}$$

Plugging (3.68) in (3.67), we obtain the result (3.61). □

Now we can derive the semi-H^1 norm error for interpolation function.

Theorem 3.8. *There exists a constant $C > 0$ independent of interface location such that*

$$|I^P_{h,T}u - u|_{1,\Omega^- \cap T^-} \leq Ch\|u\|_{2,T}, \tag{3.69}$$

for every $u \in PH^2_{int}(T)$ on any interface element $T \in \mathcal{T}^i_h$.

Proof. First we assume $u \in PC^3_{int}(T)$. By Theorem 3.7 we can expand the first order derivatives of $I^P_{h,T}u - u$ as (3.61) and (3.62). Following a similar approach in the proof of Theorem 3.6, we can derive upper bounds for F_1, F_2, and I_i, $i = 1, 2, 3, 4$ from (3.51) - (3.60). A bound of $F_{0,x}$ is given by (3.42) in the Lemma 3.10. Applying these estimates to (3.61) and (3.62) establishes (3.69) for $u \in PC^3_{int}(T)$. Then (3.69) follows for $u \in PH^2_{int}(T)$ according to the density hypothesis **(H4)**. □

For estimates on $\Omega^+ \cap T^+$, $\Omega^+ \cap T^-$ and $\Omega^- \cap T^+$, similar results can be obtained. For interface elements of other types and cases, the analysis is also similar. Putting all of these error estimates together leads to the following theorem.

Theorem 3.9. *There exists a constant $C > 0$ independent of interface location such that*

$$\|I^P_{h,T}u - u\|_{0,T} + h|I^P_{h,T}u - u|_{1,T} \leq Ch^2\|u\|_{2,T}, \tag{3.70}$$

for every $u \in PH^2_{int}(T)$ on any interface element $T \in \mathcal{T}^i_h$.

The global interpolation error bound, stated in the next theorem, follows from summing over the estimate (3.24a) on non-interface elements and estimate (3.70) on interface elements.

Theorem 3.10. *For $u \in PH^2_{int}(\Omega)$, we have the following estimate for the interpolation error*

$$\|I_h^P u - u\|_{0,\Omega} + h|I_h^P u - u|_{1,\Omega} \leq Ch^2\|u\|_{2,\Omega}. \tag{3.71}$$

We will provide numerical verification of the interpolation error estimates (3.71) in Section 3.3.

3.2.2 Error Analysis of Interpolation on $S_h^I(\Omega)$

In this subsection, we analyze interpolation error $\|I_{h,T}^I u - u\|_{k,T}$, $k = 0, 1$ on an interface element T, and then derive a global interpolation error bound for $I_h^I u - u$.

For an interface element $T \in \mathcal{T}_h^i$, we define the local interpolation $I_{h,T}^I : PH^2_{int}(T) \to S_h^i(T)$ using the set of IFE basis function $\{\phi_{i,T}^I\}_{i=1}^4$ as follows

$$I_{h,T}^I u(X) = \sum_{i=1}^{4} \left(\frac{1}{|b_i|} \int_{b_i} u(X) \mathrm{d}s \right) \phi_{i,T}^I(X). \tag{3.72}$$

Then we define the global IFE interpolation $I_h^I : PH^2_{int}(\Omega) \to S_h(\Omega)$ piece-wisely by

$$(I_h^I u)|_T = I_{h,T}^I u. \tag{3.73}$$

First we derive an error bound for IFE basis function $\phi_{i,T}^I$ in the following lemma.

Lemma 3.11. *There exists a constant $C > 0$, independent of the interface location, such that*

$$\|\phi_{i,T}^I\|_{0,T} + h|\phi_{i,T}^I|_{1,T} \leq Ch, \quad i = 1, 2, 3, 4, \tag{3.74}$$

for every interface element $T \in \mathcal{T}_h^i$.

Proof. Using the point-wise bound (3.3b) of the IFE basis function stated in Theorem 3.2, we have the following estimate

$$\|\phi_{i,T}^I\|_{0,T}^2 = \int_T \left(\phi_{i,T}^I(x,y)\right)^2 \mathrm{d}x\mathrm{d}y \leq \|\phi_{i,T}^I\|_{0,\infty,T}^2 \int_T 1 \mathrm{d}x\mathrm{d}y \leq Ch^2.$$

Similarly

$$|\phi_{i,T}^I|_{1,T}^2 = \int_T \nabla\phi_{i,T}^I(x,y) \cdot \nabla\phi_{i,T}^I(x,y) \mathrm{d}x\mathrm{d}y \leq |\phi_{i,T}^I|_{1,\infty,T}^2 \int_T 1 \mathrm{d}x\mathrm{d}y \leq C.$$

Here we use the fact that the size of an element is $|T| = O(h^2)$. Finally, the estimate (3.74) follows from combining the above estimates. □

Now we are ready to derive an error bound for the interpolation error $I_{h,T}^I u - u$.

Theorem 3.11. *There exists a constant $C > 0$ independent of interface location such that*

$$\|I_{h,T}^I u - u\|_{0,T} + h|I_{h,T}^I u - u|_{1,T} \leq Ch^2 \|u\|_{2,T}, \tag{3.75}$$

for every $u \in PH_{int}^2(T)$ on any interface element $T \in \mathcal{T}_h^i$.

Proof. By triangular inequality, we have

$$|I_{h,T}^I u - u|_{k,T} \leq |I_{h,T}^I u - I_{h,T}^P u|_{k,T} + |I_{h,T}^P u - u|_{k,T}, \quad k = 0, 1, \tag{3.76}$$

where the notation $|\cdot|_{0,T}$ means the regular L^2 norm on T, *i.e.*, $\|\cdot\|_{0,T}$. A bound of the second term on the right hand side of (3.76) is given in (3.70); hence, it suffices to derive an error bound for $|I_{h,T}^I u - I_{h,T}^P u|_{k,T}$. Using the Cauchy-Schwarz inequality on (3.72) yields

$$\begin{aligned}
\left|I_{h,T}^I u(X)\right| &= \sum_{i=1}^4 \frac{1}{|b_i|} \left| \int_{b_i} u(X) \mathrm{d}s \right| \left|\phi_{i,T}^I(X)\right| \\
&\leq \sum_{i=1}^4 \frac{1}{|b_i|} \left| \int_{b_i} |u(X)|^2 \mathrm{d}s \right|^{1/2} \left| \int_{b_i} 1 \mathrm{d}s \right|^{1/2} \left|\phi_{i,T}^I(X)\right| \\
&\leq \sum_{i=1}^4 \frac{1}{|b_i|^{1/2}} \|u\|_{0,b_i} \left|\phi_{i,T}^I(X)\right|.
\end{aligned} \tag{3.77}$$

For $k = 0, 1$, we integrate (3.77) on T, using the IFE basis function bounds (3.74) stated in Lemma 3.11 and standard trace inequality (3.4) to obtain

$$\begin{aligned}
\left|I_{h,T}^I u\right|_{k,T} &\leq \sum_{i=1}^4 \frac{1}{|b_i|^{1/2}} \|u\|_{0,b_i} \left|\phi_{i,T}^I\right|_{k,T} \\
&\leq Ch^{1-k} \sum_{i=1}^4 \frac{1}{|b_i|^{1/2}} \|u\|_{0,b_i} \\
&\leq Ch^{1-k} \sum_{i=1}^4 \frac{1}{|b_i|^{1/2}} C\left(h^{-1/2}\|u\|_{0,T} + h^{1/2}|u|_{1,T}\right) \\
&\leq C\left(h^{-k}\|u\|_{0,T} + h^{1-k}|u|_{1,T}\right).
\end{aligned} \tag{3.78}$$

Here the last inequality is due to $|b_i| = O(h)$. We note that

$$I_{h,T}^I u - I_{h,T}^P u = I_{h,T}^I u - I_{h,T}^I (I_{h,T}^P u) = I_{h,T}^I (u - I_{h,T}^P u).$$

Also, function $u - I_{h,T}^P u$ is in $H^1(T)$. Substituting u by $u - I_{h,T}^P u$ in (3.78) yields

$$|I_{h,T}^I u - I_{h,T}^P u|_{k,T} \leq C\left(h^{-k}\|u - I_{h,T}^P u\|_{0,T} + h^{1-k}|u - I_{h,T}^P u|_{1,T}\right). \tag{3.79}$$

Applying the error bounds (3.70) in Theorem 3.9, we obtain

$$|I^I_{h,T}u - I^P_{h,T}u|_{k,T} \leq C\left(h^{-k}h^2\|u\|_{2,T} + h^{1-k}h\|u\|_{2,T}\right) \leq Ch^{2-k}\|u\|_{2,T}. \tag{3.80}$$

Then (3.75) follows immediately from combining (3.80) and (3.70). □

The global interpolation error bound, stated in the next theorem, follows from summing over the estimate (3.24b) on non-interface elements and estimate (3.75) on interface elements.

Theorem 3.12. *For $u \in PH^2_{int}(\Omega)$, we have the following estimate for the interpolation error*

$$\|I^I_h u - u\|_{0,\Omega} + h|I^I_h u - u|_{1,\Omega} \leq Ch^2\|u\|_{2,\Omega}. \tag{3.81}$$

3.3 Numerical Experiments

In this section, we provide numerical verifications for error estimates of the nonconforming rotated Q_1 IFE interpolations. We let the simulation domain be a unit square, *i.e.*, $\Omega = (-1,1)\times(-1,1)$, and assume that the interface curve Γ is a circle centered at the origin with radius $r_0 = \pi/6.28$. The interface curve Γ separates the domain into the following two sub-domains

$$\Omega^- = \{(x,y)^t : x^2+y^2 < r_0^2\}, \quad \Omega^+ = \{(x,y)^t : x^2+y^2 > r_0^2\}.$$

We compute two types IFE interpolants $I^P_h u$ and $I^I_h u$ of the following function

$$u(x,y) = \begin{cases} \dfrac{r^\alpha}{\beta^-}, & \text{if } r < r_0, \\ \dfrac{r^\alpha}{\beta^+} + \left(\dfrac{1}{\beta^-} - \dfrac{1}{\beta^+}\right) r_0^\alpha, & \text{if } r > r_0, \end{cases} \tag{3.82}$$

where $\alpha = 5$, $r = \sqrt{x^2+y^2}$. The interface jump conditions (1.4) and (1.5) can be easily verified for this function u. We note that this numerical example have been used in [69, 70].

In our computation, we use a family of Cartesian meshes $\{\mathcal{T}_h\}$. Each mesh $\mathcal{T}_h$ is formed by partitioning Ω into $N\times N$ congruent squares such that the edge length of square is $h = 2/N$. Errors of interpolations are given in L^∞, L^2, and semi-H^1 norms. Errors in the L^∞ norm are defined by

$$\|I^k_h u - u\|_{0,\infty,\Omega} = \max_{T\in\mathcal{T}_h}\left(\max_{(x,y)\in\tilde{T}\subset T} |I^k_h u(x,y) - u(x,y)|\right), \quad k = P, I, \tag{3.83}$$

where $\tilde{T}$ consists of the 49 uniformly distributed points in T as illustrated in Figure 3.2. The L^2 and semi-H^1 norms are computed by suitable Gaussian quadratures. In the following

error tables, rates of convergence are computed by applying the formulas:

$$\frac{1}{\ln(2)} \ln \left(\frac{\|I_h^k u - u\|}{\|I_{h/2}^k u - u\|} \right), \quad k = P, I, \tag{3.84}$$

for a specific norm $\|\cdot\|$.

Figure 3.2: Points selected to calculate the L^∞ norm on a rectangular element T.

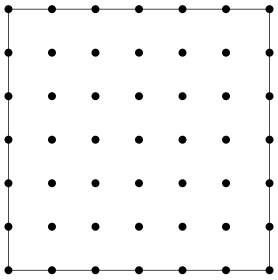

We compute errors of these interpolants with the coefficient $(\beta^-, \beta^+) = (1, 10)$ which represents a moderate discontinuity in the diffusion coefficient. Table 3.1 and Table 3.2 contain errors of nonconforming rotated Q_1 IFE interpolations $I_h^I u$ and $I_h^P u$, respectively. Data in these tables confirm that both interpolants $I_h^I u$ and $I_h^P u$ have optimal approximation capabilities in L^2 and semi-H^1 norms which are consistent with our error estimates given in Theorem 3.10 and Theorem 3.12. Moreover, the optimal point-wise convergence of these interpolations can be observed in L^∞ norm.

Table 3.1: Errors of IFE interpolations $I_h^I u$ with $\beta^- = 1$, $\beta^+ = 10$.

N	$\|\cdot\|_{0,\infty,\Omega}$	rate	$\|\cdot\|_{0,\Omega}$	rate	$\|\cdot\|_{1,\Omega}$	rate
10	$2.5948E{-2}$		$9.0458E{-3}$		$1.9610E{-1}$	
20	$7.3237E{-3}$	1.8250	$2.3194E{-3}$	1.9635	$9.9238E{-2}$	0.9826
40	$1.9438E{-3}$	1.9137	$5.8358E{-4}$	1.9908	$4.9913E{-2}$	0.9914
80	$5.0059E{-4}$	1.9572	$1.4637E{-4}$	1.9953	$2.5028E{-2}$	0.9959
160	$1.2701E{-4}$	1.9787	$3.6653E{-5}$	1.9976	$1.2532E{-2}$	0.9979
320	$3.1988E{-5}$	1.9894	$9.1718E{-6}$	1.9986	$6.2705E{-3}$	0.9989
640	$8.0266E{-6}$	1.9947	$2.2939E{-6}$	1.9994	$3.1363E{-3}$	0.9995
1280	$2.0101E{-6}$	1.9975	$5.7361E{-7}$	1.9997	$1.5685E{-3}$	0.9997

We also experiment with a larger coefficient discontinuity, *i.e.*, $(\beta^-, \beta^+) = (1, 10000)$. Table 3.3 and Table 3.4 contain errors of nonconforming rotated Q_1 IFE interpolations $I_h^I u$ and $I_h^P u$, respectively. Data in these tables again agree with our error estimates given in Theorem 3.10 and Theorem 3.12.

Table 3.2: Errors of IFE interpolations $I_h^P u$ with $\beta^- = 1$, $\beta^+ = 10$.

N	$\|\cdot\|_{0,\infty,\Omega}$	rate	$\|\cdot\|_{0,\Omega}$	rate	$\|\cdot\|_{1,\Omega}$	rate
10	$3.1141E{-2}$		$6.7927E{-3}$		$1.9985E{-1}$	
20	$8.7089E{-3}$	1.8383	$1.7281E{-3}$	1.9748	$9.9536E{-2}$	1.0056
40	$2.3010E{-3}$	1.9202	$4.3411E{-4}$	1.9930	$4.9993E{-2}$	0.9935
80	$5.9128E{-4}$	1.9604	$1.0877E{-4}$	1.9968	$2.5050E{-2}$	0.9969
160	$1.4986E{-4}$	1.9803	$2.7227E{-5}$	1.9982	$1.2539E{-2}$	0.9985
320	$3.7721E{-5}$	1.9901	$6.8099E{-6}$	1.9993	$6.2720E{-3}$	0.9994
640	$9.4625E{-6}$	1.9951	$1.7029E{-6}$	1.9996	$3.1367E{-3}$	0.9997
1280	$2.3697E{-6}$	1.9975	$4.2579E{-7}$	1.9998	$1.5685E{-3}$	0.9999

Table 3.3: Errors of IFE interpolations $I_h^I u$ with $\beta^- = 1$, $\beta^+ = 10000$.

N	$\|\cdot\|_{0,\infty,\Omega}$	rate	$\|\cdot\|_{0,\Omega}$	rate	$\|\cdot\|_{1,\Omega}$	rate
10	$6.0241E{-3}$		$1.7879E{-3}$		$4.1565E{-2}$	
20	$2.5141E{-3}$	1.2607	$6.3808E{-4}$	1.4864	$2.7186E{-2}$	0.6125
40	$7.4878E{-4}$	1.7474	$1.6818E{-4}$	1.9237	$1.4347E{-2}$	0.9220
80	$2.0398E{-4}$	1.8761	$4.3539E{-5}$	1.9496	$7.4222E{-3}$	0.9509
160	$5.3209E{-5}$	1.9487	$1.1102E{-5}$	1.9715	$3.7778E{-3}$	0.9743
320	$1.3902E{-5}$	1.9363	$2.8079E{-6}$	1.9832	$1.9058E{-3}$	0.9872
640	$3.5127E{-6}$	1.9846	$7.0567E{-7}$	1.9924	$9.5702E{-4}$	0.9937
1280	$8.8287E{-7}$	1.9923	$1.7691E{-7}$	1.9960	$4.7959E{-4}$	0.9967

Table 3.4: Errors of IFE interpolations $I_h^P u$ with $\beta^- = 1$, $\beta^+ = 10000$.

N	$\|\cdot\|_{0,\infty,\Omega}$	rate	$\|\cdot\|_{0,\Omega}$	rate	$\|\cdot\|_{1,\Omega}$	rate
10	$8.2951E{-3}$		$1.6043E{-3}$		$4.6624E{-2}$	
20	$3.3555E{-3}$	1.3057	$4.8974E{-4}$	1.7118	$2.8337E{-2}$	0.7184
40	$8.9770E{-4}$	1.9022	$1.2558E{-4}$	1.9634	$1.4709E{-2}$	0.9460
80	$2.0293E{-4}$	1.8857	$3.2030E{-5}$	1.9711	$7.5596E{-3}$	0.9603
160	$6.4204E{-5}$	1.9198	$8.1238E{-6}$	1.9792	$3.8096E{-3}$	0.9887
320	$1.6417E{-5}$	1.9675	$2.0430E{-6}$	1.9915	$1.9121E{-3}$	0.9945
640	$4.1455E{-6}$	1.9855	$5.1251E{-7}$	1.9951	$9.5868E{-4}$	0.9960
1280	$1.0438E{-6}$	1.9897	$1.2835E{-7}$	1.9975	$4.7996E{-4}$	0.9981

Chapter 4

IFE Methods and Error Estimation

In this chapter, we propose several computational schemes using nonconforming rotated Q_1 IFE functions for solving the elliptic interface problem and carry out error estimation for these methods. In Section 4.1, we consider three classes of computational schemes including the Galerkin schemes, partially penalized schemes and interior penalty discontinuous Galerkin schemes for solving the elliptic interface problem. In Section 4.2, we carry out error estimation for the partially penalized Galerkin schemes and interior penalty discontinuous Galerkin schemes. Also, we provide numerical verifications for our error analysis. In Section 4.3, we provide numerical experiments of related IFE methods to compare their performances.

4.1 IFE Methods

In this section, we consider three classes of computational schemes using nonconforming rotated Q_1 IFE functions for solving the elliptic interface problem.

Recall that we use $\mathcal{E}_h$ to denote the collection of all the edges in a Cartesian mesh $\mathcal{T}_h$. For every edge $b \in \mathcal{E}_h$, we let M_b be the midpoint of b. Moreover, we let $\mathring{\mathcal{E}}_h$, and $\mathcal{E}_h^b$ be the collections of interior edges and boundary edges, respectively. The sets of interior interface edges and interior non-interface edges are denoted by $\mathring{\mathcal{E}}_h^i$ and $\mathring{\mathcal{E}}_h^n$, respectively. To simplify the notations in the following discussion, we assume that the interface curve Γ does not intersect with the boundary, *i.e.*, $\Gamma \cap \partial\Omega = \emptyset$. As a result, the set of interface edges is a subset of the set of interior edges and $\mathring{\mathcal{E}}_h^i = \mathcal{E}_h^i$; the set of boundary edges is a subset of the set of non-interface edges and $\mathcal{E}_h^{n,b} = \mathcal{E}_h^b$.

4.1.1 Galerkin IFE Methods

The Galerkin IFE scheme has been used for solving elliptic interface problems [69, 74, 87, 95, 96]. Here we briefly discuss the Galerkin IFE scheme with nonconforming rotated Q_1 IFE functions.

Multiplying the elliptic differential equation (1.1) by a test function $v \in H_0^1(\Omega)$ and integrating over each sub-domain Ω^s, $s = +, -$, we have

$$-\int_{\Omega^s} \nabla \cdot (\beta^s \nabla u) v \, \mathrm{d}x \, \mathrm{d}y = \int_{\Omega^s} f v \, \mathrm{d}x \, \mathrm{d}y, \quad \forall v \in H_0^1(\Omega). \tag{4.1}$$

Applying the Green's formula to (4.1) leads to

$$\int_{\Omega^s} \beta^s \nabla u \cdot \nabla v \, \mathrm{d}x \, \mathrm{d}y - \int_{\partial\Omega^s} (\beta^s \nabla u \cdot \mathbf{n}) v \, \mathrm{d}s = \int_{\Omega^s} f v \, \mathrm{d}x \, \mathrm{d}y, \quad \forall v \in H_0^1(\Omega). \tag{4.2}$$

Summing (4.2) over sub-domains and applying the jump condition (1.5) yield the following weak form

$$\int_{\Omega} \beta \nabla u \cdot \nabla v \, \mathrm{d}x \, \mathrm{d}y = \int_{\Omega} f v \mathrm{d}x \mathrm{d}y, \quad \forall v \in H_0^1(\Omega). \tag{4.3}$$

The equation (4.3) is equivalent to

$$\sum_{T \in \mathcal{T}_h} \int_T \beta \nabla u \cdot \nabla v \, \mathrm{d}x \, \mathrm{d}y = \int_{\Omega} f v \, \mathrm{d}x \, \mathrm{d}y, \quad \forall v \in H_0^1(\Omega). \tag{4.4}$$

On each element T, we use nonconforming rotated Q_1 IFE functions to approximate functions in $H^1(\Omega)$ in the weak form (4.4), then we obtain two Galerkin IFE schemes: Find $u_h^k \in S_h^k(\Omega)$, $k = P$ or I, that satisfies

$$\sum_{T \in \mathcal{T}_h} \int_T \beta \nabla u_h^k \cdot \nabla v_h^k \, \mathrm{d}x \, \mathrm{d}y = \int_{\Omega} f v_h^k \, \mathrm{d}x \, \mathrm{d}y, \quad \forall \ v_h^k \in \mathring{S}_h^k(\Omega), \tag{4.5}$$

and the following boundary conditions:

$$u_h^P(M_b) = g(M_b), \quad \text{if } b \in \mathcal{E}_h^b, \tag{4.6}$$

or

$$\int_b u_h^I(X) \mathrm{d}s = \int_b g(X) \mathrm{d}s, \quad \text{if } b \in \mathcal{E}_h^b. \tag{4.7}$$

Here the nonconforming rotated Q_1 IFE test function spaces are defined by

$$\mathring{S}_h^P(\Omega) = \{v \in S_h^P(\Omega) : v(M_b) = 0, \text{ if } b \in \mathcal{E}_h^b, \text{ and } M_b \text{ is the midpoint of } b\}. \tag{4.8}$$

$$\mathring{S}_h^I(\Omega) = \{v \in S_h^I(\Omega) : \int_b v \mathrm{d}s = 0, \text{ if } b \in \mathcal{E}_h^b\}. \tag{4.9}$$

4.1.2 Partially Penalized Galerkin IFE Methods

The second group of IFE schemes to be considered are called partially penalized Galerkin (PPG) schemes. To introduce these schemes, we need to introduce a few more notations. For every interior edge $b \in \mathring{\mathcal{E}}_h$, we let $T_{b,1}$ and $T_{b,2}$ be the two elements sharing the common edge b. For a function u defined on $T_{b,1} \cup T_{b,2}$, we define its jump and average values on b as follows:

$$[u]_b = u|_{T_{b,1}} - u|_{T_{b,2}}, \qquad \{u\}_b = \frac{1}{2}\left(u|_{T_{b,1}} + u|_{T_{b,2}}\right). \tag{4.10}$$

For every boundary edge $b \in \mathcal{E}_h^b$, we let T_b be the element such that b is part of its boundary. We define its jump and average on b as follows

$$[u]_b = \{u\}_b = u|_{T_b}. \tag{4.11}$$

We usually omit the subscript in $\{\cdot\}$ and $[\cdot]$ if there is no confusion.

To derive the PPG schemes, we multiply the elliptic differential equation (1.1) by a test function $v \in \mathring{S}_h^k(\Omega)$, $k = I$ or P, and integrate over each element $T \in \mathcal{T}_h$,

$$\int_T -\nabla \cdot (\beta \nabla u) v \,\mathrm{d}x\,\mathrm{d}y = \int_T f v \,\mathrm{d}x\,\mathrm{d}y, \quad \forall v \in \mathring{S}_h^k(\Omega). \tag{4.12}$$

Applying Green's formula to (4.12) yields

$$\int_T \beta \nabla u \cdot \nabla v \,\mathrm{d}x\,\mathrm{d}y - \int_{\partial T} (\beta \nabla u \cdot \mathbf{n}_T) v \,\mathrm{d}s = \int_T f v \,\mathrm{d}x\,\mathrm{d}y, \quad \forall v \in \mathring{S}_h^k(\Omega). \tag{4.13}$$

Here $\mathbf{n}_T$ is the unit outward normal of T. Summing (4.13) over all elements leads to

$$\sum_{T\in\mathcal{T}_h} \int_T \beta \nabla u \cdot \nabla v \,\mathrm{d}x\,\mathrm{d}y - \sum_{T\in\mathcal{T}_h} \int_{\partial T} (\beta \nabla u \cdot \mathbf{n}_T) v \,\mathrm{d}s = \int_\Omega f v \,\mathrm{d}x\,\mathrm{d}y, \quad \forall v \in \mathring{S}_h^k(\Omega). \tag{4.14}$$

For every interior edge $b \in \mathring{\mathcal{E}}_h$ with $b = \partial T_{b,1} \cap \partial T_{b,2}$, we let $\mathbf{n}_{ij}$ be the unit normal vector pointing from $T_{b,i}$ to $T_{b,j}$; hence $\mathbf{n}_{12} = -\mathbf{n}_{21}$. We assign $\mathbf{n}_{12}$ to be the normal of b, *i.e.* $\mathbf{n}_b = \mathbf{n}_{12}$, then we have the following identity

$$\int_{\partial T_{b,1}\cap b} \beta \nabla u \cdot \mathbf{n}_{12} v \,\mathrm{d}s + \int_{\partial T_{b,2}\cap b} \beta \nabla u \cdot \mathbf{n}_{21} v \,\mathrm{d}s = \int_b [\beta \nabla u \cdot \mathbf{n}_b v] \,\mathrm{d}s. \tag{4.15}$$

Using the following algebraic identity

$$ab - cd = \frac{1}{2}(a+b)(c-d) + \frac{1}{2}(a-b)(c+d), \tag{4.16}$$

in the right hand side of (4.15), we obtain

$$\int_b [\beta \nabla u \cdot \mathbf{n}_b v] \,\mathrm{d}s = \int_b \{\beta \nabla u \cdot \mathbf{n}_b\}[v] \,\mathrm{d}s + \int_b [\beta \nabla u \cdot \mathbf{n}_b]\{v\} \,\mathrm{d}s. \tag{4.17}$$

Replacing the right hand side of (4.15) by (4.17) and summing (4.15) over all the elements, we obtain

$$\begin{aligned}\sum_{T\in\mathcal{T}_h}\int_{\partial T}(\beta\nabla u\cdot\mathbf{n}_T)v\,\mathrm{d}s &= \sum_{b\in\mathring{\mathcal{E}}_h}\int_b\{\beta\nabla u\cdot\mathbf{n}_b\}[v]\,\mathrm{d}s+\sum_{b\in\mathring{\mathcal{E}}_h}\int_b[\beta\nabla u\cdot\mathbf{n}_b]\{v\}\,\mathrm{d}s\\ &\quad+\sum_{b\in\mathcal{E}_h^b}\int_b\beta\nabla u\cdot\mathbf{n}_b v\,\mathrm{d}s.\end{aligned}\tag{4.18}$$

Substituting the second term in (4.14) by (4.18), we have

$$\begin{aligned}&\sum_{T\in\mathcal{T}_h}\int_T\beta\nabla u\cdot\nabla v\,\mathrm{d}x\,\mathrm{d}y-\sum_{b\in\mathring{\mathcal{E}}_h}\int_b\{\beta\nabla u\cdot\mathbf{n}_b\}[v]\mathrm{d}s-\sum_{b\in\mathring{\mathcal{E}}_h}\int_b[\beta\nabla u\cdot\mathbf{n}_b]\{v\}\mathrm{d}s\\ &\quad-\sum_{b\in\mathcal{E}_h^b}\int_b\beta\nabla u\cdot\mathbf{n}_b v\,\mathrm{d}s=\sum_{T\in\mathcal{T}_h}\int_T fv\,\mathrm{d}x\,\mathrm{d}y,\quad\forall v\in\mathring{S}_h^k(\Omega).\end{aligned}\tag{4.19}$$

Assume that u is smooth enough so that $\beta\nabla u\cdot\mathbf{n}_b$ is continuous at almost all points on every interior edge b; hence, $[\beta\nabla u\cdot\mathbf{n}_b]=0$ almost every where. Therefore the third term in (4.19) is zero and (4.19) becomes

$$\sum_{T\in\mathcal{T}_h}\int_T\beta\nabla u\cdot\nabla v\,\mathrm{d}x\,\mathrm{d}y-\sum_{b\in\mathcal{E}_h}\int_b\{\beta\nabla u\cdot\mathbf{n}_b\}[v]\mathrm{d}s=\sum_{T\in\mathcal{T}_h}\int_T fv\,\mathrm{d}x\,\mathrm{d}y,\quad\forall v\in\mathring{S}_h^k(\Omega).\tag{4.20}$$

Note the second term in (4.20) includes both interior and boundary edges and it equals the sum of the second and fourth terms in (4.19). Here we recall that the jump and average on a boundary edge b is specified in (4.11).

We assume that u is continuous almost everywhere in the interior of Ω, then $[u]=0$ almost everywhere on each interior edge b. We add two stabilization and penalty terms defined only on interface edges to (4.20), then we obtain

$$\begin{aligned}&\sum_{T\in\mathcal{T}_h}\int_T\beta\nabla u\cdot\nabla v\,\mathrm{d}x\,\mathrm{d}y-\sum_{b\in\mathcal{E}_h}\int_b\{\beta\nabla u\cdot\mathbf{n}_b\}[v]\mathrm{d}s+\epsilon\sum_{b\in\mathring{\mathcal{E}}_h^i}\int_b\{\beta\nabla v\cdot\mathbf{n}_b\}[u]\mathrm{d}s\\ &\quad+\sum_{b\in\mathring{\mathcal{E}}_h^i}\int_b\frac{\sigma_b^0}{|b|^\alpha}[u][v]\mathrm{d}s=\sum_{T\in\mathcal{T}_h}\int_T fv\,\mathrm{d}x\,\mathrm{d}y,\quad\forall v\in\mathring{S}_h^k(\Omega).\end{aligned}\tag{4.21}$$

We assume that on non-interface edges, the following quantity

$$\sum_{b\in\mathcal{E}_h^n}\int_b\{\beta\nabla u\cdot\mathbf{n}_b\}[v]\mathrm{d}s\tag{4.22}$$

is not large which suggests to ignore the term described in (4.22) in our algorithms. Then the weak form (4.21) becomes

$$\sum_{T\in\mathcal{T}_h}\int_T \beta\nabla u\cdot\nabla v\,\mathrm{d}x\,\mathrm{d}y-\sum_{b\in\mathring{\mathcal{E}}_h^i}\int_b\{\beta\nabla u\cdot\mathbf{n}_b\}[v]\mathrm{d}s+\epsilon\sum_{b\in\mathring{\mathcal{E}}_h^i}\int_b\{\beta\nabla v\cdot\mathbf{n}_b\}[u]\mathrm{d}s \tag{4.23}$$

$$+\sum_{b\in\mathring{\mathcal{E}}_h^i}\int_b\frac{\sigma_b^0}{|b|^\alpha}[u][v]\mathrm{d}s\approx\sum_{T\in\mathcal{T}_h}\int_T fv\,\mathrm{d}x\,\mathrm{d}y,\quad\forall v\in\mathring{S}_h^k(\Omega).$$

According to (4.23), we can define the partially penalized Galerkin IFE schemes: Find $u_h^k\in S_h^k(\Omega)$, $k=P,I$ that satisfies

$$a_\epsilon(u_h^k,v_h^k)=L(v_h^k),\quad\forall\ v_h^k\in\mathring{S}_h^k(\Omega), \tag{4.24}$$

subject to the following boundary conditions:

$$u_h^P(M_b)=g(M_b),\quad\text{if } b\in\mathcal{E}_h^b, \tag{4.25}$$

or

$$\int_b u_h^I(X)\mathrm{d}s=\int_b g(X)\mathrm{d}s,\quad\text{if } b\in\mathcal{E}_h^b. \tag{4.26}$$

The bilinear form and linear form in (4.24) are defined by

$$\begin{aligned}a_\epsilon(u,v) &= \sum_{T\in\mathcal{T}_h}\int_T\beta\nabla u\cdot\nabla v\,\mathrm{d}x\,\mathrm{d}y-\sum_{b\in\mathring{\mathcal{E}}_h^i}\int_b\{\beta\nabla u\cdot\mathbf{n}_b\}[v]\mathrm{d}s\\ &\quad+\epsilon\sum_{b\in\mathring{\mathcal{E}}_h^i}\int_b\{\beta\nabla v\cdot\mathbf{n}_b\}[u]\mathrm{d}s+\sum_{b\in\mathring{\mathcal{E}}_h^i}\int_b\frac{\sigma_b^0}{|b|^\alpha}[u][v]\mathrm{d}s, &(4.27)\\ L(v) &= \sum_{T\in\mathcal{T}_h}\int_T fv\,\mathrm{d}x\,\mathrm{d}y. &(4.28)\end{aligned}$$

In the bilinear form (4.27), α and σ_b^0 are penalty parameters and we will discuss the possible choices for these parameters in related error estimation later. The parameter ϵ in (4.27) has the following three popular choices:

- $\epsilon=-1$: in this case the bilinear form $a_\epsilon(\cdot,\cdot)$ is symmetric, and we call the corresponding scheme a symmetric partially penalized Galerkin **(SPPG)** IFE method.
- $\epsilon=1$: in this case the bilinear form $a_\epsilon(\cdot,\cdot)$ is nonsymmetric, and we call the corresponding scheme a nonsymmetric partially penalized Galerkin **(NPPG)** IFE method.
- $\epsilon=0$: in this case the bilinear form $a_\epsilon(\cdot,\cdot)$ is also nonsymmetric, and we call the corresponding scheme an incomplete partially penalized Galerkin **(IPPG)** IFE method.

In the above derivation, we have followed the idea of interior penalty discontinuous Galerkin (IPDG) schemes [125] to design the weak form (4.24) of the PPG IFE schemes. The idea of partially penalization is for alleviating discontinuity of IFE functions across interface edges. We note that this partially penalization idea was used in designing quadratic IFE methods [129] for the elliptic interface problem.

4.1.3 IPDG IFE Methods

Nonconforming rotated Q_1 IFE functions can be used in IPDG schemes [3, 48, 125, 127, 144] to generate methods for solving interface problems with mass conservation feature and *hp*-refinement capability.

To introduce the IPDG IFE schemes, we first define the "broken" IFE spaces as follows:

$$S_h^{DG}(\Omega) = \{v \in L^2(\Omega) : v|_T \in S_h^n(T), \text{ if } T \in \mathcal{T}_h^n; v|_T \in S_h^i(T), \text{ if } T \in \mathcal{T}_h^i\}, \quad (4.29)$$

$$\mathring{S}_h^{I,DG}(\Omega) = \{v \in S_h^{DG}(\Omega) : \int_b v \mathrm{d}s = 0, \text{ if } b \in \mathcal{E}_h^b\}, \quad (4.30)$$

$$\mathring{S}_h^{P,DG}(\Omega) = \{v \in S_h^{DG}(\Omega) : v(M_b) = 0, \text{ if } b \in \mathcal{E}_h^b\}. \quad (4.31)$$

Then we define the IPDG IFE scheme: Find $u_h^{DG} \in S_h^{DG}(\Omega)$, that satisfies

$$a_\epsilon^{DG}(u_h^{DG}, v_h^{DG}) = L(v_h^{DG}), \quad \forall\ v_h^{DG} \in \mathring{S}_h^{k,DG}(\Omega), \quad k = I, P, \quad (4.32)$$

and subject to one of the following boundary conditions:

$$\int_b u_h^{DG}(X)\mathrm{d}s = \int_b g(X)\mathrm{d}s, \quad \forall\, b \in \mathcal{E}_h^b, \quad (4.33a)$$

or

$$u_h^{DG}(M_b) = g(M_b), \quad \forall\, b \in \mathcal{E}_h^b. \quad (4.33b)$$

Here the bilinear form and linear form in (4.32) are defined as

$$\begin{aligned} a_\epsilon^{DG}(u, v) &= \sum_{T\in\mathcal{T}_h} \int_T \beta\nabla u \cdot \nabla v \,\mathrm{d}x\,\mathrm{d}y - \sum_{b\in\mathcal{E}_h} \int_b \{\beta\nabla u \cdot \mathbf{n}_b\}[v]\mathrm{d}s \\ &\quad + \epsilon \sum_{b\in\mathcal{E}_h} \int_b \{\beta\nabla v \cdot \mathbf{n}_b\}[u]\mathrm{d}s + \sum_{b\in\mathcal{E}_h} \int_b \frac{\sigma_b^0}{|b|^\alpha}[u][v]\mathrm{d}s, \quad (4.34) \\ L(v) &= \sum_{T\in\mathcal{T}_h} \int_T fv \,\mathrm{d}x\,\mathrm{d}y. \quad (4.35) \end{aligned}$$

Here, α and σ_b^0 are penalty parameters and we will discuss the possible choices for these parameters in related error estimation later. Similar to PPG IFE schemes, the parameter ϵ in the bilinear form of IPDG IFE scheme (4.34) has the following three popular choices:

- $\epsilon = -1$: in this case the bilinear form $a_\epsilon^{DG}(\cdot,\cdot)$ is symmetric, and we call this scheme a symmetric interior penalty discontinuous Galerkin **(SIPDG)** IFE method.
- $\epsilon = 1$: in this case the bilinear form $a_\epsilon^{DG}(\cdot,\cdot)$ is nonsymmetric, and we call this scheme a nonsymmetric interior penalty discontinuous Galerkin **(NIPDG)** IFE method.
- $\epsilon = 0$: in this case the bilinear form $a_\epsilon^{DG}(\cdot,\cdot)$ is also nonsymmetric, and we call this scheme an incomplete interior penalty discontinuous Galerkin **(IIPDG)** IFE method.

We note that the differences between PPG IFE schemes and IPDG IFE schemes are their choices of IFE spaces and collections of edges where penalization is applied. The number of global degrees of freedom in PPG schemes is much less than the IPDG IFE schemes. In fact, PPG IFE schemes have the same number of global degrees of freedom as the Galerkin IFE schemes. In addition, penalty terms are added only on interfaces edges for PPG schemes instead being added at all edges for IPDG schemes.

4.2 Error Estimation

In this section, we carry out the error estimation for PPG IFE and IPDG IFE schemes using nonconforming rotated Q_1 IFE functions with midpoint-value degrees of freedom and integral-value degrees of freedom. Throughout the error analysis, we assume that the collection of interface elements $\mathcal{T}_h^i$ in a Cartesian mesh $\mathcal{T}_h$ satisfies the following hypothesis:

(H5) There exists a constant C such that the number of interface element in a mesh $\mathcal{T}_h$, denoted by $|\mathcal{T}_h^i|$ satisfies

$$|\mathcal{T}_h^i| \leq Ch^{-1}. \tag{4.36}$$

4.2.1 Error Estimation for PPG IFE Solutions in $S_h^I(\Omega)$

We first derive an error estimate for the partially penalized Galerkin IFE schemes. Define the energy norm $\|\cdot\|_{h,\Omega}$ on $\mathring{S}_h^P(\Omega) \cup \mathring{S}_h^I(\Omega)$, which is a semi-norm on $S_h^P(\Omega) \cup S_h^I(\Omega)$:

$$\|v\|_{h,\Omega} = \left(\sum_{T\in\mathcal{T}_h} \int_T \beta \nabla v \cdot \nabla v \,\mathrm{d}x\,\mathrm{d}y + \sum_{b\in\mathring{\mathcal{E}}_h^i} \int_b \frac{\sigma_b^0}{|b|^\alpha} [v][v] \mathrm{d}s \right)^{1/2}. \tag{4.37}$$

The coercivity of the bilinear forms $a_\epsilon(\cdot,\cdot)$ with respect to the energy norm $\|\cdot\|_{h,\Omega}$ is given in the following lemma.

Lemma 4.1. *Assume $\alpha \geq 1$ in the bilinear form* (4.27) *and the energy norm* (4.37). *There exists a positive constant κ such that*

$$\kappa \|v\|_{h,\Omega}^2 \leq a_\epsilon(v,v), \quad \forall v \in S_h^P(\Omega) \cup S_h^I(\Omega), \tag{4.38}$$

for any positive σ_b^0 if $\epsilon = 1$, or for σ_b^0 large enough if $\epsilon = 0$ or -1.

Proof. Note that the coercivity result (4.38) is trivial for $\epsilon = 1$ and the corresponding coercivity constant $\kappa = 1$; hence, our proof below focuses on the other two cases $\epsilon = -1$ or 0.

For each interior interface edge $b \in \mathring{\mathcal{E}}_h^i$, applying the trace inequality of IFE functions stated in Theorem 3.3 and the Cauchy-Schwarz inequality, we obtain the following estimate

$$\begin{aligned}
\int_b \{\beta \nabla v \cdot \mathbf{n}_b\}[v] \mathrm{d}s &\leq \frac{1}{2}\left(\left\| (\beta \nabla v \cdot \mathbf{n}_b)|_{T_{b,1}} \right\|_{0,b} + \left\| (\beta \nabla v \cdot \mathbf{n}_b)|_{T_{b,2}} \right\|_{0,b} \right) \|[v]\|_{0,b} \\
&\leq \frac{1}{2}|b|^{\alpha/2}\left(C h_{T_{b,1}}^{-1/2} \|\beta \nabla v\|_{0,T_{b,1}} + C h_{T_{b,2}}^{-1/2} \|\beta \nabla v\|_{0,T_{b,2}} \right) \frac{1}{|b|^{\alpha/2}} \|[v]\|_{0,b} \\
&\leq C\left(\|\beta \nabla v\|_{0,T_{b,1}}^2 + \|\beta \nabla v\|_{0,T_{b,2}}^2 \right)^{1/2} \frac{1}{|b|^{\alpha/2}} \|[v]\|_{0,b}\,.
\end{aligned} \tag{4.39}$$

Summing up (4.39) over all the interior interface edges, and applying Young's inequality, we obtain

$$\begin{aligned}
\sum_{b \in \mathring{\mathcal{E}}_h^i} \int_b \{\beta \nabla v \cdot \mathbf{n}_b\}[v] \mathrm{d}s &\leq C \left(\sum_{b \in \mathring{\mathcal{E}}_h^i} \frac{1}{|b|^\alpha} \|[v]\|_{0,b}^2 \right)^{1/2} \left(\sum_{b \in \mathring{\mathcal{E}}_h^i} \left(\|\beta \nabla v\|_{0,T_{b,1}}^2 + \|\beta \nabla v\|_{0,T_{b,2}}^2 \right) \right)^{1/2} \\
&\leq \frac{\delta}{2}\left(\sum_{T \in \mathcal{T}_h} \left(\|\beta \nabla v\|_{0,T}^2 \right) \right) + \frac{C}{2\delta}\left(\sum_{b \in \mathring{\mathcal{E}}_h^i} \frac{1}{|b|^\alpha} \|[v]\|_{0,b}^2 \right),
\end{aligned}$$

for every $\delta > 0$. Thus,

$$\begin{aligned}
a_\epsilon(v,v) &\geq \left(1 - \frac{\delta|1-\epsilon|}{2} \right) \sum_{T \in \mathcal{T}_h} \|\beta \nabla v\|_{0,T}^2 + \left(\sum_{b \in \mathring{\mathcal{E}}_h^i} \frac{\sigma_b^0 - \frac{C}{2\delta}|1-\epsilon|}{|b|^\alpha} \|[v]\|_{0,b}^2 \right) \\
&\geq \min\left(1 - \frac{\delta|1-\epsilon|}{2}, \frac{\sigma_b^0 - \frac{C}{2\delta}|1-\epsilon|}{|b|^\alpha} \right) \|v\|_{h,\Omega}^2.
\end{aligned} \tag{4.40}$$

Choosing δ and σ_b^0 in (4.40) such that

$$\delta|1-\epsilon| < 2, \quad \sigma_b^0 > \frac{C}{2\delta}|1-\epsilon|,$$

we obtain (4.38) with

$$\kappa = \min\left(1 - \frac{\delta|1-\epsilon|}{2}, \frac{\sigma_b^0 - \frac{C}{2\delta}|1-\epsilon|}{|b|^\alpha}\right) > 0. \tag{4.41}$$

□

For each edge $b \in \mathcal{E}_h$, and $v \in L^2(b)$, we define $\overline{v}^b$ to be the average integral value of v over the edge b as follows

$$\overline{v}^b = \frac{1}{|b|}\int_b v \mathrm{d}s. \tag{4.42}$$

Lemma 4.2. *There exists a constant C such that*

$$\|[v_h]\|_{0,b} \le Ch^{1/2}(|v_h|_{1,T_{b,1}} + |v_h|_{1,T_{b,2}}), \quad \forall\, v_h \in S_h^P(\Omega) \cup S_h^I(\Omega), \tag{4.43}$$

for every interior edge $b \in \mathring{\mathcal{E}}_h$, and

$$\|v_h\|_{0,b} \le Ch^{1/2}|v_h|_{1,T_b}, \quad \forall\, v_h \in \mathring{S}_h^P(\Omega) \cup \mathring{S}_h^I(\Omega), \tag{4.44}$$

for every boundary edge $b \in \mathcal{E}_h^b$.

Proof. We first prove that the estimate (4.43) holds for every $v_h \in S_h^P(\Omega)$. Note that v_h is continuous at the midpoint M_b of an interior (interface or non-interface) edge b. Without loss of generality, we assume that b is a vertical line segment whose endpoints are (x_0, y_0) and $(x_0, y_0 + h)$, then by the triangle inequality we have the following estimate

$$\begin{aligned}
\|[v_h]\|_{0,b} &= \|v_h|_{T_{b,1}} - v_h|_{T_{b,2}}\|_{0,b} \\
&= \|(v_h|_{T_{b,1}} - v_h|_{T_{b,1}}(M_b)) + (v_h|_{T_{b,2}}(M_b) - v_h|_{T_{b,2}})\|_{0,b} \\
&\le \|v_h|_{T_{b,1}} - v_h|_{T_{b,1}}(M_b)\|_{0,b} + \|v_h|_{T_{b,2}} - v_h|_{T_{b,2}}(M_b)\|_{0,b} \\
&\le \sum_{j=1}^{2}\left(\int_{y_0}^{y_0+h}\left(v_h|_{T_{b,j}}(x_0, y) - v_h|_{T_{b,j}}(x_0, y_0 + \frac{h}{2})\right)^2 \mathrm{d}y\right)^{1/2} \\
&\le \sum_{j=1}^{2}\left(\int_{y_0}^{y_0+h}\left(\int_{y_0+h/2}^{y}\partial_z\big(v_h|_{T_{b,j}}(x_0, z)\big)\mathrm{d}z\right)^2 \mathrm{d}y\right)^{1/2} \\
&\le \sum_{j=1}^{2}\left(\int_{y_0}^{y_0+h} h^2|v_h|_{1,\infty,T_{b,j}}^2 \mathrm{d}y\right)^{1/2} \\
&\le Ch^{3/2}(|v_h|_{1,\infty,T_{b,1}} + |v_h|_{1,\infty,T_{b,2}})
\end{aligned} \tag{4.45}$$

We apply the standard inverse inequality (3.17) or the IFE inverse inequality (3.18) to v_h on these two elements $T_{b,1}$, $T_{b,2}$, depending on whether they are non-interface elements or interface elements. Then we have

$$|v_h|_{1,\infty,T_{b,j}} \le Ch^{-1}|v_h|_{T_{b,j}}, \quad j = 1, 2. \tag{4.46}$$

Combining the above estimates (4.45) and (4.46), we obtain

$$\|[v_h]\|_{0,b} \leq Ch^{1/2}(|v_h|_{1,T_{b,1}} + |v_h|_{1,T_{b,2}}), \quad \forall v_h \in S_h^P(\Omega). \tag{4.47}$$

For every $v_h \in S_h^I(\Omega)$, the average integral value on every interior edge b is continuous. Note that $v_h|_T$ is in $H^1(T)$ for every element $T \in \mathcal{T}_h$, then by standard approximation results stated in [37] we obtain

$$\begin{aligned} \|[v_h]\|_{0,b} &= \|v_h|_{T_{b,1}} - v_h|_{T_{b,2}}\|_{0,b} \\ &= \|(v_h|_{T_{b,1}} - \overline{v_h|_{T_{b,1}}}^b) + (\overline{v_h|_{T_{b,2}}}^b - v_h|_{T_{b,2}})\|_{0,b} \\ &\leq \|v_h|_{T_{b,1}} - \overline{v_h|_{T_{b,1}}}^b\|_{0,b} + \|v_h|_{T_{b,2}} - \overline{v_h|_{T_{b,2}}}^b\|_{0,b} \\ &\leq Ch^{1/2}(|v_h|_{1,T_{b,1}} + |v_h|_{1,T_{b,2}}). \end{aligned} \tag{4.48}$$

The estimate (4.43) follows from (4.47) and (4.48). We can prove (4.44) similarly if $b \in \mathcal{E}_h^b$ is a boundary edge. □

In the following error analysis in this subsection, we need the following hypothesis,

(H6) The interface Γ is smooth enough so that $PC_{int}^3(\Omega)$ is dense in $PH_{int}^3(\Omega)$.

The interpolation error on an interface edge is analyzed in the following lemma.

Lemma 4.3. *For every $u \in PH_{int}^3(\Omega)$, there exists a constant C such that*

$$\|\beta\nabla(u - I_{h,T}^P u) \cdot \mathbf{n}_b\|_{0,b}^2 \leq C(h^2\|u\|_{3,\Omega}^2 + h\|u\|_{2,T}^2). \tag{4.49}$$

for every interface element $T \in \mathcal{T}_h^i$ where $b \subset \partial T$ is one of its interface edges.

Proof. We consider the Type I Case 2 interface element as illustrated in Figure 3.1, and other cases can be discussed similarly. Without loss of generality, we let $b = \overline{A_1A_3}$. Recall from Theorem 3.7 that for every function $u \in PC_{int}^3(\Omega)$, its interpolation error at point $X \in \overline{EA_3}$ can be expanded as follows

$$\frac{\partial(I_{h,T}^P u(X) - u(X))}{\partial x} = (F_1 + F_2)\phi_{1,T,x}^P(X) - \frac{1}{2}F_{0,x}u_{xx}(X) + \sum_{i=1}^{4} I_i\phi_{i,T,x}^P(X). \tag{4.50}$$

Here F_0, F_1, F_2, and I_i, $i = 1, \cdots, 4$ are defined in (3.35), (3.46a) - (3.46g). To estimate the first term in (4.50), we use estimates (3.31), (3.30) in Lemma 3.8 and the bound of IFE functions (3.3a) in Theorem 3.2 to obtain

$$\int_{\overline{EA_3}} (F_i\phi_{1,T,x}^P(X))^2 \mathrm{d}s \leq Ch^2 \int_{\overline{EA_3}} |\nabla u^-|^2 \mathrm{d}s \leq Ch^2\|u\|_{2,\Omega^-}^2 \leq Ch^2\|u\|_{3,\Omega^-}^2, \quad \forall i = 1, 2. \tag{4.51}$$

Also, applying the bound of F_0 (3.42) to estimate the second term in (4.50) we obtain

$$\int_{\overline{EA_3}} \left(\frac{1}{2}F_{0,x}u^-_{xx}(X)\right)^2 \mathrm{d}s \le \int_{\overline{EA_3}} |F_{0,x}|^2 |u^-_{xx}(X)|^2 \mathrm{d}s \le Ch^2 \int_{\overline{EA_3}} |u^-_{xx}(X)|^2 \mathrm{d}s \le Ch^2 \|u\|^2_{3,\Omega^-}. \tag{4.52}$$

Using the bound of IFE functions (3.3a) in Theorem 3.2, we have the following estimation involving the term $I_{1,1}$:

$$\begin{aligned}
&\int_{\overline{EA_3}} \left(I_{1,1}\phi^P_{1,T,x}(X)\right)^2 \mathrm{d}s \\
\le\ & \int_{\overline{EA_3}} \|N^-(\widetilde{M_1}) - I\|^2 \int_0^1 \Big(u_{\xi\xi}(\xi,\eta)(\tilde{x}_1 - x)(x_1 - \tilde{x}_1) + u_{\xi\eta}(\xi,\eta)(\tilde{y}_1 - y)(x_1 - \tilde{x}_1) \\
& + u_{\eta\xi}(\xi,\eta)(\tilde{x}_1 - x)(y_1 - \tilde{y}_1) + u_{\eta\eta}(\xi,\eta)(\tilde{y}_1 - y)(y_1 - \tilde{y}_1)\Big)^2 |\phi^P_{1,T,x}(X)|^2 \mathrm{d}t\,\mathrm{d}s \\
\le\ & Ch^2 \int_{\overline{EA_3}} \int_0^1 \Big(|u_{\xi\xi}(\xi,\eta)|^2 + |u_{\xi\eta}(\xi,\eta)|^2 + |u_{\eta\xi}(\xi,\eta)|^2 + |u_{\eta\eta}(\xi,\eta)|^2\Big)\mathrm{d}t\,\mathrm{d}s \\
\le\ & Ch^2 \|u\|^2_{3,\Omega^-}.
\end{aligned} \tag{4.53}$$

Similarly, for the term involving $I_{1,2}$, we use Theorem 3.2 to obtain

$$\begin{aligned}
&\int_{\overline{EA_3}} \left(I_{1,2}\phi^P_{1,T,x}(X)\right)^2 \mathrm{d}s \\
\le\ & Ch^{-2} \int_{\overline{EA_3}} \left(\int_0^{\tilde{t}} (1-t) \frac{d^2}{dt^2} u(tM_1 + (1-t)X) dt \right)^2 \mathrm{d}s \\
\le\ & Ch^{-2} \int_{\overline{EA_3}} \int_0^{\tilde{t}} (1-t)^2 \Bigg(|u_{xx}(tM_1 + (1-t)X)|^2 (x_1 - x)^2 (x_1 - x)^2 \\
& + |u_{xy}(tM_1 + (1-t)X)|^2 (x_1 - x)^2 (y_1 - y)^2 \\
& + |u_{yx}(tM_1 + (1-t)X)|^2 (y_1 - y)^2 (x_1 - x)^2 \\
& + |u_{yy}(tM_1 + (1-t)X)|^2 (y_1 - y)^2 (y_1 - y)^2 \Bigg) \mathrm{d}t\,\mathrm{d}s \\
\le\ & Ch^2 \int_{eh}^{h} \int_0^{\tilde{t}} (1-t)^2 \left| u_{xx}\left(\frac{th}{2}, (1-t)y\right)\right|^2 + \left| u_{xy}\left(\frac{th}{2}, (1-t)y\right)\right|^2 \\
& + \left| u_{yx}\left(\frac{th}{2}, (1-t)y\right)\right|^2 + \left| u_{yy}\left(\frac{th}{2}, (1-t)y\right)\right|^2 \mathrm{d}t\,\mathrm{d}y.
\end{aligned} \tag{4.54}$$

Let $p = \frac{th}{2}$, $q = (1-t)h$, then the Jacobian of this substitute is

$$\frac{\partial(t,y)}{\partial(p,q)} = \frac{2}{h(1-t)} = \frac{1}{q}.$$

The inequality (4.54) becomes

$$\begin{aligned}
&\int_{\overline{EA_3}} \left(I_{1,2}\phi^P_{1,T,x}(X)\right)^2 \mathrm{d}s \\
\leq\ & Ch \iint_{\triangle A_3 E\tilde{M}_1} \left(|u_{xx}(p,q)|^2 + |u_{xy}(p,q)|^2 + |u_{yx}(p,q)|^2 + |u_{yy}(p,q)|^2\right) \mathrm{d}p\,\mathrm{d}q \\
\leq\ & Ch \left(\|u_{xx}\|^2_{0,\triangle A_3 E\tilde{M}_1} + \|u_{xy}\|^2_{0,\triangle A_3 E\tilde{M}_1} + \|u_{yx}\|^2_{0,\triangle A_3 E\tilde{M}_1} + \|u_{yy}\|^2_{0,\triangle A_3 E\tilde{M}_1}\right) \\
\leq\ & Ch\|u\|^2_{2,T^-}. \qquad (4.55)
\end{aligned}$$

Similarly for the term involving $I_{1,3}$, using the bound of IFE functions (3.3a) again, we obtain

$$\begin{aligned}
&\int_{\overline{EA_3}} \left(I_{1,3}\phi^P_{1,T,x}(X)\right)^2 \mathrm{d}s \\
\leq\ & Ch^{-2} \int_{\overline{EA_3}} \left(\int_{\tilde{t}}^1 (1-t)\frac{d^2}{dt^2} u(tM_1 + (1-t)X)dt\right)^2 \mathrm{d}s \\
\leq\ & Ch^2 \int_{eh}^h \int_{\tilde{t}}^1 (1-t)^2 \left|u_{xx}\left(\frac{th}{2}, (1-t)y\right)\right|^2 + \left|u_{xy}\left(\frac{th}{2}, (1-t)y\right)\right|^2 \\
&+ \left|u_{yx}\left(\frac{th}{2}, (1-t)y\right)\right|^2 + \left|u_{yy}\left(\frac{th}{2}, (1-t)y\right)\right|^2 \mathrm{d}t\,\mathrm{d}y \\
\leq\ & Ch \iint_{\triangle EM_1\tilde{M}_1} \left(|u_{xx}(p,q)|^2 + |u_{xy}(p,q)|^2 + |u_{yx}(p,q)|^2 + |u_{yy}(p,q)|^2\right) \mathrm{d}p\,\mathrm{d}q \\
\leq\ & Ch \left(\|u_{xx}\|^2_{0,\triangle EM_1\tilde{M}_1} + \|u_{xy}\|^2_{0,\triangle EM_1\tilde{M}_1} + \|u_{yx}\|^2_{0,\triangle EM_1\tilde{M}_1} + \|u_{yy}\|^2_{0,\triangle EM_1\tilde{M}_1}\right) \\
\leq\ & Ch\|u\|^2_{2,T^+}. \qquad (4.56)
\end{aligned}$$

For the term involving I_2, we have

$$\begin{aligned}
&\int_{\overline{EA_3}} \left(I_2\phi^P_{2,T,x}(X)\right)^2 \mathrm{d}s \\
\leq\ & Ch^{-2} \int_{\overline{EA_3}} \left(\int_0^1 (1-t)\frac{d^2}{dt^2} u(tM_2 + (1-t)X)dt\right)^2 \mathrm{d}s \\
\leq\ & Ch^2 \int_{eh}^h \int_0^1 (1-t)^2 \left|u_{xx}(th, \frac{th}{2} + (1-t)y)\right|^2 + \left|u_{xy}(th, \frac{th}{2} + (1-t)y)\right|^2 \\
&+ \left|u_{yx}(th, \frac{th}{2} + (1-t)y)\right|^2 + \left|u_{yy}(th, \frac{th}{2} + (1-t)y)\right|^2 \mathrm{d}t\,\mathrm{d}y
\end{aligned}$$

Let $p = th$, $q = t\frac{h}{2} + (1-t)y$, the Jacobian of this substitution is the following

$$\frac{\partial(t,y)}{\partial(p,q)} = \frac{1}{h(1-t)} = \frac{1}{h-p}.$$

Hence,

$$\begin{aligned}
&\int_{\overline{EA_3}} \left(I_2\phi^P_{2,T,x}(X)\right)^2 \mathrm{d}s \\
=\;& Ch^2 \iint_{\triangle A_3EM_2} \left(\frac{h-p}{h}\right)^2 \left(|u_{xx}(p,q)|^2 + |u_{xy}(p,q)|^2\right. \\
&\left. + |u_{yx}(p,q)|^2 + |u_{yy}(p,q)|^2\right) \frac{1}{h-p}\,\mathrm{d}p\,\mathrm{d}q \\
\le\;& Ch^2 \iint_{\triangle A_3EM_2} \left(|u_{xx}(p,q)|^2 + |u_{xy}(p,q)|^2 + |u_{yx}(p,q)|^2 + |u_{yy}(p,q)|^2\right) \frac{h-p}{h^2}\,\mathrm{d}p\,\mathrm{d}q \\
\le\;& Ch \iint_{\triangle A_3EM_2} \left(|u_{xx}(p,q)|^2 + |u_{xy}(p,q)|^2 + |u_{yx}(p,q)|^2 + |u_{yy}(p,q)|^2\right) \mathrm{d}p\,\mathrm{d}q \\
\le\;& Ch \left(\|u_{xx}\|^2_{0,\triangle A_3EM_2} + \|u_{xy}\|^2_{0,\triangle A_3EM_2} + \|u_{yx}\|^2_{0,\triangle A_3EM_2} + \|u_{yy}\|^2_{0,\triangle A_3EM_2}\right) \\
\le\;& Ch\|u\|^2_{2,T} \qquad (4.57)
\end{aligned}$$

Similarly, for I_3 we have

$$\int_{\overline{EA_3}} \left(I_3\phi^P_{3,T,x}(X)\right)^2 \mathrm{d}s \le Ch\|u\|^2_{2,T}. \qquad (4.58)$$

The term involving I_4 have the following bounds:

$$\begin{aligned}
&\int_{\overline{EA_3}} \left(I_4\phi^P_{4,T,x}(X)\right)^2 \mathrm{d}s \\
\le\;& Ch^{-2} \int_{\overline{EA_3}} \left(\int_0^1 (1-t)\frac{d^2}{dt^2}u(tM_4+(1-t)X)dt\right)^2 \mathrm{d}s \\
\le\;& Ch^{-2} \int_{eh}^{h}\int_0^1 (1-t)^2 \left|u_{yy}(0,\frac{th}{2}+(1-t)y)\right|^2 \left(\frac{h}{2}-y\right)^4 \mathrm{d}t\,\mathrm{d}y
\end{aligned}$$

Let $z = \frac{th}{2} + (1-t)y$, then $\mathrm{d}z = \left(\frac{h}{2}-y\right)\mathrm{d}t$, and $1-t = (\frac{h}{2}-z)/(\frac{h}{2}-y)$. Hence,

$$\begin{aligned}
&\int_{\overline{EA_3}} \left(I_4\phi^P_{4,T,x}(X)\right)^2 \mathrm{d}s \\
\le\;& Ch^{-2} \int_{eh}^{h} \left|\int_y^{h/2} |u_{yy}(0,z)|^2 \left(\frac{h}{2}-y\right)\left(\frac{h}{2}-z\right)^2 \mathrm{d}z\right| \mathrm{d}y \\
\le\;& Ch \left(\int_{eh}^{h}\int_{eh}^{h/2} |u_{yy}(0,z)|^2\,\mathrm{d}z\,\mathrm{d}y + \int_{eh}^{h}\int_{h/2}^{h} |u_{yy}(0,z)|^2\,\mathrm{d}z\,\mathrm{d}y\right) \\
\le\;& Ch \left(\int_{eh}^{h/2}\int_{eh}^{h} |u_{yy}(0,z)|^2\,\mathrm{d}y\,\mathrm{d}z + \int_{h/2}^{h}\int_{eh}^{h} |u_{yy}(0,z)|^2\,\mathrm{d}y\,\mathrm{d}z\right) \\
\le\;& Ch^2 \left(\int_{eh}^{h} |u_{yy}(0,z)|^2\,\mathrm{d}z\right) \\
\le\;& Ch^2\|u\|^2_{3,\Omega^-} \qquad (4.59)
\end{aligned}$$

Combining the estimates (4.51) - (4.59) and using the density hypothesis **(H4)**, we obtain for every $u \in PH^3_{int}(\Omega)$,

$$\left\|\partial_x(I^P_{h,T}u - u)\right\|^2_{0,\overline{EA_3}} \leq C\left(h\|u\|^2_{2,T} + h^2\|u\|^2_{3,\Omega^-}\right).$$

Use similar arguments by letting $X \in \overline{A_1E}$, we can also prove that

$$\left\|\partial_x(I^P_{h,T}u - u)\right\|^2_{0,\overline{A_1E}} \leq C\left(h\|u\|^2_{2,T} + h^2\|u\|^2_{3,\Omega^+}\right).$$

Note that $b = \overline{EA_3} \cup \overline{A_1E}$; hence, we obtain the following estimate

$$\left\|\partial_x(I^P_{h,T}u - u)\right\|^2_{0,b} \leq C\left(h\|u\|^2_{2,T} + h^2\|u\|^2_{3,\Omega}\right). \tag{4.60}$$

Similar arguments leads to the error estimate for y derivative:

$$\left\|\partial_y(I^P_{h,T}u - u)\right\|^2_{0,b} \leq C\left(h\|u\|^2_{2,T} + h^2\|u\|^2_{3,\Omega}\right). \tag{4.61}$$

Combining (4.60) and (4.61) yields the error estimate (4.49) for $u \in PC^3_{int}(\Omega)$. Applying the density assumption **(H6)**, we obtain (4.49) for $u \in PH^3_{int}(\Omega)$. □

Now we derive an error estimate for the interpolation $I^I_{h,T}$ on interface edges.

Lemma 4.4. *For every $u \in PH^3_{int}(\Omega)$, there exists a constant C such that*

$$\|\beta\nabla(u - I^I_{h,T}u)\cdot\mathbf{n}_b\|^2_{0,b} \leq C(h^2\|u\|^2_{3,\Omega} + h\|u\|^2_{2,T}), \tag{4.62}$$

where $T \in \mathcal{T}^i_h$ is an interface element and $b \subset \partial T$ is one of its interface edges.

Proof. By the triangle inequality, we have

$$\|\beta\nabla(u - I^I_{h,T}u)\cdot\mathbf{n}_b\|_{0,b} \leq \|\beta\nabla(u - I^P_{h,T}u)\cdot\mathbf{n}_b\|_{0,b} + \|\beta\nabla(I^P_{h,T}u - I^I_{h,T}u)\cdot\mathbf{n}_b\|_{0,b}. \tag{4.63}$$

We have derived an error bound (4.49) in Lemma 4.3 for the first term on the right hand side of (4.63). It suffices to estimate the second term on the right hand sides of (4.63).

Note that $I^P_{h,T}u - I^I_{h,T}u \in S^i_h(T)$, then by the IFE trace inequality (3.15) and the estimate (3.80) we obtain

$$\begin{aligned}\|\beta\nabla(I^P_{h,T}u - I^I_{h,T}u)\cdot\mathbf{n}_b\|_{0,b} &\leq Ch^{1/2}|T|^{-1/2}\|\sqrt{\beta}\nabla(I^P_{h,T}u - I^I_{h,T}u)\|_{0,T}\\ &\leq Ch^{1/2}|T|^{-1/2}h\|u\|_{2,T}\\ &\leq Ch^{1/2}\|u\|_{2,T}.\end{aligned} \tag{4.64}$$

Combining (4.64) and (4.49) leads to the estimate (4.62). □

The following lemma provides an error bound for the IFE interpolation in the energy norm $\|\cdot\|_{h,\Omega}$.

Lemma 4.5. *Let $u \in PH^2_{int}(\Omega)$, then there exists a constant C independent of h and interface location, such that*

$$\|I_h^k u - u\|_{h,\Omega} \leq C(h + h^{(3-\alpha)/2})\|u\|_{2,\Omega}, \quad k = I \text{ or } P. \tag{4.65}$$

Proof. By the interpolations error estimates stated in Theorem 3.9 and Theorem 3.11, and the standard trace inequality (3.4), we obtain for $k = P$ or I that

$$\begin{aligned}
\|I_h^k u - u\|^2_{h,\Omega} &= \sum_{T\in\mathcal{T}_h} \int_T \beta \nabla(I_h^k u - u)\cdot\nabla(I_h^k u - u)\mathrm{d}X + \sum_{b\in\mathcal{E}_h^i}\int_b \frac{\sigma_b^0}{|b|^\alpha}[(I_h^k u - u)]^2\mathrm{d}s \\
&\leq \sum_{T\in\mathcal{T}_h} |I_h^k u - u|^2_{1,T} + Ch^{-\alpha}\sum_{b\in\mathcal{E}_h^i}\|I_h^k u - u\|^2_{0,b} \\
&\leq C\sum_{T\in\mathcal{T}_h} h^2\|u\|^2_{2,T} + Ch^{-\alpha}\sum_{T\in\mathcal{T}_h} h^{-1}\left(\|I_h^k u - u\|^2_{0,T} + h^2|I_h^k u - u|^2_{1,T}\right) \\
&\leq C(h^2 + h^{3-\alpha})\|u\|^2_{2,\Omega}.
\end{aligned} \tag{4.66}$$

Taking square root on both sides of (4.66) leads to (4.65). □

Remark 4.1. *The error estimate* (4.65) *in Lemma 4.5 indicates that nonconforming IFE functions have optimal approximation property in energy norm if $\alpha \leq 1$. On the other hand, the coercivity property* (4.38) *in Lemma 4.1 requires $\alpha \geq 1$ for the bilinear form* (4.27) *to be coercive. The only value of α that satisfies both of these conditions is $\alpha = 1$. Therefore, from now on, we let $\alpha = 1$ in both error analysis and numerical experiment.*

Now we are ready to derive a bound for the error in the PPG IFE solution u_h^I.

Theorem 4.1. *Assume $u \in PH^3_{int}(\Omega)$ is the solution to the interface problem* (1.1) - (1.4)*, and $u_h^I \in S_h^I(\Omega)$ is the partially penalized Galerkin IFE solution to* (4.24) *and* (4.26)*, then there exists a constant C such that*

$$\|u_h^I - u\|_{h,\Omega} \leq Ch\|u\|_{3,\Omega}. \tag{4.67}$$

Proof. Note that the solution $u \in PH^3_{int}(\Omega)$ is continuous in Ω, and the flux $\beta\nabla u \cdot \mathbf{n}_b$ is

continuous across every interior edges $b \in \mathring{\mathcal{E}}_h$. By Green's formula and (4.18), we have

$$\begin{aligned}
&\sum_{b\in\mathcal{E}_h^i}\int_b \{\beta\nabla u\cdot\mathbf{n}_b\}[v_h]\mathrm{d}s\\
=\;&\sum_{b\in\mathcal{E}_h^b}\int_b \beta\nabla u\cdot\mathbf{n}_b v_h\mathrm{d}s+\sum_{b\in\mathring{\mathcal{E}}_h}\int_b \{\beta\nabla u\cdot\mathbf{n}_b\}[v_h]\mathrm{d}s-\sum_{b\in\mathcal{E}_h^n}\int_b \{\beta\nabla u\cdot\mathbf{n}_b\}[v_h]\mathrm{d}s\\
=\;&\sum_{b\in\mathcal{E}_h^b}\int_b \beta\nabla u\cdot\mathbf{n}_b v_h\mathrm{d}s+\sum_{b\in\mathring{\mathcal{E}}_h}\int_b \{\beta\nabla u\cdot\mathbf{n}_b\}[v_h]\mathrm{d}s+\sum_{b\in\mathring{\mathcal{E}}_h}\int_b \{\beta\nabla v_h\cdot\mathbf{n}_b\}[u]\mathrm{d}s\\
&-\sum_{b\in\mathcal{E}_h^n}\int_b \{\beta\nabla u\cdot\mathbf{n}_b\}[v_h]\mathrm{d}s\\
=\;&\sum_{T\in\mathcal{T}_h}\int_{\partial T}\beta\nabla u\cdot\mathbf{n}_T v_h\mathrm{d}s-\sum_{b\in\mathcal{E}_h^n}\int_b \{\beta\nabla u\cdot\mathbf{n}_b\}[v_h]\mathrm{d}s, \qquad (4.68)
\end{aligned}$$

for every $v_h \in \mathring{S}_h^I(\Omega)$. The equation (4.68) implies

$$\begin{aligned}
a_\epsilon(u,v_h) &= \sum_{T\in\mathcal{T}_h}\int_T \beta\nabla u\cdot\nabla v_h\mathrm{d}X-\sum_{b\in\mathcal{E}_h^i}\int_b \{\beta\nabla u\cdot\mathbf{n}_b\}[v_h]\mathrm{d}s\\
&= \sum_{T\in\mathcal{T}_h}\int_T \beta\nabla u\cdot\nabla v_h\mathrm{d}X-\sum_{T\in\mathcal{T}_h}\int_{\partial T}\beta\nabla u\cdot\mathbf{n}_T v_h\mathrm{d}s+\sum_{b\in\mathcal{E}_h^n}\int_b \{\beta\nabla u\cdot\mathbf{n}_b\}[v_h]\mathrm{d}s\\
&= \sum_{T\in\mathcal{T}_h}\int_T -\nabla\cdot(\beta\nabla u)v_h\mathrm{d}X+\sum_{b\in\mathcal{E}_h^n}\int_b \{\beta\nabla u\cdot\mathbf{n}_b\}[v_h]\mathrm{d}s\\
&= (f,v_h)+\sum_{b\in\mathcal{E}_h^n}\int_b \{\beta\nabla u\cdot\mathbf{n}_b\}[v_h]\mathrm{d}s. \qquad (4.69)
\end{aligned}$$

Hence, subtracting (4.69) from (4.24), we have

$$a_\epsilon(u_h^I,v_h)=a_\epsilon(u,v_h)-\sum_{b\in\mathcal{E}_h^n}\int_b \{\beta\nabla u\cdot\mathbf{n}_b\}[v_h]\mathrm{d}s,\quad \forall v_h\in\mathring{S}_h^I(\Omega). \qquad (4.70)$$

For every function w_h in $\tilde{S}_h^I(\Omega)=\{w_h\in S_h^I(\Omega):\int_b w_h\mathrm{d}s=\int_b g\mathrm{d}s,\forall b\in\mathcal{E}_h^b\}$, we subtract $a_\epsilon(w_h,v_h)$ from both sides of (4.70)

$$a_\epsilon(u_h^I-w_h,v_h)=a_\epsilon(u-w_h,v_h)-\sum_{b\in\mathcal{E}_h^n}\int_b \{\beta\nabla u\cdot\mathbf{n}_b\}[v_h]\mathrm{d}s,\quad \forall v_h\in\mathring{S}_h^I(\Omega),\ \forall w_h\in\tilde{S}_h^I(\Omega).$$

We let $v_h=u_h^I-w_h\in\mathring{S}_h^I(\Omega)$ in the above equation, then

$$a_\epsilon(u_h^I-w_h,u_h^I-w_h)=a_\epsilon(u-w_h,u_h^I-w_h)-\sum_{b\in\mathcal{E}_h^n}\int_b \{\beta\nabla u\cdot\mathbf{n}_b\}[u_h^I-w_h]\mathrm{d}s,\quad \forall w_h\in\tilde{S}_h^I(\Omega). \qquad (4.71)$$

Applying the coercivity result (4.38) to (4.71), we have

$$\begin{aligned}
&\kappa\|u_h^I - w_h\|_{h,\Omega}^2 \\
\leq\ & |a_\epsilon(u - w_h, u_h^I - w_h)| + \left|\sum_{b\in\mathcal{E}_h^n}\int_b \{\beta\nabla u\cdot\mathbf{n}_b\}[u_h^I - w_h]\mathrm{d}s\right| \\
\leq\ & \left|\sum_{T\in\mathcal{T}_h}\int_T \beta\nabla(u - w_h)\cdot\nabla(u_h^I - w_h)\mathrm{d}X\right| + \left|\sum_{b\in\mathcal{E}_h^i}\int_b \{\beta\nabla(u - w_h)\cdot\mathbf{n}_b\}[u_h^I - w_h]\mathrm{d}s\right| \\
&+ \left|\epsilon\sum_{b\in\mathcal{E}_h^i}\int_b \{\beta\nabla(u_h^I - w_h)\cdot\mathbf{n}_b\}[u - w_h]\mathrm{d}s\right| + \left|\sum_{b\in\mathcal{E}_h^i}\int_b \frac{\sigma_b^0}{|b|^\alpha}[u - w_h][u_h^I - w_h]\mathrm{d}s\right| \\
&+ \left|\sum_{b\in\mathcal{E}_h^n}\int_b \{\beta\nabla u\cdot\mathbf{n}_b\}[u_h^I - w_h]\mathrm{d}s\right| \\
\triangleq\ & Q_1 + Q_2 + Q_3 + Q_4 + Q_5. \qquad (4.72)
\end{aligned}$$

To bound Q_1 we use Cauchy-Schwarz inequality and Young's inequality to obtain the following estimate

$$\begin{aligned}
Q_1 &\leq \left(\sum_{T\in\mathcal{T}_h}\left\|\beta^{1/2}\nabla(u - w_h)\right\|_{0,T}^2\right)^{1/2}\left(\sum_{T\in\mathcal{T}_h}\left\|\beta^{1/2}\nabla(u_h^I - w_h)\right\|_{0,T}^2\right)^{1/2} \\
&\leq \frac{\kappa}{6}\sum_{T\in\mathcal{T}_h}\left\|\beta^{1/2}\nabla(u_h^I - w_h)\right\|_{0,T}^2 + C\|\nabla(u - w_h)\|_{0,\Omega}^2 \\
&\leq \frac{\kappa}{6}\|u_h^I - w_h\|_{h,\Omega}^2 + C\|\nabla(u - w_h)\|_{0,\Omega}^2. \qquad (4.73)
\end{aligned}$$

To bound Q_2, using Young's inequality we have

$$\begin{aligned}
Q_2 &\leq \left(\sum_{b\in\mathcal{E}_h^i}\|\{\beta\nabla(u - w_h)\cdot\mathbf{n}_b\}\|_{0,b}^2\right)^{1/2}\left(\sum_{b\in\mathcal{E}_h^i}\left\|\left[u_h^I - w_h\right]\right\|_{0,b}^2\right)^{1/2} \\
&\leq \frac{\kappa}{6}\sum_{b\in\mathcal{E}_h^i}\frac{\sigma_b^0}{|b|^\alpha}\left\|\left[u_h^I - w_h\right]\right\|_{0,b}^2 + C\sum_{b\in\mathcal{E}_h^i}\frac{|b|^\alpha}{\sigma_b^0}\|\{\beta\nabla(u - w_h)\cdot\mathbf{n}_b\}\|_{0,b}^2 \\
&\leq \frac{\kappa}{6}\|u_h^I - w_h\|_{h,\Omega}^2 + C\sum_{b\in\mathcal{E}_h^i}\frac{|b|^\alpha}{\sigma_b^0}\|\{\beta\nabla(u - w_h)\cdot\mathbf{n}_b\}\|_{0,b}^2. \qquad (4.74)
\end{aligned}$$

To bound Q_3, applying the trace inequality (3.4) for H^1 function $u - w_h$ and trace inequality

(3.15) for IFE function $u_h^I - w_h$, we have

$$\begin{aligned}
Q_3 &\leq |\epsilon| \left(\sum_{b\in\mathcal{E}_h^i} \left\| \{\beta\nabla(u_h^I - w_h)\cdot \mathbf{n}_b\} \right\|_{0,b}^2 \right)^{1/2} \left(\sum_{b\in\mathcal{E}_h^i} \|[u-w_h]\|_{0,b}^2 \right)^{1/2} \\
&\leq C \left(\sum_{b\in\mathcal{E}_h^i} \left\| (\beta\nabla(u_h^I - w_h)\cdot \mathbf{n}_b)|_{T_{b,1}} \right\|_{0,b}^2 + \sum_{b\in\mathcal{E}_h^i} \left\| (\beta\nabla(u_h^I - w_h)\cdot \mathbf{n}_b)|_{T_{b,2}} \right\|_{0,b}^2 \right)^{1/2} \\
&\quad \left(\sum_{b\in\mathcal{E}_h^i} \left\| (u-w_h)|_{T_{b,1}} \right\|_{0,b}^2 + \sum_{b\in\mathcal{E}_h^i} \left\| (u-w_h)|_{T_{b,2}} \right\|_{0,b}^2 \right)^{1/2} \\
&\leq Ch^{-1} \left(\sum_{b\in\mathcal{E}_h^i} \left\| (\beta^{1/2}\nabla(u_h^I - w_h) \right\|_{0,T_{b,1}}^2 + \sum_{b\in\mathcal{E}_h^i} \left\| (\beta^{1/2}\nabla(u_h^I - w_h) \right\|_{0,T_{b,2}}^2 \right)^{1/2} \\
&\quad \left(\sum_{b\in\mathcal{E}_h^i} \Big(\|(u-w_h)\|_{0,T_{b,1}}^2 + h^2 \|\nabla(u-w_h)\|_{0,T_{b,1}}^2 \right. \\
&\quad \left. + \|(u-w_h)\|_{0,T_{b,2}}^2 + h^2 \|\nabla(u-w_h)\|_{0,T_{b,2}}^2 \Big) \right)^{1/2} \\
&\leq Ch^{-1} \left(\sum_{T\in\mathcal{T}_h} \left\| \beta^{1/2}\nabla(u_h^I - w_h) \right\|_{0,T}^2 \right)^{1/2} \\
&\quad \left(\sum_{T\in\mathcal{T}_h} \Big(\|(u-w_h)\|_{L^2(T)}^2 + h^2 \|\nabla(u-w_h)\|_{0,T}^2 \Big) \right)^{1/2} \\
&\leq \frac{\kappa}{6} \|u_h^I - w_h\|_{h,\Omega}^2 + Ch^{-2} \left(\sum_{T\in\mathcal{T}_h} \Big(\|(u-w_h)\|_{0,T}^2 + h^2 \|\nabla(u-w_h)\|_{0,T}^2 \Big) \right). \qquad (4.75)
\end{aligned}$$

To bound Q_4, we have

$$\begin{aligned}
Q_4 &\leq \left(\sum_{b\in\mathcal{E}_h^i} \int_b \frac{\sigma_b^0}{|b|^\alpha} [u-w_h]^2 \mathrm{d}s \right)^{1/2} \left(\sum_{b\in\mathcal{E}_h^i} \int_b \frac{\sigma_b^0}{|b|^\alpha} [u_h^I - w_h]^2 \mathrm{d}s \right)^{1/2} \\
&\leq \frac{\kappa}{6} \|u_h^I - w_h\|_{h,\Omega}^2 + \frac{3}{2\kappa} \sum_{b\in\mathcal{E}_h^i} \frac{\sigma_b^0}{|b|^\alpha} \|[u-w_h]\|_{0,b}^2 \\
&\leq \frac{\kappa}{6} \|u_h^I - w_h\|_{h,\Omega}^2 + C \sum_{T\in\mathcal{T}_h} h^{-(1+\alpha)} \left(\sum_{T\in\mathcal{T}_h} \Big(\|(u-w_h)\|_{0,T}^2 + h^2 \|\nabla(u-w_h)\|_{0,T}^2 \Big) \right). \qquad (4.76)
\end{aligned}$$

For Q_5, note that the flux $\beta\nabla u\cdot\mathbf{n}_b$ is continuous across every interior edges $b\in\mathring{\mathcal{E}}_h$; hence $\{\beta\nabla u\cdot\mathbf{n}_b\}=\beta\nabla u\cdot\mathbf{n}_b$. Using the estimates (4.43) and (4.44) in Lemma 4.2 and the standard approximation result [37], we have

$$\begin{aligned}
Q_5 &= \left|\sum_{b\in\mathcal{E}_h^n}\int_b \beta\nabla u\cdot\mathbf{n}_b\left[u_h^I-w_h\right]\mathrm{d}s\right| \\
&= \left|\sum_{b\in\mathcal{E}_h^n}\int_b \left(\beta\nabla u\cdot\mathbf{n}_b-\overline{\beta\nabla u\cdot\mathbf{n}_b}^b\right)\left[u_h^I-w_h\right]\mathrm{d}s\right| \\
&\le C\sum_{b\in\mathcal{E}_h^n}\left\|\beta\nabla u\cdot\mathbf{n}_b-\overline{\beta\nabla u\cdot\mathbf{n}_b}^b\right\|_{0,b}\left\|\left[(u_h^I-w_h)\right]\right\|_{0,b} \\
&\le C\sum_{T\in\mathcal{T}_h} h^{1/2}\|\beta\nabla u\cdot\mathbf{n}\|_{1,T}h^{1/2}|u_h^I-w_h|_{1,T} \\
&\le Ch\sum_{T\in\mathcal{T}_h}\|u\|_{2,T}|u_h^I-w_h|_{1,T} \\
&\le Ch\left(\sum_{T\in\mathcal{T}_h}\|u\|_{2,T}^2\right)^{1/2}\left(\sum_{T\in\mathcal{T}_h}|u_h^I-w_h|_{1,T}^2\right)^{1/2} \\
&\le \frac{\kappa}{6}\|u_h^I-w_h\|_{h,\Omega}^2+Ch^2\|u\|_{2,\Omega}^2. \qquad (4.77)
\end{aligned}$$

Applying the estimates (4.73) - (4.77) to (4.72), we have

$$\begin{aligned}
&\frac{\kappa}{6}\|u_h^I-w_h\|_{h,\Omega}^2 \\
\le\ & Ch^2\|u\|_{2,\Omega}^2+C\|\nabla(u-w_h)\|_{0,\Omega}^2+C\sum_{b\in\mathcal{E}_h^i}\frac{|b|^\alpha}{\sigma_b^0}\left\|\{\beta\nabla(u-w_h)\cdot\mathbf{n}_b\}\right\|_{0,b}^2 \\
&+C(h^{-2}+h^{-(1+\alpha)})\left(\sum_{T\in\mathcal{T}_h}\left(\|(u-w_h)\|_{0,T}^2+h^2\left\|\nabla(u-w_h)\right\|_{0,T}^2\right)\right). \qquad (4.78)
\end{aligned}$$

Then, letting $w_h=I_h^Iu$ in (4.78), using the estimate (3.81) in Theorem 3.12 and (4.62) in Lemma 4.4 we have the following estimate:

$$\begin{aligned}
\|u_h^I-I_h^Iu\|_{h,\Omega}^2 &\le Ch^2\|u\|_{2,\Omega}^2+C\sum_{b\in\mathcal{E}_h^i}\frac{|b|}{\sigma_b^0}\left\|\left\{\beta\nabla(u-I_h^Iu)\cdot\mathbf{n}_b\right\}\right\|_{0,b}^2 \\
&\le Ch^2\|u\|_{2,\Omega}^2+C\sum_{T\in\mathcal{T}_h^i}h\left(h^2\|u\|_{3,\Omega}^2+h\|u\|_{2,T}^2\right) \\
&\le Ch^2\|u\|_{3,\Omega}^2. \qquad (4.79)
\end{aligned}$$

The last inequality in (4.79) is because of the hypothesis (**H5**). Note that the interpolation error is bounded as follows using the energy norm (4.66)

$$\|u-I_h^Iu\|_{h,\Omega}^2\le Ch^2\|u\|_{2,\Omega}^2. \qquad (4.80)$$

Finally, (4.67) follows from applying (4.79) (4.80) to the triangle inequality

$$\|u_h^I - u\|_{h,\Omega} \leq \|u - I_h^I u\|_{h,\Omega} + \|u_h^I - I_h^I u\|_{h,\Omega}.$$

□

Remark 4.2. *The error estimate* (4.67) *is optimal from the point view of the degree of polynomials that we use to solve the elliptic interface problem.*

To confirm our error analysis, we present several numerical examples in the following discussion. We use the function u given in (3.82) as the exact solution. The Dirichlet boundary function g and the source function f are chosen correspondingly. Errors of IFE solutions are given in L^∞, L^2, and semi-H^1 norms. Errors in the L^∞ norm are defined by

$$\|u_h - u\|_{0,\infty,\Omega} = \max_{T\in\mathcal{T}_h}\left(\max_{(x,y)\in\tilde{T}\subset T}|u_h(x,y) - u(x,y)|\right), \tag{4.81}$$

where $\tilde{T}$ consists of the 49 uniformly distributed points in T as illustrated in Figure 3.2. The L^2 and semi-H^1 norms are computed by suitable Gaussian quadratures. In the following data tables, rates of convergence in a numerical solution u_h are computed by applying the formulas:

$$\frac{1}{\ln(2)}\ln\left(\frac{\|u_h - u\|}{\|u_{h/2} - u\|}\right), \tag{4.82}$$

for a specific norm $\|\cdot\|$, where u_h denotes IFE solution based on the mesh $\mathcal{T}_h$.

Example 4.1. ***(Integral-Value Degrees of Freedom)****: In this experiment, we test the accuracy of IFE solutions u_h^I generated from PPG IFE schemes.*

We test all the three PPG IFE schemes based on IFE space $S_h^I(\Omega)$ for the elliptic interface problem (1.1) - (1.5). First, we consider the case $(\beta^-, \beta^+) = (1, 10)$ which represents a moderate discontinuity in the diffusion coefficient. Table 4.1, Table 4.2, and Table 4.3 contain errors of NPPG solutions, SPPG solutions and IPPG solutions, respectively. In the NPPG scheme, we choose $\sigma_b^0 = 1$,. In SPPG and IPPG schemes, we choose $\sigma_b^0 = 10\max(\beta^-, \beta^+)$ for all the interface edges $b \in \mathcal{E}_h^i$. The different choices of σ_b^0 are due to the coercivity requirement described in Lemma 4.1.

Convergence rates in semi-H^1 norm in Tables 4.1 through 4.3 confirm our error analysis in the energy norm (4.67). In fact, errors in the semi-H^1 norm can be bounded by the energy norm with a constant C depending only on the diffusion coefficient β, *i.e.*,

$$|u_h^I - u|_{1,\Omega} \leq C\|u_h^I - u\|_{h,\Omega}.$$

The data also suggest that the convergence rates in L^2 and L^∞ norms are approximately $O(h^2)$, which are also optimal from the point view of the degree of polynomials used to construct IFE spaces. However, the error analysis of L^2 and L^∞ norms is still open.

Table 4.1: Errors of NPPG IFE solutions $u - u_h^I$ with $\beta^- = 1$, $\beta^+ = 10$.

N	$\|\cdot\|_{0,\infty,\Omega}$	rate	$\|\cdot\|_{0,\Omega}$	rate	$\|\cdot\|_{1,\Omega}$	rate
10	$2.6184E{-2}$		$1.1379E{-2}$		$1.9532E{-1}$	
20	$7.3445E{-3}$	1.8339	$2.9869E{-3}$	1.9296	$9.9052E{-2}$	0.9796
40	$1.9455E{-3}$	1.9165	$7.4436E{-4}$	2.0046	$4.9890E{-2}$	0.9894
80	$5.0072E{-4}$	1.9581	$1.8561E{-4}$	2.0037	$2.5022E{-2}$	0.9955
160	$1.2702E{-4}$	1.9789	$4.6350E{-5}$	2.0016	$1.2530E{-2}$	0.9978
320	$3.1989E{-5}$	1.9894	$1.1671E{-5}$	1.9887	$6.2699E{-3}$	0.9989
640	$8.0267E{-6}$	1.9947	$2.9143E{-6}$	2.0026	$3.1362E{-3}$	0.9994
1280	$2.0101E{-6}$	1.9975	$7.2743E{-7}$	2.0023	$1.5684E{-3}$	0.9997

Table 4.2: Errors of SPPG IFE solutions $u - u_h^I$ with $\beta^- = 1$, $\beta^+ = 10$.

N	$\|\cdot\|_{0,\infty,\Omega}$	rate	$\|\cdot\|_{0,\Omega}$	rate	$\|\cdot\|_{1,\Omega}$	rate
10	$2.6165E{-2}$		$1.1319E{-2}$		$1.9570E{-1}$	
20	$7.3431E{-3}$	1.8332	$2.9737E{-3}$	1.9285	$9.9523E{-2}$	0.9756
40	$1.9455E{-3}$	1.9163	$7.4366E{-4}$	1.9995	$5.0008E{-2}$	0.9929
80	$5.0072E{-4}$	1.9580	$1.8547E{-4}$	2.0034	$2.5056E{-2}$	0.9970
160	$1.2702E{-4}$	1.9789	$4.6267E{-5}$	2.0032	$1.2538E{-2}$	0.9988
320	$3.1989E{-5}$	1.9894	$1.1664E{-5}$	1.9879	$6.2731E{-3}$	0.9991
640	$8.0267E{-6}$	1.9947	$2.9094E{-6}$	2.0033	$3.1368E{-3}$	0.9999
1280	$2.0101E{-6}$	1.9975	$7.2612E{-7}$	2.0024	$1.5686E{-3}$	0.9999

Table 4.3: Errors of IPPG IFE solutions $u - u_h^I$ with $\beta^- = 1$, $\beta^+ = 10$.

N	$\|\cdot\|_{0,\infty,\Omega}$	rate	$\|\cdot\|_{0,\Omega}$	rate	$\|\cdot\|_{1,\Omega}$	rate
10	$2.6165E{-2}$		$1.1320E{-2}$		$1.9570E{-1}$	
20	$7.3431E{-3}$	1.8332	$2.9743E{-3}$	1.9282	$9.9527E{-2}$	0.9755
40	$1.9455E{-3}$	1.9163	$7.4385E{-4}$	1.9995	$5.0009E{-2}$	0.9929
80	$5.0072E{-4}$	1.9580	$1.8551E{-4}$	2.0035	$2.5056E{-2}$	0.9970
160	$1.2702E{-4}$	1.9789	$4.6275E{-5}$	2.0032	$1.2538E{-2}$	0.9988
320	$3.1989E{-5}$	1.9894	$1.1665E{-5}$	1.9880	$6.2731E{-3}$	0.9991
640	$8.0267E{-6}$	1.9947	$2.9098E{-6}$	2.0033	$3.1368E{-3}$	0.9999
1280	$2.0101E{-6}$	1.9975	$7.2621E{-7}$	2.0024	$1.5686E{-3}$	0.9999

We also test PPG IFE schemes with an interface problem whose coefficient has a larger

jump, *i.e.*, $(\beta^-, \beta^+) = (1, 10000)$. Errors of nonsymmetric, symmetric and incomplete PPG IFE solutions are listed in Table 4.4, Table 4.5 and Table 4.6, respectively. These data demonstrate the optimal convergence in L^2, and semi-H^1 for all these PPG IFE schemes. Errors in L^∞ norm are slightly less than optimal rate $O(h^2)$. We also note that NPPG solutions are more accurate than SPPG and IPPG schemes in this example. In addition, the convergence rate of NPPG solutions seems to be closer to optimal in L^∞ norm compared to SPPG and IPPG schemes.

Table 4.4: Errors of NPPG IFE solutions $u - u_h^I$ with $\beta^- = 1$, $\beta^+ = 10000$.

N	$\|\cdot\|_{0,\infty,\Omega}$	rate	$\|\cdot\|_{0,\Omega}$	rate	$\|\cdot\|_{1,\Omega}$	rate
10	$6.2407E{-3}$		$2.6860E{-3}$		$4.1237E{-2}$	
20	$2.5474E{-3}$	1.2927	$1.0545E{-3}$	1.3488	$2.7853E{-2}$	0.5661
40	$7.3217E{-4}$	1.7988	$2.6021E{-4}$	2.0189	$1.4724E{-2}$	0.9197
80	$2.4255E{-4}$	1.5939	$6.3786E{-5}$	2.0284	$7.5699E{-3}$	0.9598
160	$7.0298E{-5}$	1.7867	$1.5572E{-5}$	2.0342	$3.7998E{-3}$	0.9943
320	$2.0025E{-5}$	1.8117	$4.0879E{-6}$	1.9296	$1.9164E{-3}$	0.9875
640	$5.4254E{-6}$	1.8840	$1.0077E{-6}$	2.0202	$9.5916E{-4}$	0.9985
1280	$1.4369E{-6}$	1.9168	$2.4931E{-7}$	2.0151	$4.8012E{-4}$	0.9984

Table 4.5: Errors of SPPG IFE solutions $u - u_h^I$ with $\beta^- = 1$, $\beta^+ = 10000$.

N	$\|\cdot\|_{0,\infty,\Omega}$	rate	$\|\cdot\|_{0,\Omega}$	rate	$\|\cdot\|_{1,\Omega}$	rate
10	$6.5953E{-3}$		$2.6902E{-3}$		$4.1642E{-2}$	
20	$2.5724E{-3}$	1.3583	$1.0825E{-3}$	1.3133	$2.8294E{-2}$	0.5575
40	$7.9282E{-4}$	1.6981	$2.7408E{-4}$	1.9818	$1.5064E{-2}$	0.9094
80	$3.2033E{-4}$	1.3074	$7.6080E{-5}$	1.8490	$7.8210E{-3}$	0.9457
160	$1.2195e{-4}$	1.3932	$1.7489E{-5}$	2.1211	$3.8529E{-3}$	1.0214
320	$2.6504E{-5}$	2.2020	$4.3093E{-6}$	2.0209	$1.9325E{-3}$	0.9955
640	$8.0321E{-6}$	1.7223	$1.0814E{-6}$	1.9946	$9.6213E{-4}$	1.0062
1280	$2.3285E{-6}$	1.7864	$2.5544E{-7}$	2.0819	$4.8077E{-4}$	1.0009

4.2.2 Error Estimation for IFE Solutions in $S_h^P(\Omega)$

In this subsection, we derive an error bound for the PPG IFE solutions u_h^P. The discussion in this section is based on the assumption that the solution u to the elliptic interface problem is piece-wise $W^{2,\infty}$, *i.e.*, $u|_{\Omega^s} \in W^{2,\infty}(\Omega^s)$, $s = +, -$. First, we define the following space

$$PW_{int}^{2,\infty}(\Omega) = \left\{ u \in C(\Omega), u|_{\Omega^s} \in W^{2,\infty}(\Omega^s), s = +, -, [\beta \nabla u \cdot \mathbf{n}_\Gamma] = 0 \text{ on } \Gamma \right\}. \tag{4.83}$$

Table 4.6: Errors of IPPG IFE solutions $u - u_h^I$ with $\beta^- = 1$, $\beta^+ = 10000$.

N	$\|\cdot\|_{0,\infty,\Omega}$	rate	$\|\cdot\|_{0,\Omega}$	rate	$\|\cdot\|_{1,\Omega}$	rate
10	$6.5953E{-}3$		$2.6902E{-}3$		$4.1642E{-}2$	
20	$2.5724E{-}3$	1.3583	$1.0825E{-}3$	1.3133	$2.8294E{-}2$	0.5575
40	$7.9281E{-}4$	1.6981	$2.7408E{-}4$	1.9817	$1.5064E{-}2$	0.9094
80	$3.2029E{-}4$	1.3076	$7.6078E{-}5$	1.8490	$7.8210E{-}3$	0.9457
160	$1.2191e{-}4$	1.3936	$1.7481E{-}5$	2.1217	$3.8528E{-}3$	1.0214
320	$2.6476E{-}5$	2.2030	$4.3105E{-}6$	2.0199	$1.9326E{-}3$	0.9954
640	$8.0516E{-}6$	1.7173	$1.0819E{-}6$	1.9942	$9.6215E{-}4$	1.0062
1280	$2.3298E{-}6$	1.7890	$2.5544E{-}7$	2.0825	$4.8077E{-}4$	1.0009

In the following error analysis in this subsection, we need the following hypothesis,

(H7) The interface Γ is smooth enough so that $PC_{int}^3(\Omega)$ is dense in $PW_{int}^{2,\infty}(\Omega)$.

Then, we derive the interpolation error bound on an interface edge using the norm $\|\cdot\|_{2,\infty,\Omega}$.

Lemma 4.6. *For every $u \in PW_{int}^{2,\infty}(\Omega)$, there exists a constant C such that*

$$\|\beta\nabla(u - I_{h,T}^P u)\cdot\mathbf{n}_b\|_{0,b}^2 \le Ch^3\|u\|_{2,\infty,\Omega}^2, \tag{4.84}$$

where $T \in \mathcal{T}_h^i$ is an interface element and $b \subset \partial T$ is one of its interface edges.

Proof. We consider the Type I Case 2 interface element as illustrated in Figure 3.1, and the discussion for other cases are similar. Without loss of the generality, we let $b = \overline{A_1A_3}$. Recall from (3.61) that for every function $u \in PC_{int}^3(\Omega)$, its interpolation error at a point $X \in \overline{EA_3}$ can be expanded as follows

$$\frac{\partial(I_{h,T}^P u(X) - u(X))}{\partial x} = (F_1 + F_2)\phi_{1,T,x}^P(X) - \frac{1}{2}F_{0,x}u_{xx}(X) + \sum_{i=1}^{4} I_i\phi_{i,T,x}^P(X), \tag{4.85}$$

where F_0, F_1, F_2, and I_i, $i = 1,\cdots,4$ are defined in (3.35), (3.46a) - (3.46g). To bound the first term on the right hand side of (4.85), we use (3.30), (3.31) and the bound of IFE functions (3.3a) in Theorem 3.2 to obtain

$$\int_{\overline{EA_3}}(F_i\phi_{1,T,x}^P(X))^2\mathrm{d}s \le Ch^2\int_{\overline{EA_3}}|\nabla u^-|^2\mathrm{d}s \le Ch^3\|u\|_{1,\infty,\Omega^-}^2 \le Ch^3\|u\|_{2,\infty,\Omega^-}^2, \quad \forall\, i = 1,2. \tag{4.86}$$

Also, applying the bound of F_0 from (3.42) to the second term on the right hand side of (4.85) yields

$$\begin{aligned}\int_{\overline{EA_3}}\left(\frac{1}{2}F_{0,x}u^-_{xx}(X)\right)^2\mathrm{d}s &\leq \int_{\overline{EA_3}}|F_{0,x}|^2|u^-_{xx}(X)|^2\mathrm{d}s\\ &\leq Ch^2\int_{\overline{EA_3}}|u^-_{xx}(X)|^2\mathrm{d}s\\ &\leq Ch^3\|u\|^2_{2,\infty,\Omega^-}. \end{aligned}\tag{4.87}$$

For the term involving $I_{1,1}$ we have the following estimate from (3.54) and the bound of IFE functions (3.3a) given in Theorem 3.2

$$\begin{aligned}&\int_{\overline{EA_3}}\left(I_{1,1}\phi^P_{1,T,x}(X)\right)^2\mathrm{d}s\\ \leq\ & Ch^2\int_{\overline{EA_3}}\int_0^1\left(|u_{\xi\xi}(\xi,\eta)|^2+|u_{\xi\eta}(\xi,\eta)|^2+|u_{\eta\xi}(\xi,\eta)|^2+|u_{\eta\eta}(\xi,\eta)|^2\right)\mathrm{d}t\,\mathrm{d}s\\ \leq\ & Ch^3\|u\|^2_{2,\infty,\Omega^-}. \end{aligned}\tag{4.88}$$

Similarly to (4.88), we obtain

$$\int_{\overline{EA_3}}\left(I_{1,i}\phi^P_{1,T,x}(X)\right)^2\mathrm{d}s\leq Ch^3\|u\|^2_{2,\infty,\Omega^-},\quad i=2,3.\tag{4.89}$$

For the term involving I_2 we have the following estimate using (3.3a)

$$\begin{aligned}&\int_{\overline{EA_3}}\left(I_2\phi^P_{2,T,x}(X)\right)^2\mathrm{d}s\\ \leq\ & Ch^2\int_{eh}^h\int_0^1(1-t)^2\left|u_{xx}(th,\frac{th}{2}+(1-t)y)\right|^2+\left|u_{xy}(th,\frac{th}{2}+(1-t)y)\right|^2\\ &+\left|u_{yx}(th,\frac{th}{2}+(1-t)y)\right|^2+\left|u_{yy}(th,\frac{th}{2}+(1-t)y)\right|^2\mathrm{d}t\,\mathrm{d}y\\ \leq\ & Ch^3\|u\|^2_{2,\infty,\Omega^-}. \end{aligned}\tag{4.90}$$

Similarly to (4.90), we obtain

$$\int_{\overline{EA_3}}\left(I_i\phi^P_{3,T,x}(X)\right)^2\mathrm{d}s\leq Ch^3\|u\|^2_{2,\infty,\Omega^-},\quad i=3,4.\tag{4.91}$$

Combining all estimates (4.86) - (4.91) yields

$$\left\|\partial_x(I^P_{h,T}u-u)\right\|^2_{0,\overline{EA_3}}\leq Ch^3\|u\|^2_{2,\infty,\Omega^-}.$$

Similarly, we can also show that

$$\left\|\partial_x(I^P_{h,T}u-u)\right\|^2_{0,\overline{A_1E}}\leq Ch^3\|u\|^2_{2,\infty,\Omega^+}.$$

Note that $b = \overline{EA_3} \cup \overline{A_1E}$, hence

$$\left\|\partial_x(I_{h,T}^P u - u)\right\|_{0,b}^2 \leq Ch^3 \|u\|_{2,\infty,\Omega}^2. \tag{4.92}$$

Using a similar argument we can derive an error estimate for y-derivative:

$$\left\|\partial_y(I_{h,T}^P u - u)\right\|_{0,b}^2 \leq Ch^3 \|u\|_{2,\infty,\Omega}^2. \tag{4.93}$$

Combining (4.92) and (4.93) leads to the error estimate (4.84) for $u \in PC_{int}^3(\Omega)$. Applying the density assumption **(H7)**, we obtain (4.49) for $u \in PW_{int}^{2,\infty}(\Omega)$. □

The following lemma is useful for the error analysis. The proof of the this lemma follows a similar approach in the proof of Theorem 3.3 in [85].

Lemma 4.7. *Let $u \in H^1(\Omega)$ and $u|_{\Omega_s} \in H^2(\Omega^s)$, $s = +, -$. There exists a constant C such that*

$$\sum_{b \in \partial T} \int_b (\beta \nabla u \cdot \mathbf{n}_b)\,(v_h - v_h(M_b))\,ds \leq Ch|u|_{2,T}|v_h|_{1,T}, \quad \forall\, v_h \in S_h^P(\Omega), \tag{4.94}$$

for every non-interface element $T \in \mathcal{T}_h^n$, where b is an edge of T and M_b is the midpoint of b.

Proof. We consider an element $T \in \mathcal{T}_h^n$ with vertices

$$A_1 = (x_0, y_0)^t, \quad A_2 = (x_0 + h, y_0)^t, \quad A_3 = (x_0, y_0 + h)^t, \quad A_4 = (x_0 + h, y_0 + h)^t.$$

Then we denote the edges of T as follows:

$$b_1 = \overline{A_1A_2}, \quad b_2 = \overline{A_2A_4}, \quad b_3 = \overline{A_4A_3}, \quad b_4 = \overline{A_3A_1},$$

Without loss of generality, we consider the two vertical edges b_2 and b_4. Note that the normal vectors associated to these edges satisfy $\mathbf{n}_{b_2} = -\mathbf{n}_{b_4}$. Then we have the following estimate

by using the inverse inequality (3.17):

$$\begin{aligned}
&\int_{b_2} (\nabla u \cdot \mathbf{n}_{b_2}) (v_h - v_h(M_{b_2})) \,\mathrm{d}s + \int_{b_4} (\nabla u \cdot \mathbf{n}_{b_4}) (v_h - v_h(M_{b_4})) \,\mathrm{d}s \\
= &\int_{b_2} u_x(x,y)(v_h(x,y) - v_h(M_{b_2}))\mathrm{d}s - \int_{b_4} u_x(x,y)(v_h(x,y) - v_h(M_{b_4}))\mathrm{d}s \\
= &\int_{y_0}^{y_0+h} u_x(x_0+h,y)(v_h(x_0+h,y) - v_h(x_0+h, y_0+\frac{h}{2}))\mathrm{d}y \\
&-\int_{y_0}^{y_0+h} u_x(x_0,y)(v_h(x_0,y) - v_h(x_0, y_0+\frac{h}{2}))\mathrm{d}y \\
= &\int_{y_0}^{y_0+h} u_x(x_0+h,y) \left(\int_{y_0+h/2}^{y} \frac{\partial v_h(x_0+h,y')}{\partial y'} \mathrm{d}y' \right) \mathrm{d}y \\
&-\int_{y_0}^{y_0+h} u_x(x_0,y) \left(\int_{y_0+h/2}^{y} \frac{\partial v_h(x_0,y')}{\partial y'} \mathrm{d}y' \right) \mathrm{d}y \\
= &\int_{y_0}^{y_0+h} (u_x(x_0+h,y) - u_x(x_0,y)) \left(\int_{y_0+h/2}^{y} \frac{\partial v_h(x_0+h,y')}{\partial y'} \mathrm{d}y' \right) \mathrm{d}y \\
= &\int_{y_0}^{y_0+h} \left(\int_{x_0}^{x_0+h} u_{xx}(x,y)\mathrm{d}x \right) \left(\int_{y_0+h/2}^{y} |v_h|_{1,\infty,T} \mathrm{d}y' \right) \mathrm{d}y \\
\leq &\, C|v_h|_{1,T} \int_{x_0}^{x_0+h} \int_{y_0}^{y_0+h} u_{xx}(x,y) \,\mathrm{d}x \,\mathrm{d}y \\
\leq &\, Ch|v_h|_{1,T}|u|_{2,T}.
\end{aligned}$$

Similarly, we can derive an estimate on two horizontal edges b_1 and b_3. Finally, the result (4.94) follows immediately from combining these estimates together. □

Now we are ready to prove the convergence of u_h^P.

Theorem 4.2. *Assume that $u \in PW_{int}^{2,\infty}(\Omega)$ is the solution to the interface problem* (1.1) - (1.4)*, and $u_h^P \in S_h^P(\Omega)$ is the partially penalized Galerkin IFE solution to* (4.24) *and* (4.25)*, then there exists a constant C such that*

$$\|u_h^P - u\|_{h,\Omega} \leq Ch^{1/2}\|u\|_{2,\infty,\Omega} \tag{4.95}$$

Proof. Note that the solution $u \in W_{int}^{2,\infty}(\Omega)$ is continuous inside Ω, and the flux $\beta\nabla u \cdot \mathbf{n}_b$ are continuous across every interior edge $b \in \mathring{\mathcal{E}}_h$. Similar to the derivation (4.68) in the proof of Theorem 4.1, for every $v_h \in \mathring{S}_h^P(\Omega)$, we have

$$\sum_{b\in\mathcal{E}_h^i} \int_b \{\beta\nabla u \cdot \mathbf{n}_b\}[v_h]\mathrm{d}s = \sum_{T\in\mathcal{T}_h} \int_{\partial T} \beta\nabla u \cdot \mathbf{n}_T v_h \mathrm{d}s - \sum_{b\in\mathcal{E}_h^n} \int_b \{\beta\nabla u \cdot \mathbf{n}_b\}[v_h]\mathrm{d}s. \tag{4.96}$$

Similar to the derivation (4.69), the equation (4.96) yields

$$a_\epsilon(u, v_h) = (f, v_h) + \sum_{b\in\mathcal{E}_h^n} \int_b \{\beta\nabla u \cdot \mathbf{n}_b\}[v_h]\mathrm{d}s. \tag{4.97}$$

Hence, subtracting (4.97) from (4.24), we have

$$a_\epsilon(u_h^P, v_h) = a_\epsilon(u, v_h) - \sum_{b\in\mathcal{E}_h^n} \int_b \{\beta\nabla u \cdot \mathbf{n}_b\}[v_h]\mathrm{d}s, \quad \forall v_h \in \mathring{S}_h^P(\Omega). \tag{4.98}$$

For every function w_h in $\tilde{S}_h^P(\Omega) = \{w_h \in S_h^P(\Omega) : w_h(M_b) = g(M_b), \forall\, b \in \mathcal{E}_h^b\}$, we subtract $a_\epsilon(w_h, v_h)$ from both sides of (4.98),

$$a_\epsilon(u_h^P - w_h, v_h) = a_\epsilon(u - w_h, v_h) - \sum_{b\in\mathcal{E}_h^n} \int_b \{\beta\nabla u \cdot \mathbf{n}_b\}[v_h]\mathrm{d}s, \quad \forall v_h \in \mathring{S}_h^P(\Omega),\ \forall w_h \in \tilde{S}_h^P(\Omega).$$

We let $v_h = u_h^P - w_h \in \mathring{S}_h^P(\Omega)$ in the above equation, then

$$a_\epsilon(u_h^P - w_h, u_h^P - w_h) = a_\epsilon(u - w_h, u_h^P - w_h) - \sum_{b\in\mathcal{E}_h^n} \int_b \{\beta\nabla u \cdot \mathbf{n}_b\}[u_h^P - w_h]\mathrm{d}s, \quad \forall w_h \in \tilde{S}_h^P(\Omega). \tag{4.99}$$

We can write the last term in (4.99) as the summation with respect to the element T:

$$\begin{aligned}
&\sum_{b\in\mathcal{E}_h^n} \int_b \{\beta\nabla u \cdot \mathbf{n}_b\}[u_h^P - w_h]\mathrm{d}s \\
= &\sum_{T\in\mathcal{T}_h^n} \sum_{b\subset\partial T} \int_b (\beta\nabla u \cdot \mathbf{n}_b)(u_h^P - w_h - (u_h^P(M_b) - w_h(M_b)))\mathrm{d}s \\
&+ \sum_{T\in\mathcal{T}_h^i} \sum_{b\subset\partial T, b\notin\mathcal{E}_h^i} \int_b (\beta\nabla u \cdot \mathbf{n}_b)(u_h^P - w_h - (u_h^P(M_b) - w_h(M_b)))\mathrm{d}s.
\end{aligned} \tag{4.100}$$

Applying the identity (4.100) and the coercivity result (4.38) to (4.99) yields

$$
\begin{aligned}
& \kappa\|u_h^P - w_h\|_{h,\Omega}^2 \\
\leq\ & |a_\epsilon(u-w_h, u_h^P - w_h)| + \left|\sum_{b\in\mathcal{E}_h^n}\int_b \{\beta\nabla u\cdot\mathbf{n}_b\}[u_h^I - w_h]\mathrm{d}s\right| \\
=\ & \left|\sum_{T\in\mathcal{T}_h}\int_T \beta\nabla(u-w_h)\cdot\nabla(u_h^P - w_h)\mathrm{d}X\right| + \left|\sum_{b\in\mathcal{E}_h^i}\int_b \{\beta\nabla(u-w_h)\cdot\mathbf{n}_b\}[u_h^P - w_h]\mathrm{d}s\right| \\
& + \left|\epsilon\sum_{b\in\mathcal{E}_h^i}\int_b \{\beta\nabla(u_h^P - w_h)\cdot\mathbf{n}_b\}[u-w_h]\mathrm{d}s\right| + \left|\sum_{b\in\mathcal{E}_h^i}\int_b \frac{\sigma_b^0}{|b|^\alpha}[u-w_h][u_h^P - w_h]\mathrm{d}s\right| \\
& + \left|\sum_{T\in\mathcal{T}_h^n}\sum_{b\subset\partial T}\int_b (\beta\nabla u\cdot\mathbf{n}_b)(u_h^P - w_h - (u_h^P(M_b) - w_h(M_b)))\mathrm{d}s\right| \\
& + \left|\sum_{T\in\mathcal{T}_h^i}\sum_{b\subset\partial T, b\notin\mathcal{E}_h^i}\int_b (\beta\nabla u\cdot\mathbf{n}_b)(u_h^P - w_h - (u_h^P(M_b) - w_h(M_b)))\mathrm{d}s\right| \\
\triangleq\ & Q_1^P + Q_2^P + Q_3^P + Q_4^P + Q_5^P + Q_6^P. \qquad (4.101)
\end{aligned}
$$

Following similar arguments (4.73) - (4.76) as for analyzing Q_1 through Q_4, we obtain the following estimates for Q_i^P, $i = 1, 2, 3, 4$:

$$Q_1^P \leq \frac{\kappa}{6}\|u_h^P - w_h\|_{h,\Omega}^2 + C\|\nabla(u-w_h)\|_{0,\Omega}^2, \qquad (4.102)$$

$$Q_2^P \leq \frac{\kappa}{6}\|u_h^P - w_h\|_{h,\Omega}^2 + C\sum_{b\in\mathcal{E}_h^i}\frac{|b|^\alpha}{\sigma_b^0}\|\{\beta\nabla(u-w_h)\cdot\mathbf{n}_b\}\|_{0,b}^2, \qquad (4.103)$$

$$Q_3^P \leq \frac{\kappa}{6}\|u_h^P - w_h\|_{h,\Omega}^2 + Ch^{-2}\left(\sum_{T\in\mathcal{T}_h}\left(\|(u-w_h)\|_{0,T}^2 + h^2\|\nabla(u-w_h)\|_{0,T}^2\right)\right), \qquad (4.104)$$

$$Q_4^P \leq \frac{\kappa}{6}\|u_h^P - w_h\|_{h,\Omega}^2 + C\sum_{T\in\mathcal{T}_h}h^{-(1+\alpha)}\left(\sum_{T\in\mathcal{T}_h}\left(\|(u-w_h)\|_{0,T}^2 + h^2\|\nabla(u-w_h)\|_{0,T}^2\right)\right). \qquad (4.105)$$

By Lemma 4.7, we have the following bounds for Q_5^P:

$$
\begin{aligned}
Q_5^P &\leq \left|\sum_{T\in\mathcal{T}_h^n}\sum_{b\subset\partial T}\int_b (\beta\nabla u\cdot\mathbf{n}_b)\left(u_h^P - w_h - (u_h^P(M_b) - w_h(M_b))\right)\mathrm{d}s\right| \\
&\leq Ch\left(\sum_{T\in\mathcal{T}_h^n}|u|_{2,T}^2\right)^{1/2}\left(\sum_{T\in\mathcal{T}_h}|u_h^P - w_h|_{1,T}^2\right)^{1/2} \\
&\leq \frac{\kappa}{6}\|u_h^P - w_h\|_{h,\Omega}^2 + Ch^2\|u\|_{2,\Omega}^2. \qquad (4.106)
\end{aligned}
$$

To bound Q_6^P, we let $\mathcal{T}_h^*$ be the collection of non-interface elements which are adjacent to interface elements and let $\Omega^* = \bigcup_{T\in\mathcal{T}_h^*} T$. By standard trace theorem (3.5) we have

$$\begin{aligned}
Q_6^P &\leq \left| \sum_{T\in\mathcal{T}_h^i} \sum_{b\subset\partial T, b\notin\mathcal{E}_h^i} \int_b (\beta\nabla u\cdot\mathbf{n})(u_h^P - w_h - (u_h^P(M_b) - w_h(M_b)))\mathrm{d}s \right| \\
&\leq C \sum_{T\in\mathcal{T}_h^i} \sum_{b\subset\partial T, b\notin\mathcal{E}_h^i} \|\beta\nabla u\cdot\mathbf{n}\|_{0,b} \|u_h^P - w_h - (u_h^P(M_b) - w_h(M_b))\|_{0,b} \\
&\leq C \sum_{T\in\mathcal{T}_h^*} h^{-1/2}|u|_{2,T} h^{1/2}|u_h^P - w_h|_{1,T} \\
&\leq C\left(\sum_{T\in\mathcal{T}_h^*} |u|_{2,T}^2\right)^{1/2} \left(\sum_{T\in\mathcal{T}_h} |u_h^P - w_h|_{1,T}^2\right)^{1/2} \\
&\leq \frac{\kappa}{12}\|u_h^P - w_h\|_{h,\Omega}^2 + C|u|_{2,\Omega^*}^2
\end{aligned}$$

Using the hypothesis **(H5)**, we may conclude that $meas(\Omega^*) \leq Ch$. As a result, we have

$$|u|_{2,\Omega^*}^2 = \int_{\Omega^*} \sum_{|\alpha|=2} |D^\alpha u|^2 \mathrm{d}X \leq |u|_{2,\infty,\Omega}^2 \int_{\Omega^*} 1\mathrm{d}X \leq Ch|u|_{2,\infty,\Omega}^2.$$

Hence,

$$Q_6^P \leq \frac{\kappa}{12}\|u_h^P - w_h\|_{h,\Omega}^2 + Ch|u|_{2,\infty,\Omega}^2 \tag{4.107}$$

Applying estimates (4.102) - (4.107) to (4.101), we have

$$\begin{aligned}
&\frac{\kappa}{12}\|u_h^P - w_h\|_{h,\Omega}^2 \\
\leq\ & Ch\|u\|_{2,\infty,\Omega}^2 + Ch^2\|u\|_{2,\Omega}^2 + C\|\nabla(u-w_h)\|_{0,\Omega}^2 + C\sum_{b\in\mathcal{E}_h^i} \frac{|b|^\alpha}{\sigma_b^0} \|\{\beta\nabla(u-w_h)\cdot\mathbf{n}_b\}\|_{0,b}^2 \\
&+C(h^{-2} + h^{-(1+\alpha)}) \left(\sum_{T\in\mathcal{T}_h} \left(\|(u-w_h)\|_{0,T}^2 + h^2\|\nabla(u-w_h)\|_{0,T}^2\right)\right).
\end{aligned} \tag{4.108}$$

Then we let $w_h = I_h^P u$ in (4.108) and use the estimate (3.71) in Theorem 3.10 and (4.49) in Lemma 4.3 to have the following estimate:

$$\begin{aligned}
\|u_h^P - I_h^P u\|_{h,\Omega}^2 &\leq Ch^2\|u\|_{2,\Omega}^2 + Ch\|u\|_{2,\infty,\Omega}^2 + C\sum_{b\in\mathcal{E}_h^i} \frac{|b|}{\sigma_b^0} \left\|\left\{\beta\nabla(u - I_h^P u)\cdot\mathbf{n}_b\right\}\right\|_{0,b}^2 \\
&\leq Ch^2\|u\|_{2,\Omega}^2 + Ch\|u\|_{2,\infty,\Omega}^2 + C\sum_{T\in\mathcal{T}_h} h\left(h^3\|u\|_{2,\infty,\Omega}^2\right) \\
&\leq Ch\|u\|_{2,\infty,\Omega}^2.
\end{aligned} \tag{4.109}$$

Again, we use the hypothesis **(H5)** to derive the last inequality in (4.109). Then we apply the interpolation error estimate with energy norm (4.66) to have

$$\|u - I_h^P u\|_{h,\Omega}^2 \leq Ch^2 \|u\|_{2,\Omega}^2. \tag{4.110}$$

Since $u \in PW_{int}^{2,\infty}(\Omega)$, then it can be easily verified that

$$\|u\|_{2,\Omega} \leq C\|u\|_{2,\infty,\Omega}. \tag{4.111}$$

Finally, the result (4.95) follows from applying the error bounds (4.109), (4.110) and (4.111) to the following triangle inequality

$$\|u_h^P - u\|_{h,\Omega} \leq \|u - I_h^P u\|_{h,\Omega} + \|u_h^P - I_h^P u\|_{h,\Omega}.$$

□

Note that the error bound we have derived for the PPG IFE solution u_h^P is at least suboptimal in the energy norm $\|\cdot\|_{h,\Omega}$. Next we provide a few numerical experiments to test the performance of this PPG IFE scheme. We consider the same example as we use in Example 4.1.

Example 4.2. ***(Midpoint-Value Degrees of Freedom)****: In this experiment, we test the accuracy IFE solutions u_h^P generated from PPG IFE schemes.*

We carry out numerical experiments for the moderate coefficient discontinuity $(\beta^-, \beta^+) = (1, 10)$ using the same Cartesian meshes $\mathcal{T}_h$ as we used in Example 4.1. Errors of nonsymmetric, symmetric, and incomplete PPG IFE solutions u_h^P are listed in Table 4.7, Table 4.8, and Table 4.9, respectively.

Data in these tables demonstrate convergence patterns of PPG IFE solutions with midpoint-value degrees of freedom. Errors in semi-H^1 norm seem to maintain an optimal rate $O(h)$ for all three PPG IFE schemes, although suboptimal convergence rate (4.95) has been theoretically established for the PPG IFE schemes with midpoint-value degrees of freedom.

Errors in L^2 norm seem to obey an optimal rate $O(h^2)$ for symmetric and incomplete PPG IFE schemes but only suboptimal rate for nonsymmetric scheme. Errors in L^∞ norm can only achieve suboptimal rates for all of these three PPG IFE schemes. Comparisons of these two PPG IFE schemes with different types of degrees of freedom will be provided in Section 4.3.

4.2.3 Error Estimation for IPDG IFE Solutions

In this section, we discuss the error estimation of the interior penalty discontinuous Galerkin IFE solution u_h^{DG}. We note that the analysis for u_h^{DG} is quite similar to the PPG IFE solution u_h^I; hence, we omit some details in the following discussion.

Table 4.7: Errors of NPPG IFE solutions $u - u_h^P$ with $\beta^- = 1$, $\beta^+ = 10$.

N	$\|\cdot\|_{0,\infty,\Omega}$	rate	$\|\cdot\|_{0,\Omega}$	rate	$\|\cdot\|_{1,\Omega}$	rate
10	$3.0784E{-2}$		$8.4671E{-3}$		$1.9584E{-1}$	
20	$8.6353E{-3}$	1.8339	$2.1214E{-3}$	1.9969	$9.9798E{-2}$	0.9726
40	$2.2891E{-3}$	1.9155	$5.3504E{-4}$	1.9873	$5.0319E{-2}$	0.9879
80	$5.8956E{-4}$	1.9571	$1.3560E{-4}$	1.9803	$2.5272E{-2}$	0.9935
160	$1.4962E{-4}$	1.9783	$3.4479E{-5}$	1.9755	$1.2674E{-2}$	0.9957
320	$4.6014E{-5}$	1.7012	$9.0189E{-6}$	1.9347	$6.3669E{-3}$	0.9932
640	$2.3525E{-5}$	0.9679	$2.3671E{-6}$	1.9298	$3.2019E{-3}$	0.9917
1280	$1.1957E{-5}$	0.9750	$6.4032E{-7}$	1.8863	$1.6196E{-3}$	0.9833

Table 4.8: Errors of SPPG IFE solutions $u - u_h^P$ with $\beta^- = 1$, $\beta^+ = 10$.

N	$\|\cdot\|_{0,\infty,\Omega}$	rate	$\|\cdot\|_{0,\Omega}$	rate	$\|\cdot\|_{1,\Omega}$	rate
10	$3.0780E{-2}$		$7.6671E{-3}$		$1.9716E{-1}$	
20	$8.6341E{-3}$	1.8338	$2.0929E{-3}$	1.8732	$1.0026E{-1}$	0.9756
40	$2.2891E{-3}$	1.9153	$5.2161E{-4}$	2.0045	$5.0424E{-2}$	0.9916
80	$5.8956E{-4}$	1.9571	$1.2971E{-4}$	2.0076	$2.5275E{-2}$	0.9964
160	$1.4962E{-4}$	1.9783	$3.2259E{-5}$	2.0075	$1.2652E{-2}$	0.9984
320	$3.7691E{-5}$	1.9891	$8.1360E{-6}$	1.9873	$6.3327E{-3}$	0.9985
640	$9.4586E{-6}$	1.9945	$2.0047E{-6}$	2.0210	$3.1684E{-3}$	0.9991
1280	$4.2436E{-6}$	1.1563	$4.8937E{-7}$	2.0344	$1.5863E{-3}$	0.9981

Table 4.9: Errors of IPPG IFE solutions $u - u_h^P$ with $\beta^- = 1$, $\beta^+ = 10$.

N	$\|\cdot\|_{0,\infty,\Omega}$	rate	$\|\cdot\|_{0,\Omega}$	rate	$\|\cdot\|_{1,\Omega}$	rate
10	$3.0780E{-2}$		$7.6807E{-3}$		$1.9714E{-1}$	
20	$8.6342E{-3}$	1.8339	$2.0976E{-3}$	1.8725	$1.0026E{-2}$	0.9755
40	$2.2891E{-3}$	1.9153	$5.2135E{-4}$	2.0084	$5.0424E{-2}$	0.9916
80	$5.8956E{-4}$	1.9571	$1.2982E{-4}$	2.0057	$2.5275E{-2}$	0.9964
160	$1.4962E{-4}$	1.9783	$3.2369E{-5}$	2.0039	$1.2652E{-2}$	0.9983
320	$3.7691E{-5}$	1.9891	$8.2351E{-6}$	1.9747	$6.3328E{-3}$	0.9984
640	$9.4586E{-6}$	1.9945	$2.0559E{-6}$	2.0020	$3.1685E{-3}$	0.9990
1280	$4.3463E{-6}$	1.1218	$5.1318E{-7}$	2.0022	$1.5864E{-3}$	0.9980

We define the energy norm, still denoted by $\|\cdot\|_{h,\Omega}$, on the "broken" IFE space $S_h^{DG}(\Omega)$ as

follows

$$\|v\|_{h,\Omega} = \left(\sum_{T\in\mathcal{T}_h} \int_T \beta \nabla v \cdot \nabla v \, \mathrm{d}x \, \mathrm{d}y + \sum_{b\in\mathcal{E}_h} \int_b \frac{\sigma_b^0}{|b|^\alpha} [v][v] \mathrm{d}s \right)^{1/2}. \tag{4.112}$$

Using similar arguments to those for proving Lemma 4.1, we can show that the bilinear form $a_\epsilon^{DG}(\cdot,\cdot)$ defined in (4.34) is coercive with the above energy norm (4.112).

Lemma 4.8. *Assume $\alpha \geq 1$ in the bilinear form* (4.34) *and the energy norm* (4.112)*. There exists a positive constant κ such that*

$$\kappa \|v\|_{h,\Omega}^2 \leq a_\epsilon^{DG}(v,v), \quad \forall\, v \in S_h^{DG}(\Omega), \tag{4.113}$$

for any positive σ_b^0 if $\epsilon = 1$, or for σ_b^0 large enough if $\epsilon = -1$ or 0.

The following lemma provides an estimate of interpolation errors on non-interface edges.

Lemma 4.9. *There exists a constant C such that*

$$\|\beta \nabla (u - I_{h,T}^k u) \cdot \mathbf{n}_b\|_{0,b}^2 \leq Ch|u|_{2,T}^2, \quad \forall\, u \in H^2(T),\ k = P, I. \tag{4.114}$$

for every non-interface element $T \in \mathcal{T}_h^n$ where $b \subset \partial T$ is one of its edges.

Proof. By trace inequality (3.5) we obtain

$$\|\beta \nabla (u - I_{h,T}^k u) \cdot \mathbf{n}_b\|_{0,b}^2 \leq C(h^{-1}|u - I_{h,T}^k u|_{1,T}^2 + h|u - I_{h,T}^k u|_{2,T}^2). \tag{4.115}$$

Using standard scaling argument [44] to analyze the interpolation error $u - I_{h,T}^k u$, $k = P, I$, we have

$$|u - I_{h,T}^k u|_{m,T} \leq Ch^{2-m}|u|_{2,T}, \quad m = 1, 2. \tag{4.116}$$

The estimate (4.114) follows from (4.115) and (4.116). □

An error estimate of the IPDG IFE schemes is given in the following theorem.

Theorem 4.3. *Assume $u \in PH_{int}^3(\Omega)$ is the solution to the interface problem* (1.1) - (1.4)*, and $u_h^{DG} \in S_h^{DG}(\Omega)$ is the interior penalty discontinuous Galerkin IFE solution to* (4.32) *with boundary condition* (4.33a) *or* (4.33b)*, then there exists a constant C such that*

$$\|u_h^{DG} - u\|_{h,\Omega} \leq Ch\|u\|_{3,\Omega}. \tag{4.117}$$

Proof. Note that the solution $u \in PH^3_{int}(\Omega)$ is continuous inside Ω, and the flux $\beta\nabla u \cdot \mathbf{n}_b$ is continuous across every interior edges $b \in \mathring{\mathcal{E}}_h$. By Green's formula and (4.18) we have

$$\begin{aligned}
&\sum_{b\in\mathcal{E}_h}\int_b \{\beta\nabla u\cdot\mathbf{n}_b\}[v_h]\mathrm{d}s\\
=\;&\sum_{b\in\mathcal{E}_h^b}\int_b \beta\nabla u\cdot\mathbf{n}_b v_h\mathrm{d}s+\sum_{b\in\mathring{\mathcal{E}}_h}\int_b\{\beta\nabla u\cdot\mathbf{n}_b\}[v_h]\mathrm{d}s\\
=\;&\sum_{b\in\mathcal{E}_h^b}\int_b \beta\nabla u\cdot\mathbf{n}_b v_h\mathrm{d}s+\sum_{b\in\mathring{\mathcal{E}}_h}\int_b\{\beta\nabla u\cdot\mathbf{n}_b\}[v_h]\mathrm{d}s+\sum_{b\in\mathring{\mathcal{E}}_h}\int_b\{\beta\nabla v_h\cdot\mathbf{n}_b\}[u]\mathrm{d}s\\
=\;&\sum_{T\in\mathcal{T}_h}\int_{\partial T}\beta\nabla u\cdot\mathbf{n}_T v_h\mathrm{d}s, \qquad (4.118)
\end{aligned}$$

for every $v_h \in \mathring{S}_h^{k,DG}(\Omega)$, $k = P, I$. The equation (4.118) implies

$$a_\epsilon^{DG}(u,v_h)=\sum_{T\in\mathcal{T}_h}\int_T\beta\nabla u\cdot\nabla v_h\mathrm{d}X-\sum_{T\in\mathcal{T}_h}\int_{\partial T}\beta\nabla u\cdot\mathbf{n}_T v_h\mathrm{d}s=(f,v_h). \qquad (4.119)$$

Hence, subtracting (4.119) from (4.32) we obtain

$$a_\epsilon^{DG}(u_h^{DG},v_h)=a_\epsilon^{DG}(u,v_h),\quad \forall\, v_h\in\mathring{S}_h^{k,DG}(\Omega),\quad k=P,I. \qquad (4.120)$$

For every function w_h in

$$\tilde{S}_h^{P,DG}(\Omega)=\{w_h\in S_h^{DG}(\Omega): w_h(M_b)=g(M_b),\forall\, b\in\mathcal{E}_h^b\},$$

or

$$\tilde{S}_h^{I,DG}(\Omega)=\{w_h\in S_h^{DG}(\Omega): \int_b w_h\mathrm{d}s=\int_b g\mathrm{d}s,\forall\, b\in\mathcal{E}_h^b\},$$

we subtract $a_\epsilon^{DG}(w_h,v_h)$ from (4.120) then

$$a_\epsilon^{DG}(u_h^{DG}-w_h,v_h)=a_\epsilon^{DG}(u-w_h,v_h),\quad \forall\, v_h\in\mathring{S}_h^{k,DG}(\Omega),\ \forall\, w_h\in\tilde{S}_h^{k,DG}(\Omega),\quad k=P,I.$$

We let $v_h = u_h^{DG} - w_h \in \mathring{S}_h^{k,DG}(\Omega)$ in the above equation, then

$$a_\epsilon^{DG}(u_h^{DG}-w_h,u_h^{DG}-w_h)=a_\epsilon^{DG}(u-w_h,u_h^{DG}-w_h),\quad \forall w_h\in\tilde{S}_h^{k,DG}(\Omega),\quad k=P,I. \qquad (4.121)$$

Applying the coercivity result (4.113) to (4.121), we have

$$\begin{aligned}
&\kappa\|u_h^{DG}-w_h\|_{h,\Omega}^2\\
\le\;&\left|\sum_{T\in\mathcal{T}_h}\int_T\beta\nabla(u-w_h)\cdot\nabla(u_h^{DG}-w_h)\mathrm{d}X\right|+\left|\sum_{b\in\mathcal{E}_h}\int_b\{\beta\nabla(u-w_h)\cdot\mathbf{n}_b\}[u_h^{DG}-w_h]\mathrm{d}s\right|\\
&+\left|\epsilon\sum_{b\in\mathcal{E}_h}\int_b\{\beta\nabla(u_h^{DG}-w_h)\cdot\mathbf{n}_b\}[u-w_h]\mathrm{d}s\right|+\left|\sum_{b\in\mathcal{E}_h}\int_b\frac{\sigma_b^0}{|b|^\alpha}[u-w_h][u_h^{DG}-w_h]\mathrm{d}s\right|\\
\triangleq\;&Q_1^{DG}+Q_2^{DG}+Q_3^{DG}+Q_4^{DG}. \qquad (4.122)
\end{aligned}$$

Following similar arguments (4.73) - (4.76) in analyzing Q_1 through Q_4, we obtain the following estimates for Q_i^{DG}, $i = 1, 2, 3, 4$:

$$Q_1^{DG} \leq \frac{\kappa}{6}\|u_h^{DG} - w_h\|_{h,\Omega}^2 + C\|\nabla(u - w_h)\|_{0,\Omega}^2, \tag{4.123}$$

$$Q_2^{DG} \leq \frac{\kappa}{6}\|u_h^{DG} - w_h\|_{h,\Omega}^2 + C\sum_{b\in\mathcal{E}_h}\frac{|b|^\alpha}{\sigma_b^0}\|\{\beta\nabla(u - w_h)\cdot\mathbf{n}_b\}\|_{0,b}^2, \tag{4.124}$$

$$Q_3^{DG} \leq \frac{\kappa}{6}\|u_h^{DG} - w_h\|_{h,\Omega}^2 + Ch^{-2}\left(\sum_{T\in\mathcal{T}_h}\left(\|(u - w_h)\|_{0,T}^2 + h^2\|\nabla(u - w_h)\|_{0,T}^2\right)\right), \tag{4.125}$$

$$\begin{aligned} Q_4^{DG} \leq\ & \frac{\kappa}{6}\|u_h^{DG} - w_h\|_{h,\Omega}^2 \\ & + C\sum_{T\in\mathcal{T}_h}h^{-(1+\alpha)}\left(\sum_{T\in\mathcal{T}_h}\left(\|(u - w_h)\|_{0,T}^2 + h^2\|\nabla(u - w_h)\|_{0,T}^2\right)\right). \end{aligned} \tag{4.126}$$

Applying the estimates (4.123) - (4.126) to (4.122), we have

$$\begin{aligned} \frac{\kappa}{3}\|u_h^{DG} - w_h\|_{h,\Omega}^2 \leq\ & C\|\nabla(u - w_h)\|_{0,\Omega}^2 + C\sum_{b\in\mathcal{E}_h}\frac{|b|^\alpha}{\sigma_b^0}\|\{\beta\nabla(u - w_h)\cdot\mathbf{n}_b\}\|_{0,b}^2 \\ & + C(h^{-2} + h^{-(1+\alpha)})\left(\sum_{T\in\mathcal{T}_h}\left(\|(u - w_h)\|_{0,T}^2 + h^2\|\nabla(u - w_h)\|_{0,T}^2\right)\right). \end{aligned} \tag{4.127}$$

Then, we let w_h be the IFE interpolant $I_h^I u$ or $I_h^P u$ in (4.127) and apply interpolation error estimates (3.71) if $k = P$ or (3.81) if $k = I$ to obtain

$$\begin{aligned} \|u_h^{DG} - I_h^k u\|_{h,\Omega}^2 \leq\ & Ch^2\|u\|_{2,\Omega}^2 + C\sum_{b\in\mathcal{E}_h^i}\frac{|b|}{\sigma_b^0}\left\|\left\{\beta\nabla(u - I_h^k u)\cdot\mathbf{n}_b\right\}\right\|_{0,b}^2 \\ & + C\sum_{b\in\mathcal{E}_h^n}\frac{|b|}{\sigma_b^0}\left\|\left\{\beta\nabla(u - I_h^k u)\cdot\mathbf{n}_b\right\}\right\|_{0,b}^2. \end{aligned} \tag{4.128}$$

We use the estimate (4.114) or (4.62) to bound the second term on the right hand side of (4.128) and apply the estimate (4.127) to bound the third term on the right hand side of (4.128). Then we obtain

$$\|u_h^{DG} - I_h^k u\|_{h,\Omega}^2 \leq Ch^2\|u\|_{2,\Omega}^2 + C\sum_{T\in\mathcal{T}_h^i}h\left(h^2\|u\|_{3,\Omega}^2 + h\|u\|_{2,T}^2\right) \leq Ch^2\|u\|_{3,\Omega}^2. \tag{4.129}$$

The last inequality in (4.129) is due to the hypothesis (**H5**). Finally, the estimate (4.117) follows from applying the interpolation error estimate (4.80) if $k = I$ or (4.110) if $k = P$ and (4.129) to the following triangle inequality

$$\|u_h^{DG} - u\|_{h,\Omega} \leq \|u - I_h^k u\|_{h,\Omega} + \|u_h^{DG} - I_h^k u\|_{h,\Omega}.$$

□

Again, we use some numerical experiments to confirm our error analysis.

Example 4.3. ***(IPDG IFE Schemes)****: In this experiment, we test the accuracy of interior penalty DG IFE solutions u_h^{DG} using nonconforming rotated Q_1 IFE functions.*

In this experiment, we handle the boundary conditions by matching the midpoint values of IPDG IFE solutions with the boundary function g following the approach (4.33b). We have also conduct the experiment by matching the integral values of the boundary condition (4.33a), and the numerical results are almost exactly the same; hence, these results are skipped in the discussion below. Table 4.10, Table 4.11, and Table 4.12 contain the errors of nonsymmetric, symmetric, and incomplete IPDG IFE solutions, respectively. Convergence rates in semi-H^1 norm seem to be optimal for all these three IPDG IFE schemes, which confirms our error estimate (4.117). Moreover, convergence rates of nonsymmetric IPDG IFE solutions seem to be optimal in L^2 norm. Convergence rates of symmetric and incomplete IPDG IFE schemes are observed suboptimal using coarse meshes but they tend to become optimal when mesh size is sufficient small. One may find similar observation for convergence rates in L^∞ norm.

Table 4.10: Errors of NIPDG IFE solutions $u - u_h^{DG}$ with $\beta^- = 1$, $\beta^+ = 10$.

N	$\|\cdot\|_{0,\infty,\Omega}$	rate	$\|\cdot\|_{0,\Omega}$	rate	$\|\cdot\|_{1,\Omega}$	rate
10	$3.3627E{-}2$		$6.4672E{-}3$		$1.9925E{-}1$	
20	$9.9462E{-}3$	1.7574	$2.0110E{-}3$	1.6853	$1.0026E{-}1$	0.9908
40	$2.7240E{-}3$	1.8684	$5.2330E{-}4$	1.9422	$5.0258E{-}2$	0.9963
80	$7.4953E{-}4$	1.8616	$1.3210E{-}4$	1.9861	$2.5126E{-}2$	1.0002
160	$1.9913E{-}4$	1.9123	$3.3070E{-}5$	1.9980	$1.2558E{-}2$	1.0006
320	$5.1283E{-}5$	1.9572	$8.3972E{-}6$	1.9775	$6.2769E{-}3$	1.0005
640	$1.3010E{-}5$	1.9789	$2.0901E{-}6$	2.0063	$3.1380E{-}3$	1.0002
1280	$3.2764E{-}6$	1.9895	$5.1965E{-}7$	2.0087	$1.5689E{-}3$	1.0001

4.3 Discussions on Related Schemes

In this section, we consider other related IFE schemes and compare their numerical performance with PPG IFE schemes in Section 4.2. Related IFE methods considered here include those using different computational schemes, such as Galerkin IFE schemes, or those using different IFE functions, such as bilinear IFE functions [69].

Example 4.4. ***(Comparison with Galerkin IFE Solutions)****: In this example, we solve the interface problem using Galerkin IFE method* (4.5) *with nonconforming rotated Q_1 IFE functions, and compare their numerical performance to the PPG IFE methods.*

Table 4.11: Errors of SIPDG IFE solutions $u - u_h^{DG}$ with $\beta^- = 1$, $\beta^+ = 10$.

N	$\|\cdot\|_{0,\infty,\Omega}$	rate	$\|\cdot\|_{0,\Omega}$	rate	$\|\cdot\|_{1,\Omega}$	rate
10	$7.0936E{-2}$		$4.7707E{-2}$		$2.4015E{-1}$	
20	$2.3012E{-2}$	1.6241	$1.4423E{-2}$	1.7259	$1.1275E{-1}$	1.0908
40	$9.8020E{-3}$	1.2302	$4.6083E{-3}$	1.6460	$5.8333E{-2}$	0.9508
80	$3.3163E{-3}$	1.5635	$1.5382E{-3}$	1.5830	$2.9558E{-2}$	0.9808
160	$9.0724E{-4}$	1.8700	$4.8278E{-4}$	1.6718	$1.4433E{-2}$	1.0341
320	$2.8169E{-4}$	1.6874	$1.3999E{-4}$	1.7861	$6.9319E{-3}$	1.0581
640	$9.0890E{-5}$	1.6319	$3.8144E{-5}$	1.8758	$3.3352E{-3}$	1.0555
1280	$2.6419E{-5}$	1.7749	$9.9852E{-6}$	1.9336	$1.6234E{-3}$	1.0388

Table 4.12: Errors of IIPDG IFE solutions $u - u_h^{DG}$ with $\beta^- = 1$, $\beta^+ = 10$.

N	$\|\cdot\|_{0,\infty,\Omega}$	rate	$\|\cdot\|_{0,\Omega}$	rate	$\|\cdot\|_{1,\Omega}$	rate
10	$7.1014E{-2}$		$4.8643E{-2}$		$2.3952E{-1}$	
20	$2.2933E{-2}$	1.6307	$1.4513E{-2}$	1.7449	$1.1229E{-1}$	1.0930
40	$9.7748E{-3}$	1.2302	$4.6182E{-3}$	1.6520	$5.8161E{-2}$	0.9491
80	$3.3043E{-3}$	1.5647	$1.5376E{-3}$	1.5867	$2.9491E{-2}$	0.9798
160	$9.0367E{-4}$	1.8705	$4.8184E{-4}$	1.6740	$1.4408E{-2}$	1.0334
320	$2.8045E{-4}$	1.6881	$1.3958E{-4}$	1.7875	$6.9237E{-3}$	1.0573
640	$9.0424E{-5}$	1.6329	$3.8015E{-5}$	1.8764	$3.3327E{-3}$	1.0549
1280	$2.6419E{-5}$	1.7752	$9.9491E{-6}$	1.9339	$1.6227E{-3}$	1.0383

We start by using nonconforming rotated Q_1 IFE functions with midpoint-value degrees of freedom. We test the Galerkin IFE schemes for interface problem whose diffusion coefficient has a moderate jump, *i.e.*, $(\beta^-, \beta^+) = (1, 10)$. The exact solution is chosen the same as we used in Example 4.1. Errors in L^∞, L^2, and semi-H^1 norms are listed in Table 4.13.

Data in Table 4.13 suggest that Galerkin IFE solutions cannot achieve optimal rates of convergence in L^∞ norm. For L^2, and semi-H^1 norms, optimal convergence rates are observed up to mesh size $h = 2/320$ and these rates deteriorate as we keep refining the mesh. These observation indicates that the Galerkin IFE scheme may have difficulty in retaining the optimal convergence rates in L^2, and semi-H^1 norms when the mesh size is sufficient small.

Comparing data in Table 4.13 with those in Table 4.7 through Table 4.9, we can observe that adding penalty terms over interface edges leads to prominent improvement of the numerical accuracy in the sense that convergence rates are closer to optimal and numerical errors are significantly reduced. A more illustrative comparison between Galerkin IFE solution errors and NPPG IFE solution errors can be found in Figure 4.1. We observe that errors in NPPG

Table 4.13: Errors of Galerkin IFE solutions $u - u_h^P$ with $\beta^- = 1$, $\beta^+ = 10$.

N	$\|\cdot\|_{0,\infty,\Omega}$	rate	$\|\cdot\|_{0,\Omega}$	rate	$\|\cdot\|_{1,\Omega}$	rate
10	$3.0783E{-}2$		$7.8310E{-}3$		$1.9616E{-}1$	
20	$8.6352E{-}3$	1.8338	$2.0989E{-}3$	1.8995	$9.9802E{-}2$	0.9749
40	$2.2891E{-}3$	1.9155	$5.1366E{-}4$	2.0308	$5.0359E{-}2$	0.9868
80	$7.7107E{-}4$	1.5698	$1.2297E{-}4$	2.0626	$2.5424E{-}2$	0.9860
160	$6.9062E{-}4$	0.1590	$3.0853E{-}5$	1.9948	$1.3174E{-}2$	0.9485
320	$2.8466E{-}4$	1.2787	$7.5130E{-}6$	2.0379	$6.5827E{-}3$	1.0009
640	$1.4840E{-}4$	0.9398	$3.4099E{-}6$	1.3006	$3.4749E{-}3$	0.9217
1280	$1.0162E{-}4$	0.5463	$1.6648E{-}6$	0.8734	$1.9224E{-}3$	0.8541

IFE scheme illustrated by green dash line, are smaller than errors in Galerkin IFE scheme illustrated by red solid line when mesh size is small enough. Consequently, the convergence rates are elevated for NPPG IFE scheme due to the decrease of errors.

Figure 4.1: Comparison of errors in different nonconforming rotated Q_1 IFE methods with $\beta^- = 1$, $\beta^+ = 10$.

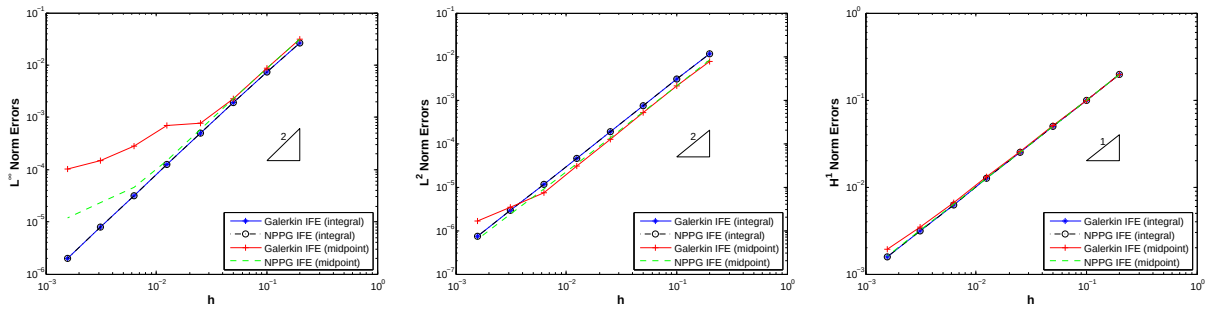

We also compare the point-wise error $e_h^P(X) = |u_h^P(X) - u(X)|$ of the Galerkin IFE scheme and NPPG IFE scheme on the same mesh containing 160×160 elements. Error functions e_h^P of these two schemes are plotted in Figure 4.2. These figures are generated by plotting the maximum error on each element. It can be observed from the left plot that the point-wise accuracy of the Galerkin IFE method is quite poor around the interface and we suspect this is because the discontinuity of IFE functions across interface could be large with different configurations of the interface location and diffusion coefficient. By penalizing the discontinuity in IFE functions, the NPPG IFE scheme can produce much better approximations around the interface as illustrated on the right plot in Figure 4.2. These observations suggest that adding penalty around interface can effectively reduce the IFE solution errors and improve the overall solution accuracy.

Figure 4.2: Point-wise error comparison of Galerkin solution and NPPG solution u_h^P.

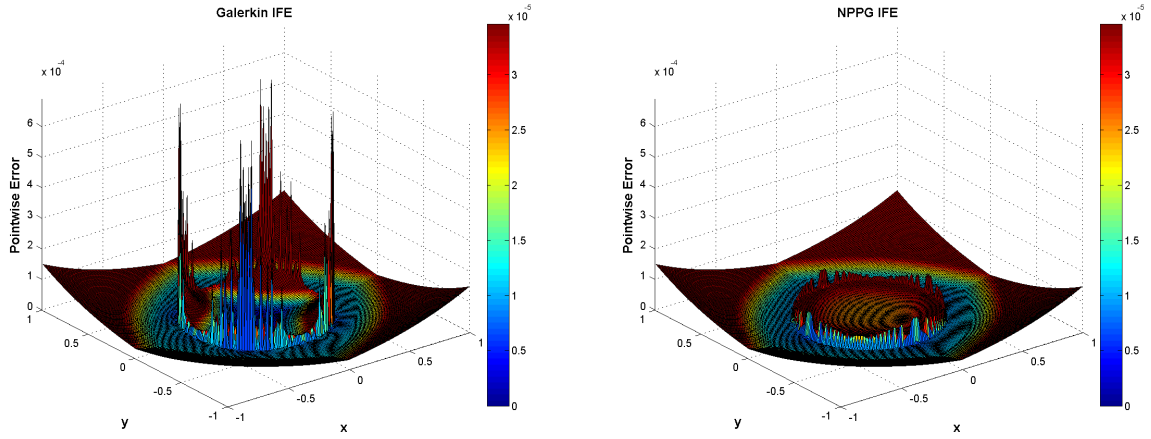

Next we use nonconforming rotated Q_1 IFE functions with integral-value degrees of freedom in the Galerkin IFE scheme. Both moderate discontinuity $(\beta^-, \beta^+) = (1, 10)$ and larger discontinuity $(\beta^-, \beta^+) = (1, 10000)$ of diffusion coefficients are considered in our experiments. For both coefficient configurations, errors in L^∞, L^2, and semi-H^1 norms are listed in Table 4.14, and Table 4.15, respectively.

Table 4.14: Errors of Galerkin IFE solutions $u - u_h^I$ with $\beta^- = 1$, $\beta^+ = 10$.

N	$\|\cdot\|_{0,\infty,\Omega}$	rate	$\|\cdot\|_{0,\Omega}$	rate	$\|\cdot\|_{1,\Omega}$	rate
10	$2.6183E{-2}$		$1.1395E{-2}$		$1.9585E{-1}$	
20	$7.3444E{-3}$	1.8339	$2.9860E{-3}$	1.9321	$9.9065E{-2}$	0.9833
40	$1.9455E{-3}$	1.9165	$7.4374E{-4}$	2.0054	$4.9894E{-2}$	0.9895
80	$5.0072E{-4}$	1.9580	$1.8547E{-4}$	2.0036	$2.5026E{-2}$	0.9955
160	$1.2702E{-4}$	1.9789	$4.6313E{-5}$	2.0017	$1.2531E{-2}$	0.9979
320	$3.1989E{-5}$	1.9894	$1.1671E{-5}$	1.9885	$6.2702E{-3}$	0.9990
640	$8.0267E{-6}$	1.9947	$2.9122E{-6}$	2.0027	$3.1363E{-3}$	0.9995
1280	$2.0101E{-6}$	1.9975	$7.2684E{-7}$	2.0024	$1.5684E{-3}$	0.9997

According to data in Table 4.14 and 4.15, optimal convergence rates are observed in L^∞, L^2, and semi-H^1 norms for Galerkin IFE solutions with integral-value degrees of freedom. Comparing the data in Table 4.14 with data in Table 4.1 through Table 4.3 for the example with moderate jump, we do not see major differences between Galerkin IFE solutions and PPG IFE solutions. Similar phenomenon can be observed for example with larger coefficient jump by comparing data in Table 4.15 with data in Tables 4.4 through 4.6. A more illustrative

Table 4.15: Errors of Galerkin IFE solutions $u - u_h^I$ with $\beta^- = 1$, $\beta^+ = 10000$.

N	$\|\cdot\|_{0,\infty,\Omega}$	rate	$\|\cdot\|_{0,\Omega}$	rate	$\|\cdot\|_{1,\Omega}$	rate
10	$5.9646E{-3}$		$2.7360E{-3}$		$4.0678E{-2}$	
20	$2.5455E{-3}$	1.2285	$1.0526E{-3}$	1.3782	$2.7824E{-2}$	0.5479
40	$7.1692E{-4}$	1.8281	$2.5767E{-4}$	2.0303	$1.4700E{-2}$	0.9205
80	$2.1533E{-4}$	1.7353	$6.3614E{-5}$	2.0181	$7.5491E{-3}$	0.9614
160	$5.9653E{-5}$	1.8519	$1.5531E{-5}$	2.0342	$3.7978E{-3}$	0.9911
320	$1.5521E{-5}$	1.9423	$4.0823E{-6}$	1.9277	$1.9146E{-3}$	0.9881
640	$4.1575E{-6}$	1.9005	$1.0069E{-6}$	2.0194	$9.5881E{-4}$	0.9977
1280	$1.0588E{-6}$	1.9733	$2.4921E{-7}$	2.0145	$4.8004E{-4}$	0.9981

comparison of these two schemes can be found in Figure 4.1 in which the plots of errors in Galerkin IFE scheme illustrated by blue solid line and errors in NPPG IFE scheme illustrated by black dash line almost coincide.

We also compare the point-wise error $e_h^I(X) = |u_h^I(X) - u(X)|$ in Galerkin IFE scheme and NPPG IFE scheme in Figure 4.3. It can be observed that these two plots are very similar. In both of these plots, point-wise errors around interface are comparable to errors far away from the interface. All of these comparisons indicate an interesting and also important feature, that is, for nonconforming rotated Q_1 IFE functions with integral-value degrees of freedom, the penalty terms in the PPG IFE schemes enable us to derive optimal error bounds, but they seem to be unnecessary for actual computation. How to theoretically prove that the Galerkin IFE scheme with nonconforming rotated Q_1 IFE functions using integral-value degrees of freedom does converge optimally is an interesting future research topic.

Example 4.5. ***(Comparison with Bilinear IFE Methods)****: In this example, we compare the numerical performances of nonconforming rotated Q_1 IFE methods with bilinear IFE methods [69].*

Bilinear IFE spaces are defined on Cartesian meshes [70, 98]; hence it is natural to compare bilinear IFE methods with nonconforming rotated Q_1 IFE methods using the same meshes. First we solve the elliptic interface problem whose exact solution is given in (3.82) using Galerkin scheme with bilinear IFE functions. Related numerical errors are listed in Table 4.16. Data in this table indicate that errors in bilinear Galerkin IFE methods have a suboptimal convergence rate in L^∞ norm. Also, the convergence rates in L^2 and semi-H^1 norms seem to be optimal for a moderately small mesh size. As we continue refining meshes, the rates of convergence in L^2 and semi-H^1 norms tend to degenerate. Note that we observe similar phenomenons in Galerkin IFE solutions using nonconforming rotated Q_1 IFE functions with midpoint-value degrees of freedom as listed in Table 4.13.

We solve the elliptic interface problem again using PPG schemes with bilinear IFE functions.

Figure 4.3: Point-wise error comparison of Galerkin solution and NPPG solution u_h^I.

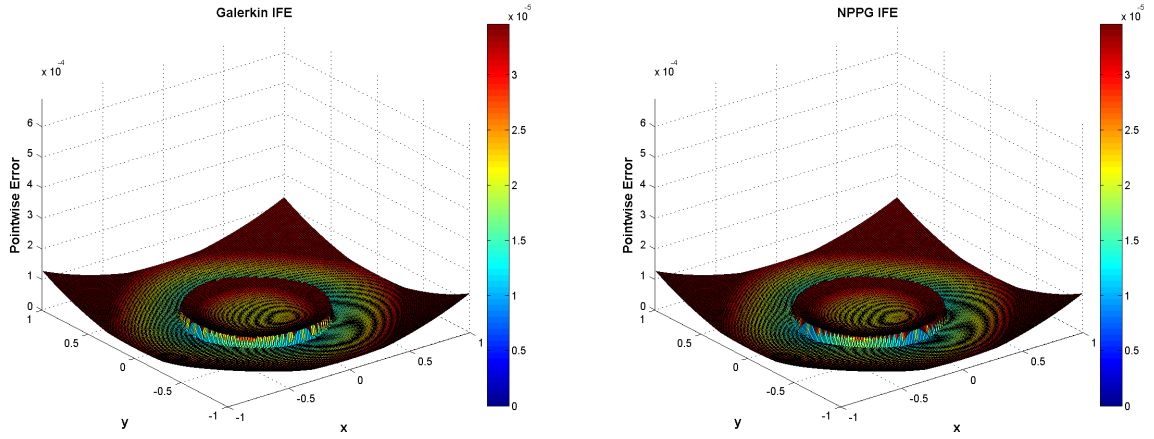

Errors in nonsymmetric, symmetric, and incomplete PPG schemes are listed in Table 4.17, Table 4.18, Table 4.19, respectively. We observe that all these PPG IFE solutions can achieve optimal convergence rates in L^∞, L^2, and semi-H^1 norms. These observations reaffirm the importance of penalizing discontinuities at interface edges for bilinear IFE solutions.

Table 4.16: Errors of bilinear Galerkin IFE solutions $u - u_h$ with $\beta^- = 1$, $\beta^+ = 10$.

N	$\|\cdot\|_{0,\infty,\Omega}$	rate	$\|\cdot\|_{0,\Omega}$	rate	$\|\cdot\|_{1,\Omega}$	rate
10	$3.3373E{-}3$		$1.6456E{-}2$		$1.2706E{-}1$	
20	$1.0969E{-}3$	1.6052	$4.3003E{-}3$	1.9361	$6.4758E{-}2$	0.9724
40	$5.4748E{-}4$	1.0026	$1.0622E{-}3$	2.0174	$3.2779E{-}2$	0.9823
80	$5.0812E{-}4$	0.1077	$2.6196E{-}4$	2.0196	$1.6596E{-}2$	0.9723
160	$2.2635E{-}4$	1.1667	$6.4952E{-}5$	2.0119	$8.4072E{-}3$	0.9811
320	$1.2290E{-}4$	0.8811	$1.6311E{-}5$	1.9935	$4.2566E{-}3$	0.9819
640	$7.0810E{-}5$	0.7954	$4.4482E{-}6$	1.8746	$2.2267E{-}3$	0.9348
1280	$3.4111E{-}5$	1.0537	$1.4445E{-}6$	1.6226	$1.1795E{-}3$	0.9167

In Figure 4.4, we compare point-wise error $e_h(X) = |u_h(X) - u(X)|$ in Galerkin IFE solution and NPPG IFE solution using bilinear IFE functions. These plots are generated by plotting the maximum error on each element in the mesh containing 160×160 elements. We observe that the error in IFE solution produced by the Galerkin scheme is much larger around the interface than other places. This might be caused by the discontinuities of IFE functions on interface edges, which can be quite large, if, for instance, the jump ratio in the coefficient is large. On the other hand, we see from the plot on the right in Figure 4.4 that the IFE

Table 4.17: Errors of bilinear NPPG IFE solutions $u - u_h$ with $\beta^- = 1$, $\beta^+ = 10$.

N	$\|\cdot\|_{0,\infty,\Omega}$	rate	$\|\cdot\|_{0,\Omega}$	rate	$\|\cdot\|_{1,\Omega}$	rate
10	$2.5705E{-3}$		$1.6384E{-2}$		$1.2672E{-1}$	
20	$1.0082E{-3}$	1.3503	$4.2869E{-3}$	1.9343	$6.4719E{-2}$	0.9694
40	$1.9172E{-4}$	2.3947	$1.0626E{-3}$	2.0124	$3.2637E{-2}$	0.9877
80	$5.4491E{-5}$	1.8149	$2.6440E{-4}$	2.0067	$1.6382E{-2}$	0.9944
160	$1.4045E{-5}$	1.9559	$6.5876E{-5}$	2.0049	$8.2063E{-3}$	0.9973
320	$3.5092E{-6}$	2.0009	$1.6594E{-5}$	1.9891	$4.1068E{-3}$	0.9987
640	$9.1942E{-7}$	1.9324	$4.1383E{-6}$	2.0035	$2.0544E{-3}$	0.9994
1280	$2.2932E{-7}$	2.0034	$1.0336E{-6}$	2.0014	$1.0274E{-3}$	0.9996

Table 4.18: Errors of bilinear SPPG IFE solutions $u - u_h$ with $\beta^- = 1$, $\beta^+ = 10$.

N	$\|\cdot\|_{0,\infty,\Omega}$	rate	$\|\cdot\|_{0,\Omega}$	rate	$\|\cdot\|_{1,\Omega}$	rate
10	$5.5595E{-3}$		$1.6702E{-2}$		$1.2703E{-1}$	
20	$1.3680E{-3}$	2.0229	$4.2945E{-3}$	1.9595	$6.4751E{-2}$	0.9722
40	$3.9775E{-4}$	1.7822	$1.0749E{-3}$	1.9983	$3.2650E{-2}$	0.9878
80	$1.0601E{-4}$	1.9077	$2.6883E{-4}$	2.0021	$1.6386E{-2}$	0.9947
160	$3.1598E{-5}$	1.7463	$6.7047E{-5}$	2.0008	$8.2081E{-3}$	0.9974
320	$7.0324E{-6}$	2.1677	$1.6829E{-5}$	1.9942	$4.1071E{-3}$	0.9988
640	$1.9288E{-6}$	1.8664	$4.2038E{-6}$	2.0012	$2.0544E{-3}$	0.9994
1280	$5.0505E{-7}$	1.9332	$1.0501E{-6}$	2.0012	$1.0274E{-3}$	0.9997

Table 4.19: Errors of bilinear IPPG IFE solutions $u - u_h$ with $\beta^- = 1$, $\beta^+ = 10$.

N	$\|\cdot\|_{0,\infty,\Omega}$	rate	$\|\cdot\|_{0,\Omega}$	rate	$\|\cdot\|_{1,\Omega}$	rate
10	$5.4440E{-2}$		$1.6660E{-2}$		$1.2709E{-1}$	
20	$1.3785E{-3}$	1.9816	$4.2989E{-3}$	1.9543	$6.4753E{-2}$	0.9728
40	$3.9769E{-4}$	1.7934	$1.0745E{-3}$	2.0003	$3.2651E{-2}$	0.9878
80	$1.0582E{-4}$	1.9100	$2.6797E{-4}$	2.0036	$1.6386E{-2}$	0.9947
160	$3.1217E{-5}$	1.7612	$6.6872E{-5}$	2.0026	$8.2082E{-3}$	0.9973
320	$6.9364E{-6}$	2.1701	$1.6794E{-5}$	1.9935	$4.1071E{-3}$	0.9989
640	$1.9213E{-6}$	1.8521	$4.1934E{-6}$	2.0017	$2.0545E{-3}$	0.9994
1280	$4.9869E{-7}$	1.9459	$1.0472E{-6}$	2.0015	$1.0274E{-3}$	0.9997

solution generated by NPPG scheme is significantly more accurate around the interface which demonstrates again the effectiveness of the penalty terms introduced on interface edges.

Figure 4.4: Point-wise error comparison of bilinear Galerkin IFE solution and NPPG IFE solution u_h.

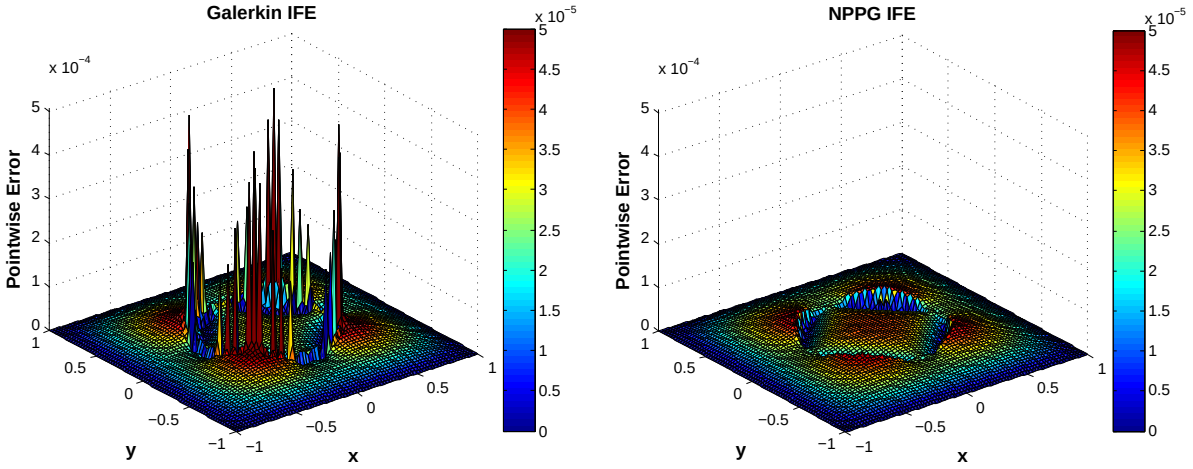

In Figure 4.5, we provide a comparison of Galerkin IFE schemes using bilinear IFE functions and nonconforming rotated Q_1 functions with both integral-value and midpoint-value degrees of freedom. Gauged in L^∞ norm, the nonconforming rotated Q_1 Galerkin IFE method with integral-value degrees of freedom seem to be the most reliable one among these three methods, because its convergence rate seems to retain optimal $O(h^2)$ and the error produced by this method is much smaller than the other two IFE methods when h is sufficiently small. In L^2 norm, the numerical solutions produced by bilinear IFE and nonconforming rotated Q_1 IFE methods with midpoint-value degrees of freedom seem to converge optimally over meshes with moderately small mesh size. However, their convergence rates in L^2 norm seem to deteriorate on finer meshes. On the other hand, the Galerkin IFE method with nonconforming rotated Q_1 IFE functions with integral-value degrees of freedom behave more stable and its optimal convergence rate is observed. In semi-H^1 norm, we have the similar observation.

A comparison of NPPG IFE schemes using these three types of IFE functions is given in Figure 4.6. In L^∞ norm, the convergence rates of NPPG schemes using nonconforming rotated Q_1 functions with integral-value degrees of freedom and the bilinear IFE functions seem to retain optimal rate $O(h^2)$. By comparing the magnitudes of errors, we observe that bilinear IFE methods generate more accurate numerical solutions than nonconforming rotated Q_1 IFE methods in this example. In L^2 and semi-H^1 norms, the performance of these methods are quite similar. Optimal convergence is observed in NPPG IFE schemes using each of these three IFE functions.

Now let us take a closer look at these IFE functions. We compare the discontinuity in global basis functions for these IFE spaces in Figure 4.7. In this figure, each column contains plots

Figure 4.5: Comparison of errors in different Galerkin IFE methods.

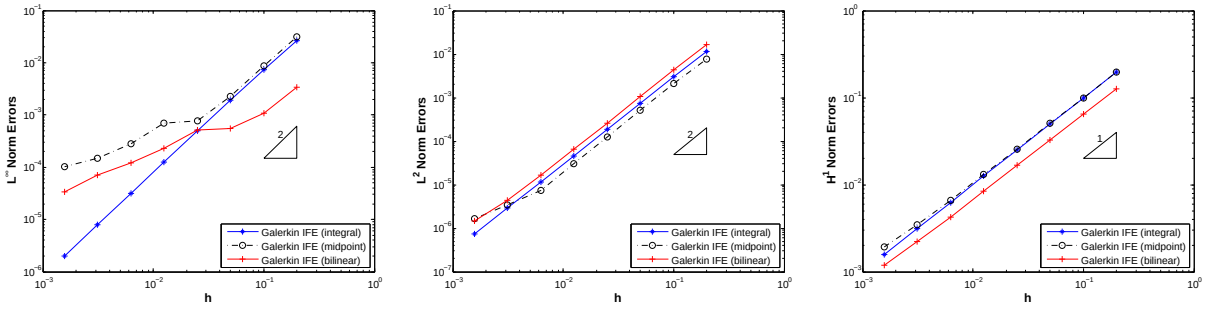

Figure 4.6: Comparison of errors in different NPPG IFE methods.

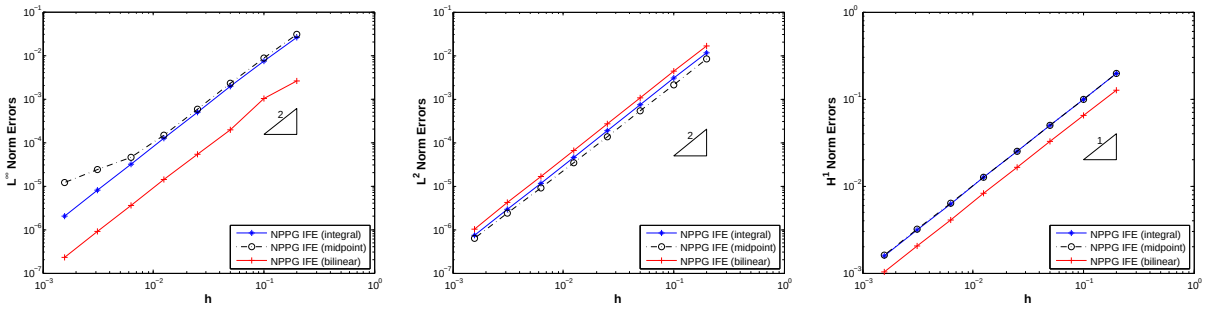

of global basis functions in these three IFE spaces corresponding to one configuration of diffusion coefficient. In each configuration, β^- is 1, but β^+ is 1, 5, 1000, respectively. Plots in the first row represent half of bilinear IFE global basis. In the second and third rows, plots represent nonconforming rotated Q_1 global basis with midpoint-value and integral-value degrees of freedom, respectively. Since these IFE basis functions have discontinuities on interface edges, we plot the difference of global IFE functions on the common interface edge in the fourth row.

Plots in the first column represent the IFE global basis functions when coefficient has no discontinuity *i.e.*, $\beta^- = \beta^+ = 1$. As a matter of fact, these global IFE bases become standard finite element global basis functions because of the consistency of IFE and FE functions stated in Theorem 3.1. Consequently, in the plot at the bottom of this column, the differences of these global FE basis functions on the common interface edge are completely zero.

Plots in the second column demonstrate the discontinuity of IFE global basis functions with a moderate coefficient discontinuity ($\beta^- = 1,\ \beta^+ = 5$). Note that all the three global IFE basis functions have discontinuity across the interface edge. In the plot at the bottom of this

Figure 4.7: Comparison of discontinuity for different IFE global basis functions with fixed value $\beta^- = 1$ and different values of $\beta^+ = 1, 5, 1000$.

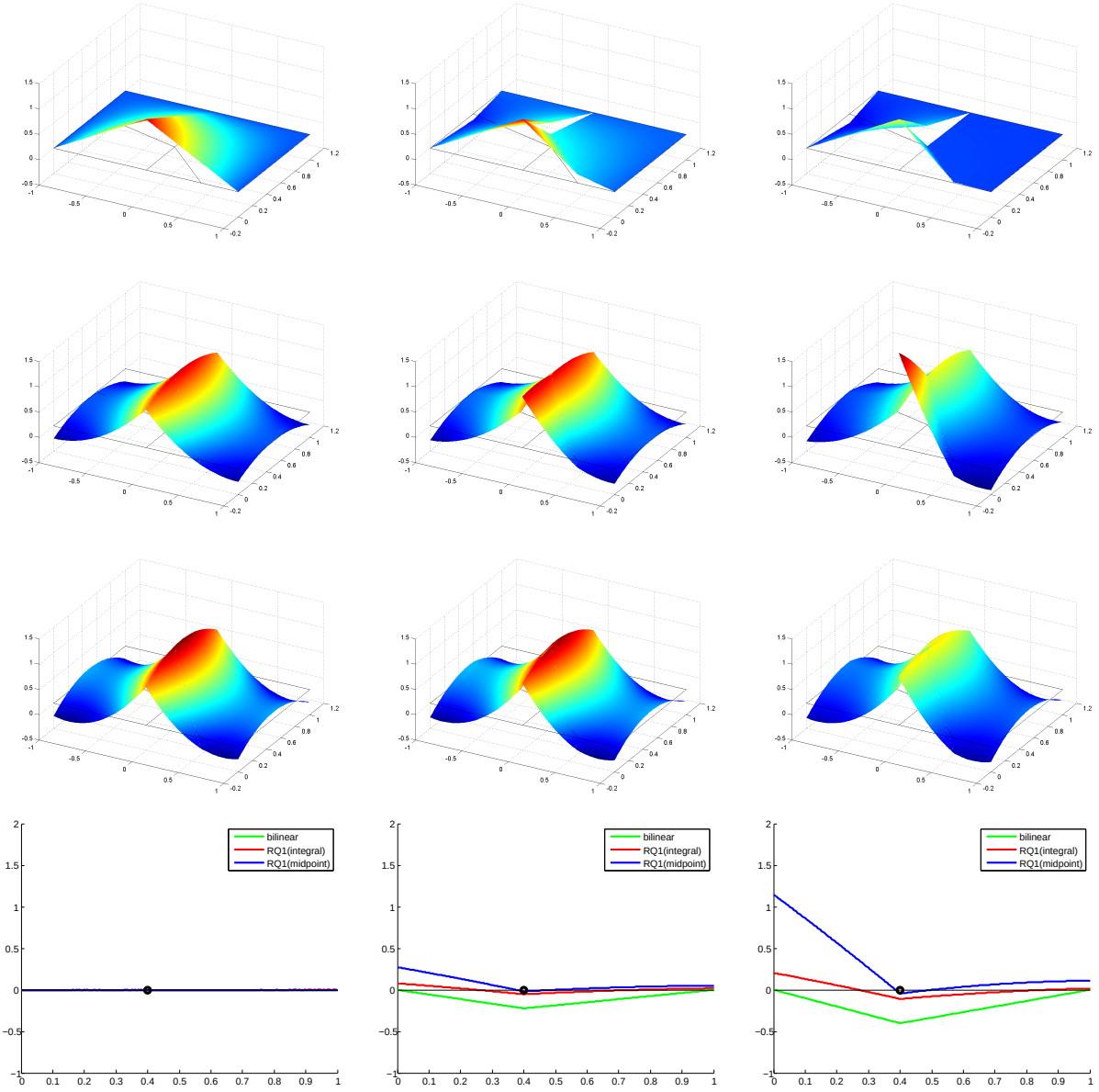

column, the blue line represents the jump of the nonconforming rotated Q_1 global IFE basis with midpoint-value degrees of freedom, which has the value of zero (no discontinuity) at the midpoint. The green line associates to the bilinear global IFE basis, which vanishes at two endpoints on the interface edge due to the continuity imposed at vertices. The red line shows the jump of the nonconforming rotated Q_1 global IFE basis with integral-value degrees of

freedom in which the average integral value of the jump is zero. By direct comparison, we observe that the nonconforming rotated Q_1 global IFE basis with the integral-value degrees of freedom has smaller discontinuity over the interface edge than the other two types of IFE bases.

Plots in the third column demonstrate the discontinuity of IFE global basis functions with a large coefficient discontinuity ($\beta^- = 1,\ \beta^+ = 1000$). Note that the discontinuity of each IFE global basis on the interface edge is larger than those with a moderate coefficient discontinuity in the second column. Observing from the plot at the bottom of this column, the discontinuity of the nonconforming rotated Q_1 global IFE basis with integral-value degrees of freedom is much smaller compared to the other two global IFE bases. We also note that even though the discontinuity in the coefficient increases greatly from the ratio of 5 to 1000, the discontinuity of the nonconforming rotated Q_1 global IFE basis with integral-value degrees of freedom does not increase dramatically as the other two IFE bases.

The comparison of the global IFE basis functions indicates that the nonconforming rotated Q_1 IFE functions with integral-value degrees of freedom usually have smaller discontinuity than bilinear IFE functions and the nonconforming rotated Q_1 IFE functions with midpoint-value degrees of freedom. We believe the reason for this phenomenon is the that the integral-value degrees of freedom impose the continuity over the whole interface edge in a "global" sense compared with the point-wise continuity "locally" imposed on the interface edge for the other two types of IFE functions. In other words, the discontinuity in a nonconforming rotated Q_1 IFE function with integral-value degrees of freedom is less prominent across an interface edge because the discontinuity is scattered throughout the interface edge which leads to a less impact. Less discontinuity on interface edges is possibly the reason why the partial penalization is unnecessary for nonconforming rotated Q_1 IFE functions with integral-value degrees of freedom.

Chapter 5

Nonconforming IFE Methods for Elasticity Interface Problems

So far we have considered the application of nonconforming IFE methods to interface problems of scalar second order elliptic equations. In this chapter, we discuss the extension of nonconforming IFE methods for solving interface problems involving a system of PDEs. In particular, we plan to develop vector-valued nonconforming rotated Q_1 IFE functions for solving planar elasticity interface problems in solid mechanics.

Finite element methods have been widely employed to calculate deformation and stress of elastic bodies subject to loads [25, 37, 45, 157]. If we model an object that consists of multiple elasticity materials separated by a definite interface, the material parameters in elasticity equilibrium equations are usually discontinuous. This leads to the elasticity interface problems.

This chapter is organized as follows. In Section 5.1, we describe the elasticity interface model problems and review existing numerical methods for these elasticity interface problems. In Section 5.2, we introduce vector-valued nonconforming rotated Q_1 IFE spaces based on the integral-value degrees of freedom for the planar elasticity interface problems. Then we investigate fundamental properties of these new IFE spaces. In Section 5.3, we provide numerical experiments to demonstrate that nonconforming rotated Q_1 Galerkin IFE methods can solve the elasticity interface problem effectively. In particular, the methods can circumvent "locking" effect when the elastic material is nearly incompressible. Some of the materials in this chapter have been reported in articles [105, 108].

5.1 Introduction

We consider the following planar elasticity pure displacement boundary value problem:

$$-\nabla \cdot \sigma(\mathbf{u}) = \mathbf{f} \quad \text{in} \quad \Omega, \tag{5.1}$$

$$\mathbf{u} = \mathbf{g} \quad \text{on} \quad \partial\Omega. \tag{5.2}$$

Without loss of generality, the solution domain $\Omega \subset \mathbb{R}^2$ is assumed to be a rectangle (or a union of several rectangles) formed with two types of elastic materials separated by an interface Γ which is assumed to be a smooth curve. That means the domain Ω is the union of two disjoint sub-domains Ω^- and Ω^+, each formed by one of the materials, such that $\overline{\Omega} = \overline{\Omega^- \cup \Omega^+ \cup \Gamma}$, as illustrated in Figure 5.1. Across the material interface Γ, the displacement and traction are assumed to be continuous, *i.e.*,

$$[\mathbf{u})]_\Gamma = \mathbf{0}, \tag{5.3}$$

$$\big[\sigma(\mathbf{u})\ \mathbf{n}\big]_\Gamma = \mathbf{0}. \tag{5.4}$$

Figure 5.1: The domain of planar elasticity interface problems.

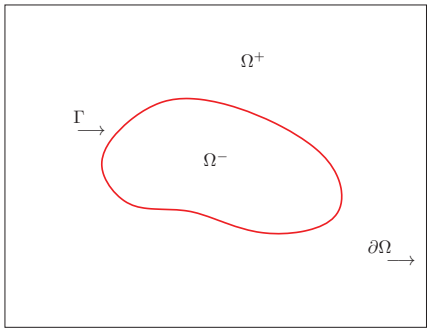

Here, we use letters in bold font to denote vector-valued functions and their associated function spaces. The function $\mathbf{u}(\mathbf{x}) = (u_1(x,y), u_2(x,y))^t$ denotes the displacement vector at a point $\mathbf{x} = (x,y)$ in the elastic body Ω. The function $\mathbf{f} = (f_1, f_2)^t$ represents the given body force and $\mathbf{g} = (g_1, g_2)^t$ is the given displacement on the boundary $\partial\Omega$. The vector $\mathbf{n}$ denotes the outward normal of Γ. Also, we use the matrix function $\epsilon(\mathbf{u})) = (\epsilon_{ij}(\mathbf{u})))_{1\le i,j\le 2}$ to denote the linearized strain tensor

$$\epsilon_{ij}(\mathbf{u}) = \frac{1}{2}\Big(\frac{\partial u_i}{\partial x_j} + \frac{\partial u_j}{\partial x_i}\Big). \tag{5.5}$$

Let λ and μ denote the Lamé parameters given by

$$\lambda = \frac{E\nu}{(1+\nu)(1-2\nu)}, \quad \mu = \frac{E}{2(1+\nu)},$$

where E and ν are Young's modulus and Poisson's ratio, respectively. Then, the stress tensor $\sigma(\mathbf{u}) = (\sigma_{ij}(\mathbf{u}))_{1\leq i,j\leq 2}$ of a linear isotropic elastic material is assumed to fulfill the following linear constitutive relation:

$$\sigma_{ij}(\mathbf{u}) = \lambda(\nabla \cdot \mathbf{u})\delta_{ij} + 2\mu\epsilon_{ij}(\mathbf{u}),$$

where δ_{ij} denotes the Kronecker delta such that

$$\delta_{ij} = \begin{cases} 1 & \text{if } i = j, \\ 0 & \text{if } i \neq j. \end{cases} \tag{5.6}$$

The Lamé parameters λ, μ are assumed to be discontinuous across the interface Γ. For the sake of simplicity, we assume that they are piece-wise constants such that

$$(\lambda(\mathbf{x}), \mu(\mathbf{x})) = \begin{cases} (\lambda^-, \mu^-), & \text{if } \mathbf{x} \in \Omega^-, \\ (\lambda^+, \mu^+), & \text{if } \mathbf{x} \in \Omega^+. \end{cases} \tag{5.7}$$

Elasticity interface problems appear in many applications such as the topology optimization of solid structures which, as one of the important applications of the elasticity interface problems, has been studied both theoretically and numerically in the past decades, see [22, 23] and the reference therein. Topology optimization is to determine certain features such as size, location and shape of holes of the target domain for finding the optimal lay-out of certain structures in the prescribed domain.

In the minimum compliance design problem [22], for example, one desires to minimize the compliance of a structure to increase its stiffness. Consider a mechanic body occupying a domain which is a subset of $\Omega \subset \mathbb{R}^2$. The reference domain Ω is chosen to define the load and boundary conditions. The aim for this design is to find the optimal choice of stiffness tensor $E_{ijkl}(x, y)$, which is a variable over the domain. Define the following energy bilinear form,

$$a(\mathbf{u}, \mathbf{v}) \triangleq \int_\Omega E_{ijkl}(x, y)\epsilon_{ij}(\mathbf{u})\epsilon_{kl}(\mathbf{v})\,\mathrm{d}x\,\mathrm{d}y, \tag{5.8}$$

with the linearized strain tensor $\epsilon(\mathbf{u})$ defined in (5.5). Also define the load linear form,

$$F(\mathbf{v}) \triangleq \int_\Omega \mathbf{f} \cdot \mathbf{v}\,\mathrm{d}x\,\mathrm{d}y.$$

Then the minimum compliance problem is described as:

$$\min_{\mathbf{u}\in\mathbf{V}} F(\mathbf{u})$$

subject to:

$$a(\mathbf{u}, \mathbf{v}) = F(\mathbf{v}), \quad \forall\ \mathbf{v} \in \mathbf{V}, \tag{5.9}$$

where $\mathbf{V}$ denotes the space of kinematically admissible displacement fields.

If the elastic body is isotropic [133], *i.e.*, the stiffness tensor has no preferred direction (an applied force will give the same displacements no matter the direction in which the force is applied), then the stiffness tensor can be written as

$$E_{ijkl}(x,y) = \lambda(x,y)\delta_{ij}\delta_{kl} + \mu(x,y)(\delta_{ik}\delta_{jl} + \delta_{il}\delta_{jk}). \tag{5.10}$$

where δ_{ij} is the Kronecker delta. Therefore the bilinear energy form (5.8) becomes

$$a(\mathbf{u},\mathbf{v}) = \int_\Omega \Big(2\mu(x,y)\,\epsilon(\mathbf{u}) : \epsilon(\mathbf{v}) + \lambda(x,y)\,\mathrm{div}(\mathbf{u})\,\mathrm{div}(\mathbf{v})\Big)\mathrm{d}x\mathrm{d}y. \tag{5.11}$$

Hence the energy form (5.9) corresponds to the equilibrium equation (5.1). When multiple material phases design problems are considered, see [57, 132], the Lame parameters $\lambda(x,y)$, and $\mu(x,y)$ distribution are discontinuous, and this set-up leads to the elasticity interface problems (5.1) - (5.4). Other applications for the elasticity interface problems include problems in the crystalline materials [136], the simulation in the microstructural evolution [79, 89], and the atomic interactions [55], etc.

There are many numerical methods developed to solve elasticity interface problems. Conventional finite element methods [28, 45, 157], as one of the most popular approaches, can work satisfactorily provided that meshes are tailored to fit interfaces, known as body-fitting meshes, as illustrated in the plot on the left in Figure 1.2. The body-fitting restriction makes conventional methods excessively expensive if interfaces evolve in a simulation. It is therefore attractive to develop numerical methods based on non-body-fitting meshes, such as Cartesian meshes, as illustrated in the middle and on the right of Figure 1.2.

There have been quite a few numerical methods developed to solve elasticity interface problems based on Cartesian meshes. In finite difference formulation, Yang, Li, and Li have developed an immersed interface method for the planar linear elasticity interface problem [150, 151]. However, the linear systems arising from this method are nonsymmetric and become ill-conditioned as elastic materials become nearly incompressible, *i.e.*, $\nu \to 1/2$. In finite element formulation, Hansbo and Hansbo have proposed a bilinear finite element method which employees a Nitsche's idea and a modified weak formulation using weighted average traction across interfaces [66]. Becker, Burman, and Hansbo have extended this Nitsche finite element method for incompressible elastic materials using a mixed formulation [21]. Hou, Li, Wang, and Wang [76] have modified the traditional finite element method by designing trial functions to be a piecewise polynomial to fit jump condition across the interface while keeping the test functions independent of interface. Due to the inconsistency of trial and test function spaces, the resulting linear system in this method is nonsymmetric, although positive-definiteness can be guaranteed under certain conditions.

IFE methods also have been applied to solve the elasticity interface problems. In [62, 97], Gong, Li, and Yang have proposed a linear IFE method to solve elasticity interface problems on triangular meshes. Point-wise convergence has been investigated in their articles. Their numerical results indicated that linear IFE solutions can achieve at least an $O(h)$ convergence in L^∞ norm. Recently, Lin and Zhang have developed a bilinear IFE method [108]

based on the rectangular Cartesian meshes. This article has studied accuracy of linear and bilinear IFE methods numerically, and the authors have reported that both linear and bilinear IFE methods could converge optimally in both L^2 and H^1 norms. Nevertheless, both of these IFE methods have limitations. First, the existence of these IFE functions cannot be guaranteed for arbitrary configuration of elastic materials in an interface problem. Moreover, both of these conforming type IFE methods can only solve the elasticity interface problem satisfactorily for compressible elastic materials; once elastic materials become nearly incompressible, *i*.e., the Poisson's ratio ν of elastic material approaches 0.5, these IFE methods encounter the "*volume locking*" effect [16]. This "locking" effect arises when displacements of the elastic body are approximated by using the lowest-order conforming type finite elements even for solving non-interface problems. As we know, in either the linear or the bilinear IFE method, the majority of elements do not intersect with the material interface, where standard conforming type finite element functions are utilized; hence, the "locking" can be considered inevitable for these IFE methods.

There are many approaches developed to circumvent the "locking" effect, such as the mixed finite element methods [4, 5, 6, 30, 122, 134], the nonconforming finite element methods [29, 53, 67, 88, 113, 153], and the discontinuous Galerkin methods [46, 68, 126, 145]. In the following sections in this chapter, we follow the route of nonconforming finite element methods to eliminate the "locking" effect for elasticity interface problems. We first construct the vector-valued nonconforming rotated Q_1 IFE functions with integral-value degrees of freedom for elasticity interface problems, and then use these IFE functions in displacement Galerkin formulation to solve the elasticity interface problems.

5.2 Vector-Valued Nonconforming IFE Spaces

In this section, we introduce the vector-valued nonconforming rotated Q_1 IFE functions with integral-value degrees of freedom for elasticity interface problems. Note that for planar elasticity problem, the displacement $\mathbf{u}$ of an elastic body has two components $\mathbf{u} = (u_1, u_2)^t$; hence, each finite element basis is a vector-valued polynomial function which contains two components. Similar to the elliptic interface problem, standard vector-valued nonconforming rotated Q_1 finite element functions are utilized on non-interface elements, and IFE functions are constructed only on interface elements with appropriately interpreted interface jump conditions. In our following discussion, we consider the integral-value degrees of freedom only, since nonconforming rotated Q_1 finite element functions with integral-value degrees of freedom perform better and have more desirable features than the midpoint-value degrees of freedom in the elliptic interface problem as shown in Section 4.3. Consequently, we omit superscript I on FE/IFE functions and corresponding spaces.

5.2.1 Nonconforming IFE functions

On each non-interface element $T \in \mathcal{T}_h^n$, we define the vector-valued nonconforming rotated Q_1 finite element space $\mathbf{S}_h^n(T)$ as follows:

$$\mathbf{S}_h^n(T) = \left\{ \mathbf{\Psi}_T = (\Psi_{1,T}, \Psi_{2,T})^t : \Psi_{j,T} \in S_h^n(T),\, j = 1, 2 \right\}, \tag{5.12}$$

where $S_h^n(T) = \text{Span}\{1, x, y, x^2 - y^2\}$ is the standard local rotated Q_1 finite element space as introduced in Section 2.2. There are eight local basis functions $\mathbf{\Psi}_{j,T} \in \mathbf{S}_h^n(T)$, $j = 1, \cdots, 8$, on each non-interface element $T \in \mathcal{T}_h^n$, which are chosen to satisfy the following average integral-value restrictions:

$$\frac{1}{|b_i|} \int_{b_i} \mathbf{\Psi}_{j,T}(x, y)\, \mathrm{d}s = \begin{pmatrix} \delta_{ij} \\ 0 \end{pmatrix}, \; j = 1, 2, 3, 4, \tag{5.13}$$

and

$$\frac{1}{|b_i|} \int_{b_i} \mathbf{\Psi}_{j,T}(x, y)\, \mathrm{d}s = \begin{pmatrix} 0 \\ \delta_{i,j-4} \end{pmatrix}, \; j = 5, 6, 7, 8, \tag{5.14}$$

where b_i, $i = 1, 2, 3, 4$ are four edges of T, as illustrated in Figure 2.1. Then the vector-valued nonconforming rotated Q_1 local FE space $\mathbf{S}_h^n(T)$ on a non-interface element T, as defined in (5.12), can be also written as follows

$$\mathbf{S}_h^n(T) = \text{Span}\left\{ \mathbf{\Psi}_{j,T} : j = 1, \cdots, 8 \right\}. \tag{5.15}$$

On an interface element $T \in \mathcal{T}_h^i$, we assume that the interface curve Γ intersects the boundary of T at points D and E. Similar to the discussion in Section 2.4, we classify interface elements in two types: if D and E locate at two adjacent edges, we classify this element as Type I interface element; if D and E locate at two opposite edges, we classify this element as Type II interface element. Figure 2.6 provides illustrations for these two types of interface elements. The line segment $\overline{DE}$ separates T into two sub-elements T^- and T^+.

Without loss of generality, we consider a typical interface element $T = \square A_1A_2A_3A_4$ with vertices

$$A_1 = \begin{pmatrix} 0 \\ 0 \end{pmatrix}, \quad A_2 = \begin{pmatrix} h \\ 0 \end{pmatrix}, \quad A_3 = \begin{pmatrix} 0 \\ h \end{pmatrix}, \quad A_4 = \begin{pmatrix} h \\ h \end{pmatrix}. \tag{5.16}$$

We label the four edges b_i, $i = 1, 2, 3, 4$, of T as follows:

$$b_1 = \overline{A_1A_2}, \quad b_2 = \overline{A_2A_4}, \quad b_3 = \overline{A_4A_3}, \quad b_4 = \overline{A_3A_1}. \tag{5.17}$$

We also assume that

$$D = \begin{pmatrix} dh \\ 0 \end{pmatrix}, \quad E = \begin{pmatrix} 0 \\ eh \end{pmatrix}$$

for a Type I interface element, where $0 < d \leq 1$, $0 < e \leq 1$, and

$$D = \begin{pmatrix} dh \\ 0 \end{pmatrix}, \quad E = \begin{pmatrix} eh \\ h \end{pmatrix}$$

for a Type II interface element, where $0 < d < 1$ and $0 < e < 1$. Note that every interface element can be mapped into one of the above interface elements via an orthogonal affine mapping.

On each interface element $T \in \mathcal{T}_h^i$, we use piecewise vector-valued polynomials to construct nonconforming local IFE functions. Specifically, on an interface element T, a vector-valued IFE function $\mathbf{\Phi}_T$ is piece-wisely defined as follows:

$$\mathbf{\Phi}_T(\mathbf{x}) = \begin{cases} \mathbf{\Phi}_T^-(\mathbf{x}) = \begin{pmatrix} \phi_{1,T}^-(x,y) \\ \phi_{2,T}^-(x,y) \end{pmatrix} = \begin{pmatrix} a_1^- + b_1^- x + c_1^- y + d_1^-(x^2-y^2) \\ a_2^- + b_2^- x + c_2^- y + d_2^-(x^2-y^2) \end{pmatrix} & \text{in } T^-, \\ \mathbf{\Phi}_T^+(\mathbf{x}) = \begin{pmatrix} \phi_{1,T}^+(x,y) \\ \phi_{2,T}^+(x,y) \end{pmatrix} = \begin{pmatrix} a_1^+ + b_1^+ x + c_1^+ y + d_1^+(x^2-y^2) \\ a_2^+ + b_2^+ x + c_2^+ y + d_2^+(x^2-y^2) \end{pmatrix} & \text{in } T^+. \end{cases} \tag{5.18}$$

Note that for every local IFE function $\mathbf{\Phi}_T$ defined in (5.18), there are 16 coefficients, *i.e.*, $a_j^s, b_j^s, c_j^s, d_j^s$, where $j = 1, 2$, and $s = +, -$. These coefficients are determined by average integral-value of $\mathbf{\Phi}_T$ on edges together with the interface jump conditions described as follows:

- *Average integral values v_i, $i = 1, \cdots, 8$, over the edges*:

$$\frac{1}{|b_i|}\int_{b_i} \mathbf{\Phi}_T(\mathbf{x})\,\mathrm{d}s = \begin{pmatrix} v_i \\ v_{i+4} \end{pmatrix}, \quad \forall\ i = 1, 2, 3, 4. \tag{5.19}$$

  These integral values provide eight restrictions.

- *Displacement continuity at the intersection points D* and *E*:

$$\mathbf{\Phi}_T^+(D) = \mathbf{\Phi}_T^-(D), \qquad \mathbf{\Phi}_T^+(E) = \mathbf{\Phi}_T^-(E). \tag{5.20}$$

  These equations provide four restrictions.

- *Traction continuity*:

$$\int_{\overline{DE}} \sigma(\mathbf{\Phi}_T^+)\,\mathbf{n}_{\overline{DE}}\,\mathrm{d}s = \int_{\overline{DE}} \sigma(\mathbf{\Phi}_T^-)\,\mathbf{n}_{\overline{DE}}\,\mathrm{d}s. \tag{5.21}$$

  This equation provides two restrictions.

- *Second derivative continuity*:

$$\frac{\partial^2 \mathbf{\Phi}_T^+}{\partial x^2} = \frac{\partial^2 \mathbf{\Phi}_T^-}{\partial x^2}. \tag{5.22}$$

  This equation provides two restrictions.

Overall we have sixteen restrictions matching the number of undetermined coefficients in (5.18). We will show that these conditions (5.19) - (5.22) are linearly independent so that

they can uniquely determine a vector-valued nonconforming rotated Q_1 IFE function $\mathbf{\Phi}_T$ on an interface element T.

Combining the conditions in (5.19)-(5.22) leads to the following algebraic system to determine $a_j^s, b_j^s, c_j^s, d_j^s$, $j = 1, 2$, $s = +, -$:

$$M_C \mathbf{C} = \mathbf{V}, \tag{5.23}$$

where

$$\mathbf{C} = \left(a_1^-, a_1^+, a_2^-, a_2^+, b_1^-, b_1^+, b_2^-, b_2^+, c_1^-, c_1^+, c_2^-, c_2^+, d_1^-, d_1^+, d_2^-, d_2^+\right)^t,$$
$$\mathbf{V} = (v_1, v_2, v_3, v_4, v_5, v_6, v_7, v_8, 0, 0, 0, 0, 0, 0, 0, 0)^t. \tag{5.24}$$

For a Type I interface element, the coefficient matrix $M_C = M_C^I = (m_{i,j}^I)_{16\times 16}$ with the normalization $h = 1$, has the following form:

$$M_C = M_C^I = \tag{5.25}$$

$$\begin{pmatrix}
d & 1-d & 0 & 0 & \frac{d^2}{2} & \frac{1-d^2}{2} & 0 & 0 & 0 & 0 & 0 & 0 & \frac{d^3}{3} & \frac{1-d^3}{3} & 0 & 0 \\
0 & 1 & 0 & 0 & 0 & 1 & 0 & 0 & 0 & \frac{1}{2} & 0 & 0 & 0 & \frac{2}{3} & 0 & 0 \\
0 & 1 & 0 & 0 & 0 & \frac{1}{2} & 0 & 0 & 0 & 1 & 0 & 0 & 0 & -\frac{2}{3} & 0 & 0 \\
e & 1-e & 0 & 0 & 0 & 0 & 0 & 0 & \frac{e^2}{2} & \frac{1-e^2}{2} & 0 & 0 & -\frac{e^3}{3} & \frac{e^3-1}{3} & 0 & 0 \\
0 & 0 & d & 1-d & 0 & 0 & \frac{d^2}{2} & \frac{1-d^2}{2} & 0 & 0 & 0 & 0 & 0 & 0 & \frac{d^3}{3} & \frac{1-d^3}{3} \\
0 & 0 & 0 & 1 & 0 & 0 & 0 & 1 & 0 & 0 & 0 & \frac{1}{2} & 0 & 0 & 0 & \frac{2}{3} \\
0 & 0 & 0 & 1 & 0 & 0 & 0 & \frac{1}{2} & 0 & 0 & 0 & 1 & 0 & 0 & 0 & -\frac{2}{3} \\
0 & 0 & e & 1-e & 0 & 0 & 0 & 0 & 0 & 0 & \frac{e^2}{2} & \frac{1-e^2}{2} & 0 & 0 & -\frac{e^3}{3} & \frac{e^3-1}{3} \\
1 & -1 & 0 & 0 & d & -d & 0 & 0 & 0 & 0 & 0 & d^2 & -d^2 & 0 & 0 & \\
0 & 0 & 1 & -1 & 0 & 0 & d & -d & 0 & 0 & 0 & 0 & 0 & d^2 & -d^2 & \\
1 & -1 & 0 & 0 & 0 & 0 & 0 & 0 & e & -e & 0 & 0 & -e^2 & e^2 & 0 & 0 \\
0 & 0 & 1 & -1 & 0 & 0 & 0 & 0 & 0 & 0 & e & -e & 0 & 0 & -e^2 & e^2 \\
0 & 0 & 0 & 0 & 0 & 0 & 0 & 0 & 0 & 0 & 0 & 0 & 2 & -2 & 0 & 0 \\
0 & 0 & 0 & 0 & 0 & 0 & 0 & 0 & 0 & 0 & 0 & 0 & 0 & 0 & 2 & -2 \\
0 & 0 & 0 & 0 & * & * & * & * & * & * & * & * & * & * & * & * \\
0 & 0 & 0 & 0 & * & * & * & * & * & * & * & * & * & * & * & *
\end{pmatrix},$$

where the components denoted by $*$ are specified as follows

$$\begin{aligned}
&m_{15,5}^I = de(\lambda^- + 2\mu^-), && m_{15,6}^I = -de(\lambda^+ + 2\mu^+), && m_{15,7}^I = d^2\mu^-, \\
&m_{15,8}^I = -d^2\mu^+, && m_{15,9}^I = d^2\mu^-, && m_{15,10}^I = -d^2\mu^+, \\
&m_{15,11}^I = de\lambda^-, && m_{15,12}^I = -de\lambda^+, && m_{15,13}^I = d^2e(\lambda^- + \mu^-), \\
&m_{15,14}^I = -d^2e(\lambda^+ + \mu^+), && m_{15,15}^I = d(-e^2\lambda^- + d^2\mu^-), && m_{15,16}^I = d(e^2\lambda^+ - d^2\mu^+), \\
&m_{16,5}^I = d^2\lambda^-, && m_{16,6}^I = -d^2\lambda^+, && m_{16,7}^I = de\mu^-, \\
&m_{16,8}^I = -de\mu^+, && m_{16,9}^I = de\mu^-, && m_{16,10}^I = -de\mu^+, \\
&m_{16,11}^I = d^2(\lambda^- + \mu^-), && m_{16,12}^I = -d^2(\lambda^+ + \mu^+), && m_{16,13}^I = d(d^2\lambda^- - e^2\mu^-), \\
&m_{16,14}^I = -d(d^2\lambda^+ - e^2\mu^+), && m_{16,15}^I = -d^2e(\lambda^- + \mu^-), && m_{16,16}^I = d^2e(\lambda^+ + \mu^+).
\end{aligned}$$

The coefficient matrix $M_C = M_C^{II} = (m_{i,j}^{II})_{16\times 16}$ for a Type II interface element with normalization $h = 1$ is given by

$$M_C = M_C^{II} = \tag{5.26}$$

$$\begin{pmatrix}
d & 1-d & 0 & 0 & \frac{d^2}{2} & \frac{1-d^2}{2} & 0 & 0 & 0 & 0 & 0 & 0 & \frac{d^3}{3} & \frac{1-d^3}{3} & 0 & 0 \\
0 & 1 & 0 & 0 & 0 & 1 & 0 & 0 & 0 & \frac{1}{2} & 0 & 0 & 0 & \frac{2}{3} & 0 & 0 \\
e & 1-e & 0 & 0 & \frac{e^2}{2} & \frac{1-e^2}{2} & 0 & 0 & e & 1-e & 0 & 0 & \frac{e^3-3e}{3} & \frac{3e-2-e^2}{3} & 0 & 0 \\
1 & 0 & 0 & 0 & 0 & 0 & 0 & 0 & \frac{1}{2} & 0 & 0 & 0 & -\frac{1}{3} & 0 & 0 & 0 \\
0 & 0 & d & 1-d & 0 & 0 & \frac{d^2}{2} & \frac{1-d^2}{2} & 0 & 0 & 0 & 0 & 0 & 0 & \frac{d^3}{3} & \frac{1-d^3}{3} \\
0 & 0 & 0 & 1 & 0 & 0 & 0 & 1 & 0 & 0 & 0 & \frac{1}{2} & 0 & 0 & 0 & \frac{2}{3} \\
0 & 0 & e & 1-e & 0 & 0 & \frac{e^2}{2} & \frac{1-e^2}{2} & 0 & 0 & e & 1-e & 0 & 0 & \frac{e^3-3e}{3} & \frac{3e-2-e^2}{3} \\
0 & 0 & 1 & 0 & 0 & 0 & 0 & 0 & 0 & 0 & \frac{1}{2} & 0 & 0 & 0 & -\frac{1}{3} & 0 \\
1 & -1 & 0 & 0 & d & -d & 0 & 0 & 0 & 0 & 0 & 0 & d^2 & -d^2 & 0 & 0 \\
0 & 0 & 1 & -1 & 0 & 0 & d & -d & 0 & 0 & 0 & 0 & 0 & 0 & d^2 & -d^2 \\
1 & -1 & 0 & 0 & e & -e & 0 & 0 & 1 & -1 & 0 & 0 & e^2-1 & 1-e^2 & 0 & 0 \\
0 & 0 & 1 & -1 & 0 & 0 & e & -e & 0 & 0 & 1 & -1 & 0 & 0 & e^2-1 & 1-e^2 \\
0 & 0 & 0 & 0 & 0 & 0 & 0 & 0 & 0 & 0 & 0 & 0 & 2 & -2 & 0 & 0 \\
0 & 0 & 0 & 0 & 0 & 0 & 0 & 0 & 0 & 0 & 0 & 0 & 0 & 0 & 2 & -2 \\
0 & 0 & 0 & 0 & * & * & * & * & * & * & * & * & * & * & * & * \\
0 & 0 & 0 & 0 & * & * & * & * & * & * & * & * & * & * & * & *
\end{pmatrix},$$

where the components denoted by $*$ are specified as follows:

$$\begin{aligned}
&m^{II}_{15,5} = \lambda^- + 2\mu^-, && m^{II}_{15,6} = -(\lambda^+ + 2\mu^+),\\
&m^{II}_{15,7} = d\mu^- - e\mu^-, && m^{II}_{15,8} = -d\mu^+ + e\mu^+,\\
&m^{II}_{15,9} = d\mu^- - e\mu^-, && m^{II}_{15,10} = -d\mu^+ + e\mu^+,\\
&m^{II}_{15,11} = \lambda^-, && m^{II}_{15,12} = -\lambda^+,\\
&m^{II}_{15,13} = (d+e)\lambda^- + (d+3e)\mu^-, && m^{II}_{15,14} = -(d+e)\lambda^+ - (d+3e)\mu^+,\\
&m^{II}_{15,15} = \lambda^- + (d^2-e^2)\mu^-, && m^{II}_{15,16} = \lambda^+ - (d^2-e^2)\mu^+,\\
&m^{II}_{16,5} = (d-e)\lambda^-, && m^{II}_{16,6} = -(d-e)\lambda^+,\\
&m^{II}_{16,7} = \mu^-, && m^{II}_{16,8} = -\mu^+,\\
&m^{II}_{16,9} = \mu^-, && m^{II}_{16,10} = -\mu^+,\\
&m^{II}_{16,11} = (d-e)(\lambda^- + 2\mu^-), && m^{II}_{16,12} = -(d-e)\lambda^+ - (2d-2e)\mu^+,\\
&m^{II}_{16,13} = (d^2-e^2)\lambda^-\mu^-, && m^{II}_{16,14} = -(d^2-e^2)\lambda^+ + \mu^+,\\
&m^{II}_{16,15} = -(d-e)\lambda^- - (d-3e)\mu^-, && m^{II}_{16,16} = (d-e)\lambda^+ + (d-3e)\mu^+.
\end{aligned}$$

The procedure of finding vector-valued nonconforming rotated Q_1 IFE basis functions on the interface element T whose geometry is specified in (5.16) and (5.17) is similar to constructing scalar-valued IFE basis functions in Section 2.3 and 2.4. We let $\mathbf{V} = \mathbf{V}_j \in \mathbb{R}^{16}$, $j = 1, \cdots, 8$ be the j-th canonical unit vector such that $v_j = 1$, and $v_i = 0$ if $i \neq j$. For each vector $\mathbf{V}_j$, we can solve for $\mathbf{C} = \mathbf{C}_j$ from (5.23) which contains the coefficients of an IFE function. Then we use the values of $\mathbf{C}_j$ in (5.18) to form the j-th vector-valued nonconforming rotated Q_1 IFE local basis function, denoted by $\mathbf{\Phi}_{j,T}$, for either Type I or Type II interface element.

A typical vector-valued nonconforming rotated Q_1 finite element local basis function $\mathbf{\Psi}_{4,T}$ on a non-interface element is plotted in Figure 5.2. The left plot is for the first component, and the one on the right is for the second component. We note that the first component of $\mathbf{\Psi}_{4,T}$ is the scalar rotated Q_1 finite element local basis function $\psi^I_{4,T}$ as formulated in

(2.12d), and the second component of $\mathbf{\Psi}_{4,T}$ is completely zero. As a comparison, the vector-valued nonconforming rotated Q_1 local IFE basis functions $\mathbf{\Phi}_{4,T}$ on Type I and Type II interface elements are plotted in Figure 5.3 and Figure 5.4, respectively. Note that, the second component of $\mathbf{\Phi}_{4,T}$ is not completely zero because the IFE basis function $\mathbf{\Phi}_{4,T}$ is constructed to satisfy the interface jump conditions (5.19) - (5.22). Since the traction continuity (5.21) involves both components of a vector-valued IFE function, in general neither of the two components in these vector-valued IFE functions is zero.

Figure 5.2: A vector-valued nonconforming rotated Q_1 finite element local basis function.

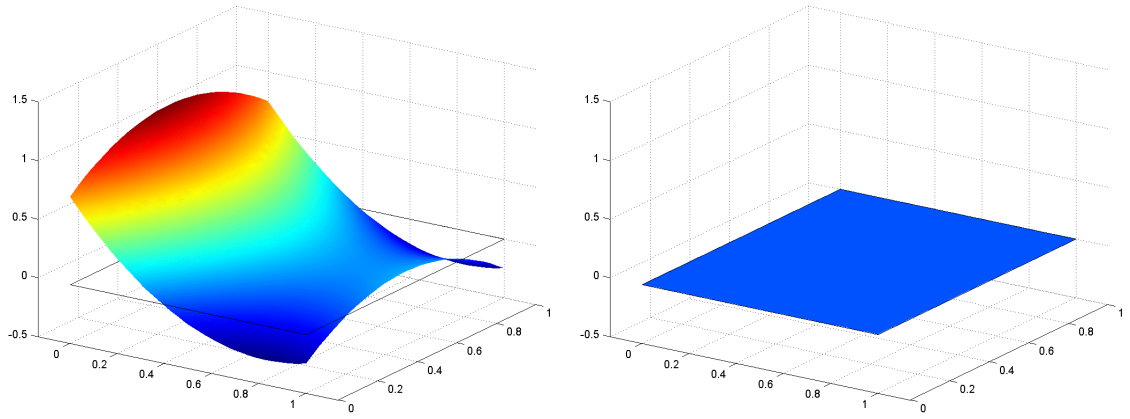

Figure 5.3: A vector-valued nonconforming rotated Q_1 IFE local basis function on a Type I interface element.

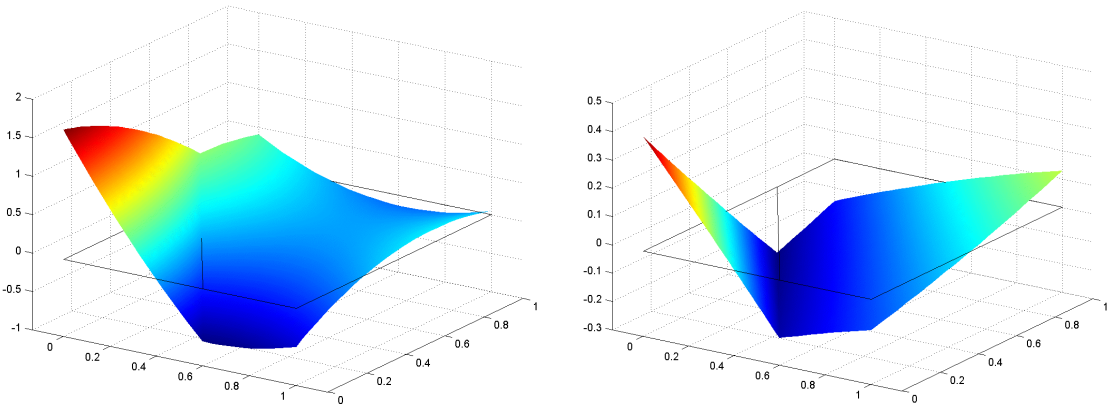

On each interface element $T \in \mathcal{T}_h^i$, we define the local IFE space $\mathbf{S}_h^i(T)$ by

$$\mathbf{S}_h^i(T) = \text{Span}\left\{\mathbf{\Phi}_{j,T} : j = 1, \cdots, 8\right\}. \tag{5.27}$$

Figure 5.4: A vector-valued nonconforming rotated Q_1 IFE local basis function on a Type II interface element.

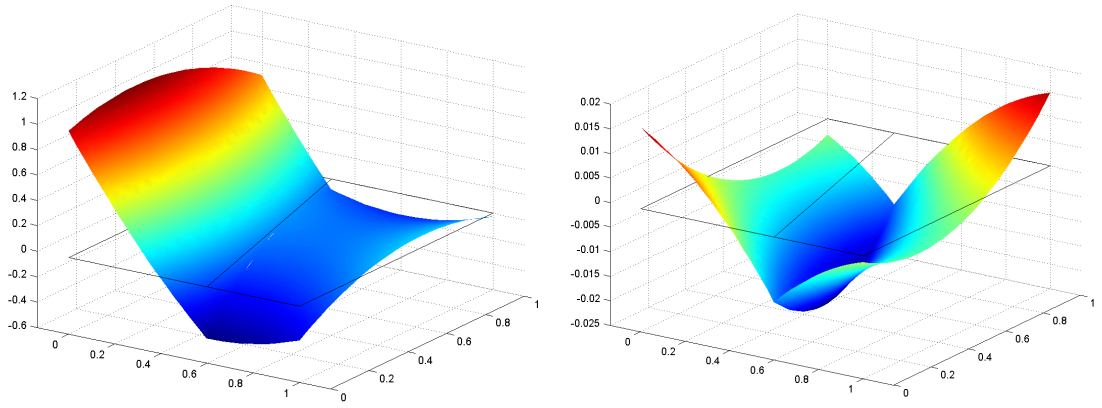

The global IFE space on Ω is then defined as follows

$$\mathbf{S}_h(\Omega) = \Big\{ \mathbf{\Phi} \in (L^2(\Omega))^2 : \ \mathbf{\Phi}|_T \in \mathbf{S}_h^n(T) \text{ if } T \in \mathcal{T}_h^n, \mathbf{\Phi}|_T \in \mathbf{S}_h^i(T) \text{ if } T \in \mathcal{T}_h^i; \\ \text{if } T_1 \cap T_2 = b, \text{ then } \int_b \mathbf{\Phi}|_{T_1} \mathrm{d}s = \int_b \mathbf{\Phi}|_{T_2} \mathrm{d}s \Big\}. \tag{5.28}$$

5.2.2 Properties of Nonconforming Rotated Q_1 IFE Spaces

In this subsection, we discuss basic properties of vector-valued nonconforming rotated Q_1 IFE basis functions and the corresponding IFE spaces.

Lemma 5.1. (Continuity) *On each interface element $T \in \mathcal{T}_h^i$, the local IFE space $\mathbf{S}_h^i(T)$ is a subspace of $\mathbf{C}(T)$.*

Proof. Note that every IFE function $\mathbf{\Phi}_T \in \mathbf{S}_h^i(T)$ is a piecewise vector-valued polynomial; hence, it suffices to show $\mathbf{\Phi}_T$ is continuous across the line segment $\overline{DE}$. Note that the jump of the function $[\mathbf{\Phi}_T] = \mathbf{\Phi}_T^+ - \mathbf{\Phi}_T^-$ is linear because $\mathbf{\Phi}_T$ is made to satisfy the condition (5.22). Then, $[\mathbf{\Phi}_T] = \mathbf{0}$ follows from (5.20). □

Lemma 5.2. (Partition of Unity) *On each interface element $T \in \mathcal{T}_h^i$, the vector-valued nonconforming rotated Q_1 IFE basis functions $\mathbf{\Phi}_{j,T} \in \mathbf{S}_h^i(T)$, $j = 1, \cdots, 8$, satisfy the following partition of unity property:*

$$\sum_{j=1}^{4} \mathbf{\Phi}_{j,T} = \begin{pmatrix} 1 \\ 0 \end{pmatrix}, \qquad \sum_{j=5}^{8} \mathbf{\Phi}_{j,T} = \begin{pmatrix} 0 \\ 1 \end{pmatrix}. \tag{5.29}$$

Proof. By direct calculations, the coefficients of the IFE basis functions satisfy the following condition

$$\sum_{j=1}^{4} a_{j,1}^{-} = 1, \quad \sum_{j=1}^{4} b_{j,1}^{-} = 0, \quad \sum_{j=1}^{4} c_{j,1}^{-} = 0, \quad \sum_{j=1}^{4} d_{j,1}^{-} = 0.$$

$$\sum_{j=1}^{4} a_{j,2}^{-} = 1, \quad \sum_{j=1}^{4} b_{j,2}^{-} = 0, \quad \sum_{j=1}^{4} c_{j,2}^{-} = 0, \quad \sum_{j=1}^{4} d_{j,2}^{-} = 0.$$

$$\sum_{j=1}^{4} a_{j,1}^{+} = 1, \quad \sum_{j=1}^{4} b_{j,1}^{+} = 0, \quad \sum_{j=1}^{4} c_{j,1}^{+} = 0, \quad \sum_{j=1}^{4} d_{j,1}^{+} = 0.$$

$$\sum_{j=1}^{4} a_{j,2}^{+} = 1, \quad \sum_{j=1}^{4} b_{j,2}^{+} = 0, \quad \sum_{j=1}^{4} c_{j,2}^{+} = 0, \quad \sum_{j=1}^{4} d_{j,2}^{+} = 0.$$

Applying these identities in (5.18) yields the first equation in (5.29). A similar argument can be carried out to show the second equation. □

Lemma 5.3. (Consistency) *On each interface element $T \in \mathcal{T}_h^i$, the vector-valued nonconforming rotated Q_1 IFE local basis functions $\mathbf{\Phi}_{j,T} \in \mathbf{S}_h^i(T)$, $j = 1, \cdots, 8$, and the standard vector-valued nonconforming rotated Q_1 FE basis functions $\mathbf{\Psi}_{j,T}$, $j = 1, \cdots, 8$, are identical, i.e., $\mathbf{\Phi}_{j,T} = \mathbf{\Psi}_{j,T}, j = 1, \cdots, 8$, under each of the following conditions:*

- *the elasticity parameters have no discontinuity, i.e., $\lambda^+ = \lambda^-$, $\mu^+ = \mu^-$;*
- $\min\{|T^-|, |T^+|\}$ *shrinks to zero, where $|T^s|$, $s = -, +$, denotes the area of the polygon T^s.*

Proof. For the first property, we let $\lambda^+ = \lambda^-$ and $\mu^+ = \mu^-$ and solve the linear system (5.23). Direct calculations leads to $\mathbf{\Phi}_{j,T} = \mathbf{\Psi}_{j,T}$, $j = 1, \cdots, 8$.

For the second property, without loss of generality, we assume the area of $|T^-|$ approaches zero. Then for Type I interface element, we have either $d \to 0$, or $e \to 0$; for Type II interface element, we have both $d \to 0$ and $e \to 0$. Direct calculations lead to $\mathbf{\Phi}_{j,T}^+ \to \mathbf{\Psi}_{j,T}$, $j = 1, \cdots, 8$ for both interface element types. Also, note that $\mathbf{\Phi}_{j,T}$ becomes $\mathbf{\Phi}_{j,T}^+$ under this assumption. □

We now consider the important unisolvent property. For the planar elasticity interface problem, both linear [62, 97] and bilinear [108] vector-valued IFE functions possess the unisolvent property under certain conditions regarding the configurations of elasticity parameters and interface location. A counter-example presented in [108] demonstrates that linear IFE functions cannot be constructed for a certain configuration of the interface and the Lamé parameters. This limitation of linear and bilinear vector-valued IFE functions for the planar

elasticity interface problem hinders their applications. Hence it is very interesting to know whether the nonconforming rotated Q_1 vector-valued IFE functions have this unisolvent property.

For the Type I interface element, the determinant of matrix M_C^I defined in (5.25) can be written as follows

$$\det(M_C^I) = P_1^I\lambda^+\mu^+ + P_2^I\lambda^-\mu^+ + P_3^I\mu^+\mu^+ + P_4^I\lambda^+\mu^- + P_5^I\lambda^-\mu^- + P_6^I\mu^+\mu^- + P_7^I\mu^-\mu^-, \quad (5.30)$$

where

$$\begin{aligned}
P_1^I &= d^2e^2\big(8d^2 - 3d^3 - 6de + 3d^2e + 2e^2 - 3de^2 + 3e^3\big)\\
&\quad \big(2d^2 + 3d^3 - 6de - 3d^2e + 8e^2 + 3de^2 - 3e^3\big),\\
P_2^I &= de\big(9d^7e + 20e^4 - 18d^6e(1+e) + d^5e(-16 + 18e + 27e^2) + 4d^4(5 + 15e^2 - 9e^4)\\
&\quad +2d^2e^2(20 + 30e^2 + 9e^3 - 9e^4) + de^3(-24 - 16e^2 - 18e^3 + 9e^4)\\
&\quad +d^3e(-24 - 104e^2 + 27e^4)\big),\\
P_3^I &= 2d^2e^2(5d^2 - 6de + 5e^2)^2,\\
P_4^I &= P_2^I,\\
P_5^I &= \big(4d^2 - 8d^3e + 3d^4e + 4e^2 + 6d^2e^2 - 3d^3e^2 - 2de^3 + 3d^2e^3 - 3de^4\big)\\
&\quad \big(4d^2 - 2d^3e - 3d^4e + 4e^2 + 6d^2e^2 + 3d^3e^2 - 8de^3 - 3d^2e^3 + 3de^4\big),\\
P_6^I &= 4de\big(5d^2 - 6de + 5e^2\big)\big(4d^2 - 5d^3e + 4e^2 + 6d^2e^2 - 5de^3\big),\\
P_7^I &= 2\big(-4d^2 + 5d^3e - 4e^2 - 6d^2e^2 + 5de^3\big)^2.
\end{aligned}$$

Note that $\lambda^\pm$ and $\mu^\pm$ are all positive, it is interesting to know whether these coefficients P_j^I, $j = 1, \cdots, 7$ are non-negative.

Lemma 5.4. *The coefficients P_j^I, $j = 1, \cdots, 7$ in (5.30) satisfy*

$$P_j^I > 0, \quad (5.31)$$

for all $0 < d \le 1$ and $0 < e \le 1$.

Proof. We can verify (5.31) by direct computations. For instance,

$$\begin{aligned}
P_1^I &= d^2e^2\left(\frac{1}{2}(3d - 2e)^2 + 3d^2(1-d) + \frac{1}{2}d^2 + \frac{3}{2}e(d^2+e^2) + \frac{3}{2}e(d-e)^2\right)\\
&\quad \left(\frac{1}{2}(3e - 2d)^2 + 3e^2(1-e) + \frac{1}{2}e^2 + \frac{3}{2}d(d^2+e^2) + \frac{3}{2}d(d-e)^2\right)\\
&\ge \frac{d^4e^4}{4}.
\end{aligned}$$

Since d, e are positive, then every term in the above equation is positive. Thus, $P_1^I > 0$ for all $0 < d \le 1$ and $0 < e \le 1$. Similar arguments can be applied to $P_j^I, j = 2, 3, \ldots, 7$. □

For Type II interface element, the determinant of the coefficient matrix M_C^{II} defined in (5.26) can be written as follows,

$$\det(M_C^{II}) = P_1^{II}\lambda^+\mu^+ + P_2^{II}\lambda^-\mu^+ + P_3^{II}\mu^+\mu^+ + P_4^{II}\lambda^+\mu^- + P_5^{II}\lambda^-\mu^- + P_6^{II}\mu^+\mu^- + P_7^{II}\mu^-\mu^-, \tag{5.32}$$

where

$$\begin{aligned}
P_1^{II} &= \big(5d - 9d^2 + 11d^3 - 3d^4 + 5e - 6de + d^2e - 3e^2 + de^2 - e^3 + 3e^4\big)\\
&\quad \big(5d - 3d^2 - d^3 + 3d^4 + 5e - 6de + d^2e - 9e^2 + de^2 + 11e^3 - 3e^4\big),\\
P_2^{II} &= 20d - 49d^2 + 100d^3 - 101d^4 + 44d^5 + 29d^6 - 36d^7 + 9d^8 + 20e - 74de + 104d^2e\\
&\quad -108d^3e + 36d^4e - 10d^5e - 49e^2 + 104de^2 - 146d^2e^2 + 136d^3e^2 - 29d^4e^2 + 100e^3\\
&\quad -108de^3 + 136d^2e^3 - 124d^3e^3 + 36d^4e^3 - 101e^4 + 36de^4 - 29d^2e^4 + 36d^3e^4\\
&\quad -18d^4e^4 + 44e^5 - 10de^5 + 29e^6 - 36e^7 + 9e^8,\\
P_3^{II} &= 2(5d - 6d^2 + 5d^3 + 5e - 6de + d^2e - 6e^2 + de^2 + 5e^3)^2,\\
P_4^{II} &= P_2^{II},\\
P_5^{II} &= \big(4 - 5d + 13d^2 - 11d^3 + 3d^4 - 5e - 2de - d^2e + 7e^2 - de^2 + e^3 - 3e^4\big)\\
&\quad \big(4 - 5d + 7d^2 + d^3 - 3d^4 - 5e - 2de - d^2e + 13e^2 - de^2 - 11e^3 + 3e^4\big),\\
P_6^{II} &= 4\big(4 - 5d + 10d^2 - 5d^3 - 5e - 2de - d^2e + 10e^2 - de^2 - 5e^3\big)\\
&\quad \big(5d - 6d^2 + 5d^3 + 5e - 6de + d^2e - 6e^2 + de^2 + 5e^3\big),\\
P_7^{II} &= 2\big(-4 + 5d - 10d^2 + 5d^3 + 5e + 2de + d^2e - 10e^2 + de^2 + 5e^3\big)^2.
\end{aligned}$$

Similarly, we can verify that the coefficients P_i^{II}, $i = 1, \cdots, 7$ are positive.

Lemma 5.5. *The coefficients P_j^{II}, $j = 1, \cdots, 7$ in* (5.32) *satisfy*

$$P_j^{II} > 0, \tag{5.33}$$

for all $0 < d < 1$ and $0 < e < 1$.

Lemma 5.4 and Lemma 5.5 imply that the matrices M_C^I and M_C^{II} are nonsingular for arbitrary interface location and elastic material configurations. Consequently, we conclude that the nonconforming rotated Q_1 vector-valued IFE functions (5.18) are unisolvent.

Theorem 5.1. *A vector-valued nonconforming rotated Q_1 IFE function $\mathbf{\Phi}_T$ defined by* (5.18) *for the planar elasticity interface problem is uniquely determined by the its average integral values stated in* (5.19) *and interface jump conditions* (5.20) - (5.22)*.*

5.2.3 Interpolation and Galerkin Method

In this subsection, we introduce vector-valued IFE interpolation to investigate the approximation capability of vector-valued nonconforming rotated Q_1 IFE spaces $\mathbf{S}_h(\Omega)$. Then we

use these vector-valued IFE functions to solve the planar elasticity interface problem (5.1) - (5.4).

Assuming that $\mathcal{T}_h$ is a Cartesian mesh of Ω, we define the local interpolation operator $\mathbf{I}_{h,T} : \mathbf{H}^1(T) \to \mathbf{S}_h(T)$ such that

$$\mathbf{I}_{h,T}\mathbf{u} = \begin{cases} \sum_{j=1}^{8} c_j \mathbf{\Phi}_{j,T} & \text{if } T \in \mathcal{T}_h^i, \\ \sum_{j=1}^{8} c_j \mathbf{\Psi}_{j,T} & \text{if } T \in \mathcal{T}_h^n, \end{cases} \tag{5.34}$$

where

$$\begin{pmatrix} c_j \\ c_{j+4} \end{pmatrix} = \frac{1}{|b_j|} \int_{b_j} \mathbf{u}(x,y)\mathrm{d}s, \qquad j = 1,2,3,4. \tag{5.35}$$

The global IFE interpolation $\mathbf{I}_h : \mathbf{H}^1(\Omega) \to \mathbf{S}_h(\Omega)$ is defined by:

$$(\mathbf{I}_h\mathbf{u})|_T = \mathbf{I}_{h,T}\mathbf{u}, \quad \forall\ T \in \mathcal{T}_h. \tag{5.36}$$

In Section 5.3, we will use numerical examples to demonstrate the optimal- convergence feature of the IFE interpolations which suggests the vector-valued nonconforming rotated Q_1 IFE spaces also have optimal approximation capabilities as their finite element counterparts.

Next, we consider the Galerkin IFE methods for solving the planar elasticity interface problems. Partial penalization idea will not be used in the following Galerkin IFE schemes since numerical examples in Section 4.3 for elliptic interface problems indicating that it may not be necessary to add penalty terms if the degrees of freedom of nonconforming rotated Q_1 functions are determined by the average integral values over edges.

Assume that $\mathbf{u} \in \mathbf{H}^1(\Omega)$ solves (5.1) - (5.4) and $\mathbf{u}|_{\Omega^s} \in \mathbf{H}^2(\Omega^s)$, $s = +, -$. Multiplying Equation (5.1) by a test function $\mathbf{v} \in \mathbf{H}_0^1(\Omega)$, integrating over each sub-domain Ω^s, $s = +, -$ and applying Green's formula lead to

$$\int_{\Omega^s} 2\mu^s \epsilon(\mathbf{u}) : \epsilon(\mathbf{v})\,\mathrm{d}x\mathrm{d}y + \int_{\Omega^s} \lambda^s (\nabla\cdot\mathbf{u})(\nabla\cdot\mathbf{v})\,\mathrm{d}x\mathrm{d}y - \int_{\Gamma} \sigma(\mathbf{u})\mathbf{n}\cdot\mathbf{v}\,\mathrm{d}s$$

$$= \int_{\Omega^s} \mathbf{f}\cdot\mathbf{v}\,\mathrm{d}x\mathrm{d}y, \quad \forall\ \mathbf{v} \in \mathbf{H}_0^1(\Omega), \tag{5.37}$$

where the inner-product of two tensors is defined by

$$\epsilon(\mathbf{u}) : \epsilon(\mathbf{v}) = \sum_{i,j=1}^{2} \epsilon_{ij}(\mathbf{u})\epsilon_{ij}(\mathbf{v}). \tag{5.38}$$

Summing (5.37) over sub-domains and applying the interface jump condition (5.4), we obtain the following weak form of the planar elasticity interface problem:

$$\int_\Omega 2\mu\epsilon(\mathbf{u}) : \epsilon(\mathbf{v})\,\mathrm{d}x\mathrm{d}y + \int_\Omega \lambda(\nabla\cdot\mathbf{u})(\nabla\cdot\mathbf{v})\,\mathrm{d}x\mathrm{d}y = \int_\Omega \mathbf{f}\cdot\mathbf{v}\mathrm{d}x\mathrm{d}y, \quad \forall\ \mathbf{v}\in\mathbf{H}_0^1(\Omega). \tag{5.39}$$

Then we define the nonconforming rotated Q_1 Galerkin IFE method by: Find $\mathbf{u}_h \in \mathbf{S}_h(\Omega)$ such that

$$\sum_{T\in\mathcal{T}_h}\int_T 2\mu\epsilon(\mathbf{u}_h) : \epsilon(\mathbf{v}_h)\mathrm{d}x\mathrm{d}y + \sum_{T\in\mathcal{T}_h}\int_T \lambda(\nabla\cdot\mathbf{u}_h)(\nabla\cdot\mathbf{v}_h)\mathrm{d}x\mathrm{d}y = \int_\Omega \mathbf{f}\cdot\mathbf{v}_h\mathrm{d}x\mathrm{d}y, \quad \forall\ \mathbf{v}_h\in\mathring{\mathbf{S}}_h(\Omega), \tag{5.40}$$

and impose the boundary condition in the following sense:

$$\int_b \mathbf{u}_h\mathrm{d}s = \int_b \mathbf{g}\mathrm{d}s, \qquad \forall\, b\in\mathcal{E}_h^b,$$

where the vector-valued nonconforming rotated Q_1 test IFE function space $\mathring{\mathbf{S}}_h(\Omega)$ is defined by

$$\mathring{\mathbf{S}}_h(\Omega) = \left\{\boldsymbol{\Phi}\in\mathbf{S}_h(\Omega) : \int_b \boldsymbol{\Phi}\mathrm{d}s = \mathbf{0} \text{ if } b\in\mathcal{E}_h^b\right\}. \tag{5.41}$$

5.3 Numerical Experiments

In this section, we use numerical examples to demonstrate features of Galerkin IFE methods for elasticity interface problems with vector-valued nonconforming rotated Q_1 IFE functions. Accuracy of both IFE interpolations and Galerkin IFE solutions with different configurations of interface and Lamé parameters will be tested.

Let $\Omega = (-1,1)\times(-1,1)$ be the solution domain. In the following experiments, we use a family of Cartesian meshes $\{\mathcal{T}_h\}$ on Ω. Each mesh $\mathcal{T}_h$ is formed by partitioning Ω into $N\times N$ congruent squares such that the edge length of square is $h = 2/N$.

For simplicity, we let $I_h u_i, i = 1, 2$ be the i-th component of the IFE interpolation $\mathbf{I}_h\mathbf{u}$ of a function $\mathbf{u}$. Similarly, we use u_{hi} to denote the i-th component of the IFE solution $\mathbf{u}_h$ to the elasticity interface problem.

Errors of an IFE approximation are given in the L^∞, L^2, and semi-H^1 norms. Errors in the L^∞ norm are defined by

$$\|v_{hj} - u_j\|_{0,\infty,\Omega} = \max_{T\in\mathcal{T}_h}\left(\max_{(x,y)\in\widetilde{T}\subset T}|v_{hj}(x,y) - u_j(x,y)|\right), \quad j = 1,2, \tag{5.42}$$

where, again, $v_{hj} = I_h u_j$ or $v_{hj} = u_{hj}$, and $\tilde{T}$ consists of the 49 uniformly distributed points in T as illustrated in Figure 3.2. In the following error tables, rates of convergence are

computed by

$$\frac{1}{\ln(2)} \ln\left(\frac{\|v_{hj} - u_j\|}{\|u_{h/2,j} - u_j\|}\right), \quad j = 1, 2, \tag{5.43}$$

for a specific norm $\|\cdot\|$, where $v_{hj} = I_h u_j$ or $v_{hj} = u_{hj}$.

The first elasticity interface problem that we consider has a circular interface Γ with radius $r_0 = \pi/8$. The interface Γ subdivides Ω into two sub-domains, denoted by Ω^- and Ω^+, *i.e.*,

$$\Omega^- = \left\{(x, y)^t : x^2 + y^2 < r_0^2\right\}, \quad \Omega^+ = \left\{(x, y)^t : x^2 + y^2 > r_0^2\right\}. \tag{5.44}$$

The boundary function $\mathbf{g}$ and the load function $\mathbf{f}$ in the interface problem (5.1) - (5.4) are chosen such that the exact solution $\mathbf{u}$ is as follows:

$$\mathbf{u}(x, y) = \begin{pmatrix} u_1(x, y) \\ u_2(x, y) \end{pmatrix} = \begin{cases} \begin{pmatrix} u_1^-(x, y) \\ u_2^-(x, y) \end{pmatrix} = \begin{pmatrix} \frac{1}{\lambda^-} r^{\alpha_1} \\ \frac{1}{\lambda^-} r^{\alpha_2} \end{pmatrix} & \text{in } \Omega^-, \\ \begin{pmatrix} u_1^+(x, y) \\ u_2^+(x, y) \end{pmatrix} = \begin{pmatrix} \frac{1}{\lambda^+} r^{\alpha_1} + \left(\frac{1}{\lambda^-} - \frac{1}{\lambda^+}\right) r_0^{\alpha_1} \\ \frac{1}{\lambda^+} r^{\alpha_2} + \left(\frac{1}{\lambda^-} - \frac{1}{\lambda^+}\right) r_0^{\alpha_2} \end{pmatrix} & \text{in } \Omega^+, \end{cases} \tag{5.45}$$

where $\alpha_1 = 5$, $\alpha_2 = 7$, and $r = \sqrt{x^2 + y^2}$.

Example 5.1. ***(Convergence Test)****: In this experiment, we test the accuracy of IFE interpolations and Galerkin IFE solutions using vector-valued nonconforming rotated Q_1 IFE functions.*

We test three configurations of Lamé parameters all of which have been investigated by bilinear IFE method in [108]. The first one is for a moderate discontinuity in the Lamé parameters, *i.e.*, $\lambda^+ = 5$, $\lambda^- = 1$, $\mu^+ = 10$, $\mu^- = 2$, and the Poisson's ratio in this Lamé parameter configuration is $\nu^\pm = 0.1667$. Errors in IFE interpolations and IFE solutions are listed in Table 5.1. The second one is for a larger discontinuity in Lamé parameters, *i.e.*, $\lambda^+ = 100$, $\lambda^- = 1$, $\mu^+ = 200$, $\mu^- = 2$, and Poisson's ratio in this case is $\nu^\pm = 0.1667$. Corresponding numerical errors are listed in Table 5.2. The third experiment is configured by flipping the Lamé parameters over the sub-domains Ω^- and Ω^+ in the second experiment, *i.e.*, $\lambda^+ = 1$, $\lambda^- = 100$, $\mu^+ = 2$, $\mu^- = 200$, and Poisson's ratio in this case is still $\nu^\pm = 0.1667$. Errors of IFE interpolations and IFE solutions are listed in Table 5.3.

Data in Table 5.1, Table 5.2, and Table 5.3 indicate that both IFE interpolations and Galerkin IFE solutions using nonconforming rotated Q_1 vector-valued IFE functions converge optimally in L^∞, L^2 and semi-H^1 norms. Comparing these results with those of bilinear IFE method in [108], we note that bilinear IFE solutions may also converge with optimal rates in L^2 and H^1 norms, but only sub-optimal convergence rates are observed in L^∞ norm.

Table 5.1: Errors of nonconforming rotated Q_1 IFE interpolations and Galerkin IFE solutions with $\lambda^+ = 5$, $\lambda^- = 1$, $\mu^+ = 10$, $\mu^- = 2$, $\nu^{\pm} = 0.1667$.

	$I_h u_1 - u_1$						$I_h u_2 - u_2$					
N	$\|\cdot\|_{0,\infty,\Omega}$	rate	$\|\cdot\|_{0,\Omega}$	rate	$\|\cdot\|_{1,\Omega}$	rate	$\|\cdot\|_{0,\infty,\Omega}$	rate	$\|\cdot\|_{0,\Omega}$	rate	$\|\cdot\|_{1,\Omega}$	rate
10	$5.19E{-2}$		$1.76E{-2}$		$3.79E{-1}$		$1.98E{-1}$		$4.52E{-2}$		$9.91E{-1}$	
20	$1.46E{-2}$	1.83	$4.46E{-3}$	1.98	$1.91E{-1}$	0.99	$5.98E{-2}$	1.72	$1.17E{-2}$	1.96	$5.06E{-1}$	0.97
40	$3.89E{-3}$	1.91	$1.12E{-3}$	2.00	$9.57E{-2}$	1.00	$1.65E{-2}$	1.86	$2.93E{-3}$	1.99	$2.55E{-1}$	0.99
80	$1.00E{-3}$	1.96	$2.80E{-4}$	2.00	$4.79E{-2}$	1.00	$4.32E{-3}$	1.93	$7.35E{-4}$	2.00	$1.27E{-1}$	1.00
160	$2.54E{-4}$	1.98	$7.00E{-5}$	2.00	$2.40E{-2}$	1.00	$1.11E{-3}$	1.97	$1.84E{-4}$	2.00	$6.37E{-2}$	1.00
320	$6.40E{-5}$	1.99	$1.75E{-5}$	2.00	$1.20E{-2}$	1.00	$2.80E{-4}$	1.98	$4.59E{-5}$	2.00	$3.19E{-2}$	1.00
640	$1.61E{-5}$	1.99	$4.38E{-6}$	2.00	$5.99E{-3}$	1.00	$7.05E{-5}$	1.99	$1.15E{-5}$	2.00	$1.59E{-2}$	1.00
	$u_{1h} - u_1$						$u_{2h} - u_2$					
N	$\|\cdot\|_{0,\infty,\Omega}$	rate	$\|\cdot\|_{0,\Omega}$	rate	$\|\cdot\|_{1,\Omega}$	rate	$\|\cdot\|_{0,\infty,\Omega}$	rate	$\|\cdot\|_{0,\Omega}$	rate	$\|\cdot\|_{1,\Omega}$	rate
10	$5.76E{-2}$		$2.28E{-2}$		$4.20E{-1}$		$1.98E{-1}$		$5.68E{-2}$		$1.05E{-0}$	
20	$1.79E{-2}$	1.69	$5.67E{-3}$	2.00	$2.09E{-1}$	1.01	$5.90E{-2}$	1.74	$1.44E{-2}$	2.00	$5.37E{-1}$	0.96
40	$5.04E{-3}$	1.83	$1.42E{-3}$	2.00	$1.04E{-1}$	1.00	$1.72E{-2}$	1.78	$3.62E{-3}$	2.00	$2.70E{-1}$	0.99
80	$1.34E{-3}$	1.91	$3.54E{-4}$	2.00	$5.22E{-2}$	1.00	$4.77E{-3}$	1.85	$9.05E{-4}$	2.00	$1.35E{-1}$	1.00
160	$3.44E{-4}$	1.96	$8.84E{-5}$	2.00	$2.61E{-2}$	1.00	$1.25E{-3}$	1.93	$2.26E{-4}$	2.00	$6.77E{-2}$	1.00
320	$8.73E{-5}$	1.98	$2.21E{-5}$	2.00	$1.31E{-2}$	1.00	$3.22E{-4}$	1.96	$5.66E{-5}$	2.00	$3.38E{-2}$	1.00
640	$2.20E{-5}$	1.99	$5.52E{-6}$	2.00	$6.53E{-3}$	1.00	$8.15E{-5}$	1.98	$1.41E{-5}$	2.00	$1.69E{-2}$	1.00

Table 5.2: Errors of nonconforming rotated Q_1 IFE interpolations and Galerkin IFE solutions with $\lambda^+ = 100$, $\lambda^- = 1$, $\mu^+ = 200$, $\mu^- = 2$, $\nu^{\pm} = 0.1667$.

	$I_h u_1 - u_1$						$I_h u_2 - u_2$					
N	$\|\cdot\|_{0,\infty,\Omega}$	rate	$\|\cdot\|_{0,\Omega}$	rate	$\|\cdot\|_{1,\Omega}$	rate	$\|\cdot\|_{0,\infty,\Omega}$	rate	$\|\cdot\|_{0,\Omega}$	rate	$\|\cdot\|_{1,\Omega}$	rate
10	$2.59E{-3}$		$1.20E{-3}$		$2.52E{-2}$		$9.88E{-3}$		$2.26E{-3}$		$4.97E{-2}$	
20	$9.70E{-4}$	1.41	$3.16E{-4}$	1.93	$1.36E{-2}$	0.89	$2.99E{-3}$	1.72	$5.84E{-4}$	1.96	$2.54E{-2}$	0.97
40	$3.46E{-4}$	1.49	$8.29E{-5}$	1.93	$7.13E{-3}$	0.93	$8.24E{-4}$	1.86	$1.47E{-4}$	1.99	$1.28E{-2}$	0.99
80	$9.64E{-5}$	1.84	$2.13E{-5}$	1.96	$3.66E{-3}$	0.96	$2.16E{-4}$	1.93	$3.69E{-5}$	2.00	$6.41E{-3}$	1.00
160	$2.55E{-5}$	1.92	$5.44E{-6}$	1.97	$1.86E{-3}$	0.98	$5.54E{-5}$	1.97	$9.24E{-6}$	2.00	$3.21E{-3}$	1.00
320	$6.55E{-6}$	1.96	$1.37E{-6}$	1.99	$9.37E{-4}$	0.99	$1.40E{-5}$	1.98	$2.31E{-6}$	2.00	$1.60E{-3}$	1.00
640	$1.68E{-6}$	1.96	$3.45E{-7}$	1.99	$4.70E{-4}$	0.99	$3.52E{-6}$	1.99	$5.78E{-7}$	2.00	$8.02E{-4}$	1.00
	$u_{1h} - u_1$						$u_{2h} - u_2$					
N	$\|\cdot\|_{0,\infty,\Omega}$	rate	$\|\cdot\|_{0,\Omega}$	rate	$\|\cdot\|_{1,\Omega}$	rate	$\|\cdot\|_{0,\infty,\Omega}$	rate	$\|\cdot\|_{0,\Omega}$	rate	$\|\cdot\|_{1,\Omega}$	rate
10	$3.54E{-3}$		$1.80E{-3}$		$2.65E{-2}$		$9.88E{-3}$		$2.91E{-3}$		$5.26E{-2}$	
20	$1.15E{-3}$	1.63	$4.58E{-4}$	1.97	$1.44E{-2}$	0.87	$2.95E{-3}$	1.74	$7.38E{-4}$	1.98	$2.70E{-2}$	0.96
40	$3.42E{-4}$	1.74	$1.22E{-4}$	1.90	$7.65E{-3}$	0.92	$8.59E{-4}$	1.78	$1.86E{-4}$	1.99	$1.36E{-2}$	0.99
80	$1.12E{-4}$	1.61	$3.07E{-5}$	1.99	$3.95E{-3}$	0.95	$2.38E{-4}$	1.85	$4.64E{-5}$	2.00	$6.82E{-3}$	1.00
160	$3.20E{-5}$	1.81	$7.66E{-6}$	2.00	$2.01E{-3}$	0.98	$6.27E{-5}$	1.93	$1.16E{-5}$	2.00	$3.41E{-3}$	1.00
320	$8.57E{-6}$	1.90	$1.90E{-6}$	2.01	$1.01E{-3}$	0.99	$1.61E{-5}$	1.96	$2.90E{-6}$	2.00	$1.70E{-3}$	1.00
640	$2.24E{-6}$	1.94	$4.79E{-7}$	1.99	$5.08E{-4}$	0.99	$4.07E{-6}$	1.98	$7.24E{-7}$	2.00	$8.52E{-4}$	1.00

Example 5.2. ***("Locking" Test)****: In this experiment, we test the nonconforming rotated Q_1 Galerkin IFE method for elasticity interface problems with nearly incompressible materials ($\nu \approx 0.5$).*

First, we test the problem with a moderate discontinuity in Lamé parameters, *i.e.*, $\lambda^+ = 20$, $\lambda^- = 1$, $\mu^+ = 0.02$, $\mu^- = 0.001$. In this case, both types of materials are nearly incompressible and their Poisson's ratios ν^+ and ν^- are approximately equal to 0.4995.

Table 5.3: Errors of nonconforming rotated Q_1 IFE interpolations and Galerkin IFE solutions with $\lambda^+ = 1$, $\lambda^- = 100$, $\mu^+ = 2$, $\mu^- = 200$, $\nu^\pm = 0.1667$.

	$I_h u_1 - u_1$						$I_h u_2 - u_2$					
N	$\|\cdot\|_{0,\infty,\Omega}$	rate	$\|\cdot\|_{0,\Omega}$	rate	$\|\cdot\|_{1,\Omega}$	rate	$\|\cdot\|_{0,\infty,\Omega}$	rate	$\|\cdot\|_{0,\Omega}$	rate	$\|\cdot\|_{1,\Omega}$	rate
10	$2.59E{-1}$		$8.79E{-2}$		$1.89E{-0}$		$9.88E{-1}$		$2.26E{-1}$		$4.95E{-0}$	
20	$7.32E{-2}$	1.83	$2.23E{-2}$	1.98	$9.53E{-1}$	0.99	$2.99E{-1}$	1.72	$5.82E{-2}$	1.96	$2.53E{-0}$	0.97
40	$1.94E{-2}$	1.91	$5.58E{-3}$	2.00	$4.78E{-1}$	1.00	$8.24E{-2}$	1.86	$1.47E{-2}$	1.99	$1.27E{-0}$	0.99
80	$5.01E{-3}$	1.96	$1.40E{-3}$	2.00	$2.29E{-1}$	1.00	$2.16E{-2}$	1.93	$3.67E{-3}$	2.00	$6.37E{-1}$	1.00
160	$1.27E{-3}$	1.98	$3.49E{-4}$	2.00	$1.20E{-1}$	1.00	$5.54E{-3}$	1.97	$9.19E{-4}$	2.00	$3.19E{-1}$	1.00
320	$3.20E{-4}$	1.99	$8.73E{-5}$	2.00	$5.98E{-2}$	1.00	$1.40E{-3}$	1.98	$2.30E{-4}$	2.00	$1.59E{-1}$	1.00
640	$8.03E{-5}$	1.99	$2.18E{-5}$	2.00	$2.99E{-2}$	1.00	$3.52E{-4}$	1.99	$5.74E{-5}$	2.00	$7.97E{-2}$	1.00
	$u_{1h} - u_1$						$u_{2h} - u_2$					
N	$\|\cdot\|_{0,\infty,\Omega}$	rate	$\|\cdot\|_{0,\Omega}$	rate	$\|\cdot\|_{1,\Omega}$	rate	$\|\cdot\|_{0,\infty,\Omega}$	rate	$\|\cdot\|_{0,\Omega}$	rate	$\|\cdot\|_{1,\Omega}$	rate
10	$2.88E{-1}$		$1.11E{-1}$		$2.07E{-0}$		$9.87E{-1}$		$2.82E{-1}$		$5.23E{-0}$	
20	$8.95E{-2}$	1.67	$2.77E{-2}$	2.00	$1.04E{-0}$	0.99	$2.95E{-1}$	1.74	$7.16E{-2}$	1.98	$2.69E{-0}$	0.96
40	$2.52E{-2}$	1.83	$6.92E{-3}$	2.00	$5.21E{-1}$	1.00	$8.58E{-2}$	1.78	$1.80E{-2}$	2.00	$1.35E{-0}$	0.90
80	$6.68E{-3}$	1.91	$1.73E{-3}$	2.00	$2.61E{-1}$	1.00	$2.38E{-2}$	1.85	$4.50E{-3}$	2.00	$6.77E{-1}$	1.00
160	$1.72E{-3}$	1.96	$4.32E{-4}$	2.00	$1.30E{-1}$	1.00	$6.27E{-3}$	1.93	$1.12E{-3}$	2.00	$3.38E{-1}$	1.00
320	$4.37E{-4}$	1.98	$1.08E{-4}$	2.00	$6.51E{-2}$	1.00	$1.61E{-3}$	1.96	$2.81E{-4}$	2.00	$1.69E{-1}$	1.00
640	$1.10E{-4}$	1.99	$2.70E{-5}$	2.00	$3.26E{-2}$	1.00	$4.07E{-4}$	1.98	$7.02E{-5}$	2.00	$8.46E{-2}$	1.00

Then we solve this interface problem on the same Cartesian meshes by both the bilinear IFE method proposed in [108] and the nonconforming rotated Q_1 IFE method. Errors of nonconforming rotated Q_1 Galerkin IFE solutions are presented in Table 5.4. Errors of the first component u_{1h} generated by these two IFE methods are also compared in Figure 5.5. The behavior of the approximations to the second component u_{2h} is similar; hence, related plots are omitted in this dissertation. Then, we compare these two IFE methods with a larger discontinuity in Lamé parameters, i.e., $\lambda^+ = 200$, $\lambda^- = 1$, $\mu^+ = 0.2$, $\mu^- = 0.001$, and $\nu^\pm \approx 0.4995$. Corresponding errors are listed in Table 5.5.

Figure 5.5: Errors of bilinear IFE solutions and nonconforming rotated Q_1 IFE solutions u_{1h}. From left to right: L^∞, L^2, H^1 norms.

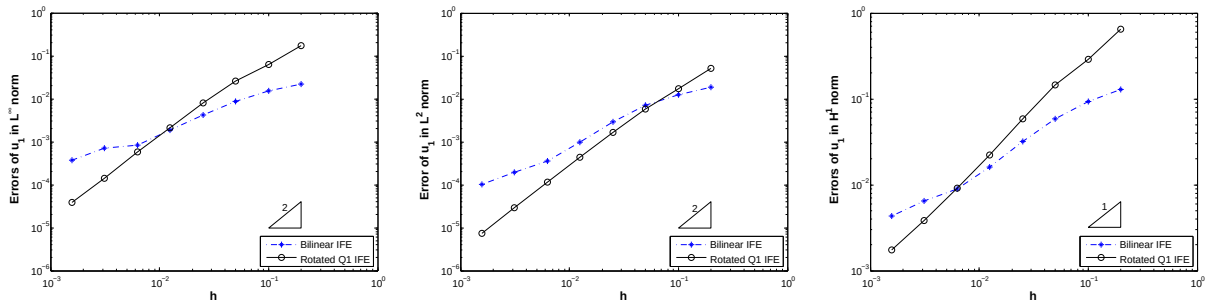

In our computations for nearly incompressible materials, the nonconforming rotated Q_1 IFE solutions $\mathbf{u}_h$ maintain the optimal convergence in the L^∞, L^2, and H^1 norms. We also observe a kind of super-convergence behavior in H^1 norm at the first several runs in this

Table 5.4: Errors of bilinear and nonconforming rotated Q_1 Galerkin IFE solutions in "locking" test with $\lambda^+ = 20$, $\lambda^- = 1$, $\mu^+ = 0.02$, $\mu^- = 0.001$, $\nu^{\pm} \approx 0.4995$.

	$u_{1h} - u_1$						$u_{2h} - u_2$					
N	$\|\cdot\|_{0,\infty,\Omega}$	rate	$\|\cdot\|_{0,\Omega}$	rate	$\|\cdot\|_{1,\Omega}$	rate	$\|\cdot\|_{0,\infty,\Omega}$	rate	$\|\cdot\|_{0,\Omega}$	rate	$\|\cdot\|_{1,\Omega}$	rate
Bilinear IFE Method												
10	$2.18E{-2}$		$1.89E{-2}$		$1.28E{-1}$		$4.18E{-2}$		$3.00E{-2}$		$2.49E{-1}$	
20	$1.53E{-2}$	0.51	$1.27E{-2}$	0.57	$9.39E{-2}$	0.44	$2.44E{-2}$	0.51	$2.06E{-2}$	0.54	$1.63E{-1}$	0.62
40	$8.74E{-3}$	0.80	$7.02E{-3}$	0.85	$5.82E{-2}$	0.69	$1.42E{-2}$	0.78	$1.20E{-2}$	0.78	$9.09E{-2}$	0.84
80	$4.14E{-3}$	1.08	$2.94E{-3}$	1.26	$3.18E{-2}$	0.87	$6.48E{-3}$	1.13	$4.88E{-3}$	1.29	$4.37E{-2}$	1.06
160	$1.85E{-3}$	1.17	$9.99E{-4}$	1.56	$1.62E{-2}$	0.98	$2.34E{-3}$	1.47	$1.68E{-3}$	1.54	$2.16E{-2}$	1.02
320	$8.47E{-4}$	1.12	$3.55E{-4}$	1.49	$8.91E{-3}$	0.86	$1.62E{-3}$	0.53	$5.96E{-4}$	1.49	$1.39E{-2}$	0.63
640	$7.01E{-4}$	0.27	$1.96E{-4}$	0.86	$6.51E{-3}$	0.45	$9.51E{-4}$	0.77	$2.93E{-4}$	1.02	$8.54E{-3}$	0.70
1280	$3.75E{-4}$	0.90	$1.03E{-4}$	0.93	$4.29E{-3}$	0.60	$4.16E{-4}$	1.19	$1.50E{-4}$	0.97	$5.14E{-3}$	0.73
Nonconforming Rotated Q_1 IFE Method												
10	$1.76E{-1}$		$5.08E{-2}$		$6.50E{-1}$		$9.69E{-2}$		$3.92E{-2}$		$5.36E{-1}$	
20	$6.21E{-2}$	1.50	$1.70E{-2}$	1.57	$2.91E{-1}$	1.16	$7.44E{-2}$	0.38	$1.48E{-2}$	1.41	$3.77E{-1}$	0.51
40	$2.60E{-2}$	1.26	$5.78E{-3}$	1.56	$1.45E{-1}$	1.01	$4.23E{-2}$	0.81	$5.27E{-3}$	1.49	$2.18E{-1}$	0.79
80	$8.02E{-3}$	1.70	$1.65E{-3}$	1.81	$5.80E{-2}$	1.32	$1.46E{-2}$	1.54	$1.53E{-3}$	1.78	$9.55E{-2}$	1.19
160	$2.14E{-3}$	1.91	$4.40E{-4}$	1.91	$2.24E{-2}$	1.37	$4.39E{-3}$	1.73	$4.12E{-4}$	1.90	$3.82E{-2}$	1.32
320	$5.77E{-4}$	1.92	$1.15E{-4}$	1.94	$9.07E{-3}$	1.30	$1.20E{-3}$	1.87	$1.08E{-4}$	1.94	$1.57E{-2}$	1.28
640	$1.43E{-4}$	2.01	$2.91E{-5}$	1.98	$3.86E{-3}$	1.23	$3.11E{-4}$	1.95	$2.74E{-5}$	1.97	$6.73E{-3}$	1.22
1280	$3.83E{-5}$	1.90	$7.33E{-6}$	1.99	$1.73E{-3}$	1.16	$8.08E{-5}$	1.94	$6.92E{-6}$	1.99	$3.02E{-3}$	1.16

Table 5.5: Errors of bilinear and nonconforming rotated Q_1 Galerkin IFE solutions in "locking" test with $\lambda^+ = 200$, $\lambda^- = 1$, $\mu^+ = 0.2$, $\mu^- = 0.001$, $\nu^{\pm} \approx 0.4995$.

	$u_{1h} - u_1$						$u_{2h} - u_2$					
N	$\|\cdot\|_{0,\infty,\Omega}$	rate	$\|\cdot\|_{0,\Omega}$	rate	$\|\cdot\|_{1,\Omega}$	rate	$\|\cdot\|_{0,\infty,\Omega}$	rate	$\|\cdot\|_{0,\Omega}$	rate	$\|\cdot\|_{1,\Omega}$	rate
Bilinear IFE Method												
10	$3.74E{-3}$		$2.37E{-3}$		$2.05E{-2}$		$4.18E{-3}$		$3.11E{-3}$		$2.55E{-2}$	
20	$4.07E{-3}$	-.12	$1.69E{-3}$	0.49	$2.11E{-2}$	-.04	$4.40E{-3}$	-.07	$2.20E{-3}$	0.49	$1.99E{-2}$	0.36
40	$3.66E{-3}$	0.15	$1.49E{-3}$	0.18	$2.03E{-2}$	0.05	$3.64E{-3}$	0.28	$1.41E{-3}$	0.65	$1.57E{-2}$	0.35
80	$3.53E{-3}$	0.05	$1.24E{-3}$	0.27	$1.97E{-2}$	0.05	$3.12E{-3}$	0.22	$8.96E{-4}$	0.65	$1.37E{-2}$	0.19
160	$1.93E{-3}$	0.87	$6.00E{-4}$	1.05	$1.27E{-2}$	0.63	$1.59E{-3}$	0.97	$4.41E{-4}$	1.02	$1.14E{-2}$	0.27
320	$6.97E{-4}$	1.47	$2.22E{-4}$	1.44	$6.05E{-3}$	1.07	$8.34E{-4}$	0.93	$1.64E{-4}$	1.43	$6.35E{-3}$	0.84
640	$3.83E{-4}$	0.86	$6.48E{-5}$	1.77	$3.58E{-3}$	0.76	$3.26E{-4}$	1.36	$6.18E{-5}$	1.41	$4.04E{-3}$	0.65
1280	$1.93E{-4}$	0.99	$2.42E{-5}$	1.42	$2.44E{-3}$	0.55	$1.61E{-4}$	1.02	$2.83E{-5}$	1.13	$2.88E{-3}$	0.49
Nonconforming Rotated Q_1 IFE Method												
10	$6.43E{-2}$		$1.50E{-2}$		$2.19E{-1}$		$2.99E{-2}$		$7.01E{-3}$		$1.08E{-1}$	
20	$2.11E{-2}$	1.61	$5.91E{-3}$	1.34	$1.01E{-1}$	1.12	$2.49E{-2}$	0.14	$3.83E{-3}$	0.87	$1.03E{-1}$	0.06
40	$1.51E{-2}$	0.48	$3.15E{-3}$	0.91	$7.99E{-2}$	0.34	$2.15E{-2}$	0.21	$2.71E{-3}$	0.50	$1.05E{-1}$	-.03
80	$6.20E{-3}$	1.29	$1.40E{-3}$	1.17	$4.32E{-2}$	0.89	$1.23E{-2}$	0.81	$1.26E{-3}$	1.10	$6.59E{-2}$	0.67
160	$1.87E{-3}$	1.73	$4.39E{-4}$	1.68	$1.75E{-2}$	1.30	$4.11E{-3}$	1.58	$4.01E{-4}$	1.65	$2.91E{-2}$	1.18
320	$5.27E{-4}$	1.83	$1.17E{-4}$	1.91	$6.60E{-3}$	1.41	$1.15E{-3}$	1.83	$1.08E{-4}$	1.90	$1.11E{-2}$	1.39
640	$1.45E{-4}$	1.86	$3.04E{-5}$	1.94	$2.44E{-3}$	1.43	$3.05E{-4}$	1.92	$2.82E{-5}$	1.93	$4.13E{-3}$	1.43
1280	$3.77E{-5}$	1.95	$7.73E{-6}$	1.98	$8.94E{-4}$	1.45	$7.90E{-5}$	1.95	$7.18E{-6}$	1.97	$1.49E{-3}$	1.47

experiment. As we refining meshes, it returns to the usual $O(h)$.

In comparison, these experiments indicate that the bilinear Galerkin IFE method encounters the "locking" phenomenon as expected. As the mesh size becomes small, the convergence rates are far below the optimal rates in the L^∞, L^2, and H^1 norms (see data in Tables 5.4

and 5.5 and illustrations in Figure 5.5). Therefore, these experiments strongly suggest that the nonconforming rotated Q_1 Galerkin IFE method is more reliable because of its desirable "locking-free" feature for solving the elasticity interface problems.

In the next few examples, we consider another interface problem described by (5.1)–(5.4) in which the interface is a straight line. Specifically, we assume that the interface Γ is a vertical straight line $x = x_0$ that divides the solution domain $\Omega = (-1, 1) \times (-1, 1)$ into two sub-domains, denoted by Ω^- and Ω^+, *i.e.*,

$$\Omega^- = \left\{(x, y)^t \in \Omega : x < x_0\right\}, \quad \Omega^+ = \left\{(x, y)^t \in \Omega : x > x_0\right\}. \tag{5.46}$$

The boundary condition function $\mathbf{g}$ and the load function $\mathbf{f}$ in this interface problem are chosen such that the exact solution $\mathbf{u}$ is as follows:

$$\mathbf{u}(x,y) = \begin{pmatrix} u_1(x,y) \\ u_2(x,y) \end{pmatrix} = \begin{cases} \begin{pmatrix} u_1^-(x,y) \\ u_2^-(x,y) \end{pmatrix} = \begin{pmatrix} \dfrac{1}{\lambda^- + 2\mu^-}(x - x_0)\cos(2xy) \\ \dfrac{1}{\mu^-}(x - x_0)\cos(2xy) \end{pmatrix} & \text{in } \Omega^-, \\ \begin{pmatrix} u_1^+(x,y) \\ u_2^+(x,y) \end{pmatrix} = \begin{pmatrix} \dfrac{1}{\lambda^+ + 2\mu^+}(x - x_0)\cos\big((x + x_0)y\big) \\ \dfrac{1}{\mu^+}(x - x_0)\cos\big((x + x_0)y\big) \end{pmatrix} & \text{in } \Omega^+. \end{cases} \tag{5.47}$$

Example 5.3. ***("Moving" Interface Test)****: In this experiment, we use one mesh to solve five elasticity interface problems whose interfaces have different locations as a kind of "moving" interface test.*

We let interfaces be vertical straight line located at $x = x_0$ where

$$x_0 = -\frac{\pi}{100}, \ -\frac{\pi}{200}, \ 0, \ \frac{\pi}{200}, \ \frac{\pi}{100},$$

The Cartesian mesh formed in $\Omega = (-1, 1) \times (-1, 1)$ contains 320×320 congruent squares. Lamé parameters in this experiment are $\lambda^+ = 2$, $\lambda^- = 1$, $\mu^+ = 3$, $\mu^- = 2$ which represent a typical compressible material configuration with a moderate coefficient jump. The materials are compressible such that $\nu^+ = 0.2, \nu^- \approx 0.1667$. Errors in the Galerkin IFE solutions generated on this fixed mesh are listed in Table 5.6. Data presented in this table indicate that IFE solutions to all of these interface problems have comparable accuracy in the L^∞, L^2, and semi-H^1 norms even though the interfaces locations differ in these problems. This phenomenon suggests that Galerkin IFE methods is potentially advantageous in applications that require to solve an elasticity interface problems with a sequence of material interfaces.

Note that when the interface line is at $x_0 = 0$, the interface line coincides with a mesh line $x = 0$. In this case, the mesh contains no interface elements so that the elasticity

interface problem is solved by nonconforming rotated Q_1 Galerkin FE method because of the consistency of the nonconforming rotated Q_1 IFE functions as stated in Lemma 5.3. Errors listed in Table 5.6 confirm that the IFE method can perform as accurately as the FE method, but the IFE method has the advantage that its mesh does not have to be generated according to the interface location.

Table 5.6: Errors of nonconforming rotated Q_1 Galerkin IFE solutions for problems whose interfaces are at different locations.

	$u_{1h}-u_1$			$u_{2h}-u_2$		
Interface: x_0	$\|\cdot\|_{0,\infty,\Omega}$	$\|\cdot\|_{0,\Omega}$	$\|\cdot\|_{1,\Omega}$	$\|\cdot\|_{0,\infty,\Omega}$	$\|\cdot\|_{0,\Omega}$	$\|\cdot\|_{1,\Omega}$
$-\pi/100$	$1.1777E{-5}$	$2.5923E{-6}$	$1.7824E{-3}$	$2.4343E{-5}$	$7.3793E{-6}$	$4.3019E{-3}$
$-\pi/200$	$1.1887E{-5}$	$2.6252E{-6}$	$1.8043E{-3}$	$2.4573E{-5}$	$7.4702E{-6}$	$4.3544E{-3}$
0	$1.1997E{-5}$	$2.6583E{-6}$	$1.8263E{-3}$	$2.4803E{-5}$	$7.5610E{-6}$	$4.4070E{-3}$
$\pi/200$	$1.2107E{-5}$	$2.6915E{-6}$	$1.8483E{-3}$	$2.5034E{-5}$	$7.6520E{-6}$	$4.4597E{-3}$
$\pi/100$	$1.2218E{-5}$	$2.7249E{-6}$	$1.8703E{-3}$	$2.5264E{-5}$	$7.7430E{-6}$	$4.5123E{-3}$

Example 5.4. ***(Boundary Layer Test)****: In this experiment, we assume that a straight line interface is located close to the boundary of* Ω*, i.e.,* $x=-1+\pi/300$*. The sub-domain* Ω^- *becomes a very thin layer.*

If the standard FE method is used to solve this interface problem, the body-fitting restriction requires that a solution mesh has to be fine enough around the interface so that an element can be placed entirely inside the thin layer. Generating a body-fitting mesh for a solution domain with a boundary layer is not only complicated, but also leads to an unstructured mesh with a large number of degrees of freedom usually. Since an IFE method allows interfaces to be immersed in some elements, a simple Cartesian mesh with much less degrees of freedom can be used for solving the same interface problem.

In Figure 5.6, we compare these two types of meshes for the thin layer interface problem. The body-fitting mesh on the left has 5128 triangular elements while the Cartesian mesh on the right contains only 400 rectangles. If the linear FE method are used on the body-fitting mesh to solve this boundary layer interface problem, the number of global degrees of freedom is 5402. On the other hand, if we solve by nonconforming rotated Q_1 Galerkin IFE method on the Cartesian mesh, the number of global degrees of freedom is 1600. Comparing of these numbers indicates that the computational costs for IFE method is much less than the FE method. Errors in both methods are listed in Table 5.7. We can observe that the accuracies of solutions obtained by smaller IFE systems and by the much larger FE system are not much different. Therefore, the IFE method has its advantage over the FE method for interface problems with thin layers.

Next, we test the convergence of the nonconforming rotated Q_1 Galerkin IFE method for this boundary layer interface. We test for both compressible ($\lambda^+=2$, $\lambda^-=1$, $\mu^+=3$, $\mu^-=2$,

Figure 5.6: A comparison of body-fitting triangular mesh with a non-body-fitting Cartesian mesh for a boundary layer problem.

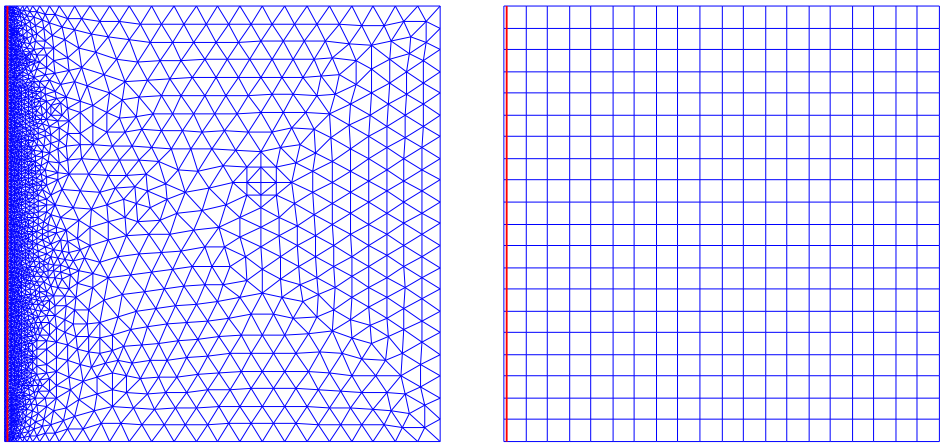

Table 5.7: Comparison of errors of the linear FE and nonconforming rotated Q_1 IFE solutions for the boundary layer example with $\lambda^+ = 2$, $\lambda^- = 1$, $\mu^+ = 3$, $\mu^- = 2$, $\nu^+ = 0.2, \nu^- \approx 0.1667$.

	$u_{1h} - u_1$			$u_{2h} - u_2$		
Method	$\|\cdot\|_{0,\infty,\Omega}$	$\|\cdot\|_{0,\Omega}$	$\|\cdot\|_{1,\Omega}$	$\|\cdot\|_{0,\infty,\Omega}$	$\|\cdot\|_{0,\Omega}$	$\|\cdot\|_{1,\Omega}$
FE method	$3.61E{-}4$	$2.38E{-}4$	$7.17E{-}3$	$7.16E{-}4$	$5.53E{-}4$	$1.89E{-}2$
IFE method	$8.70E{-}4$	$1.97E{-}4$	$8.42E{-}3$	$1.96E{-}3$	$5.34E{-}4$	$2.20E{-}2$

$\nu^+ = 0.2$, $\nu^- \approx 0.1667$) and the nearly incompressible ($\lambda^+ = 2000$, $\lambda^- = 1000$, $\mu^+ = 3$, $\mu^- = 1$, $\nu^+ \approx 0.4993$, $\nu^- \approx 0.4995$) materials. Errors of IFE solutions are listed in Table 5.8 and Table 5.9, respectively. Numerical results indicate that the nonconforming rotated Q_1 IFE method can solve the thin layer elasticity interface problem optimally in L^∞, L^2 and H^1 norms for both compressible and nearly incompressible materials. In Figure 5.7, we plot error data in different norms for the incompressible material configuration for an illustration of the convergence behavior.

We note that, in the first few runs until the mesh size reaches $h = 2/160$, the interface $x = -1 + \pi/300$ is completely in the first layer of elements adjacent to the left boundary of Ω. But on those meshes whose mesh sizes are $2/320$ and smaller, the interface line is no longer in the first layer of elements. This property demonstrates the robustness of this Galerkin IFE method from the point of view of the interface location in a mesh.

Similar to the Example 5.2, the errors in H^1 norm for a nearly incompressible case in Table 5.9 demonstrate a kind of super-convergence behavior with coarse meshes. As we continue mesh refinement, the convergence rate tends to be an optimal $O(h)$ order.

Table 5.8: Errors of nonconforming rotated Q_1 IFE solutions for the boundary layer example with $\lambda^+ = 2$, $\lambda^- = 1$, $\mu^+ = 3$, $\mu^- = 2$, $\nu^+ = 0.2, \nu^- \approx 0.1667$.

	$u_{1h} - u_1$						$u_{2h} - u_2$					
N	$\|\cdot\|_{0,\infty,\Omega}$	rate	$\|\cdot\|_{0,\Omega}$	rate	$\|\cdot\|_{1,\Omega}$	rate	$\|\cdot\|_{0,\infty,\Omega}$	rate	$\|\cdot\|_{0,\Omega}$	rate	$\|\cdot\|_{1,\Omega}$	rate
10	$3.15E{-3}$		$7.52E{-4}$		$1.68E{-2}$		$7.40E{-3}$		$2.03E{-3}$		$4.38E{-2}$	
20	$8.70E{-4}$	1.86	$1.97E{-4}$	1.94	$8.42E{-3}$	1.00	$1.96E{-3}$	1.92	$5.34E{-4}$	1.93	$2.20E{-2}$	1.00
40	$2.37E{-4}$	1.87	$5.07E{-5}$	1.95	$4.22E{-3}$	1.00	$5.36E{-4}$	1.87	$1.38E{-4}$	1.95	$1.10E{-2}$	1.00
80	$7.09E{-5}$	1.74	$1.30E{-5}$	1.97	$2.12E{-3}$	0.99	$1.53E{-4}$	1.81	$3.51E{-5}$	1.97	$5.52E{-3}$	0.99
160	$2.32E{-5}$	1.61	$3.24E{-6}$	2.00	$1.07E{-3}$	0.99	$4.61E{-5}$	1.73	$8.76E{-6}$	2.00	$2.78E{-3}$	0.99
320	$5.95E{-6}$	1.97	$8.18E{-7}$	1.98	$5.34E{-4}$	1.00	$1.28E{-5}$	1.85	$2.22E{-6}$	1.98	$1.39E{-3}$	1.00
640	$1.48E{-6}$	2.01	$2.04E{-7}$	2.00	$2.67E{-4}$	1.00	$3.38E{-6}$	1.92	$5.54E{-7}$	2.00	$6.94E{-4}$	1.00

Table 5.9: Errors of nonconforming rotated Q_1 IFE solutions for the boundary layer example with $\lambda^+ = 2000$, $\lambda^- = 1000$, $\mu^+ = 3$, $\mu^- = 1$, $\nu^+ \approx 0.4993$, and $\nu^- \approx 0.4995$.

	$u_{1h} - u_1$						$u_{2h} - u_2$					
N	$\|\cdot\|_{0,\infty,\Omega}$	rate	$\|\cdot\|_{0,\Omega}$	rate	$\|\cdot\|_{1,\Omega}$	rate	$\|\cdot\|_{0,\infty,\Omega}$	rate	$\|\cdot\|_{0,\Omega}$	rate	$\|\cdot\|_{1,\Omega}$	rate
10	$7.63E{-2}$		$6.63E{-2}$		$2.56E{-1}$		$8.86E{-2}$		$6.98E{-2}$		$2.89E{-1}$	
20	$1.83E{-2}$	2.06	$1.69E{-2}$	1.97	$6.76E{-2}$	1.92	$2.26E{-3}$	1.97	$1.78E{-2}$	1.98	$7.71E{-2}$	1.91
40	$4.69E{-3}$	1.96	$4.41E{-3}$	1.94	$1.93E{-2}$	1.81	$5.66E{-3}$	2.00	$4.52E{-3}$	1.97	$2.26E{-2}$	1.77
80	$1.23E{-3}$	1.93	$1.19E{-3}$	1.89	$6.58E{-3}$	1.55	$1.45E{-3}$	1.96	$1.17E{-3}$	1.95	$8.72E{-3}$	1.37
160	$3.23E{-4}$	1.93	$3.20E{-4}$	1.90	$2.81E{-3}$	1.23	$3.71E{-4}$	1.97	$3.07E{-4}$	1.94	$4.05E{-3}$	1.11
320	$8.00E{-5}$	2.01	$7.88E{-5}$	2.02	$1.29E{-4}$	1.12	$9.23E{-5}$	2.01	$7.59E{-5}$	2.01	$1.74E{-3}$	1.22
640	$1.98E{-5}$	2.01	$1.95E{-5}$	2.02	$6.31E{-4}$	1.03	$2.30E{-5}$	2.01	$1.88E{-5}$	2.01	$8.39E{-4}$	1.05
1280	$4.99E{-6}$	1.99	$4.91E{-6}$	1.99	$3.16E{-4}$	1.00	$5.76E{-6}$	2.00	$4.74E{-6}$	1.99	$4.17E{-4}$	1.01

Figure 5.7: Errors of nonconforming rotated Q_1 IFE solutions $\mathbf{u}_h$ for the boundary layer example in different norms.

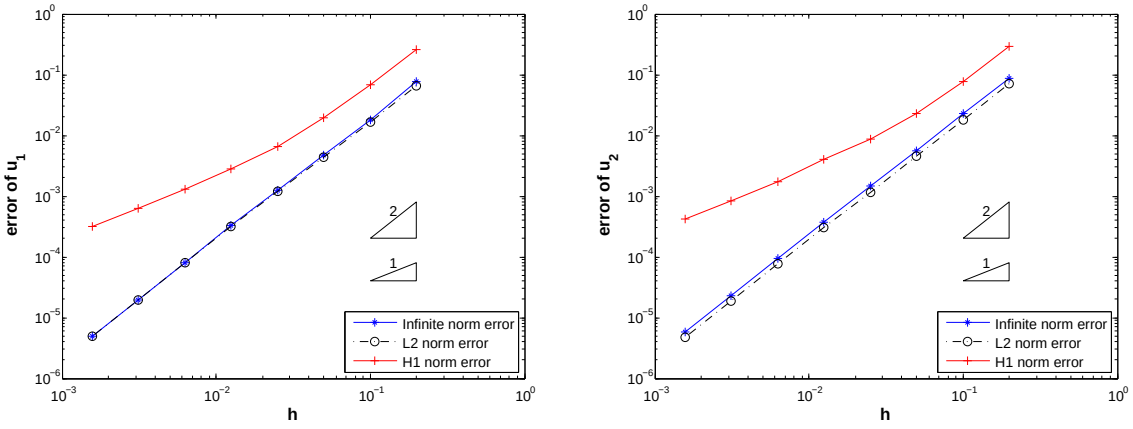

Chapter 6

Applications of IFEs to Moving Interface Problems

Many simulations in science and engineering involves a moving interface. For instance, the Stefan problem [34] describes the temperature distribution in the melting process of ice passing into water. In this simulation, the interface evolves.

As we already shown in previous chapters, in IFE methods, solution meshes are independent of the interface. For stationary interface problems, such as the elliptic and elasticity interface problems, IFE methods can use Cartesian meshes even if the interface has a nontrivial geometry. Consequently, for time dependent problems involving moving interfaces, the immediate benefit to use IFE methods is that a fixed Cartesian mesh can be used throughout the whole simulation.

In this chapter, we consider potential applications of IFE methods to moving interface problems. For simplicity, we assume that the interface location is known *a priori* for each time considered, and our effort here focus on how to solve the governing PDE efficiently. We acknowledge that in practice, the locations of moving interfaces are barely known *a priori*, but we hope the preliminary results here can be combined with evolution techniques such as front tracking methods [58, 59, 81, 138], and level set methods [19, 116, 117, 131] to solve true moving interface problems arising in applications.

In Section 6.1, we describe the parabolic type moving interface problems and discuss shortcomings and advantages of FE and IFE schemes for solving these problems. In Section 6.2, we discuss the IFE method of lines (MoL) using semi-discrete schemes for solving the parabolic moving interface problems. In Section 6.3, we consider fully discrete Crank-Nicolson (CN) IFE schemes as alternative approaches for solving these moving interface problems. In Section 6.4, we discuss some implementation issues for the IFE-MoL semi-discrete and CN-IFE fully discrete schemes. In Section 6.5, we provide numerical experiments to demonstrate features of the proposed IFE methods. Some of the materials in this chapter have been

reported in articles [75, 102].

6.1 Introduction

We consider the following parabolic moving interface problem:

$$\begin{aligned} u_t - \nabla \cdot (\beta \nabla u) &= f(t, X), \quad \text{if } X \in \Omega,\ t \in (0, T_{end}], && (6.1)\\ u(t, X) &= g(t, X), \quad \text{if } X \in \partial\Omega,\ t \in (0, T_{end}], && (6.2)\\ u(0, X) &= u_0(X), \quad \text{if } X \in \overline{\Omega}. && (6.3) \end{aligned}$$

Here, the domain $\Omega \subset \mathbb{R}^2$ is assumed to be an open rectangle (or a union of open rectangles) that is separated into two sub-domains $\Omega^+(t)$ and $\Omega^-(t)$ by a moving interface curve $\Gamma(t)$ defined by a smooth function $\Gamma : [0, T_{end}] \to \Omega$, see Figure 6.1 for an illustration of the solution domain Ω.

Figure 6.1: Solution domain of moving interface problems.

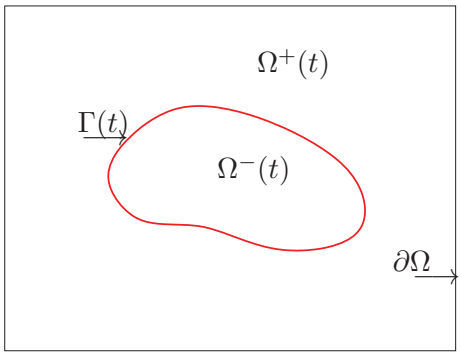

The diffusion coefficient $\beta(t, X)$ is discontinuous across the moving interface $\Gamma(t)$, which is assumed to be known *a priori*. For simplicity, we assume that $\beta(t, X)$ is a piece-wise constant function defined as follows:

$$\beta(t, X) = \begin{cases} \beta^-, & \text{if } X \in \Omega^-(t), \\ \beta^+, & \text{if } X \in \Omega^+(t). \end{cases} \qquad (6.4)$$

Across the moving interface $\Gamma(t)$, the solution $u(t, X)$ is required to satisfy the usual jump conditions:

$$\begin{aligned} [u]|_{\Gamma(t)} &= 0, && (6.5)\\ [\beta \nabla u \cdot \mathbf{n}]|_{\Gamma(t)} &= 0. && (6.6) \end{aligned}$$

Conventional finite element methods can solve the time dependent PDEs satisfactorily [137]. In dealing with interface problems, if the interface does not change its shape and location, then methods such as those discussed in [137] can be straightforwardly utilized provided that the meshes are tailored to match the interface [9, 26, 39].

However, the requirement of using body-fitting mesh makes traditional FE methods inefficient for solving moving interface problems. First, for a problem with a moving interface, the body-fitting restriction requires a new mesh to be generated at each time level. This is usually a time-consuming task, especially for those applications with complicated moving interface. Secondly, if the interface changes with respect to time in a problem, as the consequence of having to use body-fitting meshes, the number and locations of global degrees of freedom and elements in meshes at two consecutive time levels in a method based on traditional FE functions will usually be different, and this causes many difficulties including, but not limited to, those in the following list:

- **Change in Solution Dimensions**: Different number of elements in body-fitting meshes at two different time levels implies that the finite element spaces used at these time levels will usually have different global degrees of freedom. Consequently, the related FE equations (in either a semi-discrete scheme or a fully discrete scheme) will be defined through a non-square algebraic system which demands more efforts to solve. We note that it is possible to generate body-fitting meshes with the same number of elements at different time levels for a domain with a moving interface, but this usually requests an extra computational cost and has a great potential of losing accuracy unless the geometry of the interface changes in a simple way.

- **Loss of Local Assembling Feature**: The so-called "local assembling" procedure is one of the most desirable features of FE methods. To assemble a global matrix in the algebraic system of a FE method, one can first construct the related local matrix in each element and then assemble its entries into the global matrix. This simplicity is lost for a moving interface problem when assembling a global matrix involving FE functions defined at two different time levels because their meshes usually do not share any common elements. Complicated and time consuming quadrature procedures have to be developed for assembling matrices in conventional FE methods.

- **Inapplicability of Methods of Lines**: The method of lines (MoL) [124, 140, 152] is an efficient technique for solving initial boundary value problems of parabolic PDEs. This technique reduces a PDE initial boundary value problem to an initial value problem of a system of ODEs. One can then solve this ODE system via an ODE solver with desirable features to generate a solution to the original PDE problem. The abundant choices of efficient and robust ODE solvers make the MoL popular for solving the time dependent PDEs. However, for problems with moving interfaces, the body-fitting restriction on the meshes makes the application of the MoL difficult, if not impossible, in the FE formulation. The main obstacle is the change of global degrees of freedom

with respect to the time, possibly in both number and locations, and this forbids a correct formulation of the ODEs in the semi-discretization for a time dependent PDE to be solved.

Compared with a conventional FE space, an IFE space has two key features. First, by allowing the mesh to be independent of the interface, an IFE space can be defined on Cartesian meshes for interface problems with a nontrivial geometry without loss of accuracy. Second, instead of universal polynomials in each element of a mesh, an IFE function in each element cut by the interface is a piecewise polynomial of a specified degree constructed according to the interface jump conditions.

Therefore, we can use IFE functions to carry out the discretization in the spatial variables over a fixed structured (Cartesian) mesh for a parabolic PDE whose diffusion coefficient is discontinuous across a moving interface. An immediate benefit of this approach is the avoidance of regenerating meshes through the whole computational procedure, even if the interface changes with respect to time. More importantly, even though the IFE spaces at different time levels are formed according to the location of the interface, the global degrees of freedom as well as their locations in all the IFE spaces used in the whole simulation can be maintained the same.

In the following sections, we discuss the IFE method of lines semi-discrete schemes and Crank-Nicolson IFE fully discrete schemes for solving parabolic type moving interface problems.

6.2 IFE Method of Lines Semi-Discrete Schemes

In this section, we discuss the IFE method of line (MoL) semi-discrete schemes for solving the parabolic moving interface problem (6.1) - (6.6). We use linear IFE functions [95, 96] to carry out the discussion and we note that the proposed IFE-MoL schemes can be applied to other IFE functions especially nonconforming rotated Q_1 IFE functions.

Let $\mathcal{T}_h = \{T\}$ be a triangular Cartesian mesh of Ω as illustrated by the plot on the right in Figure 6.2. Let $\mathcal{T}_h^{i,t}$ and $\mathcal{T}_h^{n,t}$ denote the collections of interface elements and non-interface elements at the time t, respectively. In the discussion from now on, we assume that $\mathcal{T}_h = \mathcal{T}_h^{i,t} \cup \mathcal{T}_h^{n,t}$ does not change with respect to t while $\mathcal{T}_h^{i,t}$ and $\mathcal{T}_h^{n,t}$ may vary according to the interface location.

Let $\mathcal{N}_h = \mathcal{N}_h^0 \cup \mathcal{N}_h^b$ be the set of nodes of $\mathcal{T}_h$ where $\mathcal{N}_h^0$ and $\mathcal{N}_h^b$ denote the sets of interior nodes and boundary nodes, respectively. Also, we let $\mathcal{N}_h^{i,t}$ be the set of nodes of all interface elements at time t and let $\mathcal{N}_h^{n,t} = \mathcal{N}_h / \mathcal{N}_h^{i,t}$ be the set containing the rest of the nodes. Again, since $\mathcal{T}_h$ is time independent, the node set $\mathcal{N}_h$ is also time independent while $\mathcal{N}_h^{i,t}$ and $\mathcal{N}_h^{n,t}$ may change with respect to time.

Figure 6.2: A body-fitting triangular mesh (left) and a non-body-fitting triangular Cartesian mesh (right).

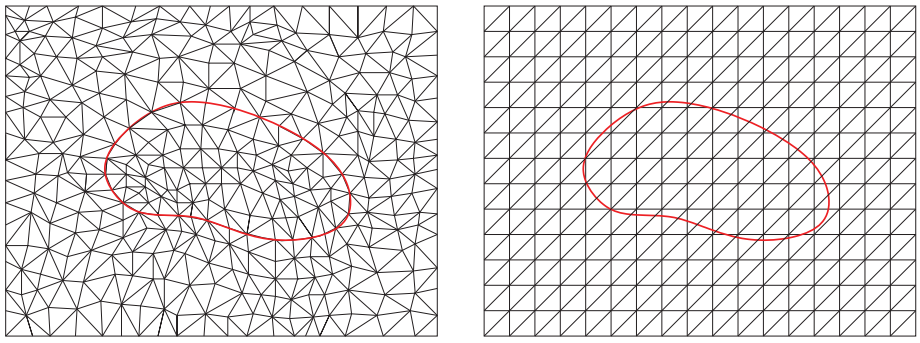

Let $S_h^t(\Omega)$ be the linear IFE space at time t. Note that each global basis function in $S_h^t(\Omega)$, denoted by ϕ_j, is associated with a node in the mesh. Therefore, a semi-discrete linear IFE solution to the parabolic interface problem (6.1) - (6.6) can be written in the following form:

$$u_h(t, X) = \sum_{X_j \in \mathcal{N}_h} u_j(t)\phi_j^t(X). \tag{6.7}$$

Here we put a superscript t on the global basis function ϕ_j^t to emphasize that some of the global basis functions depend on the interface location $\Gamma(t)$ and therefore depend on time t.

Taking the partial derivative with respect to t of the IFE solution in (6.7), we have

$$\frac{\partial u_h(t, X)}{\partial t} = \sum_{X_j \in \mathcal{N}_h} \frac{\partial u_j(t)}{\partial t}\phi_j^t(X) + \sum_{X_j \in \mathcal{N}_h^{i,t}} u_j(t)\frac{\partial \phi_j^t(X)}{\partial t}. \tag{6.8}$$

Note that the summation in the second term on the right hand side of (6.8) is only for nodes in $\mathcal{N}_h^{i,t}$ because the time derivative of $\phi_j^t(X)$ is zero if $X_j \notin \mathcal{N}_h^{i,t}$.

Now we derive the semi-discrete scheme for the moving interface problem starting from the following weak form at a given time t:

$$\int_\Omega \frac{\partial u}{\partial t} v \mathrm{d}X + \int_\Omega (\beta \nabla u) \cdot \nabla v \mathrm{d}X = \int_\Omega f v \mathrm{d}X, \quad \forall\ v \in H_0^1(\Omega), \tag{6.9}$$

which is equivalent to

$$\sum_{T \in \mathcal{T}_h} \int_T \frac{\partial u}{\partial t} v \mathrm{d}X + \sum_{T \in \mathcal{T}_h} \int_T (\beta \nabla u) \cdot \nabla v \mathrm{d}X = \int_\Omega f v \mathrm{d}X, \quad \forall\ v \in H_0^1(\Omega). \tag{6.10}$$

Consequently, this weak form leads to the following spatial discrete formulation: At each time $t \in (0, T_{end}]$, find $u_h(t,\cdot) \in S_h^t(\Omega)$, such that

$$\sum_{T\in\mathcal{T}_h}\int_T \frac{\partial u_h}{\partial t} v_h \mathrm{d}X + \sum_{T\in\mathcal{T}_h}\int_T (\beta\nabla u_h)\cdot\nabla v_h \mathrm{d}X = \int_\Omega f v_h \mathrm{d}X, \quad \forall\ v_h \in \mathring{S}_h^t(\Omega), \tag{6.11}$$

where $\mathring{S}_h^t(\Omega) = \mathrm{Span}\{\phi_j^t \in S_h^t(\Omega) : X_j \in \mathcal{N}_h^0\}$. Plugging (6.7) and (6.8) into (6.11), and substituting $\phi_i^t \in \mathring{S}_h^t(\Omega)$ for v_h, the above semi-discrete form becomes: Find the coefficient functions $u_j(t)$ in $u_h(t,X) = \sum_{X_j\in\mathcal{N}_h} u_j(t)\phi_j^t(X)$ such that

$$\begin{aligned}&\sum_{X_j\in\mathcal{N}_h} u_j'(t)\int_\Omega \phi_i^t\phi_j^t \mathrm{d}X + \sum_{X_j\in\mathcal{N}_{h,t}^i} u_j(t)\int_\Omega \phi_i^t\left(\frac{\partial}{\partial t}\phi_j^t\right)\mathrm{d}X\\ &+\sum_{X_j\in\mathcal{N}_h} u_j(t)\int_\Omega \beta\nabla\phi_i^t\cdot\nabla\phi_j^t \mathrm{d}X = \int_\Omega f\phi_i^t \mathrm{d}X, \qquad \forall\,\phi_i^t \in \mathring{S}_h^t(\Omega).\end{aligned}$$

Imposing the boundary condition (6.2), we obtain

$$\begin{aligned}&\sum_{X_j\in\mathcal{N}_h^0} u_j'(t)\int_\Omega \phi_i^t\phi_j^t \mathrm{d}X + \sum_{X_j\in\mathcal{N}_{h,t}^{i,0}} u_j(t)\int_\Omega \phi_i^t\left(\frac{\partial}{\partial t}\phi_j^t\right)\mathrm{d}X + \sum_{X_j\in\mathcal{N}_h^0} u_j(t)\int_\Omega \beta\nabla\phi_i^t\cdot\nabla\phi_j^t \mathrm{d}X\\ &\qquad = \int_\Omega f\phi_i^t \mathrm{d}X - \sum_{X_j\in\mathcal{N}_h^b} g_j'(t)\int_\Omega \phi_i^t\phi_j^t \mathrm{d}X - \sum_{X_j\in\mathcal{N}_{h,t}^{i,b}} g_j(t)\int_\Omega \phi_i^t\left(\frac{\partial}{\partial t}\phi_j^t\right)\mathrm{d}X\\ &\qquad\qquad - \sum_{X_j\in\mathcal{N}_h^b} g_j(t)\int_\Omega \beta\nabla\phi_i^t\cdot\nabla\phi_j^t \mathrm{d}X, \qquad \forall\,\phi_i^t \in \mathring{S}_h^t(\Omega)\end{aligned} \tag{6.12}$$

where $g_j(t) = g(t, X_j)$, for $X_j \in \mathcal{N}_h^b$. We can write (6.12) in the equivalent matrix form as follows

$$M(t)\mathbf{u}'(t) + \Big(K(t) + A(t)\Big)\mathbf{u}(t) = \mathbf{f}(t) - \mathbf{bc}(t), \tag{6.13}$$

with the initial condition

$$\mathbf{u}(0) = \mathbf{u_0}, \tag{6.14}$$

where

- $M(t) = (m_{ij}(t))$ is the mass matrix with $m_{ij} = \int_\Omega \phi_i^t\phi_j^t \mathrm{d}X$.
- $K(t) = (k_{ij}(t))$ with $k_{ij} = \int_\Omega \phi_i^t \frac{\partial\phi_j^t}{\partial t}\mathrm{d}X$.
- $A(t) = (a_{ij}(t))$ is the stiffness matrix with $a_{ij} = \int_\Omega \nabla\phi_i^t\cdot\left(\beta\nabla\phi_j^t\right)\mathrm{d}X$.
- $\mathbf{f}(t) = (f_i(t))$ is the source term vector with $f_i(t) = \int_\Omega f\phi_i^t \mathrm{d}X$.

- $\mathbf{u}(t) = (u_j(t))$, $\mathbf{u}'(t) = \big(u_j'(t)\big)$, and $\mathbf{u_0} = (u_0(X_j))$ with $X_j \in \mathcal{N}_h^0$.
- $\mathbf{bc}(t)$ is the boundary vector associated with the the last three terms in (6.12).

We call equations (6.13) and (6.14) an IFE-MoL for solving the parabolic moving interface problem (6.1) - (6.6).

Compared with the traditional semi-discrete FE method for the initial boundary value problems of parabolic equations, the IFE-MoL (6.13) contains an extra term involving matrix $K(t)$ that depends on the time derivative of IFE basis functions due to the moving interface. This method is consistent with the standard FE-MoL in the sense that the matrix $K(t)$ is a zero matrix and this method becomes the standard MoL if $\beta(t, X)$ is continuous, or if the interface is static and a body-fitting mesh is used.

Remark 6.1. *The matrix $K(t)$ is much sparser than the mass matrix $M(t)$ and the stiffness matrix $A(t)$, because only those IFE basis functions associated with interface nodes in $\mathcal{N}_h^{i,t}$ have non-zero time derivatives. When the mesh is fine enough, the majority of nodes are non-interface nodes which belong to $\mathcal{N}_h^{n,t}$. Consequently, it costs little time to assemble the matrix $K(t)$.*

The IFE-MoL (6.13) and (6.14) can be written in following standard ODE form for $\mathbf{u}(t)$

$$\mathbf{u}'(t) = \mathbf{F}(t, \mathbf{u}), \qquad \mathbf{u}(0) = \mathbf{u}_0. \tag{6.15}$$

where $\mathbf{u}_0 = (u_0(X_j))$, with $X_j \in \mathcal{N}_h^0$, and

$$\mathbf{F}(t, \mathbf{u}) = M^{-1}(t)\bigg(- \Big(K(t) + A(t)\Big)\mathbf{u}(t) + \mathbf{f}(t) - \mathbf{bc}(t)\bigg). \tag{6.16}$$

A preferred ODE solver can be used to solve this ODE system in the IFE-MoL.

Single Step Methods

Implicit Runge-Kutta (IRK) methods are good choices for the IFE-MoL because they are often A-stable and some of them work effectively for stiff problems. A general s-stage IRK method can be described conveniently in the following *Butcher diagram* [31]:

$$\begin{array}{c|cccc} c_1 & a_{11} & a_{12} & \cdots & a_{1s} \\ c_2 & a_{21} & a_{22} & \cdots & a_{2s} \\ \vdots & \vdots & \vdots & \ddots & \vdots \\ c_s & a_{s1} & a_{s2} & \cdots & a_{ss} \\ \hline & b_1 & b_2 & \cdots & b_s \end{array} \tag{6.17}$$

However, when a high order multistage fully implicit Runge-Kutta method is used, computing the stage values, denoted by $\mathbf{K}_i$, $i = 1, \cdots, s$, is usually a big hurdle. This is because we

have to solve for these vectors from an $(s\ dim(\mathbf{u})) \times (s\ dim(\mathbf{u}))$ block linear system whose dimension is very high when a fine mesh is used and the band structure is more complicated than that of each block. One possible way to alleviate this difficulty is to use a so-called Diagonally Implicit Runge-Kutta (DIRK) method [64] for which the coefficient matrix $(a_{ij})_{i,j=1}^{s}$ in (6.17) is a lower triangular matrix. In a DIRK method, $\mathbf{K}_i$, $i = 1, \cdots, s$ are determined by s decoupled linear systems, each of them is of the size $dim(\mathbf{u}) \times dim(\mathbf{u})$, and they all have the same band structure. Specifically, the s-stage DIRK scheme for solving (6.15) can described as follows:

Given $\mathbf{u}^n$, and τ, we find $\mathbf{u}^{n+1}$ by

1. Compute $\mathbf{K}_1$ by solving
$$\Big(M^{n+c_1} + a_{11}\tau\Big(K^{n+c_1} + A^{n+c_1}\Big)\Big)\,\mathbf{K}_1 = -\Big(K^{n+c_1} + A^{n+c_1}\Big)\mathbf{u}^n + \mathbf{f}^{n+c_1} - \mathbf{b}\mathbf{c}^{n+c_1}. \quad (6.18)$$

2. Compute $\mathbf{K}_i$, $i = 2, \cdots, s$, by solving
$$\begin{aligned}&\Big(M^{n+c_i} + a_{ii}\tau\Big(K^{n+c_i} + A^{n+c_i}\Big)\Big)\,\mathbf{K}_i\\ &= -\Big(K^{n+c_i} + A^{n+c_i}\Big)(\mathbf{u}^n + \tau\sum_{j=1}^{i-1} a_{ij}\mathbf{K}_j) + \mathbf{f}^{n+c_i} - \mathbf{b}\mathbf{c}^{n+c_i}. \quad (6.19)\end{aligned}$$

3. Find $\mathbf{u}^{n+1}$ from
$$\mathbf{u}^{n+1} = \mathbf{u}^n + \tau\sum_{i=1}^{s} b_i\mathbf{K}_i. \quad (6.20)$$

Here
$$A^{n+c_i} = A(t_n + c_i\tau),\ K^{n+c_i} = K(t_n + c_i\tau),\ M^{n+c_i} = M(t_n + c_i\tau),\quad 1 \le i \le s,$$
with the matrices $A(t), K(t)$ and $M(t)$ defined in (6.13). The same convention applies to the involved vectors.

Multi-step Methods

Compared to the DIRK methods, linear multi-step methods usually require less function evaluations per time step. The family of *Adams Methods* are popular for non-stiff problems, and *Backward Difference Formula* (BDF) methods are effective for stiff systems [7]. Since the ODE system in a MoL for an initial boundary value problem of a time dependent PDE is usually stiff, BDF methods are usually preferable. A k-step BDF method [7] can be written as
$$\sum_{i=0}^{k} \alpha_i\mathbf{u}^{n+1-i} = h\beta_0\mathbf{F}^{n+1}, \quad (6.21)$$

where $\mathbf{F}^{n+1} = \mathbf{F}(t_{n+1}, \mathbf{u}_{n+1})$. The k-step BDF scheme for solving (6.15) are described as follows:

Given $\mathbf{u}^{n-k+1}$, $\mathbf{u}^{n-k+2}$, $\cdots$, $\mathbf{u}^n$ and τ, we find $\mathbf{u}^{n+1}$ by solving

$$\Big(\alpha_0 M^{n+1} + \tau\beta_0(A^{n+1} + K^{n+1})\Big)\mathbf{u}^{n+1} = \tau\beta_0(\mathbf{f}^{n+1} - \mathbf{bc}^{n+1}) - M^{n+1}\sum_{i=1}^{k}\alpha_i\mathbf{u}^{n+1-i}, \quad (6.22)$$

where

$$A^{n+1} = A(t_{n+1}),\ K^{n+1} = K(t_{n+1}),\ M^{n+1} = M(t_{n+1}),$$

and the same convention applies to vectors.

Comparison of Single Step and Multi-Step Methods

A single step method approximates $\mathbf{u}^{n+1}$ by taking into account only the behavior of $\mathbf{u}(t)$ between t_n and t_{n+1}, while a multi-step method require information from a number of previous time steps. This means a single step method needs nothing except $\mathbf{u}_0$ to start up the iteration in time. On the other hand, to start a multi-step method, k initial values $\mathbf{u}_0, \cdots, \mathbf{u}_{k-1}$ are required. Usually, an appropriate single step method can be used to generate the rest of the initial values $\mathbf{u}_1, \cdots, \mathbf{u}_{k-1}$.

To achieve a comparable high order accuracy, a multi-step method usually requires less matrices assembling and less linear system solving at each time step than a DIRK method. At each time level, the BDF method (6.22) needs to generate $2 + \epsilon$ matrices, which are $M(t)$, $A(t)$ and $K(t)$, and solve only one linear system. Here ϵ emphasizes the fact that assembling $K(t)$ costs significantly much less time than $M(t)$, $A(t)$. On the other hand, an s-stage DIRK method needs to assemble $s(2+\epsilon)$ matrices and solve s linear systems at each time step. We also note that single step methods are convenient for the implementation of adaptivity in the time step size which is usually preferred for producing a reliable solution to a complicated ODE system.

6.3 Crank-Nicolson IFE Fully Discrete Algorithms

In this section, we consider fully discrete Crank-Nicolson IFE algorithms as alternative approaches for solving the parabolic moving interface problem (6.1) - (6.6).

We will consider two basic discretization procedures for a time-dependent problem. One of them is to discretize the space variables followed by the time variable, and the other one carries out the procedure in the reversed order.

CN-IFE Algorithm 1

As in Section 6.2, we carry out the spatial discretization first followed by the discretization in time. Linear IFE approximations are used to discrete in space. For time discretization, we use a uniform partition $0 = t_0 < t_1 < \cdots < t_{N_t} = T_{end}$, where $t_n = n\tau$ with $\tau = T_{end}/N_t$. Then we look for $\mathbf{u}^n = (u_j^n) \approx \mathbf{u}(t_n)$, for $n = 1, 2, \cdots, N_t$ in

$$u_h^n(X) = \sum_{X_j \in \mathcal{N}_h} u_j^n \phi_j^{t_n}(X)$$

to approximate $u(t_n, X)$. We apply the Crank-Nicolson scheme to fully discretize (6.13), then we obtain

$$M_h(t_{n+\frac{1}{2}}) \frac{\mathbf{u}^{n+1} - \mathbf{u}^n}{\tau} + \left(A_h(t_{n+\frac{1}{2}}) + K_h(t_{n+\frac{1}{2}}) \right) \frac{\mathbf{u}^{n+1} + \mathbf{u}^n}{2} = \mathbf{f}(t_{n+\frac{1}{2}}). \tag{6.23}$$

For simplicity, we assume the Dirichlet boundary condition is homogeneous, *i.e.*, $g = 0$. To facilitate the following discussion, we introduce some notations with multiple superscripts to describe the evaluations of different functions at different time levels. Let n_v, n_u, n_β, and n_f denote the time levels for the test function v, trial function u, coefficient function β, source function f, respectively. Then, we define the matrices and vectors as follows:

- $M_h^{n_v,n_u} = \left(m_{ij}^{n_v,n_u}\right)$ is mass matrix, where $m_{ij}^{n_v,n_u} = \int_\Omega \phi_i^{t_{n_v}} \phi_j^{t_{n_u}} \mathrm{d}X$.
- $A_h^{n_\beta,n_v,n_u} = \left(a_{ij}^{n_\beta,n_v,n_u}\right)$ is stiffness matrix, where $a_{ij}^{n_\beta,n_v,n_u} = \int_\Omega \nabla\phi_i^{t_{n_v}} \cdot (\beta^{t_{n_\beta}} \nabla\phi_j^{t_{n_u}}) \mathrm{d}X$.
- $K_h^{n_v,n_u} = \left(k_{ij}^{n_v,n_u}\right)$, where $k_{ij}^{n_v,n_u} = \int_\Omega \phi_i^{t_{n_v}} \left(\frac{\partial}{\partial t}\phi_j^{t_{n_u}}\right) \mathrm{d}X$.
- $\mathbf{f}^{n_v,n_f} = \left(f_i^{n_v,n_f}\right)$ is right hand side vector, where $f_i^{n_v,n_f} = \int_\Omega \phi_i^{t_{n_v}} f^{t_{n_f}} \mathrm{d}X$.

Using the above notations, we write (6.23) as follows

$$M_h^{n+\frac{1}{2},n+\frac{1}{2}} \frac{\mathbf{u}^{n+1} - \mathbf{u}^n}{\tau} + \left(A_h^{n+\frac{1}{2},n+\frac{1}{2},n+\frac{1}{2}} + K_h^{n+\frac{1}{2},n+\frac{1}{2}} \right) \frac{\mathbf{u}^{n+1} + \mathbf{u}^n}{2} = \mathbf{f}^{n+\frac{1}{2},n+\frac{1}{2}}, \tag{6.24}$$

which leads to the first algorithm: Given $\mathbf{u}^n$, we find $\mathbf{u}^{n+1}$ by

- **CN-IFE Algorithm 1**

$$\begin{aligned} &\left(M_h^{n+\frac{1}{2},n+\frac{1}{2}} + \frac{\tau}{2} A_h^{n+\frac{1}{2},n+\frac{1}{2},n+\frac{1}{2}} + \frac{\tau}{2} K_h^{n+\frac{1}{2},n+\frac{1}{2}} \right) \mathbf{u}^{n+1} \\ &\quad = \left(M_h^{n+\frac{1}{2},n+\frac{1}{2}} - \frac{\tau}{2} A_h^{n+\frac{1}{2},n+\frac{1}{2},n+\frac{1}{2}} - \frac{\tau}{2} K_h^{n+\frac{1}{2},n+\frac{1}{2}} \right) \mathbf{u}^n + \tau \mathbf{f}^{n+\frac{1}{2},n+\frac{1}{2}}. \end{aligned}$$

CN-IFE Algorithm 2

Another approach to obtain a fully discrete formulation is to discretize in time first, and then in space. In this way, the matrix $K_h^{n+\frac{1}{2},n+\frac{1}{2}}$ caused by the time derivative of IFE basis functions will not appear in the fully discrete formulation.

This procedure can be carried out as follows. We evaluate the parabolic equation (6.1) at time $t_{n+\frac{1}{2}}$ to have

$$u_t(t_{n+\frac{1}{2}},X)-\nabla\cdot(\beta(t_{n+\frac{1}{2}},X)\nabla u(t_{n+\frac{1}{2}},X))=f(t_{n+\frac{1}{2}},X). \tag{6.25}$$

Using central difference to approximate the time derivative in (6.25) leads to

$$\frac{u(t_{n+1},X)-u(t_n,X)}{\tau}-\nabla\cdot(\beta(t_{n+\frac{1}{2}},X)\nabla u(t_{n+\frac{1}{2}},X))\approx f(t_{n+\frac{1}{2}},X). \tag{6.26}$$

Multiplying a test function $v\in H_0^1(\Omega)$ on both side of (6.26), integrating over Ω, and applying Green's formula, we obtain

$$\begin{aligned}&\sum_{T\in\mathcal{T}_h}\int_T v(X)\frac{u(t_{n+1},X)-u(t_n,X)}{\tau}\mathrm{d}X\\ &+\sum_{T\in\mathcal{T}_h}\int_T\nabla v(X)\cdot\Big(\beta(t_{n+\frac{1}{2}},X)\nabla u(t_{n+\frac{1}{2}},X)\Big)\mathrm{d}X\\ \approx&\int_\Omega v(X)f(t_{n+\frac{1}{2}},X)\mathrm{d}X,\quad\forall v\in H_0^1(\Omega).\end{aligned} \tag{6.27}$$

We approximate $\nabla u(t_{n+\frac{1}{2}},X)$ by the average of $\nabla u(t_n,X)$ and $\nabla u(t_{n+1},X)$, then (6.27) yields

$$\begin{aligned}&\sum_{T\in\mathcal{T}_h}\int_T v(X)\frac{u(t_{n+1},X)-u(t_n,X)}{\tau}\mathrm{d}X+\\ &\qquad\sum_{T\in\mathcal{T}_h}\int_T\nabla v(X)\cdot\Big(\beta(t_{n+\frac{1}{2}},X)\frac{\nabla u(t_{n+1},X)+\nabla u(t_n,X)}{2}\Big)\mathrm{d}X\\ \approx&\int_\Omega v(X)f(t_{n+\frac{1}{2}},X)\mathrm{d}X,\quad\forall v\in H_0^1(\Omega).\end{aligned}$$

Then, we can introduce the discretization in space to obtain the following fully discrete scheme: Given $u_h^n\in S_{h,t_n}(\Omega)$, we find $u_h^{n+1}\in S_{h,t_{n+1}}(\Omega)$ in

$$\begin{aligned}&\sum_{T\in\mathcal{T}_h}\int_T v_h(X)\frac{u_h^{n+1}(X)-u_h^n(X)}{\tau}\mathrm{d}X+\\ &\qquad\sum_{T\in\mathcal{T}_h}\int_T\nabla v_h(X)\cdot\Big(\beta(t_{n+1/2},X)\frac{\nabla u_h^{n+1}(X)+\nabla u_h^n(X)}{2}\Big)\mathrm{d}X\\ =&\int_\Omega v_h(X)f(t_{n+\frac{1}{2}},X)\mathrm{d}X,\quad\forall v_h\in\mathring{S}_{h,t_{n+1/2}}.\end{aligned}$$

It is equivalent to: Given $\mathbf{u}^n$, we find $\mathbf{u}^{n+1}$ from the following equations,

$$\begin{aligned}
&\left(\frac{1}{\tau}\sum_{X_j\in\mathcal{N}_h}\int_\Omega \phi_i^{t_{n+1/2}}\phi_j^{t_{n+1}}\mathrm{d}X+\frac{1}{2}\sum_{X_j\in\mathcal{N}_h}\int_\Omega \nabla\phi_i^{t_{n+1/2}}\cdot\left(\beta^{t_{n+1/2}}\nabla\phi_j^{t_{n+1}}\right)\mathrm{d}X\right)\mathbf{u}^{n+1}\\
&+\left(-\frac{1}{\tau}\sum_{X_j\in\mathcal{N}_h}\int_\Omega \phi_i^{t_{n+1/2}}\phi_j^{t_n}\mathrm{d}X+\frac{1}{2}\sum_{X_j\in\mathcal{N}_h}\int_\Omega \nabla\phi_i^{t_{n+1/2}}\cdot\left(\beta^{t_{n+1/2}}\nabla\phi_j^{t_n}\right)\mathrm{d}X\right)\mathbf{u}^{n}\\
=&\int_\Omega \phi_i^{t_{n+1/2}}f^{t_{n+1/2}}\mathrm{d}X,\qquad \forall\,\phi_i^{t_{n+1/2}}\in\mathring{S}_{h,t_{n+1/2}}.
\end{aligned}$$

Writing the above equation using the following matrix notations leads to our second algorithm

- **CN-IFE Algorithm 2**

$$\boxed{\left(M_h^{n+\frac{1}{2},n+1}+\frac{\tau}{2}A_h^{n+\frac{1}{2},n+\frac{1}{2},n+1}\right)\mathbf{u}^{n+1}=\left(M_h^{n+\frac{1}{2},n}-\frac{\tau}{2}A_h^{n+\frac{1}{2},n+\frac{1}{2},n}\right)\mathbf{u}^{n}+\tau\mathbf{f}^{n+\frac{1}{2},n+\frac{1}{2}}.}$$

The CN-IFE Algorithm 2 is a natural extension of the classic Crank-Nicolson Algorithm for treating the moving interface. However, the matrices in this algorithm are defined by function values at different time levels.

CN-IFE Algorithm 3

Note that IFE functions are made to preserve the continuity of flux on the interface. Therefore we may average the flux instead of the gradient of u in (6.27) to have

$$\begin{aligned}
&\sum_{T\in\mathcal{T}_h}\int_T v(X)\frac{u(t_{n+1},X)-u(t_n,X)}{\tau}\mathrm{d}X+\\
&\qquad\sum_{T\in\mathcal{T}_h}\int_T\nabla v(X)\cdot\Big(\frac{\beta(t_{n+1},X)\nabla u(t_{n+1},X)+\beta(t_n,X)\nabla u(t_n,X)}{2}\Big)\mathrm{d}X\\
\approx&\int_\Omega v(X)f(t_{n+\frac{1}{2}},X)\mathrm{d}X,\quad\forall v\in H_0^1(\Omega).
\end{aligned}$$

Then, we can further discretize the spatial variables in a similar way to obtain another fully discrete scheme: Find $u_h^{n+1} \in S_{h,t_{n+1}}$ such that

$$\begin{aligned}
&\sum_{T\in\mathcal{T}_h}\int_T v_h(X)\frac{u_h^{n+1}(X)-u_h^n(X)}{\tau}\mathrm{d}X + \\
&\sum_{T\in\mathcal{T}_h}\int_T \nabla v_h(X)\cdot\Big(\frac{\beta(t_{n+1},X)\nabla u_h^{n+1}(X)+\beta(t_n,X)\nabla u_h^n(X)}{2}\Big)\mathrm{d}X \\
= &\int_\Omega v_h(X)f(t_{n+\frac{1}{2}},X)\mathrm{d}X, \quad \forall v_h \in \mathring{S}_{h,t_{n+1/2}}.
\end{aligned}$$

Writing the above equation in a matrix form, we have our third algorithm:

- **CN-IFE Algorithm 3**

$$\boxed{\left(M_h^{n+\frac{1}{2},n+1}+\frac{\tau}{2}A_h^{n+1,n+\frac{1}{2},n+1}\right)\mathbf{u}^{n+1}=\left(M_h^{n+\frac{1}{2},n}-\frac{\tau}{2}A_h^{n,n+\frac{1}{2},n}\right)\mathbf{u}^n+\tau\mathbf{f}^{n+\frac{1}{2},n+\frac{1}{2}}.}$$

In the derivation of CN-IFE Algorithm 3, we have used the average of the flux $\beta\nabla u$ rather than the gradient of u in the discretization. In this configuration, the flux continuity is retained at each time level, which is consistent with the main idea of using IFEs. However, this algorithm is different from the classic Crank-Nicolson scheme since it replaces the exact coefficient $\beta^{n+\frac{1}{2}}$ by β^n and β^{n+1} at different time levels. We note that this coefficient replacement seems to cause the CN-IFE Algorithm 3 to be conditionally stable, *i.e.*, this algorithm has to use a small time step in order to produce convergent numerical solutions especially when the diffusion coefficient has a large discontinuity.

6.4 Implementation for Moving Interfaces

In this section, we discuss some implementation issues for the CN-IFE and IFE-MoL schemes for solving parabolic moving interface problems.

At every time t, the process of assembling global matrices from local matrices follows the standard procedure for traditional FE computations. A standard FE matrix assembler can be employed to form local matrices over all non-interface elements; hence, our focus here is the process of generating local matrices on interface elements.

Local Matrices for CN-IFE-A1 and IFE-MoL

The implementations of CN-IFE Algorithm 1 and IFE-MoL are much simpler than that of CN-IFE Algorithms 2 and 3 because all test functions, trial functions and coefficient

functions are evaluated on the same time level $t = t_{n+\frac{1}{2}}$.

Assembling local mass and stiffness matrices $M(t)$ and $A(t)$ follows the same procedure as those for the IFE methods for time independent interface problems. The only difference is to update the interface location for a given value of t.

For the matrix $K(t)$ in (6.13), we note that each of its entries involves the inner product of an IFE basis function and its time derivative function, *i.e.*,

$$k_{ij}(t) = \int_\Omega \phi_i^t(X) \left(\frac{\partial}{\partial t} \phi_j^t(X) \right) \mathrm{d}X.$$

Hence, constructing $k_{ij}(t)$ needs the time derivative $\frac{\partial}{\partial t}\phi_j^t$ of the IFE basis function ϕ_j^t. As usual, we only need to derive the time derivative of the local nodal IFE basis functions on interface elements.

Without loss of generality, and in order to simplify the notations, we focus on the derivation of time derivatives of local linear IFE nodal basis functions $\phi_{i,T}^t$, $i = 1, 2, 3$, on the following triangular interface element with vertices

$$A_1 = (x_1, y_1) = (0, 0), \quad A_2 = (x_2, y_2) = (h, 0), \quad A_3 = (x_3, y_3) = (0, h).$$

Assume the intersection points $D(t) = (x_D(t), y_D(t))$ and $E(t) = (x_E(t), y_E(t))$ are on $\overline{A_1A_2}$, and $\overline{A_2A_3}$, respectively, as illustrated in Figure 6.3. We can write coordinates of $D(t)$ and $E(t)$ in terms of time dependent ratios $d(t)$, and $e(t)$ as follows,

$$x_D(t) = x_1 + d(t)(x_3 - x_1), \quad y_D(t) = y_1 + d(t)(y_3 - y_1), \tag{6.28}$$

$$x_E(t) = x_1 + e(t)(x_2 - x_1), \quad y_E(t) = y_1 + e(t)(y_2 - y_1), \tag{6.29}$$

where $0 \le d(t) \le 1$, $0 \le e(t) \le 1$.

A linear IFE function on an interface element such as the one in Figure 6.3 can be written in the following form [42, 96],

$$\phi_T^t(x, y) = \begin{cases} \phi_T^{t-}(x, y) = v_1\psi_{1,T} + c_2(t)\psi_{2,T} + c_3(t)\psi_{3,T}, & \text{if } (x, y) \in T^-(t), \\ \phi_T^{t+}(x, y) = c_1(t)\psi_{1,T} + v_2\psi_{2,T} + v_3\psi_{3,T}, & \text{if } (x, y) \in T^+(t). \end{cases} \tag{6.30}$$

Here $\psi_{i,T}$, $i = 1, 2, 3$ are standard linear FE nodal basis functions on T such that

$$\psi_{i,T}(A_j) = \delta_{ij}, \quad 1 \le i, j \le 3.$$

In (6.30), v_1, v_2, and v_3 are nodal values of the IFE function $\phi_T^t(x, y)$ at vertices A_1, A_2, and A_3, respectively. The time dependent coefficients $c_1(t)$, $c_2(t)$, and $c_3(t)$ are determined by imposing the interface jump conditions (6.5) and (6.6) on $\phi_T^t(x, y)$ [95, 96], *i.e.*,

$$\phi_T^{t+}(x_D, y_D) = \phi_T^{t-}(x_D, y_D), \quad \phi_T^{t+}(x_E, y_E) = \phi_T^{t-}(x_E, y_E), \tag{6.31}$$

Figure 6.3: A sketch of the interface configuration in a triangle at time t.

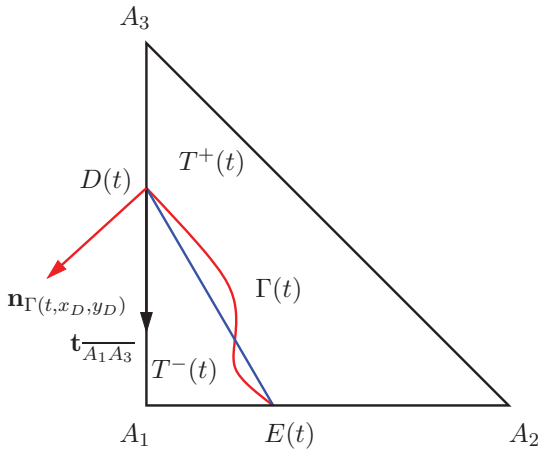

$$\beta^+\nabla\phi_T^{t+}(x,y)\cdot\mathbf{n}_{\overline{DE}}=\beta^-\nabla\phi_T^{t-}(x,y)\cdot\mathbf{n}_{\overline{DE}}. \tag{6.32}$$

It has been shown [96], for each fixed t, the coefficients $c_1(t)$, $c_2(t)$, and $c_3(t)$ are uniquely determined by the nodal values v_i, $i=1,2,3$.

Local linear IFE basis functions $\phi_{i,T}^t$, $i=1,2,3$, can be obtained by imposing the interface jump conditions (6.31) and (6.32) to (6.30). This leads to the following linear system for coefficients $c_1(t)$, $c_2(t)$, $c_3(t)$:

$$\begin{pmatrix} 1-d & 0 & -d \\ 1-e & -e & 0 \\ \beta^+(d+e) & \beta^-d & \beta^-e \end{pmatrix}\begin{pmatrix} c_1 \\ c_2 \\ c_3 \end{pmatrix}=\begin{pmatrix} 1-d & 0 & -d \\ 1-e & -e & 0 \\ \beta^-(d+e) & \beta^+d & \beta^+e \end{pmatrix}\begin{pmatrix} v_1 \\ v_2 \\ v_3 \end{pmatrix}, \tag{6.33}$$

where $d=d(t)$, and $e=e(t)$. Using (6.30) for the nodal IFE basis function $\phi_{i,T}^t$, we can calculate their time derivative as follows

$$\frac{\partial}{\partial t}\phi_{i,T}^t(x,y)=\begin{cases} \frac{\partial}{\partial t}\phi_{i,T}^{t-}(x,y)=c_2'(t)\psi_{2,T}+c_3'(t)\psi_{3,T}, & \text{if } (x,y)\in T^-(t), \\ \frac{\partial}{\partial t}\phi_{i,T}^{t+}(x,y)=c_1'(t)\psi_{1,T}, & \text{if } (x,y)\in T^+(t). \end{cases} \tag{6.34}$$

Moreover, derivatives $c_i'(t)$, $i=1,2,3$, can be calculated from the following linear system obtained by taking the derivative on both sides of (6.33),

$$\begin{aligned} &\begin{pmatrix} 1-d & 0 & -d \\ 1-e & -e & 0 \\ \beta^+(d+e) & \beta^-d & \beta^-e \end{pmatrix}\begin{pmatrix} c_1' \\ c_2' \\ c_3' \end{pmatrix} \\ &=\begin{pmatrix} -d' & 0 & -d' \\ -e' & -e' & 0 \\ \beta^-(d'+e') & \beta^+d' & \beta^+e' \end{pmatrix}\begin{pmatrix} v_1 \\ v_2 \\ v_3 \end{pmatrix}-\begin{pmatrix} -d' & 0 & -d' \\ -e' & -e' & 0 \\ \beta^+(d'+e') & \beta^-d' & \beta^-e' \end{pmatrix}\begin{pmatrix} c_1 \\ c_2 \\ c_3 \end{pmatrix}. \end{aligned} \tag{6.35}$$

Note that the coefficient matrix of $c_i'(t)$, $i = 1, 2, 3$, in (6.35) is the same as the one of $c_i(t)$, $i = 1, 2, 3$, in (6.33). Hence, the unisolvent property for IFE nodal basis [96] guarantees that $c_i'(t)$, $i = 1, 2, 3$ can be uniquely determined as long as $d'(t)$ and $e'(t)$ exist.

The remaining task is to find $d'(t)$ and $e'(t)$. Let us assume that the moving interface $\Gamma(t)$ is described by the equation $\Gamma(t, x, y) = 0$. Hence, we have

$$\Gamma(t, x_D(t), y_D(t)) = 0, \quad \Gamma(t, x_E(t), y_E(t)) = 0. \tag{6.36}$$

Taking the derivative with respect to t on both sides of these equations leads to equations about $d'(t)$ and $e'(t)$. By direct calculations, we obtain

$$d'(t) = \frac{-\Gamma_t(t, x_D, y_D)}{\Gamma_x(t, x_D, y_D)(x_3 - x_1) + \Gamma_y(t, x_D, y_D)(y_3 - y_1)}, \tag{6.37}$$

$$e'(t) = \frac{-\Gamma_t(t, x_E, y_E)}{\Gamma_x(t, x_E, y_E)(x_2 - x_1) + \Gamma_y(t, x_E, y_E)(y_2 - y_1)}. \tag{6.38}$$

The procedures developed in this section can be easily extended to assembling matrices for the IFE-MoL with other IFE functions.

Local Matrices for CN-IFE-A2 and CN-IFE-A3

The implementation for CN-IFE Algorithms 2 and 3 is more complicated than that of CN-IFE Algorithm 1 because test functions, trial functions and coefficient functions in the matrices of these algorithms are not evaluated at the same time level. Essentially, we need a local matrix assembler that can handle multiple interface curves within one element and all the possible configurations of interface locations have to be considered. We note that all the matrices are defined according to bilinear forms integrating the product of a test function and a trial function, and a coefficient function. For the CN-IFE Algorithm 2, the coefficient functions and test functions are evaluated at the same time $t_{n+\frac{1}{2}}$, but the trial functions are evaluated at different time t_n or t_{n+1}. For the CN-IFE Algorithm 3, the coefficient functions and trial functions are evaluated at the same time t_n or t_{n+1} while the test functions are evaluated at a different time $t_{n+\frac{1}{2}}$. Hence, for CN-IFE Algorithm 2 and 3, each interface element can contain up to two interfaces.

Note that the interface curve $\Gamma(t)$ restricted in an interface element is approximated by a line segment $\overline{DE}$. If an element T contains only one interface linear segment, then the related computations for generating a local matrix should be carried out through two sub-elements of T. If T contains two interfaces at two consecutive time levels, then T is partitioned into 4 or 3 sub-elements by the interface line segments depending on whether these two line segments intersect within or outside T, see illustrations in Figure 6.4 through Figure 6.9. Accordingly, the computations for assembling a local matrix should be carried out over all of these sub-elements.

Figure 6.4: Cases of interface triangle cut by two interface line segments that intersect inside the triangle.

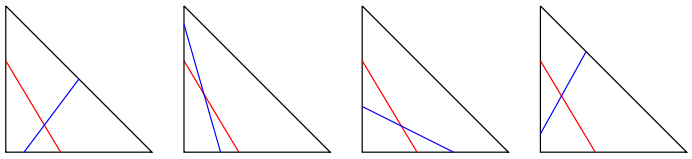

Figure 6.5: Cases of interface triangle cut by two interface line segments that intersect outside the triangle.

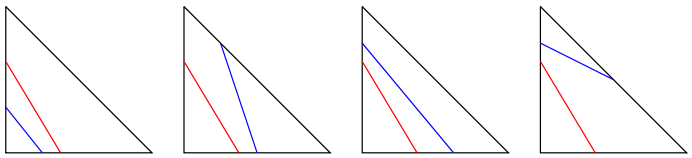

Figure 6.6: Cases of Type I interface rectangle cut by two interface line segments that intersect inside the rectangle.

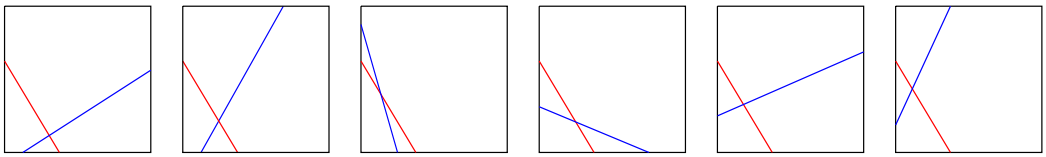

Figure 6.7: Cases of Type I interface rectangle cut by two interface line segments that intersect outside the rectangle.

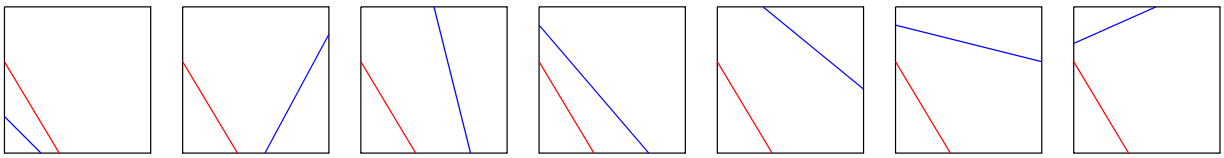

6.5 Numerical Experiments

In this section, we present numerical examples to demonstrate features of the IFE-MoL and CN-IFE algorithms for solving the parabolic moving interface problem.

Figure 6.8: Cases of Type II interface rectangle cut by two interface line segments that intersect inside the rectangle.

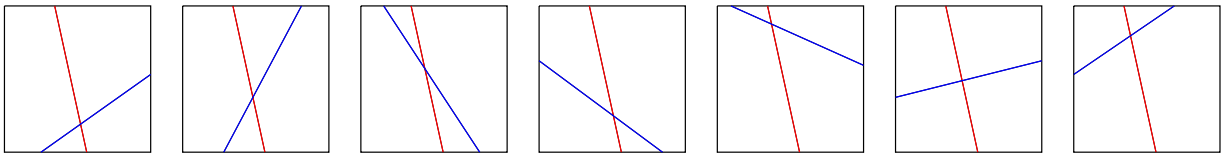

Figure 6.9: Cases of Type II reference rectangle cut by two interface line segments that intersect outside the rectangle.

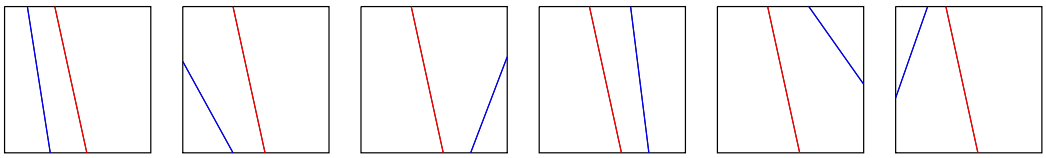

The solution domain is $\Omega \times [0,1]$, where $\Omega = (-1,1) \times (-1,1)$ and the interface $\Gamma(t)$ is a moving circle centered at origin with a radius $r(t)$ that separates Ω into two sub-domains $\Omega^-(t) = \{(x,y) \in \Omega \,:\, x^2+y^2 < r(t)^2\}$ and $\Omega^+(t) = \{(x,y) \in \Omega \,:\, x^2+y^2 > r(t)^2\}$. The exact solution is chosen as:

$$u(t,x,y) = \begin{cases} \frac{1}{\beta^-}\left(x^2+y^2\right)^{5/2}\cos(t), & (x,y) \in \Omega^-(t), \\ \frac{1}{\beta^+}\left(x^2+y^2\right)^{5/2}\cos(t) + \left(\frac{1}{\beta^-} - \frac{1}{\beta^+}\right) r(t)^5 \cos(t), & (x,y) \in \Omega^+(t). \end{cases} \tag{6.39}$$

We use triangular Cartesian meshes $\mathcal{T}_h$ which are formed by partitioning Ω with $N_s \times N_s$ rectangles of size $h = 2/N_s$ and then cutting each rectangle into two triangles alone one of its diagonal line, see right plot in Figure 6.2 for an illustration. For the discretization in the time variable, we denote its step size by τ and define $t_n = n\tau$, with $n = 1, 2, \cdots, N_t$ such that $N_t\tau = 1$.

Example 6.1. (Second Order ODE Solvers) *In this example, we test some ODE solvers which are $O(\tau^2)$ accuracy. Since the linear IFE approximation have $O(h^2)$ and $O(h)$ accuracies in L^2 norm and in H^1 norm, respectively [95], then we expect the related IFE-MoL using this kind of ODE solve to have an overall $O(h^2)$ accuracy in L^2 norm and $O(h)$ accuracy in H^1 norm if we choose $\tau = h$.*

We assume the radius of the interface circle is governed by the function $r(t) = r_0\left(\frac{\sin(t)+3}{4}\right)$ with $r_0 = \frac{\pi}{6.28}$ in Examples 6.1 and 6.2. The following second order DIRK scheme [7] is used

to solve the ODE system in the IFE-MoL:

$$\begin{array}{c|cc} \gamma & \gamma & 0 \\ 1 & \gamma & 1-\gamma \\ \hline & \gamma & 1-\gamma \end{array} \tag{6.40}$$

where $\gamma = \frac{2-\sqrt{2}}{2}$. Numerical experiments are carried out for both a small coefficient jump, $(\beta^-, \beta^+) = (1, 2)$ and a large coefficient jump $(\beta^-, \beta^+) = (1, 100)$, and in both cases, we choose $\tau = h$. Errors in numerical solutions generated by the IFE-MoL are computed at the final time level $t = 1$ in both L^2 and semi-H^1 norms and they are presented in Table 6.1. Applying linear regression on these data we can see that the IFE solutions obey the following error estimates:

- **DIRK2 (Small Jump)**

$$\|u_h^n - u(t_n, \cdot)\|_{0,\Omega} \approx 0.9686\, h^{1.9963}, \quad |u_h^n - u(t_n, \cdot)|_{1,\Omega} \approx 2.9195\, h^{0.9994},$$

- **DIRK2 (Large Jump)**

$$\|u_h^n - u(t_n, \cdot)\|_{0,\Omega} \approx 0.0412\, h^{1.8696}, \quad |u_h^n - u(t_n, \cdot)|_{1,\Omega} \approx 0.1219\, h^{0.9109},$$

which correlate well with the expected error bound:

$$\|u_h^n - u(t_n, \cdot)\|_{k,\Omega} \leq C(h^{2-k} + \tau^2), \quad k = 0, 1.$$

Table 6.1: Errors of linear IFE solutions with $\beta^- = 1$ using DIRK2 at time $t = 1$.

		$\beta^+ = 2$		$\beta^+ = 100$	
h	τ	$\|\cdot\|_{0,\Omega}$	$\|\cdot\|_{1,\Omega}$	$\|\cdot\|_{0,\Omega}$	$\|\cdot\|_{1,\Omega}$
1/16	1/16	3.8203E-2	1.8269E-1	2.4420E-4	9.6691E-3
1/32	1/32	9.5852E-4	9.1447E-2	6.0966E-5	5.2348E-3
1/64	1/64	2.4018E-4	4.5738E-2	1.6860E-5	2.7664E-3
1/128	1/128	6.0174E-5	2.2873E-2	4.4807E-6	1.4708E-3
1/256	1/256	1.5081E-5	1.1438E-2	1.3824E-6	7.7637E-4

Example 6.2. (Higher Order ODE Solvers) *One of the motivations to use a MoL for solving time dependent PDEs is the easy employment of higher order schemes for solving the related ODE system. In this example, we present numerical results generated by a representative fourth order single step method and and a fourth order multi-step method.*

For the single step method, we use the following fourth order DIRK scheme [64]:

$$\begin{array}{c|ccccc} \frac{1}{4} & \frac{1}{4} & & & & \\ \frac{3}{4} & \frac{1}{2} & \frac{1}{4} & & & \\ \frac{11}{20} & \frac{17}{20} & -\frac{1}{25} & \frac{1}{4} & & \\ \frac{1}{2} & \frac{371}{1360} & -\frac{137}{2720} & \frac{15}{544} & \frac{1}{4} & \\ 1 & \frac{25}{24} & -\frac{49}{48} & \frac{125}{16} & -\frac{85}{12} & \frac{1}{4} \\ \hline & \frac{25}{24} & -\frac{49}{48} & \frac{125}{16} & -\frac{85}{12} & \frac{1}{4} \end{array} \tag{6.41}$$

For the multi-step method, we use the following fourth order BDF scheme [7]:

$$\mathbf{u}^{n+1} = \frac{1}{25}\Big(48\mathbf{u}^n - 36\mathbf{u}^{n-1} + 16\mathbf{u}^{n-2} - 3\mathbf{u}^{n-3} + 12\tau\mathbf{F}^{n+1}\Big).$$

Table 6.2: Errors of linear IFE solutions with $\beta^- = 1$, $\beta^+ = 2$ using 4th order schemes at time $t = 1$.

		DIRK4		BDF4	
h	τ	$\|\cdot\|_{0,\Omega}$	$\|\cdot\|_{1,\Omega}$	$\|\cdot\|_{0,\Omega}$	$\|\cdot\|_{1,\Omega}$
1/8	1/8	1.5087E-2	3.6392E-1	1.5143E-2	3.6392E-1
1/32	1/16	9.3618E-4	9.1447E-2	9.5054E-4	9.1447E-2
1/128	1/32	5.6341E-5	2.2873E-2	5.9474E-5	2.2872E-2
1/512	1/64	3.1699E-6	5.7210E-3	3.7318E-6	5.7209E-3

Exact initial values $\mathbf{u}^i = (u(t_i, X_j))$, $i = 0, 1, 2, 3$, $X_j \in \mathcal{N}_h^0$ are used to start the time iteration by the BDF scheme. Errors of IFE solutions generated by both schemes at the final time level $t = 1$ are listed in Table 6.2. Since both schemes are fourth order accurate in time steps, we expect the errors to obey

$$\|u_h^n - u(t_n, \cdot)\|_{k,\Omega} \leq C(h^{2-k} + \tau^4), \quad k = 0, 1.$$

Therefore, to observe the convergence rate in term of h, we use $h = 8\tau^2$ to make h^2 proportional to τ^4 for the chosen mesh sizes. By linear regression we can see that the data in Table 6.2 have the following estimates:

- **DIRK4**

$$\|u_h^n - u(t_n, \cdot)\|_{0,\Omega} \approx 1.0627\, h^{2.0352}, \quad |u_h^n - u(t_n, \cdot)|_{1,\Omega} \approx 2.9072\, h^{0.9987},$$

- **BDF4**

$$\|u_h^n - u(t_n, \cdot)\|_{0,\Omega} \approx 0.9653\, h^{1.9979}, \quad |u_h^n - u(t_n, \cdot)|_{1,\Omega} \approx 2.9073\, h^{0.9987}.$$

The linear regression of the errors demonstrates the optimal rates of convergence in both L^2 and semi H^1 norms for the IFE-MoL combined with these higher order ODE solvers.

Example 6.3. (Adaptive ODE Solver) *An advantage to use a MoL is the availability of reliable and efficient adaptive ODE solvers that can automatically adjust the time step size according to the rate of change of the exact solution with respect to t so that the local error can be maintained within a prescribed amount. This adaptivity is particular desirable when one needs to solve a moving interface problem in which the interface changes with respect to the time in a complicated way. In this example, we combine the linear IFE approximation with an adaptive ODE solver to test the performance of the IFE-MoL.*

We consider the moving interface problem described at the beginning of this section in which a moving circular interface has the radius governed by

$$r(t) = \frac{1}{400}\exp\Big(\frac{1}{5(0.6-t)^2+0.25}\Big) + \frac{1}{300}\exp\Big(\frac{1}{(1.1-t)^2+0.19}\Big) + 0.25.$$

It is easy to see that this interface changes with respect to t at a varying rate, as illustrated in the left plot in Figure 6.10. The adaptive ODE solver used in our numerical experiments for this problem is the popular embedded DIRK45 scheme [64] described by the following Butcher diagram:

$$\begin{array}{c|ccccc}
\frac{1}{4} & \frac{1}{4} & & & & \\
\frac{3}{4} & \frac{1}{2} & \frac{1}{4} & & & \\
\frac{11}{20} & \frac{17}{20} & -\frac{1}{25} & \frac{1}{4} & & \\
\frac{1}{2} & \frac{371}{1360} & -\frac{137}{2720} & \frac{15}{544} & \frac{1}{4} & \\
1 & \frac{25}{24} & -\frac{49}{48} & \frac{125}{16} & -\frac{85}{12} & \frac{1}{4} \\
\hline
 & \frac{25}{24} & -\frac{49}{48} & \frac{125}{16} & -\frac{85}{12} & \frac{1}{4} \\
 & \frac{59}{48} & -\frac{17}{96} & \frac{225}{32} & -\frac{85}{12} & 0
\end{array} \tag{6.42}$$

When we use this DIRK45 scheme to solve the ODE system in the IFE-MoL for this moving interface problem, we set its local tolerance as $tol = h^2$, and choose the maximum time step size $\tau_{max} = 5h$. The initial step size is set as $\tau_0 = h$.

The right plot in Figure 6.10 displays a set of time step sizes automatically determined by the IFE-MoL combined with the adaptive DIRK45 ODE solver in a computation for solving this moving interface problem. Comparing this plot with the curve of $|\alpha'(t)|$ on the left, we can see that this adaptive IFE-MoL can handle the change in the interface with respect to time very well. The method uses relatively larger time step sizes for $t < 0.3$ where $|\alpha'(t)|$ is small, *i.e.*, the interface location $\alpha(t)$ changes slowly. The time step sizes used by this method decrease in $0.3 < t < 0.55$ since the interface change more rapidly within this time interval. The curve of the time step sizes has two peaks around $t = 0.6$ and $t = 0.75$ where the interface changes at smaller rates; hence larger time steps are allowed. The step sizes become smaller and smaller after $t > 0.8$ due to a faster change of the interface location.

All these observations agree well with our expectation according to the behavior of interface movement.

Figure 6.10: The left plot shows how the radius $r(t)$ of the interface circle $\Gamma(t)$ changes; the right plot is for the time step sizes used by the IFE-MoL combined with the adaptive DIRK45 ODE solver.

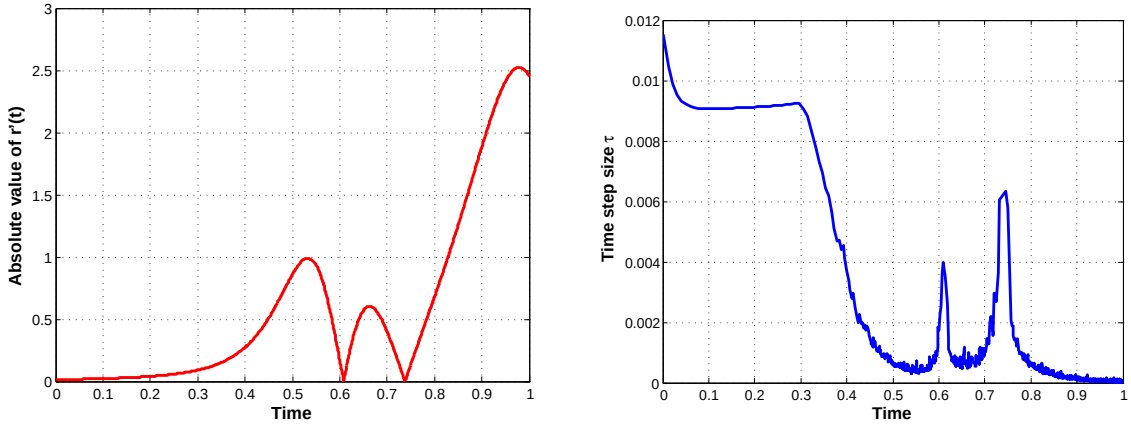

Table 6.3: Errors of linear IFE adaptive DIRK45 solutions with $\beta^- = 0.5$, $\beta^+ = 2$ at time $t = 1$.

h	N	$\|\cdot\|_{0,\Omega}$	$\|\cdot\|_{1,\Omega}$
1/8	14	1.7976E-2	4.2420E-1
1/16	49	4.4131E-3	2.1544E-1
1/32	182	1.1625E-3	1.0981E-1
1/64	667	2.9050E-4	5.5990E-2
1/128	2369	7.6317E-5	2.8762E-2

Moreover, the adaptive IFE-MoL can produce accurate solutions to moving interface problems by automatic adjustment of time step size according a prescribed error tolerance. To see this, we present some of our numerical numerical results in Table 6.3 in which errors of IFE solutions at the final time $t = 1$ in both L^2 norm and semi-H^1 norm are listed. The number N in this table denotes the total number of iterations used in each computation. By linear regression we can see that these errors obey

- **Adaptive DIRK45**

$$\|u_h^n - u(t_n, \cdot)\|_{0,\Omega} \approx 1.0592\, h^{1.9685}, \quad |u_h^n - u(t_n, \cdot)|_{1,\Omega} \approx 3.1846\, h^{0.9709},$$

which suggest the optimal convergence of the IFE-MoL.

Then, we compare the IFE solution generated by the IFE-MoL combined with the adaptive DIRK45 ODE solver on a Cartesian mesh of $h = 1/64$ with other IFE solutions produced by methods with a fixed time step size. In the computation to generate this IFE solution, the DIRK45 ODE solver automatically carries out 667 iterations in time. Then, we generate two additional IFE solutions by the IFE-MoL combined with the ODE solver DIRK4 and the CN-IFE Algorithm 1 on the same mesh, respectively, and we use 667 equally spaced time steps in both of these two methods. The L^∞ norm errors in these three IFE solutions are compared in Figure 6.11, from which we can that the adaptive IFE-MoL has a better control on the error in its solution while errors in those IFE solutions based a uniform time step size grow faster along with the time. These numerical results indicate that the adaptive IFE-MoL can produce more reliable numerical solution than methods with a fixed time step size.

Figure 6.11: The left plot contains curves of L^∞ norm error for three IFE solutions generated on the same mesh with $h = 1/64$. The right plot is the enlarged part for time between 0.8 to 1.

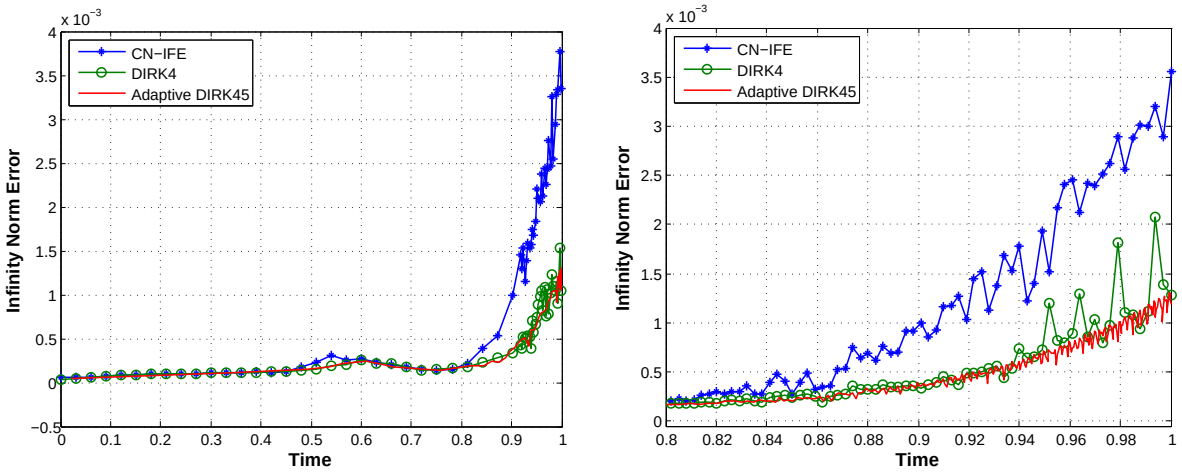

In the next few examples, we test the numerical performance for CN-IFE fully discrete schemes. Again, we assume the radius change is governed by $r(t) = r_0\left(\frac{\sin(t)+3}{4}\right)$ with $r_0 = \frac{\pi}{6.28}$ which are the same as we have used in Examples 6.1 and 6.2.

Example 6.4. (CN-IFE Small Jump) *In this example we test the numerical performance of three CN-IFE fully discrete schemes for a small coefficient discontinuity* $\beta^- = 1$, $\beta^+ = 2$.

We test these CN-IFE algorithms with $\tau = h$ and $\tau = \frac{1}{8}h$. Errors at the final time level in the L^2 and semi-H^1 norms are listed in Table 6.4 and Table 6.5, respectively. Linear regression for these data yield the following estimates:

- **CN-IFE Algorithms with $\beta^- = 1$, $\beta^+ = 2$, $\tau = h$, $n = N_t$:**

$$\begin{aligned}
&\mathbf{A1}: \quad \|u_h^n - u(t_n,\cdot)\|_{0,\Omega} \approx 1.0144h^{1.9980}, \quad |u_h^n - u(t_n,\cdot)|_{1,\Omega} \approx 2.8972h^{0.9969}.\\
&\mathbf{A2}: \quad \|u_h^n - u(t_n,\cdot)\|_{0,\Omega} \approx 1.0071h^{1.9966}, \quad |u_h^n - u(t_n,\cdot)|_{1,\Omega} \approx 2.9097h^{0.9985}.\\
&\mathbf{A3}: \quad \|u_h^n - u(t_n,\cdot)\|_{0,\Omega} \approx 0.5248h^{1.7634}, \quad |u_h^n - u(t_n,\cdot)|_{1,\Omega} \approx 1.5298h^{0.7686}.
\end{aligned}$$

- **CN-IFE Algorithms with $\beta^- = 1$, $\beta^+ = 2$, $\tau = \frac{1}{8}h$, $n = N_t$:**

$$\begin{aligned}
&\mathbf{A1}: \quad \|u_h^n - u(t_n,\cdot)\|_{0,\Omega} \approx 1.0287h^{1.9983}, \quad |u_h^n - u(t_n,\cdot)|_{1,\Omega} \approx 2.9105h^{0.9986}.\\
&\mathbf{A2}: \quad \|u_h^n - u(t_n,\cdot)\|_{0,\Omega} \approx 1.0287h^{1.9983}, \quad |u_h^n - u(t_n,\cdot)|_{1,\Omega} \approx 2.9105h^{0.9986}.\\
&\mathbf{A3}: \quad \|u_h^n - u(t_n,\cdot)\|_{0,\Omega} \approx 1.0174h^{1.9944}, \quad |u_h^n - u(t_n,\cdot)|_{1,\Omega} \approx 2.8623h^{0.9928}.
\end{aligned}$$

Table 6.4: Errors of linear CN-IFE solutions with $\beta^- = 1$, $\beta^+ = 2$ and $\tau = h$ at time $t = 1$.

	CN-IFE A1		**CN-IFE A2**		**CN-IFE A3**	
h	$\|\cdot\|_{0,\Omega}$	$\|\cdot\|_{1,\Omega}$	$\|\cdot\|_{0,\Omega}$	$\|\cdot\|_{1,\Omega}$	$\|\cdot\|_{0,\Omega}$	$\|\cdot\|_{1,\Omega}$
1/10	1.020E-2	2.918E-1	1.012E-2	2.918E-1	1.021E-2	2.932E-1
1/20	2.551E-3	1.463E-1	2.550E-3	1.462E-1	2.611E-3	1.501E-1
1/30	1.134E-3	9.759E-2	1.133E-3	9.755E-2	1.247E-3	1.061E-1
1/40	6.380E-4	7.323E-2	6.377E-4	7.318E-2	6.950E-4	8.087E-2
1/50	4.087E-4	5.861E-2	4.084E-4	5.855E-2	5.069E-4	7.150E-2
1/60	2.840E-4	4.889E-2	2.837E-4	4.880E-2	3.419E-4	5.928E-2
1/70	2.087E-4	4.193E-2	2.084E-4	4.183E-2	2.925E-4	5.884E-2
1/80	1.599E-4	3.670E-2	1.596E-4	3.661E-2	2.336E-4	5.346E-2
1/90	1.264E-4	3.264E-2	1.261E-4	3.254E-2	2.070E-4	5.192E-2
1/100	1.025E-4	2.942E-2	1.022E-4	2.930E-2	1.764E-4	5.030E-2

From Table 6.4 and Table 6.5 and their linear regression results, we can see that both CN-IFE errors in Algorithms 1 and 2 seem to have optimal orders with either large or small time steps. As we expected, CN-IFE Algorithm 3 have some difficulties when a large time step τ is used. Data in Table 6.4 suggest that numerical solutions generated by CN-IFE Algorithm 3 with $\tau = h$ converge to the exact solution, but not in an optimal rate. However, when we shrink the time step size from $\tau = h$ to $\tau = \frac{1}{8}h$, the optimal convergence for CN-IFE Algorithm 3 can be recovered.

Example 6.5. (CN-IFE Large Jump) *In this example we test the numerical performance of three CN-IFE fully discretization schemes for a large coefficient jump $\beta^- = 1$, $\beta^+ = 100$.*

We choose $\tau = \frac{1}{8}h$ in our numerical experiments, and the related errors of numerical solutions at the final time level in the L^2 and semi-H^1 norms are listed in Table 6.6. Linear regression of these errors yields

Table 6.5: Errors of linear CN-IFE solutions with $\beta^- = 1$, $\beta^+ = 2$ and $\tau = \frac{1}{8}h$ at time $t = 1$.

	CN-IFE A1		**CN-IFE A2**		**CN-IFE A3**	
h	$\|\cdot\|_{0,\Omega}$	$\|\cdot\|_{1,\Omega}$	$\|\cdot\|_{0,\Omega}$	$\|\cdot\|_{1,\Omega}$	$\|\cdot\|_{0,\Omega}$	$\|\cdot\|_{1,\Omega}$
1/10	1.032E-2	2.917E-1	1.032E-2	2.917E-1	1.032E-2	2.917E-1
1/20	2.588E-3	1.462E-1	2.588E-3	1.462E-1	2.587E-3	1.463E-1
1/30	1.150E-3	9.754E-2	1.150E-3	9.754E-2	1.150E-3	9.766E-2
1/40	6.473E-4	7.317E-2	6.473E-4	7.317E-2	6.503E-4	7.347E-2
1/50	4.144E-4	5.854E-2	4.144E-4	5.854E-2	4.154E-4	5.866E-2
1/60	2.878E-4	4.879E-2	2.878E-4	4.879E-2	2.880E-4	4.900E-2
1/70	2.115E-4	4.182E-2	2.115E-4	4.182E-2	2.131E-4	4.219E-2
1/80	1.619E-4	3.659E-2	1.619E-4	3.659E-2	1.627E-4	3.688E-2
1/90	1.280E-4	3.253E-2	1.280E-4	3.253E-2	1.286E-4	3.278E-2
1/100	1.037E-4	2.928E-2	1.037E-4	2.928E-2	1.049E-4	2.983E-2

- **CN-IFE Algorithms with $\beta^- = 1$, $\beta^+ = 100$, $\tau = \frac{1}{8}h$, $n = N_t$:**

$$\textbf{A1}: \quad \|u_h^n - u(t_n,\cdot)\|_{0,\Omega} \approx 0.0506h^{1.9256}, \quad |u_h^n - u(t_n,\cdot)|_{1,\Omega} \approx 0.1196h^{0.9064}.$$
$$\textbf{A2}: \quad \|u_h^n - u(t_n,\cdot)\|_{0,\Omega} \approx 0.0507h^{1.9266}, \quad |u_h^n - u(t_n,\cdot)|_{1,\Omega} \approx 0.1205h^{0.9090}.$$

Data in this table indicate that numerical solutions generated by CN-IFE Algorithms 1 and 2 converge to the exact solution and the convergence rates are close to optimal. On the other hand, numerical solutions generated by CN-IFE Algorithm 3 do not converge at all because of its instability. This observation further suggests that CN-IFE Algorithm 3 cannot handle large changes in the coefficient, either caused by a large jump or a large time step.

Our numerical experiments indicate that CN-IFE Algorithm 3 can still produce good numerical results provided that the time step is small enough. As we shrink the time step size τ further, the numerical solutions form CN-IFE Algorithm 3 converge and the corresponding errors become comparable to those generated by Algorithms 1 and 2. Corresponding data can be found in Table 6.7.

Example 6.6. (CN-IFE Algorithm 1*) *In this example, we consider a variant of CN-IFE Algorithm 1 by omitting those terms involving K and we call it CN-IFE Algorithm 1^*:*

$$\boxed{\left(M_h^{n+\frac{1}{2},n+\frac{1}{2}} + \frac{\tau}{2}A_h^{n+\frac{1}{2},n+\frac{1}{2},n+\frac{1}{2}}\right)\mathbf{u}^{n+1} = \left(M_h^{n+\frac{1}{2},n+\frac{1}{2}} - \frac{\tau}{2}A_h^{n+\frac{1}{2},n+\frac{1}{2},n+\frac{1}{2}}\right)\mathbf{u}^n + \tau\mathbf{f}^{n+\frac{1}{2},n+\frac{1}{2}}.}$$

CN-IFE Algorithm 1^* is simpler than CN-IFE Algorithm 1. More importantly, at each time level, the matrix in the linear system is symmetric positive definite.

Errors from the numerical solutions generated by CN-IFE Algorithm 1^* are listed in Table 6.8. By linear regression, we have

Table 6.6: Errors of linear CN-IFE solution with $\beta^- = 1$, $\beta^+ = 100$ and $\tau = \frac{1}{8}h$ at time $t = 1$.

	CN-IFE A1		**CN-IFE A2**		**CN-IFE A3**	
h	$\|\cdot\|_{0,\Omega}$	$\|\cdot\|_{1,\Omega}$	$\|\cdot\|_{0,\Omega}$	$\|\cdot\|_{1,\Omega}$	$\|\cdot\|_{0,\Omega}$	$\|\cdot\|_{1,\Omega}$
1/10	5.759E-4	1.448E-2	5.760E-4	1.449E-2	1.073E-2	4.894E-1
1/20	1.665E-4	8.055E-3	1.666E-4	8.055E-3	6.278E-1	5.292E+1
1/30	7.284E-5	5.564E-3	7.285E-5	5.565E-3	2.143E+3	2.659E+5
1/40	4.072E-5	4.271E-3	4.070E-5	4.265E-3	4.880E+6	4.374E+8
1/50	2.718E-5	3.461E-3	2.715E-5	3.457E-3	5.936E+7	1.246E+10
1/60	1.962E-5	2.914E-3	1.959E-5	2.902E-3	5.991E+10	1.432E+13
1/70	1.455E-5	2.530E-3	1.453E-5	2.519E-3	9.439E+10	1.639E+13
1/80	1.084E-5	2.247E-3	1.083E-5	2.244E-3	2.100E+17	6.150E+19
1/90	8.462E-6	2.027E-3	8.450E-6	2.019E-3	1.216E+17	3.926E+19
1/100	7.004E-6	1.815E-3	6.991E-6	1.803E-3	1.287E+25	4.480E+27

Table 6.7: Errors of linear IFE solutions in CN-IFE Algorithm 3 with $\beta^- = 1$ and $\beta^+ = 100$ at time $t = 1$.

	$\tau = h/16$		$\tau = h/64$		$\tau = h/256$	
h	$\|\cdot\|_{0,\Omega}$	$\|\cdot\|_{1,\Omega}$	$\|\cdot\|_{0,\Omega}$	$\|\cdot\|_{1,\Omega}$	$\|\cdot\|_{0,\Omega}$	$\|\cdot\|_{1,\Omega}$
1/10	6.263E-4	1.670E-2	5.768E-4	1.448E-2	5.760E-4	1.448E-2
1/20	1.146E-3	9.479E-2	1.723E-4	8.097E-3	1.674E-4	8.041E-3
1/30	1.140E-3	1.415E-1	1.606E-4	6.314E-3	8.201E-5	5.557E-3
1/40	6.639E-2	1.156E+1	9.318E-5	5.772E-3	4.377E-5	4.259E-3

- **CN-IFE A1 * with $\beta^- = 1$, $\beta^+ = 2$, $\tau = h$, $n = N_t$:**

$$\|u_h^n - u(t_n, \cdot)\|_{0,\Omega} \approx 1.0135h^{1.9977}, \quad |u_h^n - u(t_n, \cdot)|_{1,\Omega} \approx 2.8972h^{0.9969}.$$

- **CN-IFE A1* with $\beta^- = 1$, $\beta^+ = 2$, $\tau = \frac{1}{8}h$, $n = N_t$:**

$$\|u_h^n - u(t_n, \cdot)\|_{0,\Omega} \approx 1.0291h^{1.9983}, \quad |u_h^n - u(t_n, \cdot)|_{1,\Omega} \approx 2.9105h^{0.9986}.$$

- **CN-IFE A1* with $\beta^- = 1$, $\beta^+ = 100$, $\tau = \frac{1}{8}h$, $n = N_t$:**

$$\|u_h^n - u(t_n, \cdot)\|_{0,\Omega} \approx 0.0504h^{1.9255}, \quad |u_h^n - u(t_n, \cdot)|_{1,\Omega} \approx 0.1196h^{0.9064}.$$

Comparing the data in Table 6.8 with the corresponding data of CN-IFE A1 in Tables 6.4 through 6.6, we note that the numerical performance of CN-IFE Algorithm 1* is not much different from the original CN-IFE Algorithm 1. It is an interesting research topic in the future to analyze more carefully about the importance of the matrix K.

Table 6.8: Errors of linear IFE solution using CN-IFE-A1* with $\beta^- = 1$ and $\tau = h$ at time $t = 1$.

	$\beta^+ = 2$, $\tau = h$		$\beta^+ = 2$, $\tau = \frac{1}{8}h$		$\beta^+ = 100$, $\tau = \frac{1}{8}h$	
N_s	$\|\cdot\|_{0,\Omega}$	$\|\cdot\|_{1,\Omega}$	$\|\cdot\|_{0,\Omega}$	$\|\cdot\|_{1,\Omega}$	$\|\cdot\|_{0,\Omega}$	$\|\cdot\|_{1,\Omega}$
20	1.020E-2	2.918E-1	1.032E-2	2.917E-1	5.741E-4	1.448E-2
40	2.551E-3	1.463E-1	2.588E-3	1.462E-1	1.661E-4	8.055E-3
60	1.134E-3	9.759E-2	1.151E-3	9.754E-2	7.260E-5	5.564E-3
80	6.381E-4	7.323E-2	6.473E-4	7.317E-2	4.054E-5	4.271E-3
100	4.088E-4	5.861E-2	4.145E-4	5.854E-2	2.704E-5	3.461E-3
120	2.841E-4	4.889E-2	2.879E-4	4.879E-2	1.953E-5	2.914E-3
140	2.088E-4	4.193E-2	2.115E-4	4.182E-2	1.451E-5	2.530E-3
160	1.600E-4	3.670E-2	1.619E-4	3.659E-2	1.081E-5	2.247E-3
180	1.264E-4	3.264E-2	1.280E-4	3.253E-2	8.444E-6	2.027E-3
200	1.026E-4	2.942E-2	1.037E-4	2.928E-2	6.985E-6	1.815E-3

Chapter 7

Future Work

In this chapter, we list a few research topics beyond this dissertation. The future work regarding IFEs contains both developing new algorithms and error analysis.

IFE Methods for Fluid Flow Models

Fundamental equations such as incompressible Stokes and Navier-Stokes equations are used to model multi-phase flow in fluid dynamics. Viscosity and density coefficients may have discontinuity across the fluid interface. A variety of numerical methods have been developed based on finite difference formulations for solving these fluid flow interface problems on Cartesian meshes [91, 110, 120]. One of our future research topics is to develop new IFE methods to solve these fluid flow interface problems. Using Galerkin methods [27, 37] with nonconforming finite elements or mixed methods with appropriate stable finite element pairs which satisfy "inf-sup" condition will be ideal choices to be combined with IFE schemes.

IFE methods for Free Boundary Problems

Free boundary problems, such as Stefan problems [34], are another important class of interface problems. In many applications, the governing PDEs for the velocity are coupled with differential equations used for the motion of the boundary. A frequently used technique is to solve the governing PDEs with a "temporarily fixed" interface or boundary location to update velocity field and then use the computed velocity to evolve the interface or boundary. Currently, IFE methods can satisfactorily solve the moving interface PDEs if the interface is assumed *a priori* [75, 101, 102]. Combining with suitable evolution techniques, such as front tracking methods [58, 59, 81, 138], and level set methods [19, 116, 117, 131], it is possible to efficiently solve true moving interface problems arise in physical applications.

Error Analysis of IFE Methods

For elliptic interface problems, Galerkin IFE solutions using nonconforming rotated Q_1 functions with integral-value degrees of freedom are observed to have the optimal convergence. This observation motivates us to carry out error analysis for this scheme in the near future. Error analysis for elasticity interface problem will be another interesting future work. Until now there are rarely any published results concerning error estimation of related IFE methods for elasticity interface problems.

We have shown that IFE functions can be efficiently applied in the interior penalty DG formulations to solve the second order elliptic interface problems [72, 109]. One of the advantages of using DG formulations is the flexibility in performing h-, p- or hp- refinements. Adaptation of mesh refinements usually requires a reliable local error indicator, and this error indicator has to be computable. Due to this reason, it is desirable to have *a posteriori* error estimate for IFE methods. We plan to work on this topic in the future.

Bibliography

[1] Slimane Adjerid and Tao Lin. A p-th degree immersed finite element for boundary value problems with discontinuous coefficients. *Appl. Numer. Math.*, 59(6):1303–1321, 2009.

[2] Ann S. Almgren, John B. Bell, Phillip Colella, and Tyler Marthaler. A Cartesian grid projection method for the incompressible Euler equations in complex geometries. *SIAM J. Sci. Comput.*, 18(5):1289–1309, 1997.

[3] Douglas N. Arnold. An interior penalty finite element method with discontinuous elements. *SIAM J. Numer. Anal.*, 19(4):742–760, 1982.

[4] Douglas N. Arnold, Franco Brezzi, and Jim Douglas, Jr. PEERS: A new finite element for plane elasticity. *Japan J. Appl. Math.*, 1(2):347–367, 1984.

[5] Douglas N. Arnold, Jim Douglas, Jr., and Chaitan P. Gupta. A family of higher order mixed finite elements for plane elasticity. *Numer. Math.*, 45(1):1–22, 1984.

[6] Douglas N. Arnold and Ragnar Winther. Nonconforming mixed elements for elasticity. *Math. Models Methods Appl. Sci.*, 13(3):295–307, 2003.

[7] Uri M. Ascher and Linda R. Petzold. *Computer methods for ordinary differential equations and differential-algebraic equations*. Society for Industrial and Applied Mathematics (SIAM), Philadelphia, PA, 1998.

[8] Champike Attanayake and Deepthika Senaratne. Convergence of an immersed finite element method for semilinear parabolic interface problems. *Appl. Math. Sci. (Ruse)*, 5(1–4):135–147, 2011.

[9] Ivo Babuška. The finite element method for elliptic equations with discontinuous coefficients. *Computing*, 5:207–213, 1970.

[10] Ivo Babuška, Uday Banerjee, and John E. Osborn. Survey of meshless and generalized finite element methods: a unified approach. *Acta Numer.*, 12:1–125, 2003.

[11] Ivo Babuška, Gabriel Caloz, and John E. Osborn. Special finite element methods for a class of second order elliptic problems with rough coefficients. *SIAM J. Numer. Anal.*, 31(4):945–981, 1994.

[12] Ivo Babuška and Jen M. Melenk. The partition of unity finite element method: basic theory and applications. *Comput. Methods Appl. Mech. Engrg.*, 139(1–4):289–314, 1996.

[13] Ivo Babuška and Jen M. Melenk. The partition of unity method. *Internat. J. Numer. Methods Engrg.*, 40(4):727–758, 1997.

[14] Ivo Babuška, Victor Nistor, and Nicolae Tarfulea. Generalized finite element method for second-order elliptic operators with Dirichlet boundary conditions. *J. Comput. Appl. Math.*, 218(1):175–183, 2008.

[15] Ivo Babuška and John E. Osborn. Generalized finite element methods: their performance and their relation to mixed methods. *SIAM J. Numer. Anal.*, 20(3):510–536, 1983.

[16] Ivo Babuška and Manil Suri. On locking and robustness in the finite element method. *SIAM J. Numer. Anal.*, 29(5):1261–1293, 1992.

[17] Ivo Babuška and Zhiming Zhang. The partition of unity method for the elastically supported beam. *Comput. Methods Appl. Mech. Engrg.*, 152(1–2):1–18, 1998.

[18] John W. Barrett and Charles M. Elliott. Fitted and unfitted finite-element methods for elliptic equations with smooth interfaces. *IMA J. Numer. Anal.*, 7(3):283–300, 1987.

[19] Timothy J. Barth and James A. Sethian. Numerical schemes for the Hamilton-Jacobi and level set equations on triangulated domains. *J. Comput. Phys.*, 145(1):1–40, 1998.

[20] Peter Bastin and Christian Engwer. An unfitted finite element method using discontinuous Galerkin. *Internat. J. Numer. Methods Engrg.*, 79(12):1557–1576, 2009.

[21] Roland Becker, Erik Burman, and Peter Hansbo. A Nitsche extended finite element method for incompressible elasticity with discontinuous modulus of elasticity. *Comput. Methods Appl. Mech. Engrg.*, 198(41–44):3352–3360, 2009.

[22] Martin P. Bendsøe. *Optimization of Structural Topology, Shape, and Material*. Springer-Verlag, Berlin, 1995.

[23] Martin P. Bendsøe and Ole Sigmund. *Topology Optimization Theory, Methods and Applications*. Springer, 2003.

[24] Charles K. Birdsall and A. Bruce Langdon. *Plasma Physics via Computer Simulation (Series in Plasma Physics)*. Institute of Physisc Publishing, 1991.

[25] Dietrich Braess. *Finite Elements Theory, Fast Solvers and Applications in Solid Mechanics*. Cambridge University Press, second edition, 2001.

[26] James H. Bramble and J. Thomas King. A finite element method for interface problems in domains with smooth boundaries and interfaces. *Adv. Comput. Math.*, 6(2):109–138, 1996.

[27] Susanne C. Brenner. A nonconforming multigrid method for the stationary Stokes equations. *Math. Comp.*, 55(192):411–437, 1990.

[28] Susanne C. Brenner and L. Ridgway Scott. *The Mathematical Theory of Finite Element Methods*. Springer-Verlag, New York, 1994.

[29] Susanne C. Brenner and Li-Yeng Sung. Linear finite element methods for planar linear elasticity. *Math. Comp.*, 59(200):321–338, 1992.

[30] Franco Brezzi and Michel Fortin. *Mixed and hybrid finite element methods*. Springer Series in Computational Mathematics, 15. Springer-Verlag, New York, 1991.

[31] John C. Butcher. *Numerical methods for ordinary differential equations*. John Wiley & Sons, Ltd., Chichester, second edition, 2008.

[32] Donna Calhoun. A Cartesian grid method for solving the two-dimensional streamfunction-vorticity equations in irregular regions. *J. Comput. Phys.*, 176(2):231–275, 2002.

[33] Brian Camp, Tao Lin, Yanping Lin, and Weiwei Sun. Quadratic immersed finite element spaces and their approximation capabilities. *Adv. Comput. Math.*, 24(1–4):81–112, 2006.

[34] John R. Cannon. *The one-dimensional heat equation*. Addison-Wesley Publishing Company, Advanced Book Program, Reading, MA, 1984.

[35] Chuanmiao Chen. Some estimates for interpolation approximations and their applications. *Numer. Math. J. Chinese Univ.*, 6(1):35–43, 1984.

[36] Zhangxin Chen. Projection finite element methods for semiconductor device equations. *Comput. Math. Appl.*, 25(8):81–88, 1993.

[37] Zhangxin Chen. *Finite element methods and their applications.* Springer-Verlag, Berlin, 2005.

[38] Zhangxin Chen and Peter Oswald. Multigrid and multilevel methods for nonconforming Q_1 elements. *Math. Comp.*, 67(222):667–693, 1998.

[39] Zhiming Chen and Jun Zou. Finite element methods and their convergence for elliptic and parabolic interface problems. *Numer. Math.*, 79(2):175–202, 1998.

[40] Alexandre J. Chorin. Numerical solution of the Navier-Stokes equations. *Math. Comp.*, 22:745–762, 1968.

[41] So-Hsiang Chou. An immersed linear finite element method with interface flux capturing recovery. *Discrete Contin. Dyn. Syst. Ser. B*, 17(7):2343–2357, 2012.

[42] So-Hsiang Chou, Do Y. Kwak, and Kye T. Wee. Optimal convergence analysis of an immersed interface finite element method. *Adv. Comput. Math.*, 33(2):149–168, 2010.

[43] C. C. Chu, Ivan G. Graham, and Thomas Y. Hou. A new multiscale finite element method for high-contrast elliptic interface problems. *Math. Comp.*, 79(272):1915–1955, 2010.

[44] Philippe G. Ciarlet. *The finite element method for elliptic problems.*, volume 4 of *Studies in Mathematics and its Applications*. North-Holland Publishing Co., Amsterdam-New York-Oxford,, 1978.

[45] Philippe G. Ciarlet. *Mathematical Elasticity, Volume I: Three-dimensional elasticity*, volume 20 of *Studies in mathematics and its applications*. North-Holland Publishing Co., Amsterdam, 1998.

[46] Bernardo Cockburn, Dominik Schötzau, and Jing Wang. Discontinuous Galerkin methods for incompressible elastic materials. *Comput. Methods Appl. Mech. Engrg.*, 195(25–28):3184–3204, 2006.

[47] Michel Crouzeix and Pierre A. Raviart. Conforming and nonconforming finite element methods for solving the stationary Stokes equations. I. *Rev. Française Automat. Informat. Recherche Opérationnelle Sér. Rouge*, 7(R-3):33–75, 1973.

[48] Clint Dawson, Shuyu Sun, and Mary F. Wheeler. Compatible algorithms for coupled flow and transport. *Comput. Methods Appl. Mech. Engrg.*, 193(23–26):2565–2580, 2004.

[49] John Dolbow, Nicolas Moës, and Ted Belytschko. An extended finite element method for modeling crack growth with frictional contact. *Comput. Methods Appl. Mech. Engrg.*, 190(51–52):6825–6846, 2001.

[50] Jim Douglas, Jr., Juan E. Santos, Dongwoo Sheen, and Xiu Ye. Nonconforming Galerkin methods based on quadrilateral elements for second order elliptic problems. *M2AN Math. Model. Numer. Anal.*, 33(4):747–770, 1999.

[51] Miguel A. Dumett and James P. Keener. An immersed interface method for solving anisotropic elliptic boundary value problems in three dimensions. *SIAM J. Sci. Comput.*, 25(1):348–367, 2003.

[52] Yalchin Efendiev and Thomas Y. Hou. *Multiscale finite element methods. Theory and applications*. Springer, New York, 2009.

[53] Richard S. Falk. Nonconforming finite element methods for the equations of linear elasticity. *Math. Comp.*, 57(196):529–550, 1991.

[54] Ronald P. Fedkiw, Tariq Aslam, Barry Merriman, and Stanley J. Osher. A non-oscillatory eulerian approach to interfaces in multimaterial flows (the ghost fluid method). *J. Comput. Phys.*, 152(2):457–492, 1999.

[55] Huajian Gao, Yonggang Huang, and Farid F. Abraham. Continuum and atomistic studies of intersonic crack propagation. *J. Mech. Phys. Solids.*, 49(9):2113–2132, 2001.

[56] Hansen A. Gersborg, Martin P. Bendsøe, and Ole Sigmund. Topology optimization of heat conduction problems using the finite volume method. *Struct. Multidiscip. Optim.*, 31(4):251–259, 2006.

[57] Leonid V. Gibiansky and Ole Sigmund. Multiphase composites with extremal bulk modulus. *J. Mech. Phys. Solids*, 48(3):461–498, 2000.

[58] James Glimm, John W. Grove, Xiaolin Li, Keh-Ming Shyue, Yanni Zeng, and Qiang Zhang. Three-dimensional front tracking. *SIAM J. Sci. Comput.*, 19(3):703–727, 1998.

[59] James Glimm, John W. Grove, Xiaolin Li, and De Chun Tan. Robust computational algorithms for dynamic interface tracking in three dimensions. *SIAM J. Sci. Comput.*, 21(6):2240–2256, 2000.

[60] Yan Gong. *Immersed-interface finite-element methods for elliptic and elasticity interface problems*. PhD thesis, North Carolina State University, 2007.

[61] Yan Gong, Bo Li, and Zhilin Li. Immersed-interface finite-element methods for elliptic interface problems with nonhomogeneous jump conditions. *SIAM J. Numer. Anal.*, 46(1):472–495, 2007/08.

[62] Yan Gong and Zhilin Li. Immersed interface finite element methods for elasticity interface problems with non-homogeneous jump conditions. *Numer. Math. Theory Methods Appl.*, 3(1):23–39, 2010.

[63] Grégory Guyomarc'h, Chang-Ock Lee, and Kiwan Jeon. A discontinuous Galerkin method for elliptic interface problems with application to electroporation. *Comm. Numer. Methods Engrg.*, 25(10):991–1008, 2009.

[64] Ernst Hairer and Gerhard Wanner. *Solving ordinary differential equations*, volume II of *Springer Series in Computational Mathematics, 14*. Springer-Verlag, Berlin, 1996.

[65] Anita Hansbo and Peter Hansbo. An unfitted finite element method, based on Nitsche's method, for elliptic interface problems. *Comput. Methods Appl. Mech. Engrg.*, 191(47–48):5537–5552, 2002.

[66] Anita Hansbo and Peter Hansbo. A finite element method for the simulation of strong and weak discontinuities in solid mechanics. *Comput. Methods Appl. Mech. Engrg.*, 193(33–35):3523–3540, 2004.

[67] Peter Hansbo. A nonconforming rotated Q_1 approximation on tetrahedra. *Comput. Methods Appl. Mech. Engrg.*, 200(9–12):1311–1316, 2011.

[68] Peter Hansbo and Mats G. Larson. Discontinuous Galerkin and the Crouzeix-Raviart element: application to elasticity. *M2AN Math. Model. Numer. Anal.*, 37(1):63–72, 2003.

[69] Xiaoming He. *Bilinear Immersed Finite Elements For Interface Problems*. PhD thesis, Virginia Tech, 2009.

[70] Xiaoming He, Tao Lin, and Yanping Lin. Approximation capability of a bilinear immersed finite element space. *Numer. Methods Partial Differential Equations*, 24(5):1265–1300, 2008.

[71] Xiaoming He, Tao Lin, and Yanping Lin. A bilinear immersed finite volume element method for the diffusion equation with discontinuous coefficient. *Commun. Comput. Phys.*, 6(1):185–202, 2009.

[72] Xiaoming He, Tao Lin, and Yanping Lin. Interior penalty bilinear IFE discontinuous Galerkin methods for elliptic equations with discontinuous coefficient. *J. Syst. Sci. Complex.*, 23(3):467–483, 2010.

[73] Xiaoming He, Tao Lin, and Yanping Lin. Immersed finite element methods for elliptic interface problems with non-homogeneous jump conditions. *Int. J. Numer. Anal. Model.*, 8(2):284–301, 2011.

[74] Xiaoming He, Tao Lin, and Yanping Lin. The convergence of the bilinear and linear immersed finite element solutions to interface problems. *Numer. Methods Partial Differential Equations*, 28(1):312–330, 2012.

[75] Xiaoming He, Tao Lin, Yanping Lin, and Xu Zhang. Immersed finite element methods for parabolic equations with moving interface. *Numer. Methods Partial Differential Equations*, 29(2):619–646, 2013.

[76] Songming Hou, Zhilin Li, Liqun Wang, and Wei Wang. A numerical method for solving elasticity equations with interfaces. *Commun. Comput. Phys.*, 12(2):595–612, 2012.

[77] Thomas Y. Hou and Brian T. R. Wetton. Second-order convergence of a projection scheme for the incompressible Navier-Stokes equations with boundaries. *SIAM J. Numer. Anal.*, 30(3):609–629, 1993.

[78] Thomas Y. Hou and Xiao-Hui Wu. A multiscale finite element method for elliptic problems in composite materials and porous media. *J. Comput. Phys.*, 134(1):169–189, 1997.

[79] H. J. Jou, Perry H. Leo, and John S. Lowengrub. Microstructural evolution in inhomogeneous elastic media. *J. Comput. Phys.*, 131(1):109–148, 1997.

[80] Benjamin L. Vaughan Jr., Bryan G. Smith, and David L. Chopp. A comparison of the extended finite element method with the immersed interface method for elliptic equations with discontinuous coefficients and singular sources. *Commun. Appl. Math. Comput. Sci.*, 1:207–228, 2006.

[81] Damir Juric and Grétar Tryggvason. A front-tracking method for dendritic solidification. *J. Comput. Phys.*, 123(1):127–148, 1996.

[82] Raed Kafafy, Tao Lin, Yanping Lin, and Joseph Wang. Three-dimensional immersed finite element methods for electric field simulation in composite materials. *Internat. J. Numer. Methods Engrg.*, 64(7):940–972, 2005.

[83] Raed Kafafy and Joseph Wang. Whole ion optics gridlet simulations using a hybrid-grid immersed-finite-element particle-in-cell code. *J. Propulsion Power*, 23(1):59–68, 2007.

[84] Raed Kafafy, Joseph Wang, and Tao Lin. A hybrid-grid immersed-finite-element particle-in-cell simulation model of ion optics plasma dynamics. *Dyn. Contin. Discrete Impuls. Syst. Ser. B Appl. Algorithms*, 12b:1–16, 2005.

[85] Petr Klouček, Bo Li, and Michell Luskin. Analysis of a class of nonconforming finite elements for crystalline microstructures. *Math. Comp.*, 65(215):1111–1135, 1996.

[86] Petr Klouček, Bo Li, and Michell Luskin. Nonconforming finite element approximation of crystalline microstructure. *Math. Comp.*, 67(223):917–946, 1998.

[87] Do Y. Kwak, Kye T. Wee, and Kwang S. Chang. An analysis of a broken P_1-nonconforming finite element method for interface problems. *SIAM J. Numer. Anal.*, 48(6):2117–2134, 2010.

[88] Chang-Ock Lee, Jongwoo Lee, and Dongwoo Sheen. A locking-free nonconforming finite element method for planar linear elasticity. *Adv. Comput. Math.*, 19(1–3):277–291, 2003.

[89] Perry H. Leo, John S. Lowengrub, and Qing Nie. Microstructural evolution in orthotropic elastic media. *J. Comput. Phys.*, 157(1):44–88, 2000.

[90] Randall J. LeVeque and Zhilin Li. The immersed interface method for elliptic equations with discontinuous coefficients and singular sources. *SIAM J. Numer. Anal.*, 31(4):1019–1044, 1994.

[91] Randall J. LeVeque and Zhilin Li. Immersed interface methods for Stokes flow with elastic boundaries or surface tension. *SIAM J. Sci. Comput.*, 18(3):709–735, 1997.

[92] Zhilin Li. Immersed interface methods for moving interface problems. *Numer. Algorithms*, 14(4):269–293, 1997.

[93] Zhilin Li. The immersed interface method using a finite element formulation. *Appl. Numer. Math.*, 27(3):253–267, 1998.

[94] Zhilin Li and Kazufumi Ito. *The immersed interface method. Numerical solutions of PDEs involving interfaces and irregular domains.* Frontiers in Applied Mathematics, 33. Society for Industrial and Applied Mathematics (SIAM), Philadelphia, PA, 2006.

[95] Zhilin Li, Tao Lin, Yanping Lin, and Robert C. Rogers. An immersed finite element space and its approximation capability. *Numer. Methods Partial Differential Equations*, 20(3):338–367, 2004.

[96] Zhilin Li, Tao Lin, and Xaiohui Wu. New Cartesian grid methods for interface problems using the finite element formulation. *Numer. Math.*, 96(1):61–98, 2003.

[97] Zhilin Li and Xingzhou Yang. An immersed finite element method for elasticity equations with interfaces. In *Contemp. Math., 383*, pages 285–298. Amer. Math. Soc., 2005.

[98] Tao Lin, Yanping Lin, Robert Rogers, and M. Lynne Ryan. A rectangular immersed finite element space for interface problems. *Adv. Comput. Theory Pract.*, 7:107–114, 2001.

[99] Tao Lin, Yanping Lin, and Weiwei Sun. Error estimation of a class of quadratic immersed finite element methods for elliptic interface problems. *Discrete Contin. Dyn. Syst. Ser. B*, 7(4):807–823, 2007.

[100] Tao Lin, Yanping Lin, Weiwei Sun, and Zheng Wang. Immersed finite element methods for 4th order differential equations. *J. Comput. Appl. Math.*, 235(13):3953–3964, 2011.

[101] Tao Lin, Yanping Lin, and Xu Zhang. Immersed finite element method of lines for moving interface problems with nonhomogeneous flux jump. *Contemp. Math.*, 2013. to appear.

[102] Tao Lin, Yanping Lin, and Xu Zhang. A method of lines based on immersed finite elements for parabolic moving interface problems. *Adv. Appl. Math. Mech.*, 2013. to appear.

[103] Tao Lin, Yanping Lin, and Xu Zhang. Partially penalized immersed finite element methods for elliptic interface problems. *submitted*, 2013.

[104] Tao Lin and Dongwoo Sheen. The immersed finite element method for parabolic problems with the Laplace transformation in time discretization. *Int. J. Numer. Anal. Model.*, 10(2):298–313, 2013.

[105] Tao Lin, Dongwoo Sheen, and Xu Zhang. A locking-free immersed finite element method for planar elasticity interface problems. *J. Comput. Phys.*, 2013. to appear.

[106] Tao Lin and Joseph Wang. An immersed finite element electric field solver for ion optics modeling. In *Proceedings of AIAA Joint Propulsion Conference*, Indianapolis, IN, Jul 2002. AIAA.

[107] Tao Lin and Joseph Wang. The immersed finite element method for plasma particle simulation. In *Proceedings of AIAA Aerospace Sciences Meeting*, Reno, NV, Jan 2003. AIAA.

[108] Tao Lin and Xu Zhang. Linear and bilinear immersed finite elements for planar elasticity interface problems. *J. Comput. Appl. Math.*, 236(18):4681–4699, 2012.

[109] Tao Lin and Xu Zhang. Interior penalty immersed finite element discontinuous Galerkin methods for elliptic interface problems. *in preparation*, 2013.

[110] Mark N. Linnick and Hermann F. Fasel. A high-order immersed interface method for simulating unsteady incompressible flows on irregular domains. *J. Comput. Phys.*, 204(1):157–192, 2005.

[111] Xu-Dong Liu, Ronald P. Fedkiw, and Myungjoo Kang. A boundary condition capturing method for Poisson's equation on irregular domains. *J. Comput. Phys.*, 160(1):151–178, 2000.

[112] Xu-Dong Liu and Thomas C. Sideris. Convergence of the ghost fluid method for elliptic equations with interfaces. *Math. Comp.*, 72(244):1731–1746, 2003.

[113] Shipeng Mao and Shaochun Chen. A quadrilateral nonconforming finite element for linear elasticity problem. *Adv. Comput. Math.*, 28(1):81–100, 2008.

[114] William McLean. *Strongly elliptic systems and boundary integral equations*. Cambridge University Press, Cambridge, 2000.

[115] Nicolas Moës, John Dolbow, and Ted Belytschko. A finite element method for crack growth without remeshing. *Internat. J. Numer. Methods Engrg.*, 46(1):131–150, 1999.

[116] Stanley Osher and Ronald Fedkiw. *Level set methods and dynamic implicit surfaces*. Applied Mathematical Sciences, 153. Springer-Verlag, New York, 2003.

[117] Stanley Osher and James A. Sethian. Fronts propagating with curvature-dependent speed: algorithms based on Hamilton-Jacobi formulations. *J. Comput. Phys.*, 79(1):12–49, 1988.

[118] Chunjae Park and Dongwoo Sheen. P_1-nonconforming quadrilateral finite element methods for second-order elliptic problems. *SIAM J. Numer. Anal.*, 41(2):624–640, 2003.

[119] Richard B. Pember, John B. Bell, Phillip Colella, William Y. Crutchfield, and Michael L. Welcome. An adaptive Cartesian grid method for unsteady compressible flow in irregular regions. *J. Comput. Phys.*, 120(2):278–304, 1995.

[120] Charles S. Peskin. Numerical analysis of blood flow in the heart. *J. Computational Phys.*, 25(3):220–252, 1977.

[121] Charles S. Peskin. The immersed boundary method. *Acta Numer.*, 11:479–517, 2002.

[122] Juhani Pitkäranta and Rolf Stenberg. Analysis of some mixed finite element methods for plane elasticity equations. *Math. Comp.*, 41(164):399–423, 1983.

[123] Rolf Ranacher and Stefan Turek. Simple nonconforming quadrilateral Stokes element. *Numer. Methods Partial Differential Equations*, 8(2):97–111, 1992.

[124] Satish C. Reddy and Lloyd N. Trefethen. Stability of the method of lines. *Numer. Math.*, 62(2):235–267, 1992.

[125] Béatrice Rivière. *Discontinuous Galerkin methods for solving elliptic and parabolic equations*. Frontiers in Applied Mathematics, 35. Society for Industrial and Applied Mathematics (SIAM), Philadelphia, PA, 2008.

[126] Béatrice Rivière, Simon Shaw, Mary F. Wheeler, and John R. Whiteman. Discontinuous Galerkin finite element methods for linear elasticity and quasistatic linear viscoelasticity. *Numer. Math.*, 95(2):347–376, 2003.

[127] Béatrice Rivière, Mary F. Wheeler, and Vivette Girault. Improved energy estimates for interior penalty, constrained and discontinuous Galerkin methods for elliptic problems. I. *Comput. Geosci.*, 3(3–4):337–360, 1999.

[128] Alexandre M. Roma, Charles S. Peskin, and Marsha J. Berger. An adaptive version of the immersed boundary method. *J. Comput. Phys.*, 153(2):509–534, 1999.

[129] Mohamed Ben Romdhane. *Higher-degree immersed finite elements for second-rrder elliptic interface problems*. PhD thesis, Virginia Tech, 2011.

[130] Stefan A. Sauter and R. Warnke. Composite finite elements for elliptic boundary value problems with discontinuous coefficients. *Computing*, 77(1):29–55, 2006.

[131] James A. Sethian. *Level set methods and fast marching methods*. Cambridge Monographs on Applied and Computational Mathematics, 3. Cambridge University Press, Cambridge, second edition edition, 1999.

[132] Ole Sigmund. Design of multiphysics actuators using topology optimization Part II: Two-material structures. *Comput. Methods Appl. Mech. Engrg.*, 190(49-50):6605–6627, 2001.

[133] Ivan S. Sokolnikoff. *Mathematical theory of elasticity*. McGraw-Hill Book Company, Inc., New York-Toronto-London, 2d ed. edition, 1956.

[134] Rolf Stenberg. A family of mixed finite elements for the elasticity problem. *Numer. Math.*, 53(5):513–538, 1988.

[135] Natarajan Sukumar, David L. Chopp, Nicolas Moës, and Ted Belytschko. Modeling holes and inclusions by level sets in the extended finite-element method. *Comput. Methods Appl. Mech. Engrg.*, 190(46–47):6183–6200, 2001.

[136] Adrian P. Sutton and Robert W. Balluffi. *Interfaces in Crystalline Materials*. Oxford Science Publications, 1995.

[137] Vidar Thomée. *Galerkin finite element methods for parabolic problems*. Springer Series in Computational Mathematics, 25. Springer-Verlag, Berlin, second edition, 2006.

[138] Salih Ozen Unverdi and Grétar Tryggvason. A front-tracking method for dendritic solidification. *J. Comput. Phys.*, 100(1):25–37, 1992.

[139] Sylvain Vallaghé and Théodore Papadopoulo. A trilinear immersed finite element method for solving the electroencephalography forward problem. *SIAM J. Sci. Comput.*, 32(4):2379–2394, 2010.

[140] Jan G. Verwer and Jesús M. Sanz-Serna. Convergence of method of lines approximations to partial differential equations. *Computing*, 33(3–4):297–313, 1984.

[141] Joseph Wang, Xiaoming He, and Yong Cao. Modeling electrostatic levitation of dust particles on lunar surface. *IEEE TRANSACTIONS ON PLASMA SCIENCE*, 36(5):2459–2466, 2008.

[142] Kaixin Wang, Hong Wang, and Xijun Yu. An immersed Eulerian-Lagrangian localized adjoint method for transient advection-diffusion equations with interfaces. *Int. J. Numer. Anal. Model.*, 9(1):29–42, 2012.

[143] Shuyan Wang and Huanzhen Chen. The optimal convergence analysis for an immersed linite element method. In *2011 International Conference on Information Science and Technology (ICIST 2011)*, pages 255–258, Nanjing, Jiangsu, China, 2011.

[144] Mary F. Wheeler. An elliptic collocation-finite element method with interior penalties. *SIAM J. Numer. Anal.*, 15(1):152–161, 1978.

[145] Thomas P. Wihler. Locking-free adaptive discontinuous Galerkin FEM for linear elasticity problems. *Math. Comp.*, 75(255):1087–1102, 2006.

[146] Joseph Wloka. *Partial differential equations*. Cambridge University Press, Cambridge, 1987.

[147] Chin-Tien Wu, Zhilin Li, and Ming-Chih Lai. Adaptive mesh refinement for elliptic interface problems using the non-conforming immersed finite element method. *Int. J. Numer. Anal. Model.*, 8(3):466–483, 2011.

[148] Haijun Wu and Yuanming Xiao. An unfitted hp-interface penalty finite element method for elliptic interface problems. *Submitted*, page arXiv:1007.2893v1, 2010.

[149] Jinchao Xu. Estimate of the convergence rate of the finite element solutions to elliptic equation of second order with discontinuous coefficients. *Natural Science Journal of Xiangtan University*, 1:1–5, 1982.

[150] Xingzhou Yang. *Immersed interface method for elasticity problems with interfaces*. PhD thesis, North Carolina State University, 2004.

[151] Xingzhou Yang, Bo Li, and Zhilin Li. The immersed interface method for elasticity problems with interfaces. *Dyn. Contin. Discrete Impuls. Syst. Ser. A Math. Anal.*, 10(5):783–808, 2003.

[152] A. Zafarullah. Application of the method of lines to parabolic partial differential equations with error estimates. *J. Assoc. Comput. Mach.*, 17:294–302, 1970.

[153] Zhimin Zhang. Analysis of some quadrilateral nonconforming elements for incompressible elasticity. *SIAM J. Numer. Anal.*, 34(2):640–663, 1997.

[154] Shan Zhao and Guowei Wei. High-order FDTD methods via derivative matching for Maxwell's equations with material interfaces. *J. Comput. Phys.*, 200(1):60–103, 2004.

[155] Yongchen Zhou and Guowei Wei. On the fictitious-domain and interpolation formulations of the matched interface and boundary (MIB) method. *J. Comput. Phys.*, 219(1):228–246, 2006.

[156] Yongcheng Zhou, Shan Zhao, Michael Feig, and Guowei Wei. High order matched interface and boundary method for elliptic equations with discontinuous coefficients and singular sources. *J. Comput. Phys.*, 213(1):1–30, 2006.

[157] Olgierd C. Zienkiewicz and Robert L. Taylor. *The Finte Element Method: Vol 2, Solid Mechanics*. Butterworth-Heinemann, 2000.